Doctoral School of Geosciences

The hydrocarbon system of the central part of the Hungarian Palaeogene Basin (Pannonian Basin)

Az Észak-magyarországi Paleogén-medence központi részének szénhidrogén rendszere (Pannon-medence)

Ph.D. Dissertation

Author

Sándor Körmös

Supervisor

Félix Schubert Ph.D.

assistant professor, Department of Mineralogy, Geochemistry and Petrology

Department of Mineralogy, Geochemistry and Petrology

Faculty of Science and Informatics

University of Szeged

2022

Szeged

This page was left blank intentionally.

Table of contents

List of Figures

List of Tables

List of supplementary Figures

List of supplementary Tables

Abbreviations used in the dissertation

II. and III. Chapter

%Rr or Rr – mean random vitrinite reflectance
Ad–3 – Alcsútdoboz–3
ASTM – American Society for Testing and Materials
avg. – average
Bgy–5 – Balassagyarmat–5
BI – bitumen index
C_{27} – an organic compound with carbon numbers indicated
C_{31}(R) – 17α,21β–C_{31} (22R) homohopane
C_{34}(S) – 17α,21β–C_{34} (22S) homohopane
C_{35}(S) – 17α,21β–C_{35} (22S) homohopane
$C_{35}/C_{31–35}$ – 17α,21β–C_{35} homohopane/17α,21β–$C_{31–35}$ homohopane
C_{Eq} – calcite equivalent
CPI – carbon preference index
Csv–1 – Cserépváralja–1
DBT – dibenzothiophene
DMDBT – dimethyl–dibenzothiophene
DMN – dimethylnapthalene
DMP – dimethylphenanthrene
EOM – extractable organic matter
GC – gas chromatography
GWI_{AC} – groundwater influence index
H – 17α,21β–C_{30} hopane
HI – hydrogen index
i-C_{13} – acyclic isoprenoid with carbon numbers indicated
ICCP – International Committee for Coal Petrology
K–20 – Kosd–20
max. – maximum
MDBT – methyl–dibenzothiophene
MGSH – Mining and Geological Survey of Hungary
min. – minimum
mmf – mineral matter free
MN – methylnaphthalene
MP – methylphenanthrene
N – naphthalene
n-C_{13} – normal alkane with carbon numbers indicated
n-$C_{15–19}$ – short-chain normal alkanes
n-$C_{21–25}$ – mid-chain normal alkanes
n-$C_{27–31}$ or *n*-C_{27+} – long-chain normal alkanes
NH – 17α,21β–C_{30} norhopane
NP21, NP23 – nannoplankton zones
NSO – nitrogen, sulphur and oxygen-containing compounds
Nv–1 – Noszvaj–1
Ol – 18α(H)–oleanane
P – phenanthrene
Ph – phytane
PI – production index
PP – petroleum potential
Pr – pristane
QI – quality index
$Rc_{(MPI\ 1)}$ – calculated vitrinite reflectance index based on methylphenanthrene index
S1 – free hydrocarbons recorded during Rock-Eval pyrolysis
S2 – hydrocarbons generated during Rock-Eval pyrolysis
TC – total carbon
TeT – tetracyclic terpane
TIC – total inorganic carbon
Tm – 18α–C_{27} trisnorneohopane
Tmax – temperature of maximum hydrocarbon generation during Rock-Eval pyrolysis
TMDBT – trimethyl–dibenzothiophene
TMN – trimethylnapthalene
TMP – trimethylphenanthrene
TOC – total organic carbon
Ts – 17α–C_{27} trisnorhopane
TS – total sulphur
TT – tricyclic terpane
UV – ultraviolet
V–75 – Varbó–75
V-PDB – Vienna Pee Dee Belemnite standard
W–1 and so on – Well–1 and so on
W–1o and so on – oil sample from Well–1 and so on
$\delta^{13}C_{ARO}$ – stable carbon isotope composition of the aromatic hydrocarbon fractions
$\delta^{13}C_{SAT}$ – stable carbon isotope composition of the saturated hydrocarbon fractions

IV. Chapter

AI – aqueous inclusion
avg – average
BSE – backscattered electron image
Cal_{EQ} – equant calcite
Cal_{EU} – euhedral calcite
Cal_{FF} – fracture-filling calcite

CIE – Commission Internationale d'Eclairage
CL – cathodoluminescence
dol1 – planar dolomite
dol2 – non-planar dolomite
Eh – activity of electrons
FI – fluid inclusion
FIA – fluid inclusion assemblage
HCFI – hydrocarbon-bearing fluid inclusion
L_{aq} – aqueous liquid phase
L_{hc} – hydrocarbon-bearing liquid phase
MD – measured depth
n=x – number of the analysed samples
NE – northeast
pH – activity of hydrogen ions
PPL – plane-polarized light
RWL – reflected white light
S_{bit} – solid bitumen phase
SE – secondary electron image
SW – southwest
T_h – homogenisation temperature
T_m(Ice) – final ice melting temperature
UV – ultraviolet
V – vapour phase
V-PDB – Vienna Pee Dee Belemnite standard
V-SMOW – Vienna Standard Mean Ocean Water standard
W–1 and so on – Well–1 and so on
XPL – cross-polarized light
$\delta^{13}C$ – stable carbon isotope
$\delta^{18}O$ – stable oxygen isotope
φ_V – volume fractions of the vapour *vs.* liquid phases

I. CHAPTER

Introduction and aims

The growth of the global population during the last few decades and, as a consequence, the rise of the average living standard of the society, resulted in significant use of raw materials. A slow but continuous transformation of the energy market towards renewables, so-called green energy sources, has begun in the twentieth century. Regardless of the appropriate natural resource, the utilization of new scientific results is essential in the exploration and production phase for the stakeholders of the energy industry, in order to preserve ecological and natural values, as well as to ensure sustainable economic development. Despite the social acceptance of renewable energy sources, the community of the twenty-first century is still accustomed to hydrocarbon-based mobility and energy production.

All geological objects and processes, necessary for the generation and accumulation of hydrocarbons are considered as the hydrocarbon or petroleum system. The concept was developed in the 1970s (Magoon and Dow, 1994). The key geological elements are the source rock, reservoir rock, seal rock and overburden rock. Whereas the generation, migration and trapping of hydrocarbons are extremely important processes. Without them, no economic hydrocarbon accumulation can develop. The research of certain elements of the hydrocarbon system is crucial to exploring economic production technology and future research directions. Therefore, detailed analyses of an irreplaceable element of the hydrocarbon system are fundamental to satisfying the growing needs.

In the Pannonian Basin, there are six known hydrocarbon systems and the Palaeogene petroleum system is one of the most complex one (Dolton 2006), even though that detailed and published investigations of the key elements are scarce. The Palaeogene hydrocarbon system belongs to the Hungarian Palaeogene Basin, which is located in the northern-central part of Hungary. The Neogene Pannonian Basin formed part of the Central Paratethys and is underlain by the Eocene and Oligocene sediments of the Hungarian Palaeogene Basin (Tari et al., 1993). The Hungarian Palaeogene Basin is interpreted as a retro-arc flexural foreland basin, where the depositional facies migrated towards the east-northeast according to the present position (Tari et al., 1993; Kováč et al., 2016). The tectonic evolution has been related to normal faulting and strike-slip regimes (Palotai, 2013 and references therein). The term Palaeogene Basin comprises all sedimentary sequences, forming a single cycle from the Eocene to the Early Ottnangian (Sztanó and Tari, 1993).

Hydrocarbon exploration has begun in the early twentieth century with limited exploration results. Since the appropriate tools for the exploration geologists developed, more and more attention was focused on the Hungarian Palaeogene Basin (Kovács and Gyuricza, 2014). The Palaeogene sediments are unconformably overly the Mesozoic basement. The generalized lithostratigraphy begins with sediments showing a continuous upward transition from a terrigenous to a lagoonal environment, the Eocene Kosd Formation (Gidai, 1978; Less, 2005). The Kosd Formation is overlain by the shelf deposits of the Szépvölgy Limestone Formation (Kázmér, 1985). The continued subsidence and the east-northeast trending of the depositional facies caused the deposition of the Buda Marl Formation under oxygen-depleted conditions across the Eocene-Oligocene transition (Less, 2005; Nagymarosy and Báldi-Beke, 1988; Ozsvárt et al., 2016). The sediments of the Tard Clay Formation accumulated in a euxinic basin (Báldi, 1984, Bechtel et al., 2012) then the Kiscell Clay Formation settled down in a well-oxygenated depositional environment (Báldi and Báldi-Beke, 1985). The sedimentary sequence of the Hungarian Palaeogene Basin is covered by thick Neogene sediments.

In the last few decades, several hydrocarbon reservoirs have been discovered in the Hungarian Palaeogene Basin. Hydrocarbons were detected in the fractured and weathered Mesozoic basement rocks in the research area. The basal conglomerate and breccia and the sandstone sequence of the Kosd Formation also form reservoirs and host substantial amounts of hydrocarbons. The karstified Szépvölgy Limestone and turbidite sandstone bodies within the Kiscell Clay Formation and the clastic sediments of the Miocene formations also serve as targets of exploration activities (Dolton, 2006). The reservoirs were discovered along with various structural, stratigraphic and combination trap types within the study area (Kokai, 1994; Dolton, 2006) and the faults are believed to conduct hydrocarbons toward the reservoir rocks.

Fine-grained, organic matter-rich sediments within the Eocene and Oligocene succession were recognized as potential source rocks (e.g., Badics and Vető, 2012; Bechtel et al., 2012; Brukner-Wein et al., 1990; Milota et al., 1995). It is widely accepted that the Lower Oligocene Tard Clay Formation provides the most important source rocks (Bechtel et al., 2012; Brukner-Wein et al., 1990; Hertelendi and Vető, 1991; Milota et al., 1995). However, the Late Eocene Buda Marl Formation (Sachsenhofer et al., 2018a, 2018b) and Late Oligocene Kiscell Clay Formation (Milota et al., 1995) were also considered as potential source rocks.

Boreholes, drilled in the early 2000s in the southern-central part of the Hungarian Palaeogene Basin, penetrated coal-bearing sequences of the Kosd Formation beneath Oligocene source rocks. The Oligocene source rocks have been investigated by several authors (e.g., Badics and Vető, 2012; Bechtel et al., 2012; Milota et al., 1995; Sachsenhofer et al., 2018), but the Eocene Kosd Formation remained largely uninvestigated. Comprehensive organic geochemical studies have only been performed on sediments of the Tard Clay Formation (Bechtel et al., 2012), whereas in-depth investigations are still missing for the Kosd, Buda Marl and Kiscell Clay formations. Furthermore, the detailed analysis of crude oils and thorough oil-to-source rock correlation are also absent. Besides the missing organic geochemical analyses of the potential source rocks and oil-to-source rock correlation, the Eocene mixed siliciclastic-carbonate reservoir section also waits for detailed investigation. Despite the known fact that the initial high production capacity can only be maintained by multiple workover activities (Radovics et al., 2017).

This study focuses on the southern-central part of the Hungarian Palaeogene Basin. The aims are to (i) enhance the understanding of the depositional environment and organic matter sources of the coal-bearing Kosd Formation, and (ii) estimate the hydrocarbon potential of deep Eocene Kosd coal. Moreover, to (iii) advance the knowledge of the petroleum system by characterising the maturity and source rock potential of the Upper Eocene (Kosd and Buda Marl formations) and Oligocene (Tard Clay and Kiscell Clay formations) succession, (iv) determine the source rock facies of crude oils produced in several oil fields in the Hungarian Palaeogene Basin, and (v) correlate these crude oils to a specific source rock formation. Furthermore, to (vi) describe specific diagenetic processes that determine the quality of the Eocene mixed siliciclastic-carbonate reservoirs and their surroundings in the Hungarian Palaeogene Basin.

To achieve these goals, organic petrological and organic geochemical analyses were performed. Maceral composition, petrography-based facies indicators and biomarker analysis were used to reconstruct the paleoenvironments and peat-forming floral changes. Maturity and source rock potential of the Palaeogene succession were assessed using numerous Rock-Eval data from deep boreholes. Biomarker data of the crude oil samples were applied to reconstruct the depositional environment of their source rocks. Oil-to-source rock correlation was based on biomarker and compound-specific isotope data from oil and source rock samples. Moreover, inorganic optical petrography, qualitative and semi-quantitative analysis of the mineral phases, stable isotope and fluid inclusion analyses were performed to understand the diagenetic processes of the Eocene mixed siliciclastic-carbonate succession.

II. CHAPTER

Petrographic and organic geochemical study of the Eocene Kosd Formation (northern Pannonian Basin): Implications for paleoenvironment and hydrocarbon source potential

Sándor Körmös

University of Szeged, Department of Mineralogy, Geochemistry and Petrology, Egyetem u. 2, H-6722 Szeged, Hungary; MOL Plc, Október huszonharmadika u. 18, H-1117 Budapest, Hungary

email address: sandor.kormos@geo.u-szeged.hu

Achim Bechtel

Montanuniversität Leoben, Petroleum Geology, Peter-Tunner-str. 5, A-8700 Leoben, Austria

email address: Achim.Bechtel@outlook.de

Reinhard F. Sachsenhofer

Montanuniversität Leoben, Petroleum Geology, Peter-Tunner-str. 5, A-8700 Leoben, Austria

email address: reinhard.sachsenhofer@unileoben.ac.at

Balázs Géza Radovics

MOL Plc, Október huszonharmadika u. 18, H-1117 Budapest, Hungary

email address: BGRadovics@mol.hu

Katalin Milota

MOL Plc, Október huszonharmadika u. 18, H-1117 Budapest, Hungary

email address: KMilota@mol.hu

Félix Schubert

University of Szeged, Department of Mineralogy, Geochemistry and Petrology, Egyetem u. 2, H-6722 Szeged, Hungary

email address: schubert@geo.u-szeged.hu

International Journal of Coal Geology

228, 103555 (2020) DOI 10.1016/j.coal.2020.103555

Petrographic and organic geochemical study of the Eocene Kosd Formation (northern Pannonian Basin): Implications for paleoenvironment and hydrocarbon source potential

by: Sándor Körmös, Achim Bechtel, Reinhard F. Sachsenhofer, Balázs Géza Radovics, Katalin Milota, Félix Schubert

Abstract

The Eocene Kosd Formation forms part of the Hungarian Palaeogene Basin. The coal measure of this formation was investigated using an 18 m drill core from borehole W–1. Petrographic and organic geochemical investigations (Rock-Eval pyrolysis, biomarker analysis) were performed in order to characterise the depositional environment, to determine the source of the organic matter within, and to assess the hydrocarbon generative potential.

The presence of marine fossils, high TOC/TS ratios and ash yields show that the deposition of the coal measure occurred in a marine delta with individual coal layers accumulating in low-lying, rheotrophic mires. The distribution of land plant-derived biomarkers demonstrates that the peat-forming vegetation was dominated by angiosperms, but the relative contribution of gymnosperms varied through time. In addition to land plants, algae and aquatic macrophytes contributed to the biomass. This dense vegetation established a CO_2-limited environment forcing aquatic plants to utilise HCO_3^- during photosynthesis. The marine environment, as well as the predominance of carbonate rocks in the hinterland, caused slightly alkaline conditions, which, together with reduced oxygen availability, stimulated sulphate-reducing bacterial activity and the microbial degradation of plant remains. Consequently, Kosd Formation coal is very rich in sulphur (up to 8.8 wt%). Moreover, the coal contains vitrinite with a strong orange-brown fluorescence colour and swells strongly during pyrolysis. These features are typical for coals with marine influences.

Vitrinite reflectance, Tmax, and biomarker proxies indicate that the organic matter is thermally mature and that the Kosd coal reached the high volatile bituminous rank in the deep borehole (~2.6 km depth). Rock-Eval parameters imply that the coal is gas- and oil-prone and reached the maturity threshold critical for first gas generation and the onset of oil expulsion.

2.1. Introduction

During the Eocene, the Mesozoic Tethys Ocean decayed into a series of intercontinental seas (Rögl, 1999). This new configuration of land and sea areas modified oceanic circulation and climate (Popov et al., 2001). In the Late Eocene, Europe formed an archipelago and was enclosed by a subtropical sea, where variations in sea level significantly affected the distribution of depositional environments (Sachsenhofer et al., 2018).

The Hungarian and Slovenian Palaeogene Basin is a predecessor of the Pannonian Basin (Tari et al., 1993). During the Eocene, sedimentation in this basin was characterised by a generally transgressive nature, where depocenters shifted north-eastwards through time (Báldi and Báldi-Beke, 1985; Kováč et al., 2016). Hence, coal formation started earlier in the area of the present-day Transdanubian Mountains (the Middle Eocene Dorog Coal Formation) than in the North Hungarian Mountains (the Upper Eocene coal-bearing Kosd Formation; Báldi-Beke, 2003a, b; Gidai, 1978; Hámor-Vidó and Hámor, 2007; Figs. II.1, II.2). The Kosd Formation includes economic coal seams (Gidai, 1978). The Kosd coalfield (location is shown in Fig.

II.1) is registered in the national coal cadastre of Hungary (MGSH, 2019), however, mining of this sub-bituminous coal ended in the 1930s (Némedi Varga, 2010).

Maceral composition, petrography-based facies indicators and biomarker analysis became essential tools during the last decades for the reconstruction of paleoenvironments and peat-forming floral changes (e.g., Bechtel et al., 2003, 2007; Gross et al., 2015; Sachsenhofer et al., 2010). Additionally, the stable carbon isotope composition of individual biological markers allows the identification of specific sources (Hayes et al., 1987). Primary producers fix inorganic carbon through photosynthesis, which leads to specific fractionation of carbon isotopes (Diefendorf and Freimuth, 2017; Holtvoeth et al., 2019). Ficken et al. (1998a) found that accumulating organic matter experiences rapid microbial degradation and associated diagenetic changes in the top few centimetres of sediment. Other studies, however, have reported no significant changes in $\delta^{13}C$ during early diagenesis (Li et al., 2017, and references therein). The thermal maturation of organic matter may nonetheless affect the carbon isotope composition (Bjorøy et al., 1992; Clayton, 1991; Rooney et al., 1998). The degree of isotope fractionation depends on the temperature, but the effect is limited to a range of 2‰ as maturity progresses (Clayton, 1991; Schoell, 1984). Therefore, biologically controlled isotope compositions can be used to identify precursor sources after diagenesis (e.g., Collister et al., 1994; Freeman et al., 1990; Rieley et al., 1991).

The current study is based on samples from borehole W–1, located about 50 km southeast of the abandoned Kosd coalfield (Fig. II.1), which drilled the Eocene succession beneath potential Oligocene hydrocarbon source rocks. Whereas the Oligocene source rocks have been investigated by several authors (e.g., Badics and Vető, 2012; Bechtel et al., 2012; Milota et al., 1995; Sachsenhofer et al., 2018), the Eocene Kosd Formation remained largely uninvestigated.

The aims of this study are therefore to enhance understanding of the depositional environment and organic matter sources in this formation, and to estimate the hydrocarbon potential of deep Eocene Kosd coal. To achieve this goal, organic petrological and organic geochemical analyses were performed.

2.2. Geological setting

A series of sub-bituminous coalfields of the Middle Eocene Dorog Coal Formation occur along the Transdanubian Mountains (Hámor-Vidó and Hámor, 2007; Bechtel et al., 2007). Eocene coal in the North Hungarian Mountains belongs to the Upper Eocene Kosd Formation (Fig. II.1; Gidai, 1978; Báldi-Beke, 2003a, 2003b). The diachronous development of depocenters followed the gradual north-eastward trend of the Eocene transgression (Báldi and Báldi-Beke, 1985). In the western part of the Transdanubian Mountains, the initial transgression took place during the early Lutetian. The next transgression flooded the entire Transdanubian Range during the late Lutetian (the Dorog Coal Formation; Fig. II.2). In contrast, for the eastern part of the Transdanubian Mountains and the North Hungarian Mountains, the transgression occurred during the Bartonian and Priabonian (the Kosd Formation; Fig. II.2; Báldi-Beke, 2003a, b; Kercsmár et al., 2015; Kováč et al., 2016).

The Kosd Formation crops out in small areas throughout the Buda Hills, the Left Side Blocks of Danube and the Bükk Mountains. In the subsurface, it extends towards the south into the Gödöllő Hills (Fig. II.1), where it was encountered by several boreholes (e.g., Bauer et al., 2016; Palotai and Csontos, 2010).

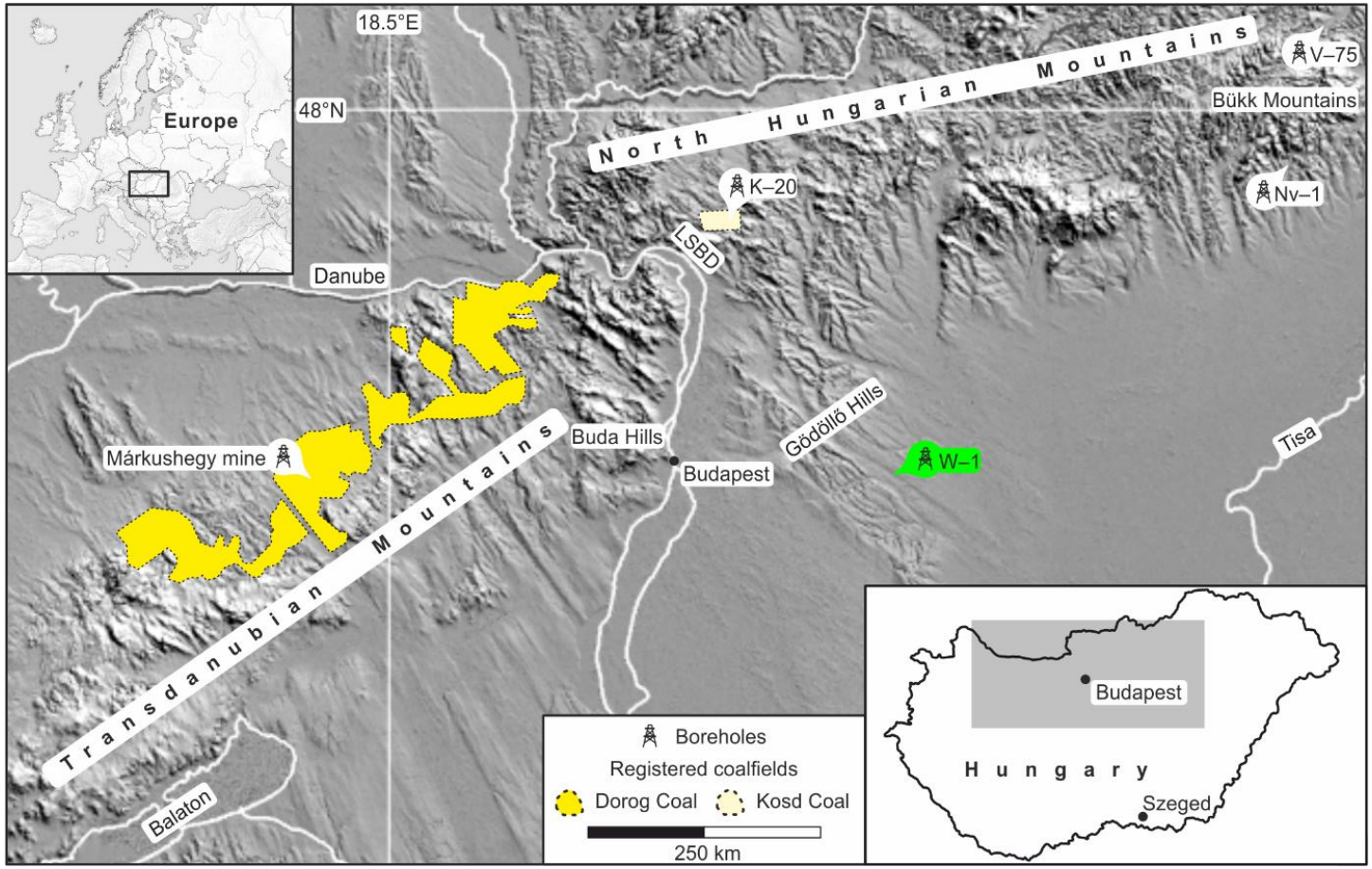

Fig. II.1. Location of registered Eocene sub-bituminous coalfields: Kosd–20 (K–20), Varbó–75 (V–75), Noszvaj–1 (Nv–1), and the investigated W–1 boreholes. Modified following the digital elevation model and digital coal cadastre of Hungary (Horváth et al., 2005; MGSH, 2019). LSBD – Left Side Blocks of Danube.

The Kosd Formation unconformably overlies the Mesozoic basement, which belongs to different mega-units. In the Buda Hills and the Left Side Blocks of Danube (Transdanubian Range Unit) the basement is represented by Ladinian to Norian platform carbonates (e.g., the Budaörs Dolomite Formation; the Dachstein Limestone Formation), and cherty basinal carbonates (e.g., the Mátyáshegy Formation; Haas and Kovács, 2012). In the Bükk Mountains (Bükk Unit), in addition to Ladinian to Norian platform carbonates (e.g., the Berva Limestone Formation; the Kisfennsík Limestone Formation) and basinal carbonates (the Felsőtárkány Limestone Formation), a deep marine Middle to Upper Jurassic sedimentary succession, with debris flows and turbidites, are present (the Mónosbél Group; Pelikán, 2005). The Mesozoic strata were uplifted during the Late Cretaceous and as a consequence of the subaerial exposure intense karstification occurred (Haas and Kovács, 2012).

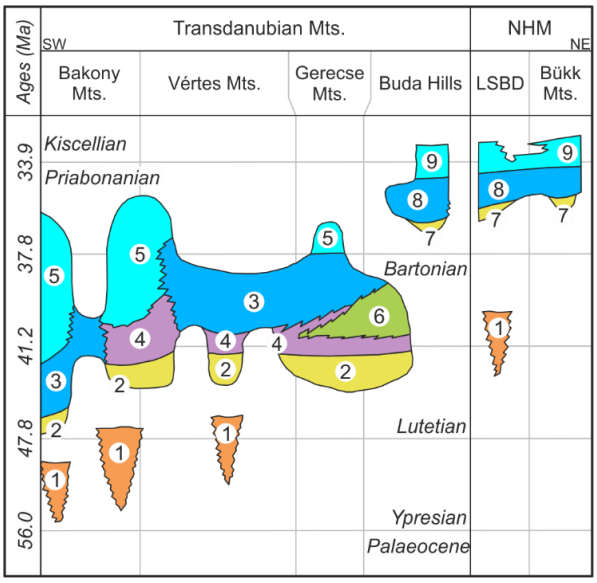

Fig. II.2. Eocene lithostratigraphy across the North-Hungarian range (modified after Kercsmár et al., 2015; Less, 2015 oral communication). NHM – North Hungarian Mountains and LSBD – Left Side Blocks of Danube. 1 – Gánt Bauxite Formation, 2 – Dorog Coal Formation, 3 – Szőc Limestone Formation, 4 – Csolnok Formation, 5 – Padrag Marl Formation, 6 – Tokod Formation, 7 – Kosd Formation, 8 – Szépvölgy Limestone Formation, 9 – Buda Marl Formation.

Depending on the palaeotopography of the karst surface, the thickness of the Kosd Formation varies considerably and reaches 244 m in borehole Noszvaj–1 (Nv–1; the location is shown in Fig. II.1; Less, 2005). The Kosd Formation was described in detail in two wells (Kosd–20 [K–20]; Varbó–75 [V–75]; Fig. II.1) by Gidai (1978) and Less (2005). In both wells, the Kosd Formation is characterised by two different sedimentary facies. The lower facies contains fossil- and carbonate-free variegated clay with different amounts of rock debris, deposited in a terrestrial environment. The overlying sediments include claystone, siltstone with varying carbonate content, marl and thin coal layers (Gidai, 1978; Less, 2005). The thickness of the lower and upper sedimentary sequences is 63 and 12 m, respectively, at V–75 well (Less, 2005) and 9 and 123 m, respectively, at K–20 well (Gidai, 1978). The coal is intercalated into calcareous claystone and marl at V–75 and K–20 wells, respectively, whereas the direct underlying sediments are characterised by varicoloured clay with carbonate debris. The overlying sediments grade into Miliolina-bearing calcareous marl. Gidai (1978) and Less (2005) noted an upward transition from a freshwater environment, indicated by gastropods (*Melanopsis* sp.) to a shallow marine, lagoonal environment marked by the presence of nanoplankton (*Isthmolithus recurves*) and foraminifers (*Quinqueloculina*, *Nummulites* sp.). Moreover, a proximal coastal environment is supported by mangrove vegetation, represented by Nypa palm pollens (Kvaček, 2010, and references therein; Rákosi, 1978). Coaly layers were noted by Gidai (1978) and Less (2005) in boreholes K–20 and V–75, but were not investigated in detail.

The Kosd Formation grades upward into shallow marine platform carbonates of the Szépvölgy Limestone Formation (Fig. II.2). The presence of the corallinacean algae and the frequently-occurring monospecific *Nummulites fabianii* indicate deposition on the inner shelf, while a diverse fauna including orthophragminas in the upper part of the formation, marks a transition to an outer shelf environment during the deposition of Szépvölgy Limestone (Less, 2005). Continuing basin subsidence caused deposition of the shallow bathyal Buda Marl

Formation, in low-oxic environments across the Eocene-Oligocene transition (Ozsvárt et al., 2016). The Tard Clay Formation accumulated in oxygen-depleted conditions (Bechtel et al., 2012; Ozsvárt et al., 2016), and the Kiscell Clay Formation was deposited in a more oxygenated environment (Bechtel et al., 2012). A sequence of siliciclastic and carbonate platform sediments terminates the Palaeogene succession, which is followed by thick Neogene deposits (Less, 2005; Kercsmár et al., 2015).

The coal measures of the Kosd Formation in the former Kosd coalfield (Fig. II.1) are 5 to 32 m thick and include three seams (Kubacska, 1925; Gidai, 1978; Némedi Varga, 2010). The lower seam is 0.5 to 2.5 m thick and was exploited between 1904 and 1931 *via* an underground mine approximately 130 m below the surface. The coal reaches the sub-bituminous stage in the shallow mine. Based on contemporary data (Papp, 1913), the coal includes 3–4 wt% moisture and the ash yield varies from 6 to 20 wt%. The elemental composition of the coal is 56–67 wt% carbon, 4–6 wt% hydrogen, 1 wt% nitrogen and 5–6 wt% sulphur (Papp, 1913). According to Némedi Varga (2010), the average calorific value is 19 MJ/kg and the potential reserves were estimated as 15 Mt.

2.3. Samples and analytical methods

2.3.1. Samples

Borehole W–1, drilled in the early 2000s in the southern part of the Gödöllő Hills by MOL Plc. (Fig. II.1), penetrated the Kosd Formation from 2415 m to 2791 m. A drill core, representing the upper section of the coal measures in the Kosd Formation, was recovered from 2587 m to 2605 m. In total, 35 samples (Table II.1) were obtained from this drill core, each of them was selected based on lithological differences and is representative of a 20 cm interval. In order to avoid contamination, about 0.5 cm of the outer rim of each core was removed. Moreover, to prevent outlier readings, samples containing pyrite aggregates or nodules were not selected during sample collection. Pyrite crystals in the macroscopic range were hand-picked from the samples prior to pulverization.

2.3.2. Petrographic analysis

Fifteen core samples, including all coal and coaly shale samples as well as selected mudstone samples, were prepared as whole-rock polished blocks for maceral analyses. Each sample was cut perpendicular to the bedding plane, embedded in epoxy resin and polished according to standard procedures (ASTM, 2015). Organic matter was identified by reflected white- and UV-fluorescent light microscopy using a Leica DM4P microscope equipped with a 50x oil-immersion objective and a point counter equipped with an OptiScan fully automated scanning stage. Maceral analyses were performed using a single scan method (Taylor et al., 1998) considering at least 1500 individual points to assess the minimum 500 counts of macerals. The terminology and classification of macerals used in this study are based on the ICCP system (ICCP, 1998; 2001; Pickel et al., 2017).

Mean random reflectance (%Rr) of telovitrinite was measured according to the methods of Taylor et al. (1998), and was performed under monochromatic (546 nm) light using an Olympus BX41 microscope equipped with a 50x oil-immersion objective and optical standards of Buehler Ltd. Reflectance values were processed by image analysis (Taylor et al., 1998).

2.3.3. Organic geochemical analysis

Powdered rock samples were analysed in duplicate for total sulphur (TS) and total carbon (TC) contents using an ELTRA Helios CS-580A analyser. Samples pre-treated by hot and diluted H_3PO_4 were used to determine total organic carbon (TOC) content. Total inorganic carbon (TIC = TC – TOC) was used to calculate calcite equivalent (CEq) percentages (CEq = TIC x 8.34 [%]). Ash yields were determined according to standard procedures (ASTM, 2018).

Table II.1. Bulk geochemical parameters of samples from the Kosd Formation.

ID	Depth	Lithotype	TIC	TOC	CEq	TS	Ash yield	TOC/TS	S1	S2	HI	BI	QI	PI	Tmax
#	[m; MD]		[wt%, db]						[mg HC/g rock]		[mg HC/g TOC]				[°C]
1	2587.10	siltstone	0.6	0.6	4.9	2.5	–	0.2	0.1	0.3	51	–	–	0.30	441
2	2587.75	siltstone	2.5	0.5	20.5	2.1	–	0.2	0.1	0.4	75	–	–	0.24	446
3	2588.00	siltstone	1.3	0.6	10.9	2.4	–	0.2	0.2	0.4	63	–	–	0.31	446
4	2589.20	siltstone	1.3	0.7	10.4	2.8	–	0.3	0.3	0.5	71	–	–	0.35	445
5	2590.00	coaly shale	0.8	29.5	6.8	4.0	59.4	7.3	10.0	71.9	243	34	277	0.12	441
6	2590.20	claystone	–	7.2	–	1.6	–	4.6	2.5	20.9	289	–	–	0.11	443
7	2591.00	siltstone	0.9	1.2	7.5	2.9	–	0.4	0.6	1.0	80	–	–	0.39	443
8	2591.80	siltstone	2.8	0.5	23.6	2.3	–	0.2	0.3	0.5	102	–	–	0.37	439
9	2592.20	siltstone	4.3	0.5	36.1	1.7	–	0.3	0.1	0.3	62	–	–	0.32	443
10	2593.00	siltstone	0.8	0.6	6.6	1.4	–	0.4	0.2	0.3	60	–	–	0.31	446
11	2593.70	siltstone	2.3	0.6	18.9	2.5	–	0.3	0.3	0.4	65	–	–	0.39	446
12	2594.40	siltstone	0.9	0.4	7.3	2.5	–	0.2	0.1	0.1	36	–	–	0.33	439
13	2594.55	coaly shale	0.7	12.7	5.7	3.5	77.9	3.6	3.8	31.9	251	30	280	0.11	441
14	2594.92	siltstone	0.9	1.5	7.8	2.6	–	0.6	0.7	1.0	68	–	–	0.40	439
15	2596.80	siltstone	0.9	0.5	7.8	1.7	–	0.3	0.5	0.3	66	–	–	0.61	446
16	2597.00	siltstone	0.9	0.5	7.6	2.4	–	0.2	0.1	0.2	40	–	–	0.38	438
17	2597.40	siltstone	1.0	0.8	8.4	3.2	–	0.3	0.3	0.5	64	–	–	0.36	447
18	2598.30	siltstone	0.8	0.9	6.3	2.4	–	0.4	0.6	0.6	65	–	–	0.51	437
19	2598.50	siltstone	0.6	0.8	5.2	2.5	–	0.3	0.6	0.5	54	–	–	0.56	432
20	2599.00	siltstone	0.1	1.0	0.5	3.2	–	0.3	0.4	0.4	39	–	–	0.47	431
21	2599.90	coal	0.4	78.4	3.6	3.4	5.8	23.0	23.4	186.3	238	30	267	0.11	443
22	2600.00	claystone	–	2.9	–	4.8	–	0.6	1.1	3.0	103	–	–	0.27	443
23	2600.60	claystone	0.1	2.9	1.0	3.0	–	1.0	1.5	2.9	101	–	–	0.34	445
24	2600.95	coal	–	45.7	–	8.8	32.1	5.2	14.6	133.1	291	32	323	0.10	441
25	2601.00	siltstone	–	3.8	–	4.5	–	0.9	1.8	6.6	171	–	–	0.22	448
26	2601.20	coaly shale	0.3	25.0	2.7	5.9	62.0	4.2	9.3	66.1	264	37	301	0.12	440
27	2601.40	siltstone	1.1	3.0	9.3	4.7	–	0.6	1.1	4.9	165	–	–	0.19	446
28	2602.00	coaly shale	–	21.8	–	4.9	66.2	4.5	6.6	53.8	247	30	277	0.11	438
29	2602.40	siltstone	1.4	1.0	11.9	3.4	–	0.3	0.9	0.8	82	–	–	0.52	444
30	2602.60	siltstone	1.1	1.0	8.8	3.1	–	0.3	0.9	0.7	71	–	–	0.55	441
31	2603.30	siltstone	1.1	0.7	9.1	3.0	–	0.2	0.5	0.6	90	–	–	0.47	441
32	2603.50	siltstone	1.8	0.7	15.4	3.1	–	0.2	0.5	0.7	97	–	–	0.41	442
33	2604.10	siltstone	3.5	0.8	29.3	2.1	–	0.4	0.4	0.7	92	–	–	0.38	443
34	2604.90	coal	1.1	57.2	9.0	3.4	30.5	16.6	17.2	130.8	229	30	259	0.12	444
35	2605.00	claystone	1.1	0.8	9.4	2.6	–	0.3	0.5	0.9	107	–	–	0.38	444

MD – measured depth; TIC – total inorganic carbon content, TOC – total organic carbon content, CEq – calcite equivalent, TS – sulphur content, TOC/TS – ratio of total organic carbon versus total sulphur content, S1 – free hydrocarbons, S2 – hydrocarbons generated during Rock-Eval pyrolysis, HI – hydrogen index, BI – bitumen index, QI – quality index, PI – production index, Tmax – temperature of maximum hydrocarbon generation.

Pyrolysis was carried out in duplicate using a Rock-Eval 6 instrument (Lafargue et al., 1998). The S1 and S2 peaks were recorded in order to determine the quantities of free (S1 [mg HC/g rock]) and generated hydrocarbons (S2 [mg HC/g rock]). The temperature of maximum hydrocarbon generation (Tmax [°C]) was recorded and used as a maturity indicator. Derived parameters were also calculated, such as the hydrogen index (HI; HI = S2 x 100/TOC [mg HC/g TOC]), production index (PI; PI = S1/(S1 + S2) [-]; Espitalié et al., 1977), bitumen index (BI; BI = S1 x 100/TOC [mg HC/g TOC]; Killops et al., 1998) and quality index (QI; QI = (S1 + S2) x 100/TOC [mg HC/g TOC]; Pepper and Corvi, 1995).

Based on the results of Rock-Eval pyrolysis and the diverse lithologies observed, ten samples (#20 to #29) representing the depth interval between 2599.0 and 2602.4 m were chosen for solvent extraction. The upper- and lowermost samples represent typical low-TOC intercalating lithologies, whereas the others are coaly shale and coal samples together with their adjacent sediments.

Representative portions of powdered rock samples were extracted using a Dionex ASE350 accelerated solvent extractor. A dichloromethane solvent was used at confined conditions of 75 °C and 110 bar (full details of this procedure are given in Gross et al., 2015). The saturated compounds were further separated into normal alkanes and branched–cyclic alkanes for compound-specific isotopic analyses using an activated molecular sieve (Merck, 500 pm pore space), cyclohexane, and a cyclohexane–*n*-pentane (12:88) solution.

Saturated and aromatic hydrocarbon fractions were analysed using a gas chromatograph equipped with a 30 m DB-5MS fused silica capillary column (i.d. 0.25 mm; 0.25 µm film thickness) and coupled to a ThermoFisher ISQ mass spectrometer. The measuring process followed is described in Gross et al. (2015).

Stable carbon isotope measurements of *n*-alkanes and acyclic isoprenoids were performed on selected samples using a Trace GC instrument attached to a ThermoFisher DELTA-V isotope ratio mass spectrometer *via* a combustion interface (GC isolink, ThermoFisher). CO_2 was injected at the beginning and the end of each analysis in order to perform instrumental calibration. The GC column and temperature program used were the same as above. Stable isotope ratios are reported in delta notation ($\delta^{13}C$; Coplen, 2011) relative to the Vienna Pee Dee Belemnite (V-PDB) standard ($\delta^{13}C = [(\delta^{13}C/\delta^{12}C)_{sample}/(\delta^{13}C/\delta^{12}C)_{standard} - 1]$). Delta notation is expressed in parts per thousand or per mil (‰). The analytical error was better than 0.2‰.

2.4. Results

2.4.1. Lithology

Based on drill cuttings and well logs (gamma ray, density, porosity) the Kosd Formation is 376 m thick and includes two coal horizons at depths between 2594 and 2649 m (Fig. II.3a). The lower and upper coal horizons are about 9 m and 36 m thick, respectively. The sediments between the coal horizons consist of grey sandstone, sandy siltstone, silty claystone, and conglomerate. Non-coal layers within the coal horizons comprise grey, sandy-, argillaceous-, calcareous- and coaly siltstones. Individual coal beds are 0.1 to 2.1 m thick and include coal and coaly shale, and intercalations of siltstone and claystone (Fig. II.3a).

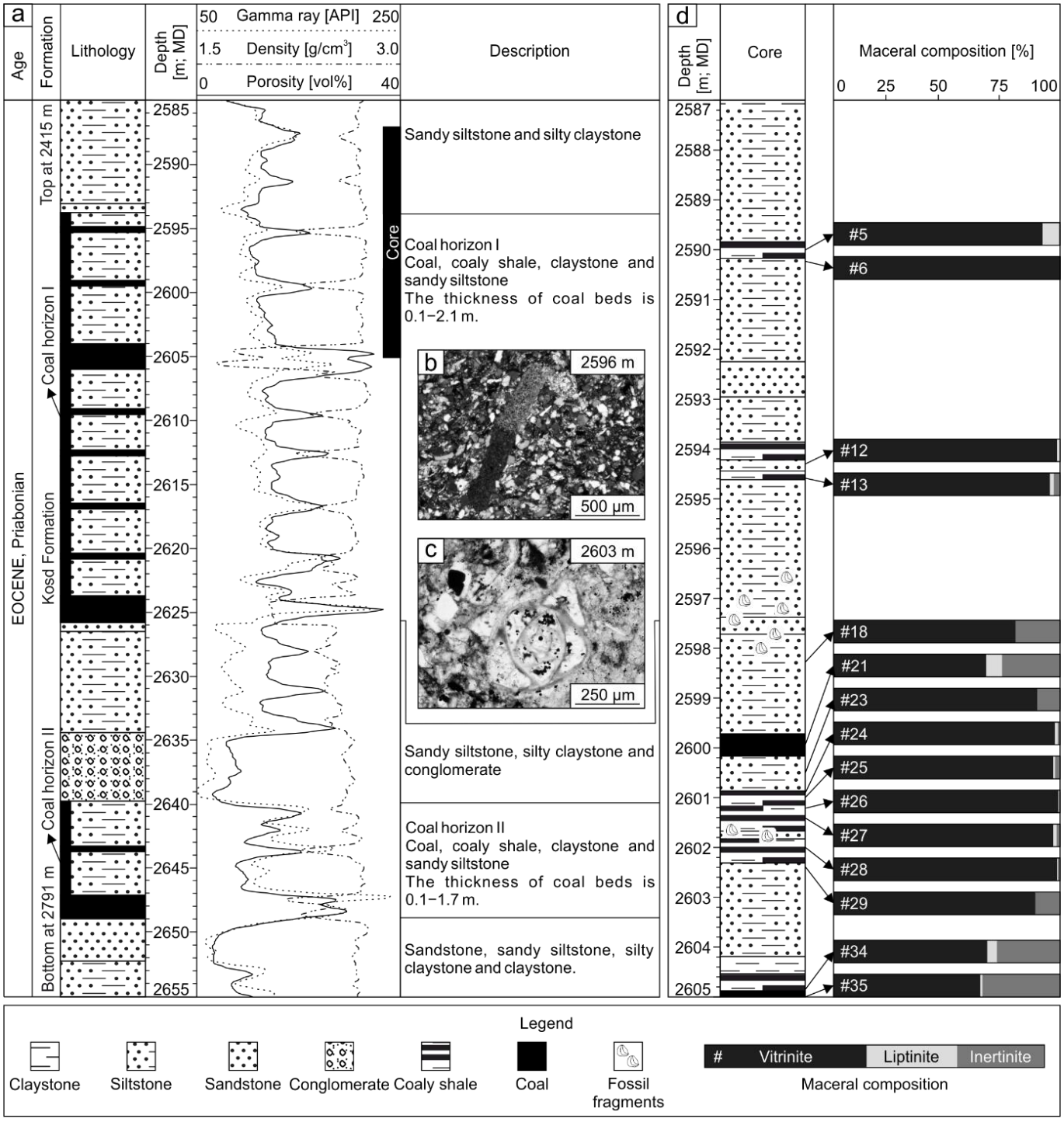

Fig. II.3. Simplified lithostratigraphy of the investigated section at the W–1 well. **a)** Lithologies are assigned based on well logs and drill cuttings. Drill core was recovered from 2587 m to 2605 m. **b)** Preserved fossils in the siltstone, including echinoid fragment (crossed Nicols) and **c)** miliolid foraminifer (plane polarized light). **d)** Location of organic matter rich samples in the higher resolution stratigraphy sequence selected for organic petrology and their maceral composition. Sample depth is given as measured depth (MD).

The studied drill core (2587–2605 m depth) represents the upper portion of the coal horizon I (Fig. II.3). Its base is located in the upper part of a 2 m-thick coal bed at a depth of 2605 m. The core includes coal layers, which are black, consolidated and hard. Two different lithotypes can be distinguished: (i) a generally bright, finely banded clarain coal, which is brittle, exhibits uneven fracture and occurs as 5 to 50 cm thick layers; and (ii) a stratified coaly shale, including intercalations of thin (<1 cm) siltstone and claystone layers, in which the thickness varies from 5 to 40 cm. The interseam sediments are dominated by sandy siltstone, which is variably calcareous and argillaceous. Original sedimentary structures are not visible due to bioturbation; however, slumps are recognizable. Two distinct intervals with shell fragments are observed (2596.5–2598.0 m; 2601.5–2602.0 m). Microscopic investigation revealed that the siltstone is rich in fossils, including mollusc, brachiopod, echinoid fragments and miliolid foraminifers (Figs. II.3b, c).

2.4.2. Bulk geochemical parameters

The TOC contents of coal and coaly shale range between 45.7 and 78.4 wt% (avg. 60.4 wt%) and between 12.7 and 29.5 wt% (avg. 22.3 wt%), respectively, whereas the TOC contents of the interseam lithologies vary between 0.4 and 7.2 wt% (avg. 1.3 wt%). Generally, the TOC contents of samples are greater than 2.9 wt% from 2599.9 m to 2602.0 m (#21 to #28), including coal beds and interseam sediments (Table II.1). The ash yield of coals varies between 5.8 and 77.9 wt% (Table II.1). The maximum calcite equivalent percentage in coals and intercalating sediments is 6.8 and 36.1 wt% (avg. 4.0 and 10.0 wt%), respectively (Table II.1).

The sulphur content of coaly layers ranges between 3.4 and 8.8 wt% (avg. 4.9 wt%). In the non-coaly intervals, sulphur contents vary between 1.4 and 4.8 wt% (avg. 2.8 wt%). In most cases, below the depth of 2599 m (#20), the sulphur contents are greater than 2.8 wt%, except sample #35. The TOC/TS ratio varies between 3.6 and 23.0 (avg. 9.2) in coaly lithotypes, whereas its value in interseam sediments ranges from 0.2 to 4.6 (avg. 0.5; Table II.1).

Tmax values range from 431 to 448 °C (Table II.1). The HI ranges from 36 to 291 mg HC/g TOC (Table II.1). In Tmax vs. HI plots (Figs. II.4a, b), samples can be subdivided into two populations, reflecting those with less or more than 150 mg HC/g TOC. The HI of coaly lithotypes varies from 229 to 291 mg HC/g TOC (avg. 252 mg HC/g TOC). The HI in the interseam sediments is from 36 to 289 mg HC/g TOC (avg. 87 mg HC/g TOC), however, higher readings (>150 mg HC/g TOC) were recorded at samples #6, #25 and #27, which are adjacent to coals (Table II.1). BI and QI were calculated for coals and coaly shales, and vary from 30 to 37 mg HC/g TOC and from 259 to 323 mg HC/g TOC, respectively (Figs. 4c, d; Table 1). An important observation noted during Rock-Eval pyrolysis is that coaly samples undergo stronger swelling, i.e., their volume increases significantly during heating.

The amount of extractable organic matter (EOM) varies between 31 and 212 mg/g TOC and yields of EOM are usually higher in intercalating sediments (Table II.3). EOM is dominated by polar compounds (34–50 wt%), except in samples #20 and #29, where the saturated compounds are prevalent (38 and 43 wt%, respectively). The saturated and aromatic hydrocarbon contents ranging from 5 to 43 wt% and 14 to 28 wt%, respectively. The amount of asphaltene is between 9 and 31 wt% (Table II.3). Aside from the general dominance of polar compounds, coaly lithotypes are found to be characterised by similar average percentages of aromatic hydrocarbons and asphaltenes (avg. 24 and 25 wt%, respectively), and the quantity of saturated hydrocarbons is low (avg. 5 wt%). In contrast, interseam lithologies are characterised by similar amounts of saturated and aromatic hydrocarbons (avg. 24 and 22 wt%, respectively) and a lower amount of asphaltenes (avg. 13 wt%; Table II.3).

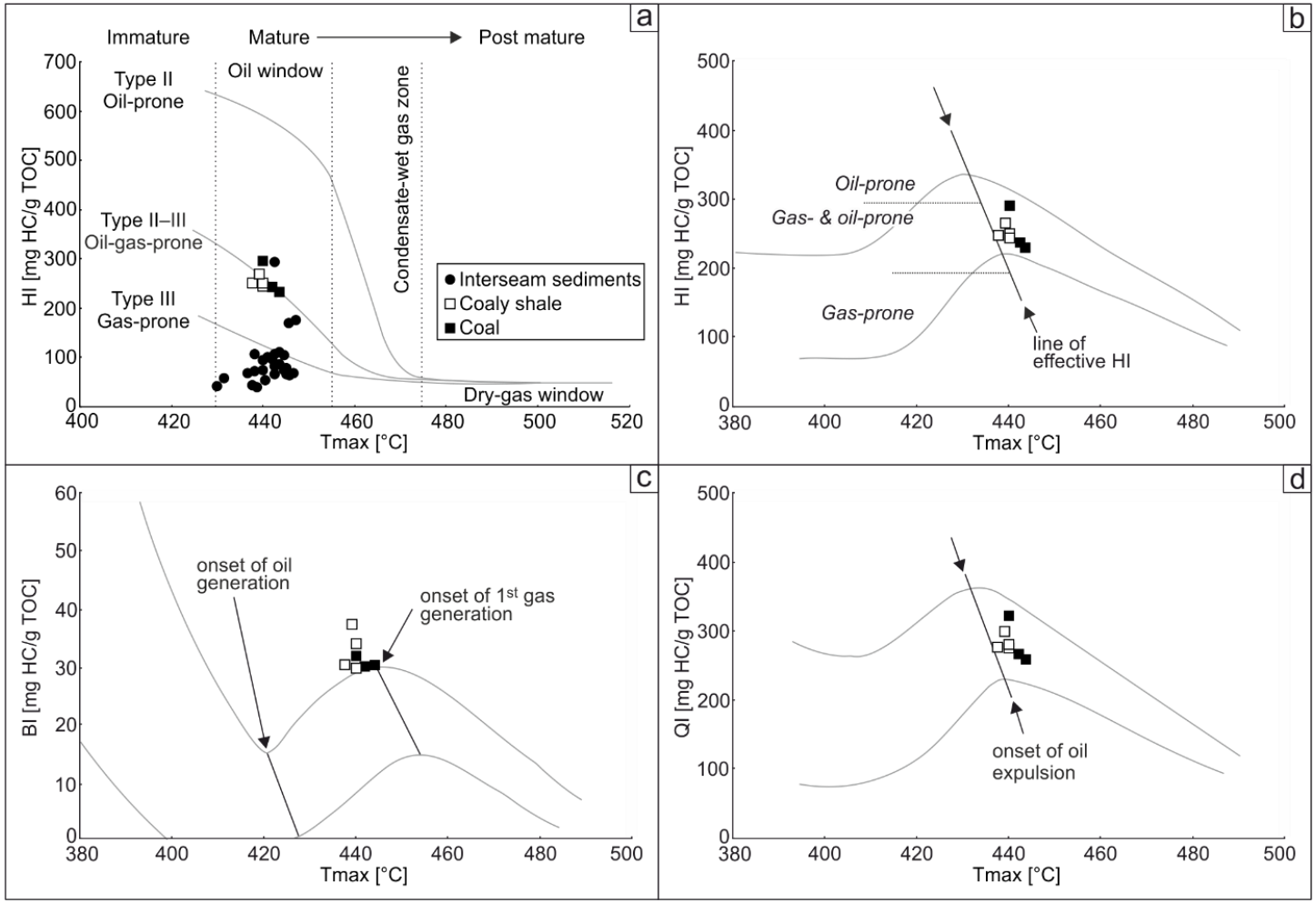

Fig. II.4. Petroleum potential assessment. **a)** Plot of Tmax vs. HI, showing the maturity and type of kerogen present in the investigated samples (after Espitalié et al., 1984). **b)** Plot of Tmax vs. HI, highlighting the increase in HI prior to the onset of oil expulsion (after Sykes and Snowdon, 2002). **c)** Rank threshold for oil- and gas generation indicated by BI (after Sykes and Snowdon, 2002). **d)** Rank threshold for oil expulsion determined by QI (after Sykes and Snowdon, 2002).

2.4.3. Maceral composition and vitrinite reflectance

Maceral analyses were performed on 15 samples, including coal, coaly shale, and claystone/siltstone (Table II.2). Vitrinite group macerals predominate in all samples (Figs. II.3d, 5; Table II.2). In coals, vitrinite macerals account for between 67 and 99 vol%. Collotelinite (37–46 vol%), collodetrinite (7–48 vol%) and gelinite (10–21 vol%) are the most abundant vitrinite macerals present. Collotelinite and collodetrinite exhibit an orange-brown fluorescent colour under UV light irradiation (Fig. II.5). Inertinite macerals are typically in the range of 1 to 3 vol% but reach significantly higher values in banded coal samples (26 and 28 vol%, in #21 and #34, respectively). In banded coal samples, funginite and inertodetrinite are present in addition to fusinite. The percentages of liptinite macerals reach 8 vol% and sporinite and alginite are present in substantial amounts (max. 4 vol%) in some samples.

In claystone/siltstone samples, vitrinite maceral contents vary from 65 to 100 vol%. Inertinite macerals are abundant in the lowermost sample (#35: 34 vol%; Fig. II.3d; Table II.2). Liptinite macerals, mainly sporinite, are generally rare and do not exceed 2 vol% (Fig. II.3d; Table II.2).

Framboidal pyrite occurs in substantial quantity throughout all samples, however, the highest contents are observed in the claystone/siltstone samples (Table II.2).

Vegetation- (VI) and groundwater influence indices (GWI_{AC}) were calculated for coaly sediments based on Calder et al. (1991) and Stock et al. (2016; Fig. II.6; Table II.2). VI ranges from 0.7 to 4.8 and GWI_{AC} varies between 2.9 and 39.2 (Table II.2).

Mean random vitrinite reflectance was found to range from 0.67 to 0.78 (Table II.2).

2.4.4. Molecular composition of hydrocarbons

2.4.4.1. Straight chain alkanes and isoprenoids

The concentration of *n*-alkanes (Tables II.3, 4) varies considerably across the investigated section. The compositions of identified *n*-alkanes vary within the range of *n*-C_{13} to *n*-C_{37}. Patterns of *n*-alkane distribution are characterised by a relatively uniform proportion of mid-chain *n*-alkanes (*n*-$C_{21–25}$; 27–38% of the total *n*-alkanes; Fig. II.7; Table II.4). Coaly lithologies (#21, #24, #26 and #28) and their adjacent sediments (#22 and #27) are dominated by short-chain *n*-alkanes (*n*-$C_{15–19}$; 30–46%; Fig. II.8). In contrast, interseam lithologies are generally dominated by long-chain *n*-alkanes (*n*-$C_{27–31}$; 24–31%; Fig. II.8). Furthermore, *n*-alkane envelopes exhibit a bimodal distribution pattern. The carbon preference index (CPI; Bray and Evans, 1961) is close to one (0.93–1.04; Table II.4).

The acyclic isoprenoids, including *i*-C_{13}, farnesane, *i*-C_{16}, norpristane, pristane (Pr) and phytane (Ph), are present in great abundance in all samples (Table II.3). The ratios of Pr/Ph range from 3.0 to 4.2 (Table II.4).

The stable carbon isotopic composition ($\delta^{13}C$) of *n*-alkanes, Pr and Ph is similar for all studied samples (Fig. II.9). With increasing chain length, $\delta^{13}C$ values of the *n*-$C_{15–19}$ and *n*-$C_{21–25}$ alkanes of selected samples show a decline of about 1‰, respectively. In contrast, long-chain alkanes (*n*-C_{27+}) show a reversed trend and increasing $\delta^{13}C$ with carbon number. Pr and Ph exhibit similar isotopic compositions, but Ph is observed to be slightly depleted in ^{13}C in comparison to Pr (Fig. II.9).

Table II.2. Mineral matter-free (mmf) maceral-, mineral composition, petrographic indices and random vitrinite reflectance of the investigated samples.

ID	Ct	Vd	Cd	Cg	G	Σ VIT	S	A	Σ LIP	F	Sf	Fg	Ma	Mi	Id	Σ IN	Pyr	DM	VI	GWI_{AC}	%Rr ± SD
#	[vol%, mmf]																[vol%]				
5	44.0	4.0	33.1	–	9.8	90.9	3.5	3.9	7.4	0.5	1.2	–	–	–	–	1.8	17.4	44.7	1.1	29.8	0.72 ± 0.03
6	–	–	–	–	–	100.0	–	–	–	–	–	–	–	–	–	–	25.0	71.0	–	–	0.73 ± 0.05
12	–	–	–	–	–	98.7	–	–	1.3	–	–	–	–	–	–	–	13.2	73.8	–	–	0.68 ± 0.05
13	45.9	–	32.2	–	17.4	95.5	1.1	0.5	1.6	1.0	1.8	–	–	–	–	2.8	8.5	27.6	1.4	39.2	0.73 ± 0.04
18	–	–	–	–	–	80.4	–	–	–	–	–	–	–	–	–	19.6	17.3	79.3	–	–	0.74 ± 0.06
21	59.1	–	7.4	0.6	0.2	67.4	5.7	1.3	6.9	9.1	12.7	0.3	–	1.1	2.5	25.7	0.1	0.8	4.8	2.9	0.76 ± 0.04
23	–	–	–	–	–	90.0	–	–	–	–	–	–	–	–	–	10.0	13.3	78.7	–	–	0.78 ± 0.06
24	36.9	–	40.2	–	20.6	97.7	1.2	–	1.2	0.4	0.6	–	–	–	–	1.0	8.8	24.0	0.9	16.3	0.71 ± 0.02
25	–	–	–	–	–	97.0	–	–	0.8	–	–	–	–	–	–	2.3	15.8	76.1	–	–	0.78 ± 0.04
26	32.8	0.6	47.7	–	17.0	98.1	0.5	–	0.5	0.6	0.8	–	–	–	–	1.4	8.2	28.9	0.7	31.2	0.68 ± 0.02
27	–	–	–	–	–	97.0	–	–	1.5	–	–	–	–	–	–	1.5	14.5	73.2	–	–	0.75 ± 0.03
28	38.2	–	40.1	–	20.3	98.7	0.3	–	0.3	0.6	0.4	–	–	–	–	1.0	6.1	50.2	1.0	33.4	0.67 ± 0.04
29	–	–	–	–	–	90.9	–	–	–	–	–	–	–	–	–	9.1	4.4	92.0	–	–	0.73 ± 0.06
34	48.5	0.4	9.8	2.8	6.4	67.9	4.1	–	4.1	16.7	4.8	0.1	1.4	1.0	3.8	27.9	8.0	44.7	4.1	15.4	0.75 ± 0.03
35	–	–	–	–	–	64.8	–	–	0.9	–	–	–	–	–	–	34.3	14.8	78.2	–	–	0.74 ± 0.04

Macerals that were not counted and are in very low percentages (<<0.1 vol%) are not included in the table, however, resinite, liptodetrinite and cutinite occur in the samples. Ct – Collotelinite, Vd – Vitrodetrinite, Cd – Collodetrinite, Cg – Corpogelinite, G – Gelinite, Σ VIT – Total Vitrinite, S – Sporinite, A – Alginite, Σ LIP – Total Liptinite, F – Fusinite, Sf – Semifusinite, Fg – Funginite, Ma – Macrinite, Mi – Micrinite, Id – Inertodetrinite, Σ IN – Total Inertinite, Pyr – Pyrite, DM – Detrital minerals, VI – Vegetation Index, GWI_{AC} – Groundwater Index, %Rr ± SD – mean random vitrinite reflectance ± standard deviation. VI = (telovitrinite + fusinite + semifusinte + cutinite + sporinite + suberinite + resinite) / (detrovitrinite + inertodetrinite + alginite + Liptodetrinite + exsudatinite + chlorophyllinite + bituminite; Calder et al., 1991), GWI_{AC} = (gelovitrinite + (ash yield / 2)) / (telovitrinite + vitrodetrinite); Stock et al., 2016).

2.4.4.2. Steroids

The concentration of steranes is very low in all samples (Table II.3), however, in the saturated hydrocarbon fraction, 5α,14α,17α(H) steranes dominate over 5β,14α,17α(H) isomers, and are present in the C_{27}–C_{29} range. Normalized values of steranes were plotted on a ternary diagram of C_{27}, C_{28} and C_{29} regular steranes (Huang and Meinschein, 1979), showing the relative distribution of steranes indicating organic matter depositional facies (Fig. II.10). C_{29} homologues are found to prevail in the samples, followed by C_{28} and C_{27} steranes. In organic matter-rich samples, C_{29} steranes predominate in the distributions (Fig. II.10; Table II.3). The corresponding diasteranes are found in even lower abundance (Table II.3), and exhibit similar carbon number distributions as the regular steranes. In the aromatic hydrocarbon fractions, monoaromatic (C_{29}) stigmastanes and triaromatic (C_{28}) stigmastanes were identified at very low concentrations.

The stereoisomer ratios of S/(S+R) of ααα C_{29} steranes and ββ/(ββ + αα) of C_{29} steranes were assessed as a thermal maturity parameter. Ratios of the 20S/(20S + 20R) isomers of the 5α,14α,17α(H)–C_{29} steranes range between 0.40 and 0.53. Moreover, ratios of αββ/(αββ + ααα) isomers of C_{29} steranes range from 0.65 to 0.69 (Table II.4).

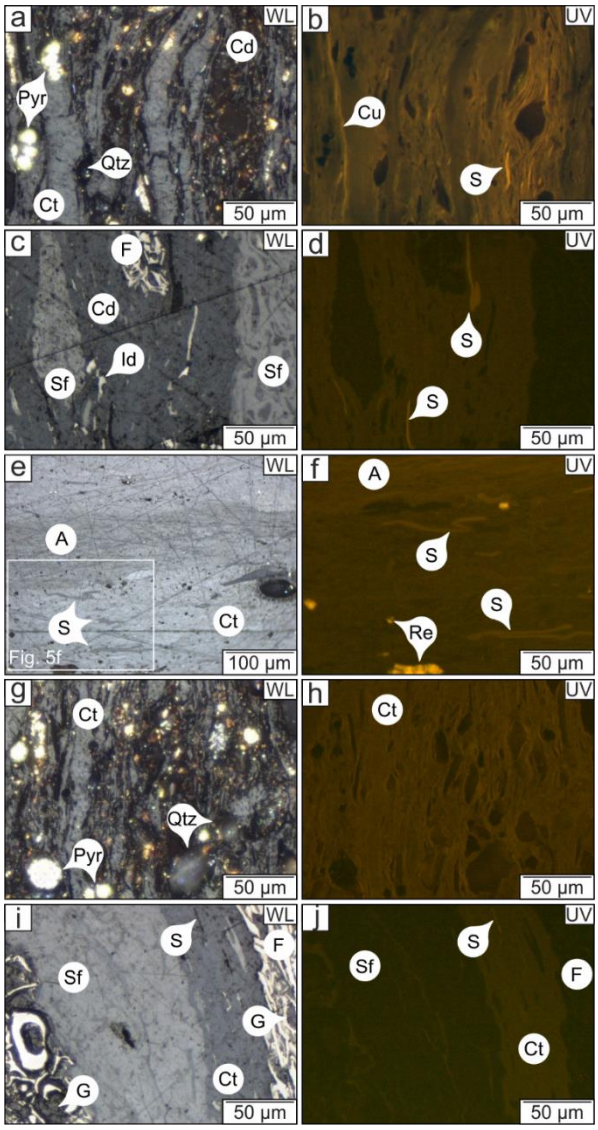

Fig. II.5. Photomicrographs of coal samples studied. Images were taken under reflected white light (WL) and ultraviolet light (UV) using oil immersion objective. Samples are #5 (**a, b**), #21 (**c, d, e, f**), #26 (**g, h**) and #34 (i, j). A – Alginite, Cd – Collodetrinite, Ct – Collotelinite, Cu – Cutinite, F – Fusinite, G – Gelinite, Id – Inertodetrinite, Pyr – Pyrite, Qtz – Quartz, Re – Resinite, S – Sporinite and Sf – Semifusinite.

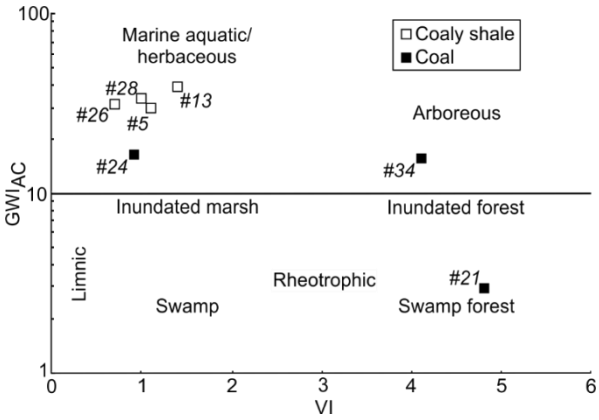

Fig. II.6. Chart of vegetation- (VI) and groundwater influence index (GWI_{AC}; after Calder et al., 1991).

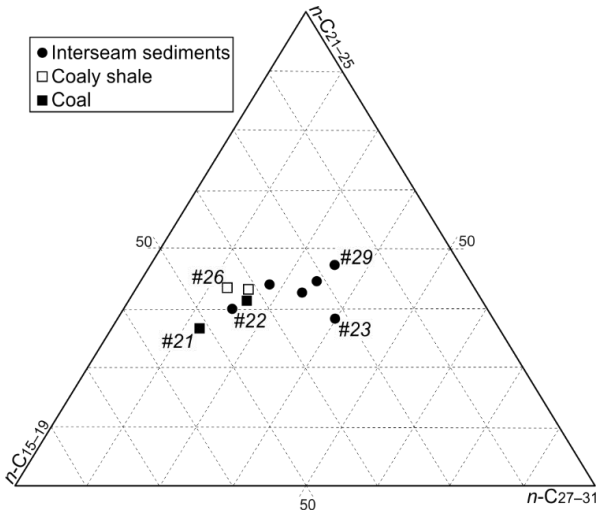

Fig. II.7. Normalised distribution of short- (*n*-$C_{15–19}$), mid- (*n*-$C_{21–25}$) and long-chain (*n*-$C_{27–31}$) n-alkanes in the studied samples.

Table II.3. Rock extracts, percentage of extract fractions and concentrations of hydrocarbon species of investigated samples in the Kosd Formation.

ID	a	b	c	d	e	f	g	h	i	j	k	l	m	n	o	p	q	r	s	t	u	v	w
#	[mg/g TOC]	[wt%]				[µg/g TOC]																	
20	164	38	19	35	9	14973	2082	44	10	221	74	241	17	112	218	300	1	1336	270	1682	244	1050	216
21	31	5	26	50	19	235	78	5	1	56	21	98	2	25	21	113	12	1245	112	515	95	300	87
22	84	10	28	48	13	2018	524	11	2	59	49	321	5	100	54	373	1	3300	319	1809	321	1228	285
23	146	26	21	40	13	11588	2605	55	12	233	257	379	21	88	586	256	56	2348	220	1198	231	994	209
24	57	5	23	46	25	410	158	14	1	60	41	151	8	38	115	131	8	1277	129	630	129	452	102
25	95	13	27	42	18	2497	794	20	4	83	123	297	12	66	239	216	10	2087	190	1007	201	811	169
26	60	6	24	46	24	733	223	14	2	28	35	211	4	38	154	166	3	1451	159	703	161	475	139
27	83	12	24	47	17	2527	571	14	3	96	85	247	8	53	261	276	4	2125	236	1118	235	842	220
28	62	6	21	42	31	639	159	9	1	77	35	142	4	27	108	172	2	1334	159	691	149	497	131
29	212	43	14	34	9	28999	3485	76	21	351	151	254	21	48	908	173	1	843	262	1399	198	835	212

a – extracted organic matter, b – saturated hydrocarbons, c – aromatic hydrocarbons, d – polar compounds, e – asphaltenes, f – *n*-alkanes, g – isoprenoids, h – steranes, i – diasteranes, j – hopanes, k – sesquiterpenoids, l – aromatic sesquiterpenoids, m – diterpenoids, n – aromatic diterpenoids, o – triterpenoids, p – aromatic triterpenoids, q – naphthalenes, r – alkylated naphthalenes, s – phenanthrenes, t – alkylated phenanthrenes, u – dibenzothiophenes, v – alkylated dibenzothiophenes, w – benzonaphthothiophenes.

Table II.4. Concentration ratios of compounds in hydrocarbon fractions of samples from the Kosd Formation.

ID	a	b	c	d	e	f	g	h	i	j	k	l	m	n	o
#	[%]					[%]							[%]		
20	22	35	25	1.00	3.30	30	24	46	0.13	0.42	0.65	0.55	0.75	0.89	0.20
21	46	27	12	1.04	4.10	14	23	63	0.06	0.50	0.67	0.57	0.71	0.83	0.17
22	39	31	15	0.97	4.22	20	23	57	0.11	0.53	0.68	0.56	0.73	0.99	0.20
23	18	29	31	0.97	3.52	26	30	44	0.10	0.43	0.66	0.59	0.74	1.03	0.11
24	35	32	17	0.96	3.76	17	17	66	0.11	0.45	0.67	0.59	0.73	0.98	0.16
25	24	33	24	0.97	3.96	26	28	45	0.10	0.44	0.67	0.57	0.72	1.04	0.15
26	34	34	16	0.93	3.63	21	27	52	0.15	0.42	0.66	0.63	0.72	1.00	0.12
27	30	35	19	1.00	3.57	25	28	46	0.06	0.46	0.66	0.59	0.73	0.98	0.10
28	37	34	13	0.96	3.30	18	20	62	0.06	0.49	0.69	0.57	0.72	0.92	0.10
29	17	38	26	1.03	3.01	38	26	36	0.09	0.40	0.66	0.57	0.73	0.74	0.06

a – *n*-$C_{15–19}$/*n*-$C_{15–35}$, b – *n*-$C_{21–25}$/*n*-$C_{15–35}$, c – *n*-$C_{27–31}$/*n*-$C_{15–35}$, d – CPI (Bray and Evans, 1961), e – Pr/Ph, f – C_{27} steranes/Σ regular steranes, g – C_{28} steranes/Σ regular steranes, h – C_{29} steranes/Σ regular steranes, i – steranes/hopanes, j – 20S/(20S + 20R) ααα C_{29} steranes, k – abb/(abb + aaa) C_{29} steranes, l – 22S/(22S + 22R) C_{32} hopane, m – $R_{c(MPI\ 1)}$ (Radke and Welte, 1983), n – DBT/P (Hughes et al., 1995), o – Di- / (Di- + Triterpenoids; Bechtel et al., 2003).

2.4.4.3. Hopanoids

Hopanoids are important constituents of non-aromatic cyclic triterpenoids (Table II.3). The measured hopanoid patterns are characterised by the occurrence of 17α,21β(H)– and 17β,21β(H)–type hopanes from C_{27} to C_{35} with C_{28} hopanes being absent. The predominant hopanoids in most samples are 17α,21β–C_{30} and 17β,21α–C_{29} hopane. The 17α,21β(H)–type homohopanes show a dominant pattern of exponential decrease in peak height with increasing carbon number. In most samples, a series of C_{32}– to C_{35}–benzohopanes was identified in the aromatic hydrocarbon fractions. In all investigated samples, the ratios of steroids to hopanoids are between 0.06 and 0.15 (Table II.4).

The stereoisomer ratio of 22S/(22S + 22R) isomers of 17α,21β(H)–C_{32} hopanes, a thermal maturity parameter, ranges from 0.55 to 0.63 (Table II.4).

2.4.4.4. Sesquiterpenoids, diterpenoids, non-hopanoid triterpenoids

Bicyclic sesquiterpenoids are characterised by the occurrence of 8β(H)–homodrimane, 8β(H)–drimane, and 4β(H)–eudesmane. Furthermore, rearranged drimenes and pentamethyl–trans–decalins are also present in the studied samples. Decalins were identified as 2,2,4a,7,8–pentamethyl–trans–decalin and 1,2,2,5,5–pentamethyl–trans–decalin according to Nytoft et al. (2009). Diterpenoids consist of bicyclic- (8β(H)–labdane), tricyclic- (pimarane, isopimarane and abietane) and tetracyclic diterpanes (16β(H)–phyllocladane). The tetra- and pentacyclic triterpenoids occur in the analysed samples and the following oleanane, ursane and lupane types were identified in non-aromatic hydrocarbon fractions: des–A–olean–12–ene, des–A–urs–12–ene, 10β(H)–des–A–oleanane, 10β(H)–des–A–lupane, 10β(H)–des–A–ursane, lupane, urs–12–ene, and 18β(H)–oleanane, with a substantial amount of 18α(H)–oleanane.

Aromatic sesquiterpenes are represented by cadalene, calamenene and 5,6,7,8–tetrahydrocadalene. Abietane-type aromatic diterpenoids are present and consist of 1,2,3,4–tetrahydroretene, norsimonellite, simonellite, and retene. The following aromatic tetra- and pentacyclic triterpenoids are identified in the aromatic hydrocarbon fractions: tetramethyl–octahydro–chrysenes, trimethyl–tetrahydro–chrysenes, and tri- and tetra aromatic pentacyclic triterpenoids of the oleanane- and ursane-types (tetramethyl–octahydro–picenes, trimethyl–tetrahydro–picenes).

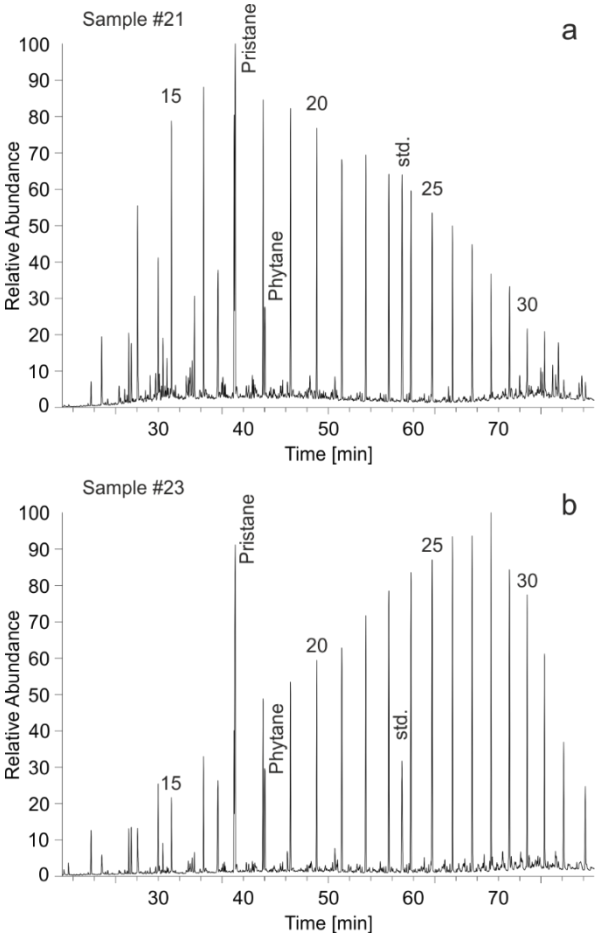

Fig. II.8. Gas chromatograms (total ion current) of saturated hydrocarbon fraction of **a)** coal, sample #21 and **b)** claystone, sample #23. *n*-Alkanes are labelled according to the carbon number. std. – standard (deuterated *n*-tetracosane).

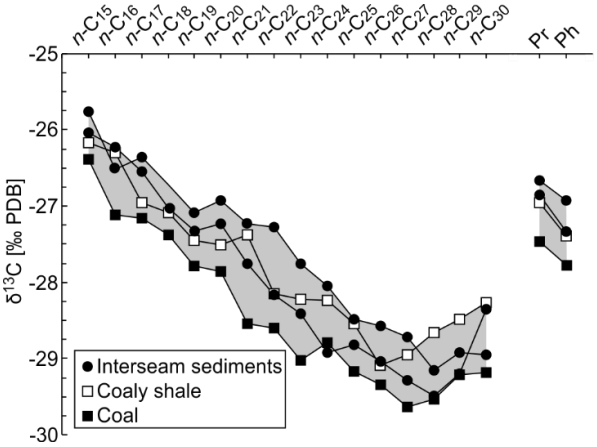

Fig. II.9. Carbon isotopic composition of *n*-alkanes, pristane and phytane in coal (#24), coaly shale (#26) and interseam sediments (#25, #27).

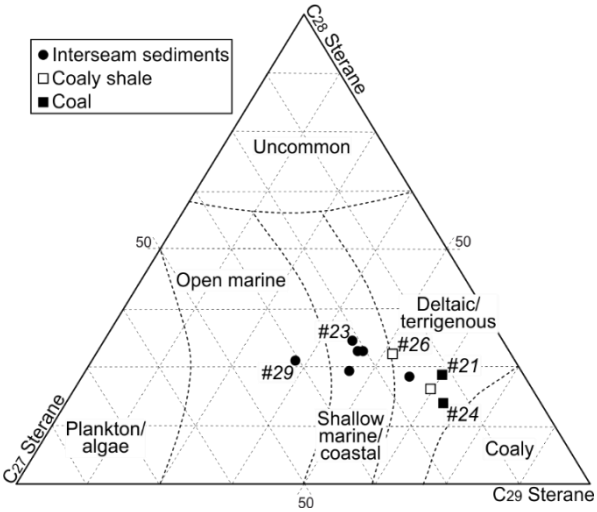

Fig. II.10. Ternary plot of regular steranes showing the normalized abundance of C_{27}, C_{28} and C_{29} sterane isomers and their depositional facies (after Huang and Meinschein, 1979).

2.4.4.5. Polycyclic aromatic hydrocarbons

The total ion chromatograms of aromatic hydrocarbon fractions are dominated by naphthalenes and phenanthrenes (Table II.3). Naphthalene (N) occurs at low concentrations, however, its alkylated counterparts, methyl- (MN), dimethyl- (DMN) and trimethylnaphthalenes (TMN), are present at a higher amount. The methylnaphthalenes (2– and 1–MN) are present in equal quantities, whereas 1,6–DMN and 1,2,5– and 1,2,7–TMN predominate the dimethyl- and trimethylnaphthalenes, respectively.

Phenanthrene (P), alkylated phenanthrenes (methyl- (MP), dimethyl- (DMP) and trimethylphenanthrenes (TMP)) occur in considerable concentrations in the investigated samples. The 9–, 1– and 2–MP characterise the methylphenanthrenes. The methylphenantrene index (MPI 1; Radke et al., 1982a, b) varies between 0.52 and 0.59 and calculated vitrinite reflectance values ($\%R_{c(MPI\ 1)}$; Radke and Welte, 1983) vary between 0.71 and 0.75%Rc (Table II.4). The pattern of dimethylphenanthrenes is predominated by 1,7–DMP, and the co-eluting 1,3,7–, 1,3,9– and 2,7,10–TMP dominate the trimethylphenanthrenes.

Beside the naphthalenes and phenanthrenes, polycyclic aromatic hydrocarbons identified include chrysene, alkylated chrysenes, and perylene.

2.4.4.6. Sulphur-aromatic compounds

The sulphur-containing aromatic compounds identified include dibenzothiophenes and benzonaphthothiophenes, both of which occur in considerable quantities in the investigated samples (Table II.3). Dibenzothiophenes are represented by dibenzothiophene (DBT), methyl- (MDBT), dimethyl- (DMDBT) and trimethyldibenzothiophenes (TMDBT). Methyldibenzothiophenes are characterised by 4–MDBT, co-eluting 3– + 2–MDBT and 1–MDBT, in descending order of concentration. The benzonaphthothiophenes are dominated by benzo[b]naphtho[2,1]thiophene, whereas benzo[b]naphtho[1,2]thiophene and benzo[b]naphtho[2,3]thiophene occur in lower quantities.

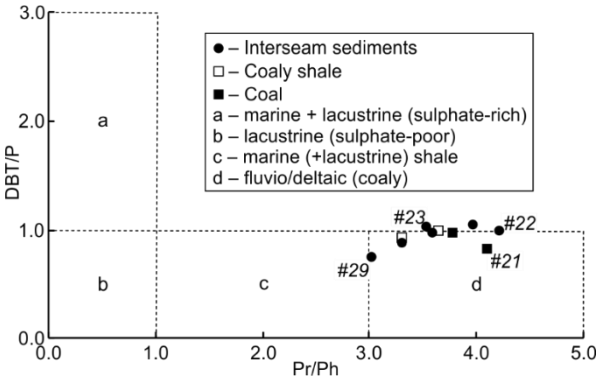

Fig. II.11. Cross-plot of pristane/phytane (Pr/Ph) vs. dibenzothiophenes/phenanthrene (DBT/P) ratios (after Hughes et al., 1995).

The DBT/P ratios (Hughes et al., 1995) range between 0.74 and 1.04 (Fig. II.11; Table II.4).

2.5. Discussion

2.5.1. Thermal maturity

Vitrinite reflectance (0.67–0.78 %Rr; Table II.2) and Tmax values (431–448 °C; Table II.1) indicate that the coals of the Kosd Formation reached a high-volatile bituminous rank (Taylor et al., 1998) and that the organic matter is mature, but did not yet reach peak oil window maturity (0.8 %Rr; e.g., Peters and Cassa, 1994). Nevertheless, values of Rr and Tmax vary slightly and point to lower values in coaly lithotypes. The content of liptinite group macerals is limited, however, organic matter is dominated by fluorescent vitrinite (Fig. II.5; Table II.2). The orange-brown fluorescence colour of the vitrinite and the strong swelling during pyrolysis both suggest the predominance of hydrogen-rich vitrinite (Wilkins and George, 2002). Hence, the vitrinite reflectance of coaly lithotypes may be suppressed due to the diagenetic

enrichment in hydrogen and sulphur (e.g., Peters et al., 2018 *cum lit.*). Considering the relatively low content of liptinite macerals and extractable organic matter, suppression due to sorption of generated bitumen (Carr, 2000; Taylor et al., 1998; Wilkins and George, 2002) seems less likely.

Hopane (22S/22S + 22R C_{32}) and sterane (20S/(20S + 20R) ααα C_{29}) isomerisation ratios range from 0.55 to 0.63 and from 0.40 to 0.53, respectively (Table II.4). Although this indicates that C_{32} hopane isomerisation ratios reached their equilibrium value, sterane isomerisation ratios of C_{29} suggest that steranes did not. This denotes maturities corresponding to the oil window (0.6–0.8 %Rr; Mackenzie et al., 1980; Mackenzie and Maxwell, 1981; Seifert and Moldowan, 1986; Peters et al., 2005). This maturity assessment is supported by ratios of ββ/(ββ + αα) isomers of the 5α,14α,17α (H)–C_{29} steranes (0.65–0.69; Table 4), which are close to their equilibrium value of 0.7 (Seifert and Moldowan, 1986). CPI values close to 1 (0.93–1.04) further confirm this maturity assessment.

The methylphenanthrene index (MPI) is a well-established parameter for classifying maturity (Radke et al., 1982a, b) and can be used to calculate vitrinite reflectance values (Radke and Welte, 1983). The calculated vitrinite reflectance values are between 0.71 and 0.75 %Rc (Table II.4), which fits well with the measured values.

2.5.2. Source of organic matter

The Kosd coal is generally dominated by vitrinite and inertinite subgroup macerals (Table II.2), which are derived from woody tissues of herbaceous and arborescent plants (ICCP, 1994). Petrography-based facies indicators have been determined for the coaly lithotypes. The vegetation index (VI; Table II.2) contrasts macerals of forest affinity with those of herbaceous and marginal aquatic affinity (Calder et al., 1991). All studied samples of Kosd coal, except #21 and #34, are characterised by VI values below 3 (Fig. II.6; Table II.2), indicating a predominance of herbaceous peat-forming flora.

Long-chain lipids are typically attributed to higher terrestrial plants (Eglinton and Hamilton, 1967), whereas mid-chain *n*-alkanes are reported in aquatic macrophytes and *Sphagnum* (Bingham et al., 2010; Dehmer, 1995; Ficken et al., 2000; Nott et al., 2000), and short-chain *n*-alkanes are identified predominantly in algae and other microorganisms (Cranwell, 1977; Cranwell et al. 1987). Hence, it is surprising that the studied coaly samples (TOC > 20 wt.%) are characterised by significantly higher amounts of short-chain *n*-alkanes than long-chain *n*-alkanes (Table II.4). For example, the clean coal #21 (TOC 78.4 wt.%; ash yield: 5.2 wt.%) contains the highest relative percentage of short-chain *n*-alkanes (max. 46%) and the lowest relative percentage of long-chain *n*-alkanes (min. 12%; Table II.4). A shift toward shorter *n*-alkanes may be caused by advanced maturity (e.g., Radke et al., 1980), but this effect alone cannot explain the pattern observed since some low-TOC samples also contain high percentages of long-chain *n*-alkanes (e.g., #23; 31%). The high amounts of short-chain *n*-alkanes in coal samples are related to the strong fluorescence of vitrinite macerals, high S1 and BI values (Table II.1; Fig. II.4c) and may be caused by either migration (Littke et al., 1990) or bacterial activity. Whereas relative amounts of long- and short-chain *n*-alkanes vary significantly, mid-chain *n*-alkanes are found at high, relatively constant proportions (27–34%).

$\delta^{13}C$-values of *n*-alkanes in the selected samples (Fig. II.9) are consistent with previous studies performed on coal samples (e.g., Gross et al., 2015; Schoell et al., 1994; Simoneit et al., 1995; Schwarzbauer et al., 2013; Tuo et al., 2003). Variations of carbon isotopic compositions of individual compounds are within 1‰, indicating a positive correlation between sample sets (Sofer, 1984). $\delta^{13}C$-values also show a decreasing trend, becoming more depleted in ^{13}C with increasing chain length in all samples (Fig. II.9), a phenomenon often observed in coals (e.g.,

Doković et al., 2018; Schoell et al., 1994; Schwarzbauer et al., 2013; Tuo et al., 2003). The long-chain *n*-alkane compounds, however, show an opposite tendency, getting more enriched in ^{13}C with increasing chain length (Fig. II.9). Both long-chain *n*-alkane production and the biosynthetic fractionation of carbon isotopes vary among plant types (Diefendorf et al., 2011; Lockheart et al., 1997) and studies have pointed to ^{13}C enrichment with chain length in recent terrestrial plants (e.g., Collister et al., 1994; Diefendorf et al., 2011; Diefendorf et al., 2015; Lockheart et al., 1997; Mead et al., 2005). Nevertheless, the effect of thermal maturation on the carbon isotopic composition of organic matter has already been considered by several authors (e.g., Bjorøy et al., 1992; Rooney et al., 1998; Schoell, 1984). Diefendorf et al. (2015) found that the catagenic stage of maturation can lead to variations in the magnitude and direction of the change in $\delta^{13}C$-values according to species and chain length. Therefore, the effect of thermal maturation on the $\delta^{13}C$-values measured cannot be ruled out in the present study.

The $\delta^{13}C$-values correspond to common carbon isotope values of C3 plants and freshwater algae (e.g., Close, 2019; Diefendorf and Freimuth, 2017; Holtvoeth et al., 2019; Lamb et al, 2006; Meyers, 1997; O'Leary, 1981). Terrestrial plants utilize atmospheric CO_2 during photosynthesis, whereas aquatic photoautotrophs use dissolved $CO_{2[AQ]}$ or, in the case of alkaline or CO_2-limited conditions, can fix HCO_3^- as the inorganic carbon source for photosynthesis (Holtvoeth et al., 2019; Lamb et al., 2006; Meyers, 1997). The assimilation of HCO_3^- leads to ^{13}C enrichment (Aichner et al., 2010; Lamb et al., 2006; Meyers, 1997). The intermediate-weight *n*-alkanes are isotopically heavier than long-chain *n*-alkanes (Fig. II.9), moreover, $\delta^{13}C$ isotopic differences could be more explicit prior to the thermal alteration. Furthermore, low-molecular weight *n*-alkanes are characterised by ^{13}C enrichment relative to mid-chain *n*-alkanes (Fig. II.9). However, the carbon isotopic composition of lake-derived organic matter is typically indistinguishable from the surrounding watershed (Meyers, 1997). Nevertheless, the contribution of algae to the carbon isotope compositions measured is also suggested by the presence of lamalginite.

The predominance of C_{29} steroids in coals is consistent with a dominant origin of organic matter from vascular plants (Fig. II.10; Table II.4; Huang and Meinschein, 1979), which also explains the low amount of regular steranes (Doković et al., 2018; Volkman, 1986). Besides the vascular plants, the constant proportion of C_{28} steranes and the occurrence of perylene has been suggested to indicate a contribution from wood-degrading fungi (Marynowski et al., 2013). Hopane derivatives occur in the investigated samples, in which the bacteriohopanepolyols have been suggested to be the most probable biological precursors, and have been identified both in bacteria and in some cryptogams (e.g., moss, ferns; Ourisson et al., 1979; Rohmer, 1993; Talbot et al., 2016). The occurrence of C_{32} to C_{35} benzohopanes (Hussler et al., 1984) in the aromatic hydrocarbon fractions also suggests that bacteriohopanetetrol was a significant constituent of the precursor biomass. Furthermore, both the low sterane to hopane ratio and the presence of drimane-type sesquiterpenoids suggest microbially reworked organic matter (Alexander et al., 1983; 1984; Tissot and Welte, 1984).

Sesquiterpenoids and diterpenoids are present in the analysed sample sets (Table II.3). The biological precursors of cadalane-type sesquiterpenoids are widely distributed throughout all conifer families (Simoneit et al., 1986; Otto et al., 1997, and references therein). Eudesmane is also a non-specific indicator of higher land plants (Alexander et al., 1983), hitherto missing in species of Araucariaceae and Taxaceae (Otto and Wilde, 2001). Labdane-type compounds are the most common diterpenoids in conifers and have been described in all families except in Cephalotaxaceae (Otto and Wilde, 2001). More than 100 pimarane- and isopimarane-type diterpenoids have been detected in species of Pinaceae, Taxodiaceae, Araucariaceae, and Cupressaceae (Sukh Dev, 1989). Phyllocladane-type diterpenoids are widespread among coniferales families, except in Pinaceae (Otto and Wilde, 2001). Abietane-type diterpenoids can be generated by the transformation of pimarane (Wakeham et al., 1980), the progressive thermal alteration of phyllocladane (Alexander et al., 1987), or the dehydrogenation of abietic acids

(Peters et al., 2005). Alkylated phenanthrenes have been genetically related to abietic- and pimaric acid (Alexander et al., 1995; Laflamme and Hites, 1978; Radke et al., 1998). Based on the composition of diterpenoids present in the studied samples, Cupressaceae genera presumably contributed to the arboreal vegetation.

Non-hopanoid triterpenoids of oleanane-, ursane- and lupane-types are significant constituents of leaf waxes, wood, roots, and bark (Karrer et al., 1977), and the oleanane- and ursane-types are particularly predominant in the samples investigated. These compounds are formed by the transformation of β-amyrin, α-amyrin, and lupeol (Havelcová et al., 2012) and are significant biomarkers of angiosperm inputs into organic matter (Sukh Dev, 1989; Karrer et al., 1977). Aside from non-hopanoid triterpenoids, di- and trimethylnaphthalenes can also originate from angiosperms (van Aarssen et al., 1992; Strachan et al., 1988).

The di-/(di- + triterpenoids) ratio can be used to estimate the relative contribution of gymnosperms and angiosperms to organic matter (Bechtel et al., 2003). Very low ratios (≤0.2; Table II.4) indicate that angiosperm-derived biomarkers predominate in all analysed samples of the Kosd Formation. These results are consistent with previous observations on Eocene coal deposits throughout central Europe (Bechtel et al., 2007, 2008) and are supported by palynological data from throughout the Transdanubian Mountains, which further indicates an angiosperm-dominated vegetation (Kvaček, 2010, and references therein; Rákosi, 1978). Although the vegetation was dominated by angiosperms, a continuous upward increase in the di-/(di- + triterpenoids) ratio from 0.06 to 0.20 (Table II.4) indicates an increasing relative contribution of gymnosperms during deposition of the studied depth interval (2602.4–2599.0 m).

2.5.3. Depositional environment

GWI_{AC} values (>10) in the studied section suggest that the deposition of the coaly lithotypes occurred in a low-lying mire with rheotrophic conditions (Fig. II.6; Table II.2; Calder et al., 1991). The presence of inertinite and liptinite in the investigated Kosd coal implies the existence of a paleomire influenced by the fluctuation of the water table (Diessel, 1992; Eble et al. 2019), allowing the accumulation of lamalginite during high-, and the oxidation of plant tissues during low water table conditions.

The *n*-alkane isotope profile shows a generally declining pattern (Fig. II.9; Table II.5), which has previously been assigned to fluvio-deltaic origins (e.g., Bjorøy et al., 1991; Cortes et al., 2010; Dzou and Hughes, 1993; Murray et al, 1994; Odden et al., 2002; Tuo et al., 2003; Wilhelms et al., 1994). The Pr/Ph *vs.* DBT/P plot also indicates a fluvio-deltaic environment (Fig. II.11; Hughes et al., 1995). The composition of regular steranes (Fig. II.10; Table II.4; Huang and Meinschein, 1979) suggests a transition between shallow marine and deltaic paleoenvironments, which provided an appropriate setting for the preservation of higher plant triterpenoids (Strachan et al., 1988).

The sulphur content of the analysed samples has a general tendency towards higher readings with increasing organic carbon content (Table II.3). Variations in sulphur content can be explained by an influx of saline water towards the paleomire (Petersen and Ratanasthein, 2011) or by changes in pH (Markič and Sachsenhofer, 1997). Considering the occurrence of marine miliolid foraminifers (Fig. II.3c), an influx of marine water is obvious. In addition, low TOC/TS ratios (Table II.1) support marine influence (Berner, 1982; 1984). Denudation of Mesozoic carbonate rocks underlying the Kosd Formation may have enhanced the concentration of bicarbonate ions. Moreover, the chemical weathering in the hinterland provided nutrients to the paleovegetation. Alkaline conditions control both, bacterial decomposition of plant remnants and reduction of sulphates by sulphate-reducing bacteria (Markič and Sachsenhofer, 1997). In the case of available reactive iron, the transformation of sulphide phases into dense-

ly packed framboidal aggregates of pyrite crystals is a prevalent process driven by bacterial sulphate reduction (Casagrande, 1987; Hámor, 1994; Maclean et al., 2008; Morad, 1998; Sweeney and Kaplan, 1973). Nevertheless, there is a poor fit between the TS and pyrite contents, which indicates the presence of organic sulphur. Organic sulphur-bearing compounds (e.g., dibenzothiophenes) have been detected in considerable concentrations (Table II.3). The prevalence of organic sulphur has also been described for Eocene coals by Hámor-Vidó and Hámor (2007). The marine influence and the presence of mobile Ca^{2+} and HCO_3^- ions in the continental runoff are confirmed by the local elevation of calcite equivalent percentages (at #2, #8, #9, #11 and #33) in the interseam sediments (Table II.1).

In the studied samples, Pr and Ph exhibit similar carbon isotopic compositions, and are enriched in ^{13}C relative to terrestrial plant-derived *n*-alkanes, arguing for chlorophyll as their common source (Fig. II.9; Collister et al., 1992; Hayes et al., 1990; Hayes, 1993). Confined pyrolysis studies of coal samples support a maturation tendency of Pr/Ph (Monthioux and Landais, 1989; Radke et al., 1980). Therefore, the interpretation of redox conditions during sedimentation based strictly on Pr/Ph ratios (Didyk et al., 1978) is limited in the current study due to interferences resulting from thermal maturity. Nevertheless, the occurrence of des-A-triterpenes suggests dysoxic conditions (Jacob et al., 2007, and references therein). Furthermore, in immature terrigenous organic matter, perylene has been related to the activity of wood-degrading fungi and indicates reducing conditions in subsurface sediments during early diagenesis (Marynowski et al., 2013). Although the studied coals are mature, the presence of framboidal pyrite, as well as perylene, indicates eogenetic origin and locally reducing conditions (Sweeney and Kaplan, 1973).

Whereas Gidai (1978) and Less (2005) have mentioned the presence of coaly layers in wells K–20 and V–75, they did not investigate the organic material. Nevertheless, the new results on well W–1 agree well with the sedimentological and palaeontological data reported by these authors. Despite the strongly varying thickness, all three wells show a general trend from non-marine fine-grained rocks with debris flow deposits to brackish and marine sediments. Coaly layers occur within the transition zone. According to Less (2005), the upper marine part of the Kosd Formation in V–75 represents a lagoonal environment dominated by fine-grained rocks. Based on the lithological and faunal description provided by Gidai (1978), a similar environment can be assumed for well K–20. In contrast, the studied interval in well W–1 includes sandstones and conglomerates representing a delta environment. Moreover, the total thickness of the Kosd Formation in well W–1 (376 m) is higher than in any other well (*cf.* Less, 2005).

2.5.4. Hydrocarbon generation potential

The remaining hydrocarbon generation potential of the Kosd Formation samples can be characterised using TOC contents and the amount of free (S1) and generated hydrocarbons (S2). TOC contents of the analysed samples are generally greater than 0.5 wt% (Table II.1). The obtained HI values suggest that type III and II–III kerogen is dominant, nevertheless, type IV kerogen also occurs (#12, #16 and #20; Fig. II.4a; Table II.1). The coaly lithotypes and their adjacent intercalating sediments have excellent and fair-good petroleum potential, respectively (Peters, 1986; Peters and Cassa, 1994). In total, 69% of the analysed samples have HI values between 50–200 mg HC/g TOC and are gas-prone, whereas 22% possess oil- and gas-prone kerogen (Peters and Cassa, 1994).

Following the approach of Sykes and Snowdon (2002), coaly samples were plotted onto diagrams of HI, BI and QI *vs.* Tmax (Figs. II.4b-d). These diagrams suggest that all coaly samples are gas- and oil-prone (Fig. II.4b) and have passed the rank threshold for oil generation (BI; Fig. II.4c) and expulsion (QI; Fig. II.4d), furthermore, have reached the maturity threshold for the first gas generation (BI; Fig. II.4c). Fig. II.4c emphasizes the high BI of the coal

samples, which is linked to abundant short-chain *n*-alkanes and probably causes the strong fluorescence observed in vitrinite macerals.

2.6. Conclusion

The investigation of the coal measure of the Eocene Kosd Formation in the northern Pannonian Basin has yielded important new results regarding its depositional environment, organic matter source and hydrocarbon potential:

(1) The coal measure evolved in a marine deltaic environment. The accumulation of peat-forming vegetation in a low-lying, rheotrophic mire was affected by fluctuations of the water table.

(2) Slightly alkaline conditions and the depletion in dissolved oxygen noted in the sediments promoted the reduction of sulphates by sulphate-reducing bacteria and bacterial decomposition of plant remains. In addition to the high sulphur contents observed (max. 8.8 wt%), the orange-brown fluorescence colour of vitrinite and its strong swelling during pyrolysis are typical indicators of marine-influenced coals.

(3) The peat-forming flora was dominated by land plants with varying contributions of algae and aquatic macrophytes. Similar to other Eocene coal seams, angiosperms predominated over gymnosperms. An upward increase in the relative contribution of gymnosperms (e.g., Cupressaceae) to the biomass is observed at depth between 2599.0 and 2604.4 m. The organic matter in the paleomire was highly reworked by microbial processing. Dense flourishing vegetation established a CO_2-limited environment forcing aquatic plants to utilise HCO_3^- during photosynthesis.

(4) Vitrinite reflectance, Tmax, and biomarker indices denote that organic matter in the Kosd Formation (as identified in deep borehole W–1) is thermally mature and suggests that the Kosd coal reached high-volatile bituminous rank in the research area. This is higher than the rank of the sub-bituminous coal in the shallow Kosd coalfield of the North Hungarian Mountains. This advanced maturity influenced the molecular and isotopic composition of hydrocarbons.

(5) Rock-Eval pyrolysis results indicate that the coaly samples studied are gas- and oil-prone and have reached the maturity threshold for first gas generation and the onset of oil expulsion.

III. CHAPTER

Source rock potential, crude oil characteristics and oil-to-source rock correlation in a Central Paratethys sub-basin, the Hungarian Palaeogene Basin (Pannonian Basin)

Sándor Körmös

University of Szeged, Department of Mineralogy, Geochemistry and Petrology, Egyetem u. 2, H-6722 Szeged, Hungary; MOL Plc, Október huszonharmadika u. 18, H-1117 Budapest, Hungary

email address: sandor.kormos@geo.u-szeged.hu

Reinhard F. Sachsenhofer

Montanuniversität Leoben, Petroleum Geology, Peter-Tunner-str. 5, A-8700 Leoben, Austria

email address: reinhard.sachsenhofer@unileoben.ac.at

Achim Bechtel

Montanuniversität Leoben, Petroleum Geology, Peter-Tunner-str. 5, A-8700 Leoben, Austria

email address: Achim.Bechtel@outlook.de

Balázs Géza Radovics

MOL Plc, Október huszonharmadika u. 18, H-1117 Budapest, Hungary

email address: BGRadovics@mol.hu

Katalin Milota

MOL Plc, Október huszonharmadika u. 18, H-1117 Budapest, Hungary

email address: KMilota@mol.hu

Félix Schubert

University of Szeged, Department of Mineralogy, Geochemistry and Petrology, Egyetem u. 2, H-6722 Szeged, Hungary

email address: schubert@geo.u-szeged.hu

Marine and Petroleum Geology

127, 104955 (2021) DOI 10.1016/j.marpetgeo.2021.104955

Source rock potential, crude oil characteristics and oil-to-source rock correlation in a Central Paratethys sub-basin, the Hungarian Palaeogene Basin (Pannonian Basin)

by: Sándor Körmös, Reinhard F. Sachsenhofer, Achim Bechtel, Balázs Géza Radovics, Katalin Milota, Félix Schubert

Abstract

Eocene and Lower Oligocene rocks are potential source rocks for crude oil accumulations in the Hungarian Palaeogene Basin. To enhance the understanding of the hydrocarbon system, this study (i) assesses the petroleum potential of Palaeogene formations, (ii) characterises the source rock facies of the accumulated oils, and (iii) provides an oil-to-source correlation.

Rock-Eval data of samples from three boreholes (W–1, W–9 and W–12) show that most Palaeogene formations are mature at depths exceeding 2.1–2.5 km. The coal-bearing Kosd Formation includes good to excellent gas- (and oil-) prone source rocks. The overlying Buda Marl Formation is typically organic matter-lean but contains oil-prone rocks with up to 2.3 wt% TOC and a fair petroleum potential in borehole W–9. The Tard Clay Formation in W–12 reaches up to 1.9 wt% TOC and shows HI values up to 440 mg HC/g TOC, characterising the deposits as good petroleum source rocks. Based on low TOC contents, the Kiscell Clay Formation is not considered a source rock.

Molecular parameters of 12 crude oil samples indicate a shaly source rock deposited in a marine/brackish environment. Salinity stratification, causing the development of oxygen-depleted conditions, is likely. The organic matter is dominated by aquatic biomass, including algae, dinoflagellates and chemoautotrophic bacteria. Minor angiosperm-dominated organic matter was transported into the basin from the shoreline.

Specific V-shaped compound-specific carbon isotope patterns of *n*-alkanes observed in crude oils and extracts from the Tard Clay prove the dominant source rock. Minor differences between biomarker ratios are related to vertical and lateral facies variations with the Tard Clay Formation. The accumulated oils are slightly more mature than the Tard Clay in borehole W–12.

3.1. Introduction

During the Palaeogene, the closure of the Mesozoic Tethyan basin and subsequent basin isolation caused the birth of the Paratethys Sea (Schulz et al., 2005). The process resulted in water masses with varying salinity and redox conditions favouring the accumulation of organic matter-rich rocks (Popov et al., 2001, 2004; Rögl, 1999; Sachsenhofer et al., 2018a, b). The Paratethys basin system has been subdivided into three parts because of diachronous geotectonic events: (i) the Western Paratethys, formed by the Rhône Basin and Alpine Foreland Basin, west of Munich), (ii) the Central Paratethys, composed by the remaining Alpine Foreland Basin, Carpathian Basin and Hungarian Palaeogene Basin and (iii) the larger Eastern Paratethys (Popov et al., 2004).

The Neogene Pannonian Basin formed part of the Central Paratethys and is underlain by Eocene and Oligocene sediments of the Hungarian Palaeogene Basin (Fig. III.1; Tari et al., 1993). Fine-grained, organic matter-rich sediments within the Eocene and Oligocene succession were recognized as potential source rocks (e.g., Badics and Vető, 2012; Bechtel et al., 2012; Brukner-Wein et al., 1990; Körmös et al., 2020; Milota et al., 1995). Whereas it is

widely accepted that the Lower Oligocene Tard Clay Formation provides the most important source rocks (Fig. III.2; Bechtel et al., 2012; Brukner-Wein et al., 1990; Hertelendi and Vető, 1991; Milota et al., 1995), the Middle Eocene Kosd Formation (Körmös et al., 2020), Late Eocene Buda Marl Formation (Sachsenhofer et al., 2018a, 2018b) and Late Oligocene Kiscell Clay Formation (Milota et al., 1995) were also considered as potential source rocks (Fig. III.2). Nevertheless, comprehensive organic geochemical studies have only been performed on sediments of the Tard Clay and Kosd formations (Bechtel et al., 2012; Körmös et al., 2020), whereas in-depth investigations are still missing for the Buda Marl and Kiscell Clay formations. Furthermore, detailed analysis of crude oils and thorough oil-to-source rock correlation are also absent.

This study focuses on the central-southern part of the Hungarian Palaeogene Basin. The study aims are to advance the understanding of the petroleum system by (i) characterising the maturity and source rock potential of the Upper Eocene (Kosd and Buda Marl formations) and Lower Oligocene (Tard Clay and Kiscell Clay formations) succession, (ii) determining the source rock facies of crude oils produced in several oil fields in the Hungarian Palaeogene Basin, and (iii) correlating these crude oils to a specific source rock formation.

Maturity and source rock potential of the Palaeogene succession are assessed using numerous Rock-Eval data from deep boreholes W–1, W–9 and W–12 (for location see Fig. III.1b). Biomarker data of 12 crude oil samples are applied to reconstruct the depositional environment of their source rocks. Oil-to-source rock correlation is based on biomarker and compound-specific isotope data from oil samples, which are compared with new source rock data and source rock data published by Bechtel et al. (2012) and Körmös et al. (2020), who discussed the origin of the source organic matter, established on biomarker parameters, in the Tard Clay and Kosd formations, respectively.

3.2. Geological setting

The study area is located in the southern part of the central Hungarian Palaeogene Basin (Fig. III.1), which overlies a basement constructed of the Mid-Hungarian Zone (Kovács and Haas, 2010). The Hungarian Palaeogene Basin is interpreted as a retro-arc flexural foreland basin, where the depositional facies migrated towards the east-norteast according to the present position (Fig. III.2; Tari et al., 1993; Kováč et al., 2016). The tectonic evolution has been related to normal faulting and strike-slip regimes (Palotai, 2013 and references therein). The term Palaeogene Basin comprises all sedimentary sequences, forming a single cycle from the Eocene to the Early Ottnangian (Fig. III.2; Sztanó and Tari, 1993).

The Alpine Orogeny resulted in the exhumation of the Mesozoic strata during the Late Cretaceous. Subaerial exposure caused continental denudation until the Late Eocene (Haas and Kovács, 2012). The Palaeogene sediments unconformably overlie the Mesozoic basement. The sedimentary succession starts with a terrigenous basal conglomerate, breccia and variegated clay (Bauer et al., 2016). The Kosd Formation reflects a continuous upward transition to a lagoonal environment (Gidai, 1978; Less, 2005), showing the first sign of the Priabonian transgression (Báldi and Báldi-Beke, 1985). The upper part of the Kosd Formation is coal-bearing and includes pelitic sediments with varying carbonate content (Gidai, 1978; Less, 2005; Körmös et al., 2020). The Kosd Formation is overlain by the shelf deposits of the Szépvölgy Limestone Formation (Kázmér, 1985). Continued subsidence caused the deposition of the Buda Marl Formation across the Eocene-Oligocene transition, which contains marl and calcareous marl, allodapic limestones and calcareous turbidites deposited under oxygen-depleted conditions (Less, 2005; Nagymarosy and Báldi-Beke, 1988; Ozsvárt et al., 2016).

The Buda Marl Formation is overlain by the Tard Clay Formation. This formation accumulated in a euxinic basin, which was filled from the west (according to the present position; Fodor et al., 1994) by a prograding siliciclastic delta. Hence, the Tard Clay Formation is missing in the west of the Buda Hills. The Tard Clay Formation includes laminated and non-laminated shale and sandstone (Brukner-Wein et al., 1990). The degree of lamination varies considerably within the formation but is often the highest in its middle part, representing the nannozone NP23 (Nagymarosy, 1983), where dark grey siltstone alternates with white coccolith layers. These intervals are characterised by high TOC contents (max. 5 wt% TOC; Brukner-Wein et al., 1990) and represent oxygen-depleted conditions (Báldi, 1984; Bechtel et al., 2012). The overlying Kiscell Clay Formation is accumulated in a deep bathyal, well-oxygenated depositional environment (Báldi and Báldi-Beke, 1985), comprising intercalated siltstones and turbiditic sandstone bodies (Less, 2005; Milota et al., 1995).

The Palaeogene succession is terminated by interfingering heteropic sediments, including, from west (Buda Hills) to east (Bükk Mts.) the shallow sublittoral Törökbálint Sandstone Formation, the deep sublittoral–shallow bathyal Szécsény Schlier Formation and the deep sublittoral Eger Formation (Kercsmár et al., 2015). The littoral–sublittoral Budafok Formation covers the Törökbálint Sandstone, which is laterally intercalating with the upper part of the Szécsény Schlier Formation (Sztanó and Tari, 1993). The latter grades eastwards into the shallow marine Pétervására Sandstone Formation, composed of several coast parallel facies units (Sztanó and Tari, 1993). Gradual uplift in late Eggenburgian time resulted in subaerial exposure and the deposition of the Zagyvapálfalva Formation in a coastal plain setting. The Gyulakeszi Rhyolite Tuff covers the eroded surface of the Palaeogene to Eggenburgian formations (Nagymarosy, 2013). The sedimentary sequence of the Hungarian Palaeogene Basin is covered by thick Neogene sediments.

3.2.1. Source potential of the Palaeogene sediments

Whereas the Tard Clay Formation is the most widely accepted potential source rock in the Hungarian Palaeogene Basin, organic matter rich intervals in the Buda Marl and Kiscell Clay formations were also considered (Badics and Vető, 2012; Sachsenhofer et al., 2018a, 2018b). Recently, Körmös et al. (2020) investigated the hydrocarbon potential of the coal-bearing Kosd Formation.

The Eocene Kosd Formation includes an up to 36-m-thick coal horizon. The coaly layers accumulated in a marine delta and are intercalating with siltstone containing miliolid foraminifers. The high volatile bituminous coal and coaly shale are characterised by HI values between 200 and 300 mg HC/g TOC in the deep well W–1. The coal measure is gas- and oil-prone and have reached the rank threshold for the first gas generation (Körmös et al., 2020).

The TOC contents of the Buda Marl Formation are generally below 1 wt% (max. 2.3 wt%), and HI values (<150 mg HC/g TOC) fall within the range of type III and type IV kerogen (Bechtel et al., 2012; Sachsenhofer et al., 2018a, 2018b).

The non- to weakly-laminated lower section of the Tard Clay Formation contains TOC contents up to 5 wt% (Brukner-Wein et al., 1990) but with low HI values (<185 mg HC/g TOC; Bechtel et al., 2012). Higher HI values (up to 440 mg HC/g TOC) occur in the strongly-laminated middle part of the formation, deposited in a brackish environment during the Solenovian Event (Bechtel et al., 2012; Brukner-Wein et al., 1990; Hertelendi and Vető, 1991). The upper part of the Tard Clay is characterised by gradually declining TOC and HI values (down to 0.5 wt% TOC and 75 mg HC/g TOC, respectively) with rising salinity in the water column (Bechtel et al., 2012).

The Kiscell Clay is characterised by low TOC and HI values (<1 wt% and <200 mg HC/g TOC, respectively; Milota et al., 1995) but published data are scarce.

3.2.2. Hydrocarbon reservoirs and traps in the study area

Hydrocarbons were detected in the fractured and weathered Mesozoic basement rocks in the research area. The basal conglomerate and breccia and the sandstone sequence of the Kosd Formation also form reservoirs and host substantial amounts of hydrocarbons. The karstified Szépvölgy Limestone and turbidite sandstone bodies within the Kiscell Clay Formation and the clastic sediments of the Miocene formations also serve as targets of exploration activities (Dolton, 2006). Various structural, stratigraphic and combination trap types were discovered within the study area. Compactional anticlines occur over basement highs. Fault-closed features, associated roll-overs and closures in flower structures are also common (Kokai, 1994; Dolton, 2006).

3.3. Samples and analytical methods

3.3.1. Samples

This study is based on rock and oil samples from boreholes W–1 to W–13, drilled by MOL Plc. during the last decades (for location see Fig. 1b). Twenty-four drill core samples, representing the Kosd Formation and Tard Clay Formation were sampled from wells W–1 and W–12. Drill cores are complemented by 196 cuttings, washed and wet samples, containing Palaeogene sediments from boreholes W–1, W–9, and W–12 provided by MOL Plc. The wells were drilled using water-based mud and were selected because of the systematically performed lag-time checks for accurate depth readings for taking drill cuttings. Intervals containing lost circulation materials and mud additives (e.g., nutshells, lignite) were avoided whenever it was possible, otherwise handpicking of solid contaminants and cavings was achieved before analysis. Moreover, sections with observed crude oil indications on the shale shakers were not considered for sampling. The organic geochemical data of core samples from the Kosd Formation were described recently by Körmös et al. (2020).

Crude oil samples were obtained from Triassic, Eocene and Oligocene reservoirs from W–1 to W–3, W–8 and W–10 to W–13 wells. MOL Plc provided additional results for oil from boreholes W–4 to W–7. The reservoirs are characterised by hydrostatic pressure (Boncz, 2004, 2013; Kiss, 1999). Table III.1 lists the age and lithology of the reservoir rocks and depth of the oil-water contact.

The study is also supplemented by results acquired during investigating the Tard Clay Formation by Bechtel et al. (2012) at Alcsútdoboz–3, Cserépváralja–1 and Balassagyarmat–5 (Ad–3, Csv–1 and Bgy–5, respectively; for location see Fig. III.1a).

3.3.2. Organic geochemical analyses

The total organic carbon (TOC) contents and Rock-Eval parameters of cutting and core samples were determined in the laboratories of MOL and Montanuniversität Leoben, respectively. An ELTRA Helios CS-580A analyser was used to obtain the TOC contents on duplicates of powdered core samples, pre-treated by H_3PO_4, by combustion. The TOC contents of cutting samples were determined by Rock-Eval pyrolysis on duplicates of pulverized samples. The TOC contents achieved by pyrolysis of bulk rocks (Rock-Eval 6) and by combustion of samples, pre-treated by acid (ELTRA), agree very well (*cf.* Behar et al., 2001).

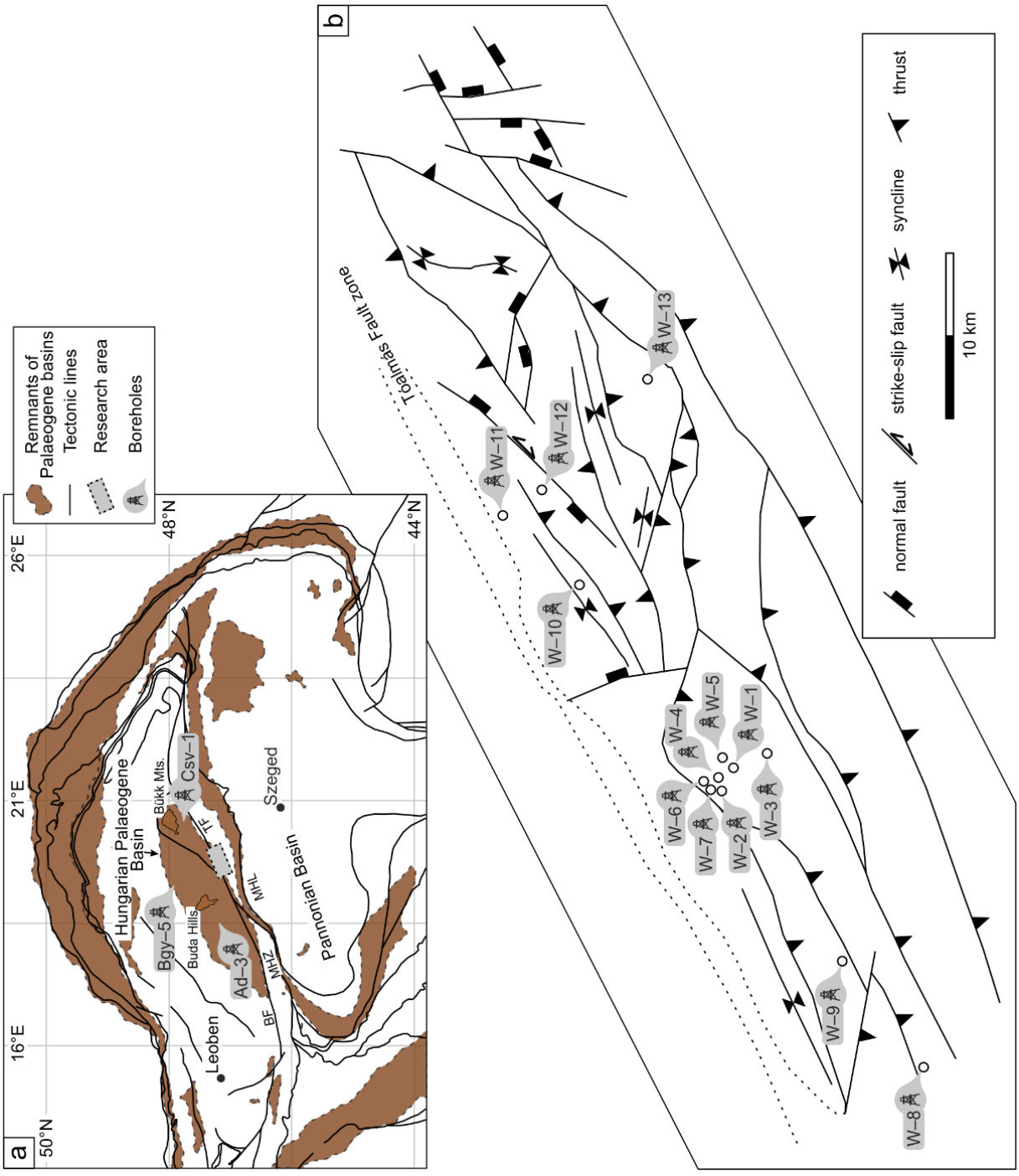

Fig. III.1. Regional setting of **a**) the Hungarian Palaeogene Basin and **b)** the study area (modified after Kováč et al., 2016; Ozsvárt et al., 2016; Palotai, 2013; Schmid et al., 2008). BF – Balaton Fault, MHZ – Mid-Hungarian Zone, MHL – Mid-Hungarian Line, TF – Tóalmás Fault, Ad–3 – Alcsútdoboz–3, Bgy–5 – Balassagyarmat–5, Csv–1 – Cserépváralja–1, W–1 to W–13 are studied boreholes.

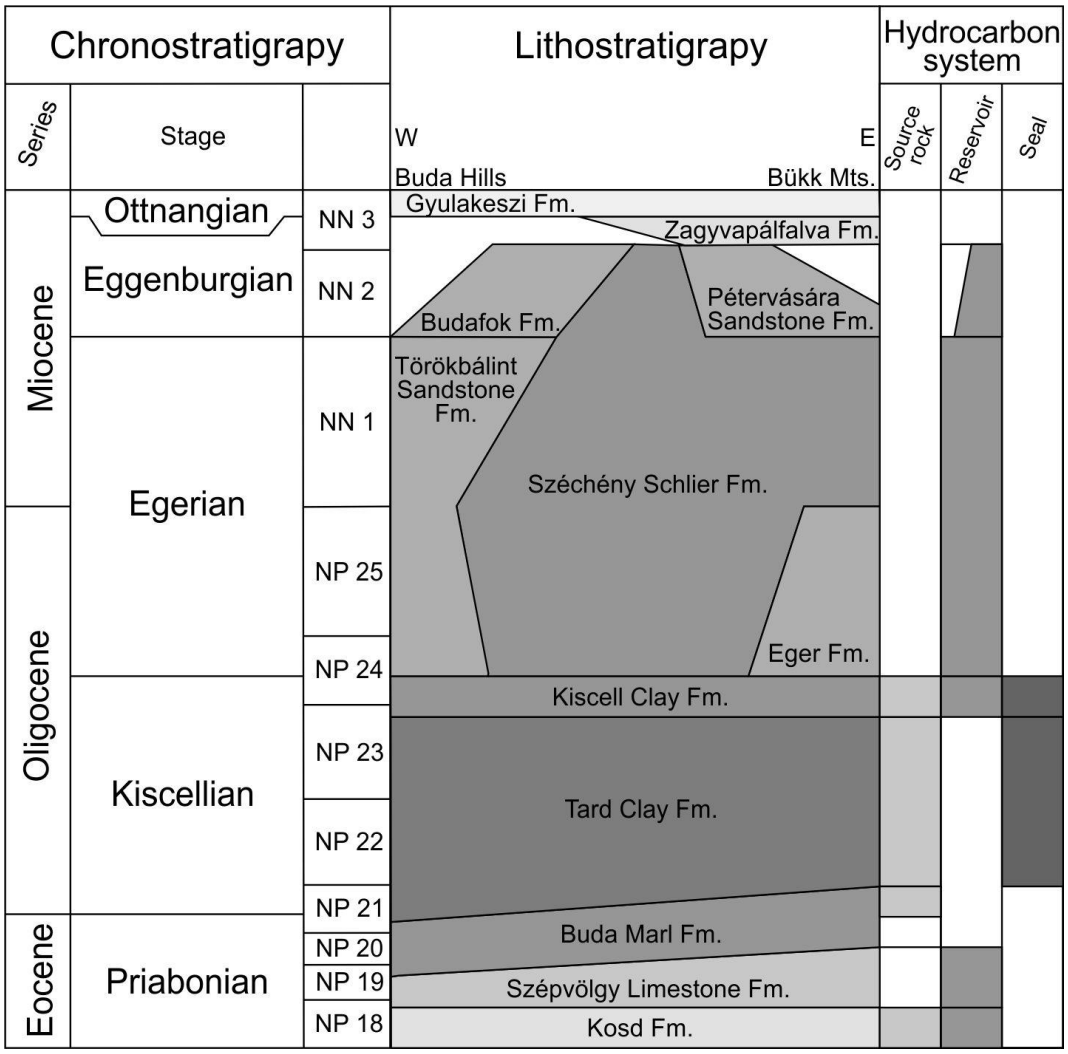

Fig. III.2. Simplified lithostratigraphy of the sedimentary succession in the Hungarian Palaeogene Basin and elements of the hydrocarbon system in the study area (after Kercsmár et al., 2015; Less, 2015 oral communication; Tari et al., 1993). The nannoplankton zonation is based on Less (2005), Ozsvárt et al. (2016) and Tari et al. (1993).

Rock-Eval 6 instruments were employed to quantify the free and generated hydrocarbons (S1 and S2 peaks, respectively) in both laboratories (Lafargue et al., 1998). The temperature at the maximum hydrocarbon generation (Tmax [°C]) was detected and applied as a maturity indicator. Derived Rock-Eval parameters include the hydrogen index (HI = S2 × 100/TOC [mg HC/g TOC]), the production index (PI = S1/(S1 + S2) [—]; Espitalié et al., 1977) and the petroleum potential (PP = S1 + S2 [mg HC/g rock]).

Table. III.1. Age, lithology and depth of the oil-water contact for reservoirs of studied oil samples (after Boncz, 2004, 2013 and Kiss, 1999).

Well name	Age	Lithology	Oil-water contact
			[m; MD]
W–1	Eocene	Sandstone, polymict conglomerate	2469
W–2	Eocene and Triassic	Sandstone, polymict conglomerate and limestone	2513
W–3	Eocene	Sandstone, polymict conglomerate	2490
W–4	Eocene and Triassic	Sandstone, polymict conglomerate and limestone	2453
W–5	Eocene	Sandstone, polymict conglomerate	2495
W–6	Eocene	Sandstone, polymict conglomerate	2510
W–7	Eocene	Sandstone, polymict conglomerate	2449
W–8	Eocene	Limestone breccia	1722
W–10	Eocene and Triassic	Fractured- and karstified limestone	1780
W–11	Jurassic	Limestone	2491
W–12	Oligocene and Eocene	Fractured siltstone and biogenic limestone	2316
W–13	Triassic	Fractured limestone	2249

MD – measured depth.

Aliquots of powdered rock samples, 10 g each, were extracted using dichloromethane solvent at 75 °C and 110 bar over 1 h utilizing a Dionex ASE 350 accelerated solvent extractor. The elemental sulphur content of the solution was removed by adding copper. The extracts were concentrated to 1 ml solution by a Zymark TurboVap 500 closed cell concentrator. The crude oil samples, 50 mg each, and the concentrated extracts were diluted by a mixture of hexane–dichloromethane (80:1) solution and insoluble asphaltenes were precipitated, and separated by centrifugation. Hexane diluted and dissolved the maltenes, which were injected into a Margot Köhnen-Willsch medium-pressure liquid chromatography instrument to separate the NSO (containing nitrogen, sulphur and oxygen), saturated and aromatic compounds (Radke et al. 1980b). The saturated and aromatic compounds were concentrated and internal standards were added (deuterated *n*-tetracosane and 1,1'-binaphthyl, respectively). The normal and branched–cyclic alkanes were further separated for compound-specific isotope analyses using an improved 5Å molecular sieve method (Grice et al., 2008). The isotope fractionation of compounds seems unlikely based on the low-temperature-controlled chemical reactions during sample preparation.

The saturated hydrocarbon fractions were analysed using a Thermo Scientific TraceGC gas chromatograph attached to a flame ionisation detector, installed with an HP-PONA fused silica capillary column (50 m, i.d. 0.2 mm; 0.5 μm film thickness). The samples were injected in split mode at 270 °C. The oven temperature was programmed to an initial 5 min period at 32 °C, followed by 2.5 °C/min heating rate to 310 °C and hold for 30 min. Helium was used as the carrier gas. The flame ionization detector was operated at 320 °C with 350 and 35 ml/min flow rate of air and hydrogen, respectively. Data were processed using an Xcalibur data system. Individual compounds were identified based on retention time. The concentration of n-alkanes and acyclic isoprenoids, as well as the corresponding concentration ratios, are based on peak area integration compared to the internal standard.

A gas chromatograph coupled to a ThermoFisher ISQ mass spectrometer equipped with a DB-5MS fused silica capillary column (60 m, i.d. 0.25 mm; 0.25 μm film thickness) was used to analyse the saturated and aromatic hydrocarbon fractions. The oven temperature was programmed to an initial 70 °C and raised to 300 °C at 4 °C/min rate, followed by an isothermal period of 15 min. The carrier gas was helium. The samples were injected through an injector at 275 °C in splitless mode. Electron ionisation of the molecular species was achieved over a scan range of 50–600 m/z with a total scan time of 500 msec during the analyses. Data were processed using an Xcalibur data system. Individual compounds were identified in the total ion current (TIC) chromatogram based on retention time and fragment ions of m/z 191, 217, 218, 231, and 259 were chosen for recognition of hopanoids and steranes (Ensminger et al., 1978; Summons et al., 1987; Wingert and Pomerantz, 1986), as well as the mass spectra were compared with published data. The 4-methylsteranes were distinguished on the diagnostic ion, m/z 231 mass chromatograms, and 24–*n*–propylcholestanes were determined according to the registered mass spectra (Moldowan et al., 1990). Absolute concentrations and relative percentages of different compound groups were estimated using peak areas of internal standards in the TIC chromatograms, or by integrating peak areas in convenient mass chromatograms employing response factors to quantify the total ion abundance.

Stable carbon isotope measurements of *n*-alkanes were performed on selected samples, including crude oils and rock extracts from drill cores, using a Trace GC instrument coupled to a ThermoFisher DELTA-V IR mass spectrometer *via* a GC isolink combustion interface. CO_2 was injected during each analysis as monitoring gas. The GC column and temperature programme used were the same as above. The saturated and aromatic hydrocarbon fractions of selected crude oils and rock extracts from drill cuttings were placed into tinfoil boats for the bulk carbon isotope analyses and combusted in an oxygen atmosphere using an elemental analyser (Flash EA 1112) at 1020 °C. The evolving CO_2 was separated by column chromatography and analysed online using a DELTA-V IR-MS. The $^{13}C/^{12}C$ isotope ratios of CO_2 were compared with the monitoring gas. Stable isotope ratios are expressed relative to the Vienna Pee Dee Belemnite (V-PDB) standard in delta notation ($\delta^{13}C = [(\delta^{13}C/\delta^{12}C)_{sample}/(\delta^{13}C/\delta^{12}C)_{standard} - 1]$; Coplen, 2011). Delta notation is reported in parts per thousand or per mil (‰). The analytical error during the measurements was better than 0.2‰.

3.4. Results

3.4.1. Bulk geochemical parameters of source rocks

Several wells, including W–1, W–9 and W–12, penetrated the potential source rocks, which were sampled for hydrocarbon generation potential assessment (Fig. III.3). Rock-Eval data are compiled in Supplementary Table 1 (W–1), 2 (W–9) and 3 (W–12). The assignment of the sediments to stratigraphic units follows the internal reports of MOL Plc.

The Kosd Formation was penetrated by wells W–1 and W–9. TOC contents in samples from the Kosd Formation vary widely from 0.10 to 78.39 wt%, reflecting the presence of different lithotypes, including organic matter-lean siltstone, claystone, coaly shale and coal. The Tmax and HI values range from 431 to 451 °C and from 31 to 348 mg HC/g TOC, respectively (Fig. III.4a). The PP varies between 0.05 and 209.64 mg HC/g rock and averages at 52.09 mg HC/g rock in high TOC (> 2 wt%) intervals.

The sediments of Buda Marl Formation in wells W–1, W–9 and W–12 are characterised by TOC contents ranging from 0.04 to 2.65 wt% (avg. 0.73 wt%). The Tmax values range from 430 to 444 °C and the HI varies from 33 to 325 mg HC/g TOC (Fig. III.4b). The PP reaches a maximum of 10.55 mg HC/g rock in well W–9 and averages at 4.78 mg HC/g rock at intervals where the TOC content is greater than 1 wt%.

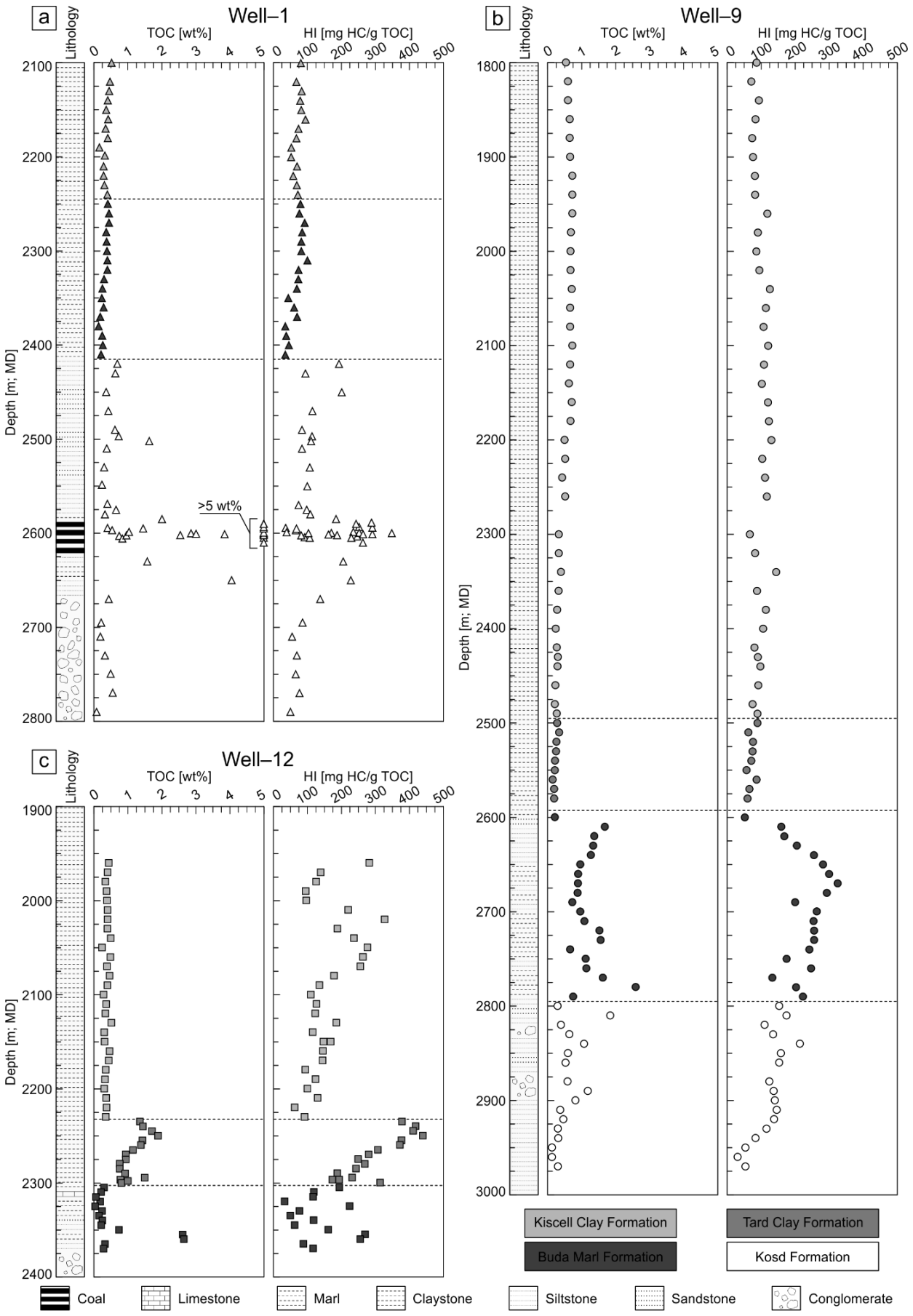

Fig. III.3. Organic geochemical depth logs of the **a)** W–1, **b)** W–9 and **c)** W–12 wells based on Supplementary Tables 1, 2 and 3. The simplified lithologies presented according to the description of drill cuttings for each well. MD – measured depth.

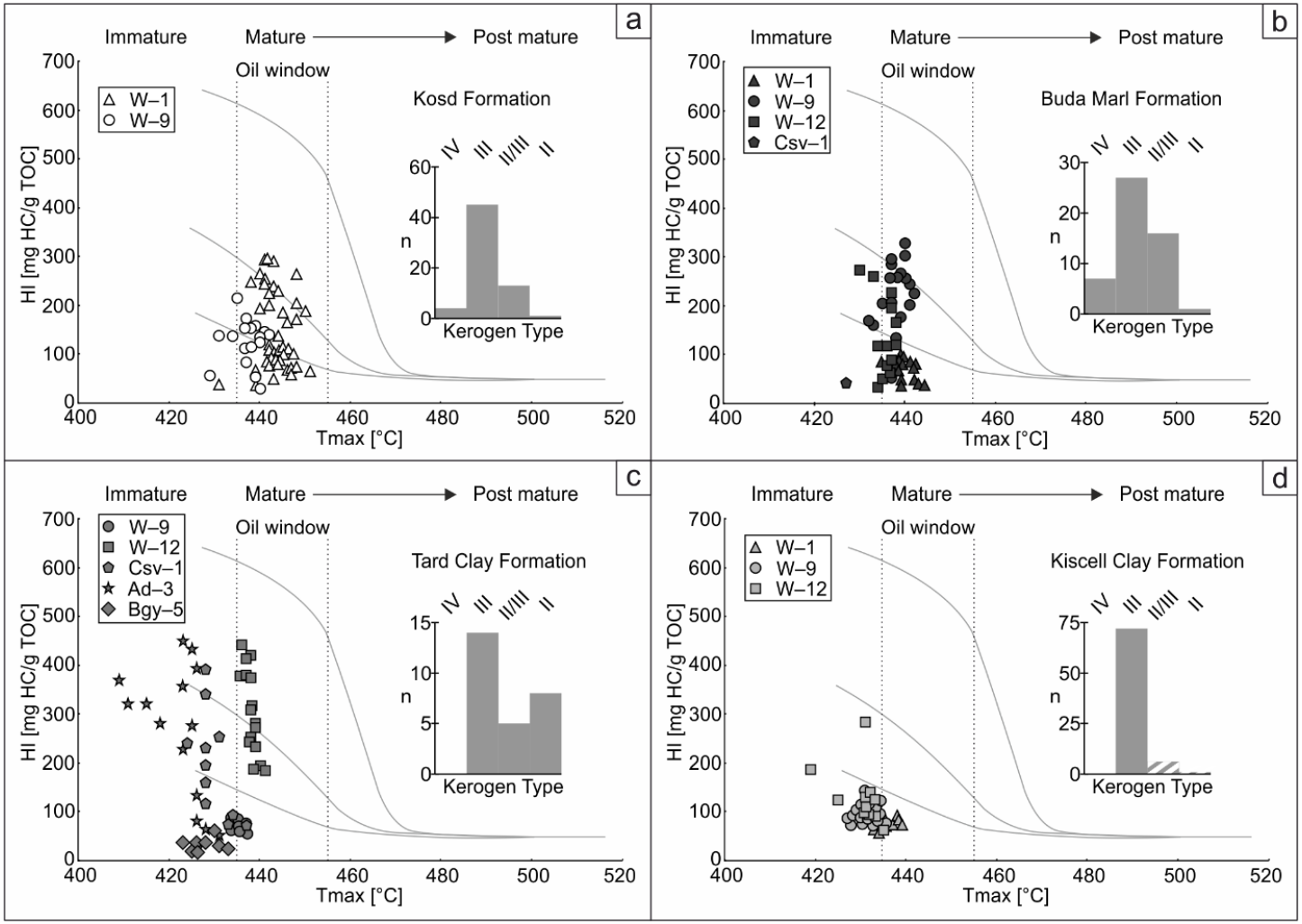

Fig. III.4. Hydrocarbon generation potential assessment of **a)** Kosd Formation, **b)** Buda Marl Formation, **c)** Tard Clay Formation and **d)** Kiscell Clay Formation. Results presented for Csv–1, Ad–3 and Bgy–5 boreholes are taken form Bechtel et al. (2012). The hatched columns of the frequency diagram in Fig. 4d represent kerogen types without recorded Tmax values.

Significant differences exist between organic matter contents and HI values of the Tard Clay Formation in the western well W–9 (0.15–0.30 wt% TOC; 65–104 mg HC/g TOC) and the eastern well W–12 (0.80–1.89 wt% TOC; 189–439 mg HC/g TOC). The Tmax values range from 434 and 441 °C (Fig. III.4c). The PP is between 1.94 and 9.31 mg HC/g rock in well W–12 and averages at 6.14 mg HC/g rock in the upper high TOC (> 1 wt%) interval.

The TOC contents of the Kiscell Clay Formation in wells W–1, W–9 and W–12 range from 0.16 to 0.71 wt% (avg. 0.45 wt%). The Tmax values vary from 419 to 439 °C and the HI values are between 55 and 327 mg HC/g TOC (Fig. III.4d). The PP is generally below 1 mg HC/g rock (max. 1.44 mg HC/g rock).

3.4.2. Crude oils

Crude oil samples from different hydrocarbon accumulations in the study area were analysed. Reservoir rocks include Mesozoic fractured carbonates, Eocene karstified carbonates, Eocene and Oligocene clastic reservoirs (Table III.1). Eight samples were analysed in this study (W–1o to W–3o and W–8o to W–13o; Table III.2), whereas MOL Plc provided data of the samples W–4o to W–7o (Table III.2).

3.4.2.1. Molecular composition

The saturated hydrocarbons dominate in the oil samples, except in W–3o and W–11o. In the latter, the polar fractions prevail over the hydrocarbons (Table III.2). The NSO compounds also appear in greater proportion in W–1o, W–8o, W–12o and W–13o samples, whereas the aromatic and asphaltene fractions remain constant in most samples (Table III.2).

Table III.2. Percentage of extracted fractions and concentration ratios of selected compounds and compound groups within the hydrocarbon fractions of the crude oil samples.

ID	a	b	c	d	e	f	g	H	i	j	k	l	m	n	o	p	q	r	s	t	u
#	[wt%]				[‰; V-PDB]		[%]							[%]							
W–1o	55	16	26	3	n.d.	n.d.	36	33	17	1.06	0.96	0.54	1.79	23	42	35	1.20	0.16	0.22	0.51	0.74
W–2o	72	13	10	4	n.d.	n.d.	35	33	16	1.05	0.89	0.48	1.83	26	40	34	1.18	0.23	0.26	0.56	0.74
W–3o	19	4	74	4	n.d.	n.d.	35	33	17	1.00	0.88	0.50	1.78	24	40	36	1.11	0.20	0.23	0.52	0.75
W–4o	77	10	7	6	–27.7	–26.3	36	31	18	1.03	0.86	0.47	2.01	29	33	38	0.87	n.d.	0.24	0.52	0.68
W–5o	79	11	3	7	–27.8	–26.6	36	31	18	1.02	0.86	0.48	1.96	30	34	36	0.94	n.d.	0.22	0.53	0.69
W–6o	79	11	3	8	–27.4	–26.5	36	31	18	1.03	0.84	0.48	1.96	29	33	38	0.87	n.d.	0.24	0.54	0.69
W–7o	80	11	2	8	–27.7	–26.6	36	31	18	1.05	0.93	0.51	2.04	29	33	38	0.87	n.d.	0.22	0.53	0.69
W–8o	45	14	34	7	n.d.	n.d.	27	34	27	1.05	0.82	0.55	1.66	35	30	35	0.86	0.02	0.36	0.52	0.80
W–10o	70	12	11	7	n.d.	n.d.	18	34	35	1.12	0.92	0.43	2.19	27	32	40	0.80	0.04	0.42	0.51	0.62
W–11o	28	12	58	3	n.d.	n.d.	35	33	17	1.01	1.01	0.56	1.77	23	40	36	1.11	0.16	0.19	0.50	0.71
W–12o	60	10	26	4	n.d.	n.d.	39	31	15	1.06	0.68	0.38	1.91	24	38	38	1.00	0.11	0.31	0.56	0.67
W–13o	56	10	32	3	n.d.	n.d.	27	33	28	1.06	0.64	0.39	1.68	34	32	35	0.91	0.10	0.49	0.51	0.77

a – saturated hydrocarbons, b – aromatic hydrocarbons, c – polar compounds, d – asphaltenes, e – $\delta^{13}C$ saturated hydrocarbons, f – $\delta^{13}C$ aromatic hydrocarbons, g – *n*-$C_{15–19}$/*n*-$C_{15–33}$, h – *n*-$C_{21–25}$/*n*-$C_{15–33}$, i – *n*-$C_{27–31}$/*n*-$C_{15–33}$, j – CPI (Bray and Evans, 1961), k – Pr/*n*-C_{17}, l – Ph/*n*-C_{18}, m – Pr/Ph, n – ααα(20R) C_{27} steranes/Σ ααα(20R) regular steranes, o – ααα(20R) C_{28} steranes/Σ ααα(20R) regular steranes, p – ααα(20R) C_{29} steranes/Σ ααα(20R) regular steranes, q – C_{28}/C_{29} ααα(20R) steranes, r – $C_{21–22}$/$C_{27–29}$ steranes, s – C_{27} diaS/(diaS+regS), t – 20S/(20S+20R) ααα C_{29} sterane, u – αββ/(αββ+ααα) C_{29} sterane, n.d. – not determined.

3.4.2.1.1. Straight-chain alkanes and isoprenoids

The *n*-alkanes dominate the aliphatic fraction of the crude oils (Fig. III.5a). Short-chain *n*-alkanes (*n*-C_{15-19}) are typically slightly more abundant than mid-chain *n*-alkanes (*n*-C_{21-25}), but mid-chain *n*-alkanes predominate in samples W–8o, W–10o and W–13o (Table III.2). Long-chain *n*-alkanes (*n*-C_{27-31}) are also abundant in samples W–8o, W–10o and W–13o (Table III.2). No distinct odd-over-even carbon number preference exists; the CPI values are close to one (max. 1.12; Table III.2). Acyclic isoprenoids (*i*-$C_{13–20}$) are considerably abundant (Fig. III.5a). Pristane dominates over phytane (Fig. III.5a; Table III.2). The Pr/*n*-C_{17} (0.82–1.01) and Ph/*n*-C_{18} (0.43–0.56) ratios are similar in most oils but significantly lower in samples W–12o and W–13o (0.64–0.68 and 0.38–0.39, respectively; Fig. III.6; Table III.2).

3.4.2.1.2. Steroids

The C_{27}–C_{29} 5α,14β,17β (H) and 5α,14α,17α(H) sterane isomers are present in the crude oils (Fig. III.7a). Normalised values of ααα(20R) steranes are provided on a ternary diagram (Huang and Meinschein, 1979), used to assess the depositional facies of organic matter (Fig. III.8). The C_{28} and C_{29} homologues show a slight prevalence and are present in similar percentages (C_{28}/C_{29}: avg. 0.98; Fig. III.8; Table III.2). The 24-*n*-propylcholestane and C_{28}–C_{30} homologues of the 4–methylsteranes are also identified in significant amounts (Fig. III.7a). Diasteranes occur in lower concentration than the regular steranes (Fig. III.7a) but show similar carbon number distribution. The values of the C_{27} diasteranes relative to the C_{27} regular steranes (C_{27} diaS/(diaS+regS)) vary from 0.19 to 0.49 (avg. 0.28; Table III.2).

Pregnanes are also present in the samples and the C_{21}–C_{22} homologues show prominent peaks in most oil samples (Fig. III.7a). The ratio of pregnanes to regular steranes ($C_{21–22}$/$C_{27–29}$) reaches a maximum of 0.23 (avg. 0.13; Table III.2). The stereoisomer ratios of αααC_{29} steranes range from 0.50 and 0.56 (avg. 0.52) and the ratios of αββ/(αββ+ααα) isomers vary from 0.62 to 0.80 (avg. 0.72; Table III.2).

3.4.2.1.3. Terpenoids

The occurrence of C_{27} to C_{35} 17α,21β(H)–type hopanes dominates the hopanoids pattern with the absence of C_{28} hopanes. The predominant hopanoid in most samples is 17α,21β–C_{30} hopane (H; Fig. III.7b). The 17α,21β(H)–type homohopanes show an exponentially decreasing pattern in peak height with increasing carbon numbers (Fig. III.7b). The 18α(H)–oleanane (Ol) is also present in considerable concentration (Fig. III.7b). A series of C_{19}– to C_{29}– tricyclic terpanes (TT) appears. Whereas C_{22}TT and C_{27}TT are absent, a slight dominance of C_{23}TT occurs (Fig. III.7b), also reflected by low C_{19}/C_{23}TT, C_{20}/C_{23}TT, C_{21}/C_{23}TT and C_{24}/C_{23}TT ratios (avg. 0.55, 0.59, 0.83, 0.68, respectively; Table III.3). The C_{24} tetracyclic terpane (TeT) and degraded TeT (10β(H)–des–A–oleanane and 10β(H)–des–A–lupane) are also identified in the samples (Fig. III.7b). Gammacerane is present in low concentrations (Fig III.7b). The source-related biomarker ratios are similar in most of the analysed crude oils (Table III.3). The stereoisomer ratio 22S/(22S+22R) of 17α,21β(H)–C_{32} hopanes varies from 0.55 to 0.61 (avg. 0.58; Table III.3).

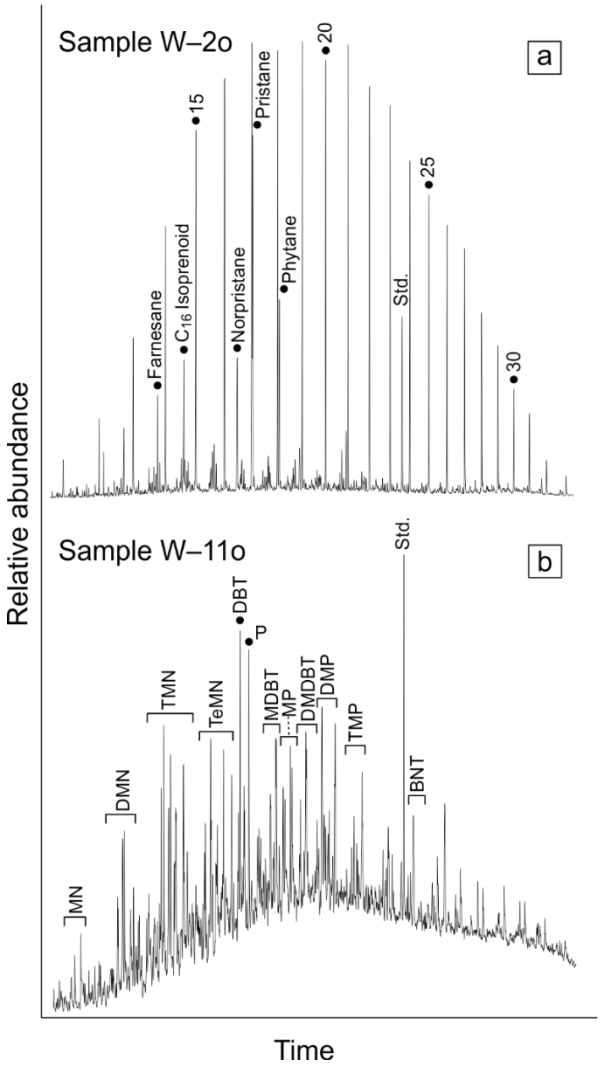

Fig. III.5. Gas chromatograms (total ion current) of the **a)** saturated and **b)** aromatic hydrocarbon fractions. *n*-Alkanes are labelled according to the carbon number. MN – methylnapthalenes, DMN – dimethylnapthalenes, TMN – trimethylnapthalenes, TeMN – tetramethylnapthalenes, P – phenanthrene, MP – methylphenanthrenen, DMP – dymethyphenanthrene, TMP – trimethylphenanthrene, DBT – dibenzothiophene, MDBT – methyldibenzothiophene, DMDBT – dimethyldibenzothiophene, BNT – benzonaphthothiophene, Std. – standard (deuterated *n*-tetracosane and 1,1'–binaphthyl, respectively).

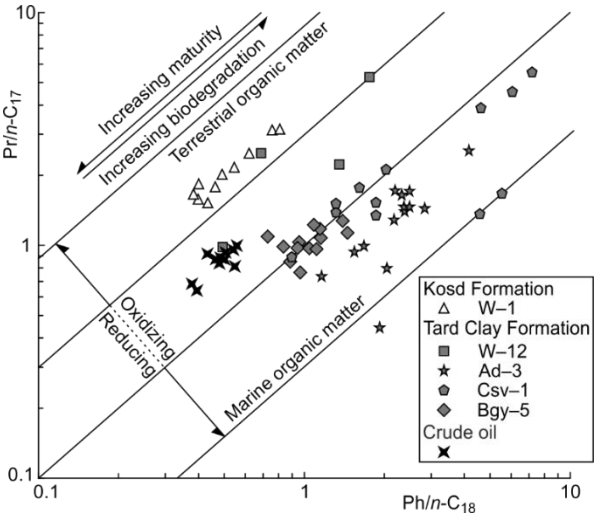

Fig. III.6. Cross plot of phytane/*n*-C_{18} vs. pristane/*n*-C_{17} of source rock and crude oil samples (after Connan and Cassou, 1980). Results representing W–1, Ad–3, Csv–1 and Bgy–5 wells are taken from Körmös et al. (2020) and Bechtel et al. (2012).

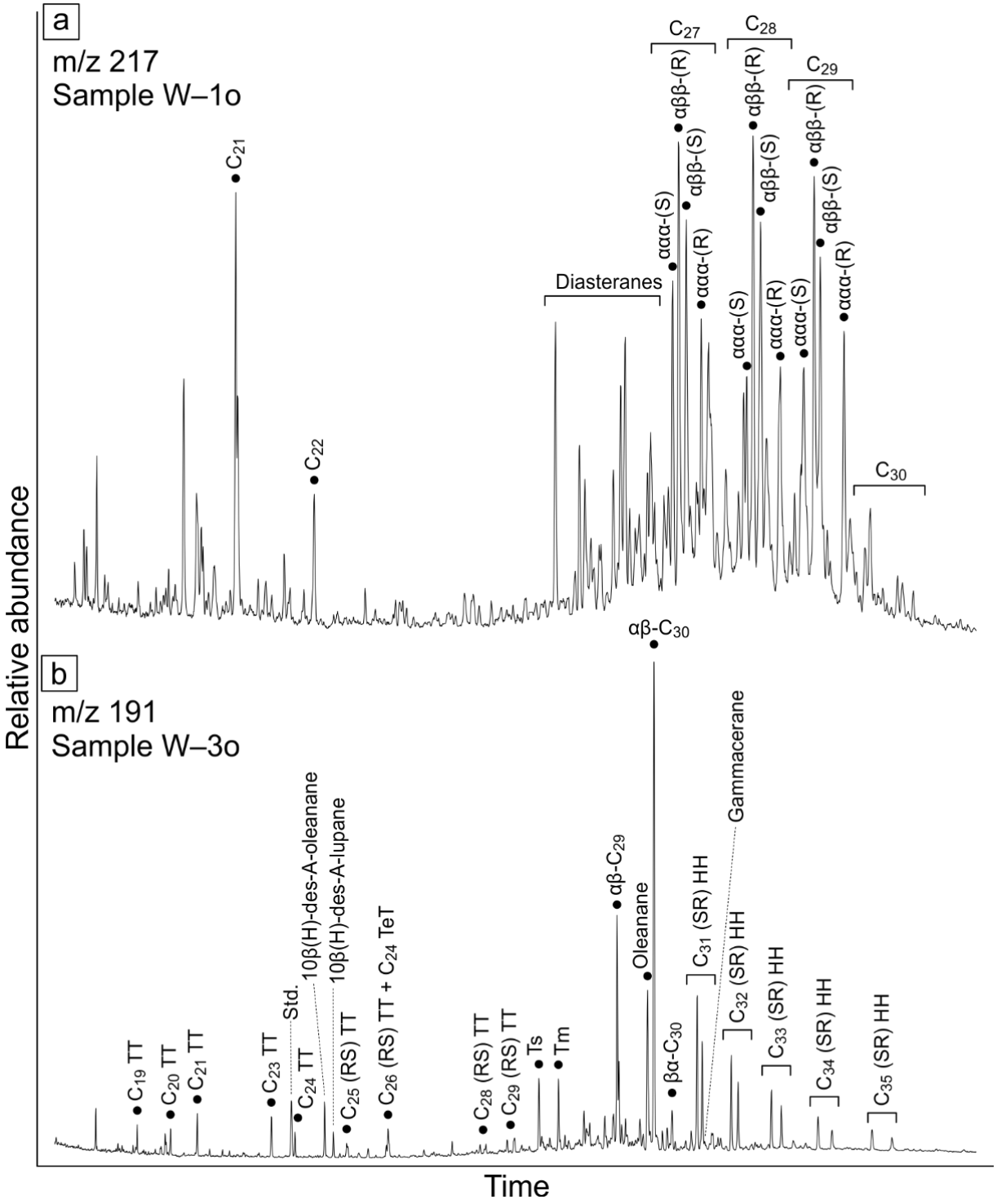

Fig. III.7. Representative mass chromatograms of the **a)** steranes (m/z 217) and **b)** terpanes (m/z 191). TT – tricyclic terpane, TeT – tetracyclic terpane, HH – homohopanes, Std. – standard (deuterated *n*-tetracosane).

3.4.2.1.4. Aromatic hydrocarbons

The aromatic hydrocarbon fractions of the crude oils are characterised by the occurrence of naphthalene, phenanthrene, dibenzothiophene and their alkylated counterparts (Fig. III.7b). Benzonaphthothiophenes are also present at a higher concentration in the samples (Fig. III.7b).

Vitrinite reflectance values based on the methylphenanthrene index (MPI 1; Radke et al., 1982a, 1982b) vary between 0.75 and 0.96% $Rc_{(MPI\ 1)}$ (avg. 0.84% $Rc_{(MPI\ 1)}$; Table III.3; Radke and Welte, 1983). The dibenzothiophene/phenanthrene ratios (DBT/P; Hughes et al., 1995) range from 0.22 to 1.27 (avg. 0.66; Fig. III.9; Table III.3).

Table. III.3. Source- and maturity-related biomarker and non-biomarker ratios of crude oil samples.

ID	a	b	c	d	e	f	g	h	i	j	k	l	m	n	o	p
#															[%]	
W–1o	0.56	0.57	0.83	0.57	0.93	0.07	0.30	0.46	0.25	0.68	0.09	0.31	0.57	0.51	0.81	0.75
W–2o	0.60	0.68	0.81	0.61	0.80	0.09	0.30	0.40	0.29	0.75	0.09	0.32	0.55	0.56	0.87	0.72
W–3o	0.58	0.65	0.86	0.76	0.88	0.08	0.31	0.45	0.23	0.71	0.08	0.34	0.56	0.52	0.84	0.68
W–4o	n.d.	n.d.	n.d.	0.54	0.84	0.12	0.39	0.45	0.29	0.86	0.11	0.31	0.59	0.52	0.87	0.59
W–5o	n.d.	n.d.	n.d.	0.58	0.95	0.09	0.40	0.46	0.33	0.88	0.12	0.32	0.60	0.53	0.86	0.58
W–6o	n.d.	n.d.	n.d.	0.57	0.95	0.09	0.40	0.45	0.30	0.87	0.12	0.31	0.61	0.54	0.87	0.59
W–7o	n.d.	n.d.	n.d.	0.45	1.06	0.10	0.40	0.46	0.33	0.88	0.12	0.32	0.60	0.53	0.75	0.57
W–8o	0.31	0.66	0.79	0.89	1.02	0.04	0.19	0.43	0.31	0.64	0.10	0.39	0.60	0.50	0.82	0.59
W–10o	0.65	0.77	0.72	0.86	0.77	0.04	0.19	0.49	0.31	0.90	0.10	0.41	0.58	0.49	0.87	0.55
W–11o	0.68	0.74	0.96	0.59	0.94	0.08	0.17	0.40	0.24	0.64	0.08	0.22	0.55	0.50	0.76	1.27
W–12o	0.54	0.43	0.77	0.59	0.78	0.05	0.24	0.41	0.26	0.78	0.09	0.33	0.58	0.56	0.77	0.22
W–13o	0.48	0.21	0.87	1.09	0.84	0.04	0.21	0.54	0.35	0.88	0.10	0.32	0.59	0.62	0.96	0.83

a – $C_{19}/C_{23}TT$, b – $C_{20}/C_{23}TT$, c – $C_{21}/C_{23}TT$, d – $C_{24}/C_{23}TT$, e – $C_{26}/C_{25}TT$, f – $C_{23}TT/17\alpha,21\beta–C_{30}$ hopane ($C_{23}TT/H$), g – Ol/(Ol+H); h – $17\alpha,21\beta–C_{30}$ norhopane/$17\alpha,21\beta–C_{30}$ hopane (NH/H), i – $17\alpha,21\beta–C_{31}$ (22R) homohopane/$17\alpha,21\beta–C_{30}$ hopane ($C_{31}(R)/H$), j – $17\alpha,21\beta–C_{35}$ (22S) homohopane/$17\alpha,21\beta–C_{34}$ (22S) homohopane ($C_{35}(S)/C_{34}(S)$), k – $17\alpha,21\beta–C_{35}$ homohopane/$17\alpha,21\beta–C_{31–35}$ homohopane ($C_{35}/C_{31–35}$), l – steranes/hopanes, m – 22S/(22S+22R) $17\alpha,21\beta–C_{32}$ homohopane, n – $17\alpha–C_{27}$ trisnorhopane/($17\alpha–C_{27}$ trisnorhopane+$18\alpha–C_{27}$ trisnorneohopane (Ts/(Ts+Tm)), o – $\%Rc_{(MPI\ 1)}$; Radke and Welte, 1983, p – DBT/P (Hughes et al., 1995).

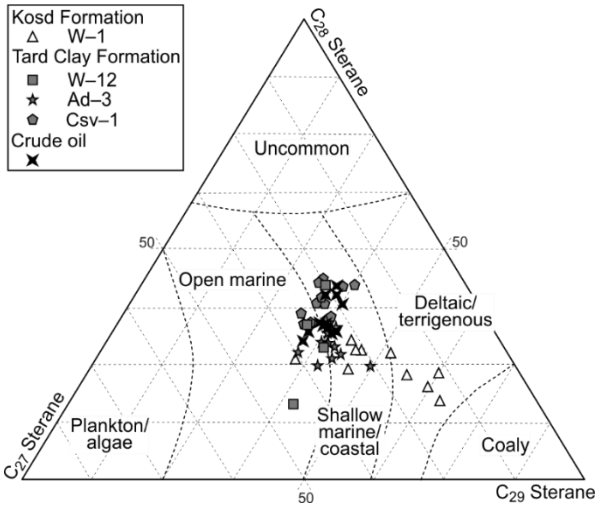

Fig. III.8. Ternary plot of ααα(20R) regular steranes (modified after Huang and Meinschein, 1979). The normalised abundance of the regular steranes in the Tard Clay and Kosd Formation from wells Ad–3, Csv–1 and W–1 are taken from Bechtel et al. (2012) and Körmös et al. (2020).

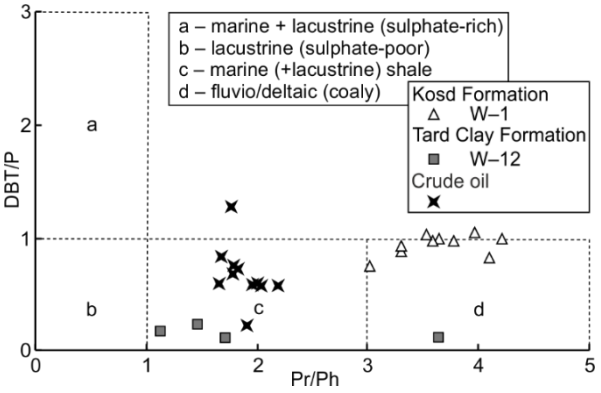

Fig. III.9. Cross plot of pristane/phytane vs. dibenzothiophenes/phenanthrene ratios of the studied samples (after Hughes et al., 1995). The ratios in the Kosd Formation from well W–1 is taken from Körmös et al. (2020). Pr – pristane, Ph – phytane, DBT – dibenzothiophenes, P – phenanthrene.

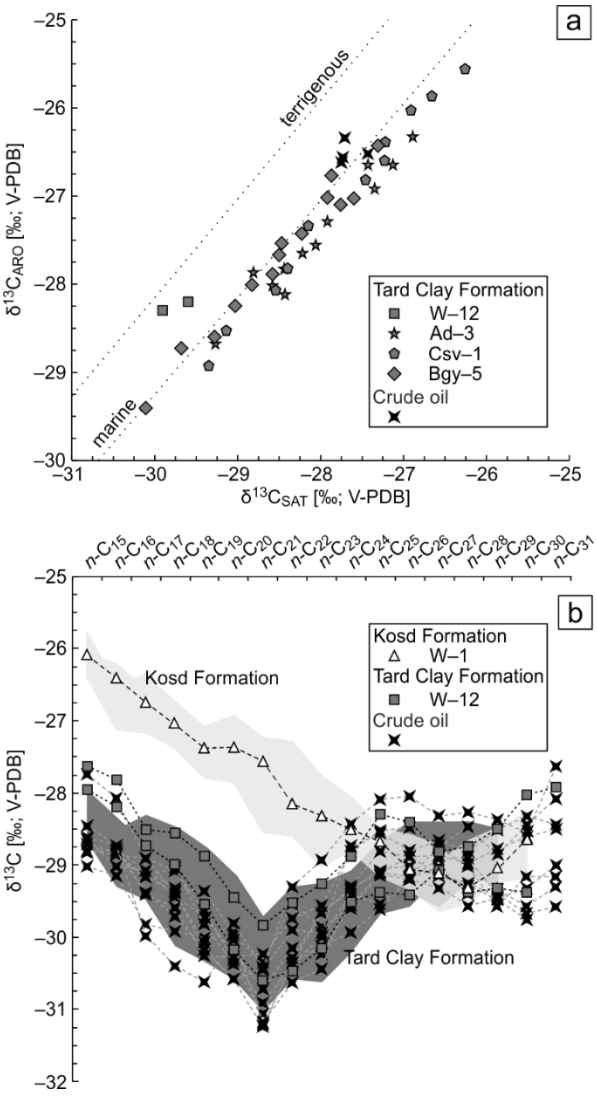

Fig. III.10. Stable carbon isotope composition of the **a)** saturated and aromatic hydrocarbon fraction of the Tard Clay and crude oil sam-ples. The $\delta^{13}C$ values of the Tard Clay from Ad–3, Csv–1 and Bgy–5 wells are taken from Bechtel et al. (2012). The marine and terri-genous lines are based on Sofer (1984). **b)** Compound-specific isotope of *n*-alkanes in the studied samples. The grey shaded areas represent $\delta^{13}C$ values of the Tard Clay (Bechtel et al., 2012) and Kosd Formation (Körmös et al., 2020). Mean values of four samples are presented for Kosd Formation from W–1 well.

3.4.2.2. Stable carbon isotope data

The stable carbon isotope composition ($\delta^{13}C$) of the saturated hydrocarbon fractions in crude oils W–4o to W–7o ranges from −27.8‰ to −27.4‰. The $\delta^{13}C$ values of the aromatic hydrocarbon fractions vary from −26.6‰ to −26.3‰ (Fig. III.10a; Table III.2).

Compound-specific $\delta^{13}C$ data of *n*-alkanes are plotted versus chain length in Fig. III.10b. Short-chain *n*-alkanes show a trend towards lower values (enrichment in ^{12}C) with increasing chain length (Table III.4). Minima occur at *n*-C_{21}, except in W–6o and W–8o, where the minima occur at *n*-C_{20}. The mid-chain *n*-alkanes (*n*-$C_{21\text{-}27}$) show an increasing trend. In contrast, long-chain *n*-alkanes (*n*-C_{27+}) exhibit slightly decreasing $\delta^{13}C$ values with an increase at *n*-C_{30} (Fig. III.10b; Table III.4).

Table III.4. Compound-specific stable carbon isotope of investigated oil samples.

ID	*n*-C_{15}	*n*-C_{16}	*n*-C_{17}	*n*-C_{18}	*n*-C_{19}	*n*-C_{20}	*n*-C_{21}	*n*-C_{22}	*n*-C_{23}	*n*-C_{24}	*n*-C_{25}	*n*-C_{26}	*n*-C_{27}	*n*-C_{28}	*n*-C_{29}	*n*-C_{30}	*n*-C_{31}
#	[‰; V-PDB]																
W–1o	–28.8	–28.9	–28.9	–29.1	–29.6	–30.3	–30.9	–30.4	–29.7	–29.3	–29.1	–29.2	–28.8	–29.0	–29.6	–29.2	–29.2
W–2o	–28.7	–29.0	–29.1	–29.3	–29.4	–30.0	–31.2	–30.4	–30.0	–29.4	–29.5	–29.2	–28.9	–28.9	–29.4	–29.7	–29.6
W–3o	n.d.	–28.9	–29.2	–29.0	–29.8	–30.4	–31.1	–30.3	–29.7	–29.4	–29.1	–29.0	–29.1	–29.3	–29.5	–29.8	n.d.
W–5o	–28.6	–28.7	–29.4	–29.6	–30.3	–30.3	–30.2	–29.7	–29.6	–28.8	–28.5	–28.5	–28.7	–28.5	–28.9	–28.4	–28.1
W–6o	–28.8	–28.8	–29.4	–29.7	–30.2	–30.6	–30.5	–29.9	–29.9	–28.7	–28.6	–28.8	–28.7	–28.8	–28.5	–28.3	–28.4
W–8o	–27.7	–28.1	–28.9	–29.4	–30.1	–29.8	–30.4	–29.3	–28.9	–28.4	–28.1	–28.1	–28.3	–28.3	–28.4	–28.6	–27.6
W–10o	–29.0	–29.2	–29.8	–29.9	–30.0	–30.0	–30.4	–29.5	–29.9	–29.6	–29.1	–29.2	–29.3	–29.6	–29.5	–29.3	–29.0
W–11o	–28.7	–28.8	–29.2	–29.4	–30.2	–30.6	–31.2	–30.4	–30.1	–29.9	–29.6	–29.2	–29.0	–29.4	–29.3	–29.6	–29.3
W–12o	n.d.	–28.8	–29.1	–29.4	–29.7	–30.2	–30.7	–30.1	–30.2	–29.6	–29.1	–28.9	–29.1	–29.3	–29.4	n.d.	n.d.
W–13o	–28.5	–28.7	–30.0	–30.4	–30.6	–30.0	–31.2	–30.6	–30.4	–29.3	–28.8	–28.9	–28.9	–29.0	–28.8	–28.6	–28.5

n.d. – not determined.

3.5. Discussion

The study (i) assesses the petroleum potential of Upper Eocene to Lower Oligocene sediments in the Hungarian Palaeogene Basin, (ii) characterises the facies of the source rocks of the accumulated oils and (iii) correlate the accumulated oils to a specific source rock formation. Therefore, a detailed biomarker-based interpretation of the source rocks is beyond the scope of the discussion. Nevertheless, Table III.5 summarises source and maturity related biomarker parameters, calculated for the Kosd and Tard Clay formations.

3.5.1. Hydrocarbon generation potential of the Eocene to Lower Oligocene succession

The TOC contents and Rock-Eval parameters are used to assess the remaining hydrocarbon generation potential of the investigated samples. The Kosd Formation was encountered at W–1 well with a thickness of 376 m, which includes a 36-m-thick coal measure (Körmös et al., 2020). In the W–9 well, the Kosd Formation is ~200 m thick. The HI reaches 350 mg HC/g TOC (Supplementary Table 1); however, HI values greater than 250 mg HC/g TOC are rare. The HI values of the drill cuttings suggest the presence of kerogen type IV to II/III (Peters, 1986), with a dominance of the type III kerogen (Fig. III.4a). The HI values increase with increasing TOC content (Fig. III.3; Supplementary Tables 1 and 2), correlating with a previous study (Körmös et al., 2020). Tmax values are higher in W–1 well (avg. 445 °C at 2400–2800 m) than in the W–9 well (avg. 437 °C at 2800–3000 m). Nevertheless, oil window maturity (Bordenave et al., 1993) is reached in both wells. The high TOC contents and HI values

point to a gas-and-oil-generating source with a very good and excellent petroleum potential (avg. 16.05 mg HC/g rock; Fig III.11a; Supplementary Tables 1 and 2; Peters and Cassa, 1994).

The Buda Marl Formation was studied in wells W–1, W–9 and W–12. The thickness of the formation reaches a maximum of 190 m at W–9, which is thicker than reported before (e.g. Less, 2005). Bechtel et al. (2012) and Sachsenhofer et al. (2018a, 2018b) demonstrated that the uppermost part of the Buda Marl Formation, ~20 m thick, contains a maximum of 2.3 wt% TOC and HI values below 150 mg HC/g TOC at well Ad–3. Based on the obtained HI values, the kerogen type varies between type IV and II/III (Fig. III.4b; Peters, 1986), whereas kerogen type III prevails. The Tmax values indicate oil window maturity in all wells (avg. 440 °C; Bordenave et al., 1993). Sediments with HI values exceeding 200 mg HC/g TOC occur in wells W–9 and W–12 and contain an average TOC of 1.25 wt%. These intervals within the Buda Marl Formation, which could reach a thickness of 100 m, are classified as fair oil source rocks with an average petroleum potential of 3.97 mg HC/g rock (Fig. III.11b; Supplementary Table 2; Peters and Cassa, 1994).

The Tard Clay Formation is a well-known and exhaustively studied potential source rock (e.g. Badics and Vető, 2012; Bechtel et al., 2012; Brukner-Wein et al., 1990; Milota et al., 1995). It was studied in wells W–9 and W–12. In W–12, the Tard Clay Formation is ~70 m thick. TOC contents (0.8–1.9 wt%) and HI values (190–440 mg HC/g TOC) increase upwards. The prevalence of kerogen type II and II/III (Figs. III.3 and III.4c; Supplementary Table 3) agrees with previously published data from this formation (e.g. Badics and Vető, 2012; Bechtel et al., 2012; Brukner-Wein et al., 1990). The sharp decrease of TOC contents and HI values at the top of the Tard Clay Formation (Fig. III.3) suggests an unconformity. Therefore, the uppermost part of the formation could be missing. In contrast to W–12, Tard Clay Formation in well W–9 (or its time-equivalent) is organic matter-lean (avg. 0.23 wt%) and contains type III kerogen. The Tmax values indicate oil window maturity in both wells (avg. 437 °C; Bordenave et al., 1993). The Tard Clay Formation in W–12 is characterised as a fair oil source with a good petroleum potential in the upper 30 m (avg. 6.47 mg HC/g rock; Fig. III.11c; Supplementary Table 3; Peters and Cassa, 1994).

Based on Milota et al. (1995), the Kiscell Clay Formation could reach a thickness of 500 m and some pelitic beds within the formation have been evaluated as a fair quality source. In the studied wells, the formation is up to 690 m thick (W–9; Fig. III.3; Supplementary Table 2). The TOC content remains below 0.7 wt% (Supplementary Tables 1, 2 and 3). The HI values reveal the predominance of type III kerogen (Fig. III.4d; Peters, 1986). Surprisingly, and despite low TOC contents (max. 0.51 wt%), type II/III and II kerogens occur in well W–12 between 1960 m and 2070 m depth (Supplementary Table 3). The Tmax values indicate that the organic matter is marginally matured in all wells (avg. 432 °C; Bordenave et al., 1993). The petroleum potential classifies the Kiscell Clay Formation as poor source rock (avg. 0.56 mg HC/g rock; Fig. III.11d; Supplementary Tables 1, 2 and 3; Peters and Cassa, 1994).

Overall, the reviewed formations show significant variations in thickness, TOC contents and HI values. However, apart from the Kiscell Clay Formation, all formations include intervals that are capable of hydrocarbon generation.

Table III.5. Source- and maturity-related biomarker and non-biomarker indices of the selected source rock samples.

Fms	well	depth	a	b	c	d	e	f	g	h	i	j	k	l	m	n	o	p	q	r	s	t	u	v	w	x
		[m; MD]		[%]																					[%]	
Kosd Formation	W–1	2599.9	14	23	63	0.37	0.06	0.09	0.50	0.67	28.80	10.59	1.18	1.57	0.34	0.01	0.28	0.35	0.38	0.66	0.06	0.06	0.57	0.29	0.71	0.84
		2600.9	17	17	66	0.26	0.07	0.08	0.45	0.67	10.66	4.65	0.99	1.13	0.33	0.04	0.78	0.56	0.45	0.75	0.06	0.11	0.59	0.27	0.73	1.00
		2601.2	21	27	52	0.52	0.07	0.12	0.42	0.66	2.70	1.53	1.41	1.19	0.34	0.33	0.96	0.51	0.67	0.59	0.05	0.15	0.63	0.20	0.72	1.01
		2602.0	18	20	62	0.32	0.09	0.11	0.49	0.69	8.26	4.13	1.03	0.75	0.39	0.02	0.62	0.41	0.35	0.65	0.06	0.06	0.57	0.44	0.72	0.94
Tard Clay Formation	W–12	2250.0	24	44	32	1.39	0.04	0.30	0.52	0.58	0.23	0.42	0.63	0.71	1.07	0.02	0.12	0.38	0.38	0.89	0.13	0.26	0.59	0.48	0.72	0.18
		2260.0	32	36	33	1.08	0.06	0.42	0.54	0.47	0.47	0.80	0.62	0.63	1.01	0.02	0.10	0.42	0.29	0.77	0.10	0.15	0.57	0.49	0.74	0.23
		2294.6	43	16	40	0.40	0.14	0.32	0.52	0.58	0.44	0.74	0.73	0.38	0.69	0.01	0.08	0.40	0.21	0.41	0.05	0.12	0.55	0.58	0.74	0.12
		2298.1	32	29	39	0.74	0.16	0.16	0.50	0.63	0.73	0.69	0.96	0.58	1.01	0.05	0.23	0.44	0.25	0.75	0.08	0.16	0.57	0.53	0.76	0.11

Fms – formations, a – C_{27} steranes/Σ regular steranes, b – C_{28} steranes/Σ regular steranes, c – C_{29} steranes/Σ regular steranes, d – C_{28}/C_{29} steranes, e – $C_{21–22}/C_{27–29}$ steranes, f – C_{27} diaS/(diaS+regS), g – 20S/(20S+20R) ααα C_{29} sterane, h – αββ/(αββ+ααα) C_{29} sterane, i – C_{19}/C_{23}TT, j – C_{20}/C_{23}TT, k – C_{21}/C_{23}TT, l – C_{24}/C_{23}TT, m – C_{26}/C_{25}TT, n – C_{23}TT/H, o – Ol/(Ol+H), p – NH/H, q – C_{31}(R)/H, r – C_{35}(S)/C_{34}(S), s – $C_{35}/C_{31–35}$, t – steranes/hopanes, u – 22S/(22S+22R) 17α,21β–C_{32} homohopane, v – Ts/(Ts+Tm), w – $\%Rc_{(MPI\ 1)}$ (Radke and Welte, 1983), x – DBT/P (Hughes et al., 1995), MD – measured depth.

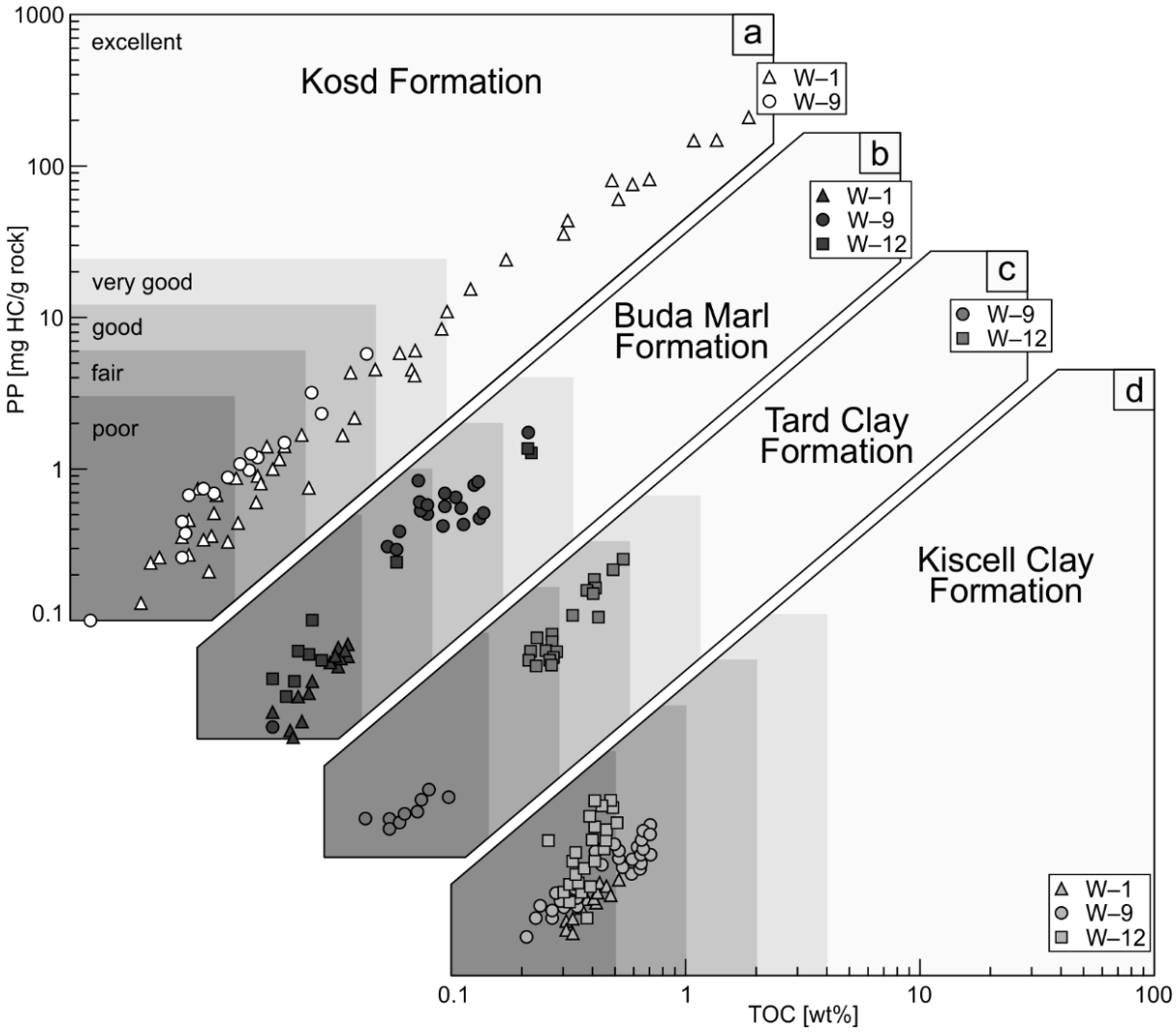

Fig. III.11. Assessment of the hydrocarbon generation potential (modified after Peters and Cassa 1994) for the **a)** Kosd Formation, **b)** Buda Marl Formation, **c)** Tard Clay Formation and **d)** Kiscell Clay Formation.

3.5.2. Depositional facies of the source organic matter of oil samples

The low- and intermediate-molecular weight *n*-alkanes are present in a high and relatively constant proportion in most of the crude oils, except in W–8o, W–10o and W–13o (Fig. III.5a; Table III.2), representing shallow reservoirs (oil-water contact between 1722–2249 m depth; Table III.1). The short-chain *n*-alkanes (*n*-$C_{15–19}$) were identified in algae and microorganisms (Cranwell, 1977; Cranwell et al. 1987). The $\delta^{13}C$-values of short-chain *n*-alkanes (Fig. III.10b; Table III.4) agree with carbon isotope values often found in freshwater algae (e.g., Lamb et al., 2006). Aquatic autotroph organisms utilise dissolved $CO_{2[AQ]}$ or HCO_3^- as the inorganic carbon source and rather take $CO_{2[AQ]}$ until the source is exhausted, which leads to ^{12}C enrichment (Lamb et al., 2006; Meyers, 1997). The concentration of $CO_{2[AQ]}$ in the water mass is the function of pH and temperature, therefore, marine organisms are characterised by heavier carbon isotope composition (Lamb et al., 2006). Nevertheless, the enzymatically mediated biological processes of bacteria are likely to lower the $\delta^{13}C$ composition of the biomass (Cloern et al., 2002), especially in oxygen-depleted conditions (Teece et al., 1999). The degradation of organic constituents of marine algae may produce similar carbon isotope composition than in the studied samples (Meyers, 1997). The mid-chain *n*-alkanes (*n*-$C_{21–25}$) were reported to predominate in extracts from aquatic macrophytes and *Sphagnum* (Bingham et al., 2010; Dehmer, 1995; Ficken et al., 2000; Nott et al., 2000). The carbon isotope composition of mid-chain *n*-alkanes does not differ greatly from the short-chain homologues (Fig. III.10b; Table III.4) and corresponds well to the $\delta^{13}C$-values of C3 plants (e.g., Meyers, 1997). Submerged macrophytes behave like algae in the process of inorganic carbon fixation (Lamb et al., 2006; Meyers, 1997), and species, photosynthesising according to the C3 pathway, were noticed before (e.g., Ficken et al., 1998b; Mortillaro et al., 2016). The high-molecular weight *n*-alkanes (*n*-$C_{27–31}$) were derived from plant-waxes (Eglinton and Hamilton, 1967) and reached a maximum of 35% of the total *n*-alkanes in sample W–10o (Table III.2). The $\delta^{13}C$-values are comparable with the typical carbon isotope values of C3 plants (e.g., Meyers, 1997). Terrestrial plants employ atmospheric CO_2 during photosynthesis (Lamb et al., 2006; Meyers, 1997) but the biosynthesis and maturation-induced fractionations of carbon isotopes vary among plant types (Diefendorf et al., 2011, 2015; Lockheart et al., 1997) and are comparable with the observed values.

The V-shape character of the compound-specific stable carbon isotope in the range of short- and mid-chain *n*-alkanes (Fig. III.10b; Table III.4) could not be explained based on the mechanism of the carbon assimilation by primary producers. Bacteria may have an impact on the isotope composition as they produce short- and mid-chain *n*-alkanoic acids, *n*-alkanols and *n*-alkanes (e.g., Pearson et al., 2007), which were noticed to be enriched in ^{12}C with increasing chain length (e.g., Shah et al., 2013). Nevertheless, extensive heterotrophic consumption of organic matter is not expected because of the negligible fractionation of carbon isotopes between bacterial heterotrophs and source organic carbon (Blair et al., 1985). On the contrary, the metabolism of chemoautotroph bacteria may yield ^{13}C depleted compounds (Shah et al., 2013, Wakeham et al., 2007) and is probably responsible for the V-shape pattern of *n*-alkane carbon isotope. The stable carbon isotope composition and distribution of the *n*-alkanes (Fig. III.5a and III.10b; Table III.2 and III.4), and the ratio of the isoprenoids to *n*-alkanes (Fig. III.6) suggest organic matter from mixed marine/lacustrine and terrigenous, bacterial sources.

The distribution of regular steranes indicate a slight dominance of C_{29} and C_{28} homologues over C_{27}, but the minimum percentage of the C_{27} homologue is still 23% (e.g., W–11o; Figs. III.7a and III.8; Table III.2). Algae were identified as the primary producer of the C_{27} sterols (Volkman, 1986). Moreover, microalgae could contain a substantial amount of 24–ethylcholesterol (Volkman et al., 1999). Furthermore, the 24–*n*–propylcholestane confirms the contribution of marine algae (Chrysophyte; Moldowan et al., 1990) to organic matter. The C_{29} sterols are typically assigned to terrestrial origin (e.g. land plants; Volkman, 1986). The C_{28} sterols are derived from diverse precursors (Grantham and Wakefield, 1988; Peters et al.,

1989, 2000), but the high contribution of C_{28} steranes (Fig. III.8) and high ratio of C_{28}/C_{29} steranes (Table III.2) argue for an origin related to phytoplankton (e.g., diatoms, coccolithophores, dinoflagellates; Grantham and Wakefield, 1988). That is also supported by the presence of C_{30}–methylsteranes derived from 4α–methylsterols, indicative of the presence of dinoflagellates (Wolff et al., 1986). The relative abundances of the regular steroids argue for an open and shallow marine paleoenvironment with biomass that includes marine or brackish phytoplankton assemblages, living in the photic zone of the water column, and the contribution of terrestrial organic matter (e.g., vascular plants; Fig. 8).

The ratios of C_{19}/C_{23}TT and C_{20}/C_{23}TT could reflect the relative distribution of terrigenous and marine organic matter (e.g., Tao et al., 2015; Xiao et al., 2019). The C_{19}TT and C_{20}TT occur in higher concentration in terrestrial oils, whereas the C_{23}TT is frequently detected as the dominant TT in marine oils (Aquino Neto et al., 1983; Ekweozor and Strausz, 1983; Peters and Moldowan, 1993). The high abundance of C_{23}TT and low ratios of C_{19}/C_{23}TT and C_{20}/C_{23}TT suggest the dominance of marine organic matter in the precursor biomass of crude oils (Fig. III.7b; Table III.3). Nevertheless, the occurrence of C_{24}TeT (e.g., 10β(H)–des–A–oleanane and 10β(H)–des–A–lupane; Woodhouse et al., 1992; Xiao et al., 2018) and 18α(H)–oleanane (Ekweozor et al., 1979) indicate the contribution of vascular plants (e.g., angiosperms) to the organic matter (Fig. III.7b).

Beside the *n*-alkane distribution and composition of steroids and terpenoids, the stable carbon isotope composition of hydrocarbon fractions (Fig. III.10a; Table III.3) point to the dominance of marine biological precursors (Sofer, 1984).

The identified hopane derivatives (Fig. III.7b) could originate from bacteriohopanepolyols (Ourisson et al., 1979; Rohmer, 1993), identified in bacteria and some cryptogames (e.g., moss, ferns). Beside the compound-specific carbon isotope, the low sterane to hopane ratios (Table III.3) also suggest a microbially altered organic matter (Tissot and Welte, 1984) and can be assigned to a special bacteria-influenced depositional environment (Mackenzie, 1984).The plot of DBT/P *vs.* Pr/Ph points to a marine/lacustrine environment (Fig. III.9). The presence of diasteranes (Fig. III.7a) and ratios of C_{27} diasteranes and C_{27} regular steranes (C_{27} diaS/(diaS+regS); Table III.2) emphasise the extent of the clay catalytic effect during diagenesis (Sieskind et al., 1979). Both, the ratios of C_{26}/C_{25}TT *vs.* C_{31}(R)/H and NH/H *vs.* C_{35}(S)/C_{34}(S) suggest that a marine shale is the most probable source rock of the crude oils studied (Figs. III.12a and b; Peters et al., 2005).

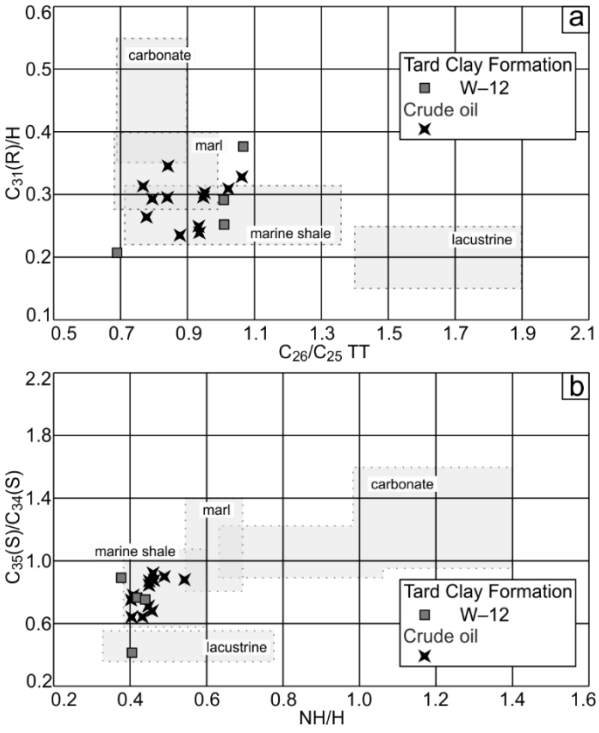

Fig. III.12. The appraisal of the depositional environment based on biomarker and non-biomarker ratios. Cross plots of the **a)** C_{26}/C_{25} tricyclic terpanes vs. C_{31}(R)/H hopanes (after Peters et al., 2005), **b)** NH/H hopanes vs. C_{35}(S)/C_{34}(S) hopanes (after Peters et al., 2005).

The Pr/Ph ratio is a potential indicator of redox conditions and the determined ratios between one and three (avg. 1.88; Table III.2) were proposed to indicate dysoxic conditions during sedimentation (Didyk et al., 1978). However, the Pr/Ph ratio could be influenced by thermal maturation (Radke et al., 1980a;

Tissot and Welte 1984) and differences of the precursor organic matter (Blumer et al., 1963; Goossens et al. 1984; Volkman and Maxwell 1986; ten Haven et al. 1987; Rowland, 1990). Dysoxic conditions are also supported by the cross plot of phytane/*n*-C_{18} *vs*. pristane/*n*-C_{17} (Fig. III.6) and the occurrence of des-A-triterpenes (Connan and Cassou, 1980; Jacob et al., 2007, and references therein).

The C_{35} hopanes are present in subordinate amounts than any other homohopanes in all investigated samples, and the homohopane index remains below 0.12 (Fig. III.7b; Table III.3). Similarly, the NH/H ratio does not reach 0.5, except in the most mature W–13o oil (Table III.3). High concentrations of C_{35} hopanes and C_{29} 17α–norhopanes were interpreted as indicators of strongly reducing conditions during deposition, but maturity also affects the ratios (Peters and Moldowan, 1991).

The DBT/P ratios are low and reach a maximum of 1.27 only in the early mature oil W–11o (Table III.3), indicating generally low but varying amounts of free H_2S near the sediment-water interface during source rock deposition. Low sterane to hopane ratios and the V-shape pattern of *n*-alkane isotope evidence strong bacterial activity (Table III.3). Accordingly, the bacterial sulphate reduction probably transformed the available reactive iron, incorporated onto clay minerals and the sulphide phases into pyrite framboids (Casagrande, 1987; Maclean et al., 2008; Morad, 1998; Sweeney and Kaplan, 1973), indicating, at least, locally reducing conditions.

The C_{21} pregnane and homopregnane are present in high abundance in most oils (Fig. III.7a; Table III.2). ten Haven et al. (1986) demonstrated that pregnane is often enhanced in hypersaline environments, but pregnanes are also known to be enriched in biodegraded oils (Peters et al. 2005). In the case of the studied oils, *n*-alkane distributions (Fig. III.5a) and low proportions of isoprenoids relative to *n*-alkanes (Fig. III.6) do not indicate biodegradation. Nevertheless, considering the low gammacerane peaks (Fig. III.8b), hypersaline conditions during source rock deposition are unlikely.

3.5.3. Oil-to-source rock correlation

The occurrence of 18α(H)–oleanane (Fig. III.7b) and high ratios of C_{28}/C_{29} steranes (Table III.2) in the crude oils suggest an Upper Cretaceous or younger age of the potential source rocks. Furthermore, the source-related biomarker indicators suggest marine/lacustrine shales as the most potential source rocks of the oils.

These criteria comply for all investigated source rock formations, but the Kiscell Clay Formation is not considered further because of its poor petroleum potential. Biomarker data are available for the Tard Clay Formation from different locations in the Hungarian Palaeogene Basin (Bechtel et al., 2012). This study included five additional Tard Clay samples from well W–12. The Kosd Formation in well W–1 was studied recently by Körmös et al. (2020). Table III.5 lists the maturity- and source-related biomarker parameters for the Kosd and Tard Clay formation samples and used for oil-to-source rock correlation.

3.5.3.1. Thermal maturity

In the deep borehole W–12, the organic matter is marginally mature below 2230 m depth as indicated by Tmax values. The same maturity was recorded in well W–9 below 2500 m, and in well W–1 at 2100 m (Supplementary Tables 1, 2 and 3). Tmax values exceeding 435 °C (up to 451 °C) suggest oil window maturity (Supplementary Tables 1, 2 and 3; Bordenave et al., 1993). In contrast, in the shallow boreholes Ad–3, Csv–1 and Bgy–5, the organic matter is

immature (Bechtel et al., 2012). Badics and Vető (2012) and Körmös et al. (2020) presented variations in the thermal maturity of the Tard Clay and Kosd Formation across the Hungarian Palaeogene Basin. The vast extension and great thickness of the investigated sediments point to local and large-scale differences in maturity within the studied formations.

Sterane and hopane isomerisation ratios for rock extracts and oils were calculated for further thermal maturity assessment. The ratios of 17α,21β(H)–C_{32} stereoisomers, 22S/(22S+22R) are in equilibrium (Tables III.3 and III.5; Mackenzie et al., 1982; Seifert and Moldowan, 1980), suggesting that oil generation in the early phase (Peters et al., 2005) was reached in case of the Tard Clay (avg. 0.57) and Kosd (avg. 0.59) formations in the deep wells and by the crude oils (avg. 0.58). The S/(S+R) isomerisation ratios of the 5α,14α,17α(H)–C_{29} steranes (Tables III.2 and 5) are close to the equilibrium value (0.55; Mackenzie and Maxwell, 1981; Seifert and Moldowan, 1986). Also, the ratios of the ββ/(ββ+αα) isomers of the C_{29} steranes equilibrate in the crude oils (avg. 0.71; Table III.2), whereas, source rock samples are characterised by lower values (avg. 0.67 and 0.57, respectively; Table III.5; Seifert and Moldowan, 1986). The range of both sterane isomerisation ratios indicates mature samples in the peak oil window range (Peters et al., 2005).

CPI values of crude oils close to one (Table III.2) also agree with this maturity assessment. Additionally, the ratios of 17α–trisnorhopane and 18α–trisnorneohopane (Ts/(Ts+Tm); Tables III.3 and 5; Seifert and Moldowan, 1978) support the previous assumption. Even though the Ts/(Ts+Tm) ratios are strongly affected by differences in source facies (Seifert and Moldowan, 1978), the values of Tard Clay (0.48–0.58; Table III.5) and crude oils are in the same range (0.46–0.62; Table III.3).

Thermal maturity controls the distributions of methyl-homologs of phenanthrene in the range of 0.6–1.7% vitrinite reflectance (Radke et al., 1982b). The methylphenanthrene index (MPI 1) is a well-established non-biomarker maturity parameter (Radke et al., 1982a, 1982b) and was used to determine the vitrinite reflectance ($Rc_{(MPI\ 1)}$; Radke and Welte, 1983). The calculated $Rc_{(MPI\ 1)}$ values indicate peak oil window maturity for crude oils (0.76–0.96% $Rc_{(MPI\ 1)}$; Table III.3) and slightly lower maturity for source rocks (0.71–0.76% $Rc_{(MPI\ 1)}$; Table III.5). The MPI 1 was calibrated using type III kerogen (e.g. coal); thus, the calculated vitrinite reflectance values could be biased by the mixture of the marine and terrigenous organic matter.

Considering the variable thickness and great lateral extent of the Tard Clay and Kosd formations (e.g. Badics and Vető, 2012; Körmös et al., 2020), local- and large-scale variations in thermal maturity were expected. Such differences are reflected by the immature character of the Tard Clay in wells Ad–3, Csv–1 and Bgy–5 (Bechtel et al., 2012), contrasting the results of samples from boreholes W–9 and W–12, indicating oil window maturity (Fig. III.4c). The determined thermal maturity parameters are comparable between the source rock extracts from the deep boreholes (W–1 and W–12) and crude oils. However, based on phytane/*n*-C_{18} *vs.* pristane/*n*-C_{17} ratios (Fig. III.6) and $Rc_{(MPI\ 1)}$% (Tables III.3 and 5) the crude oils are thermally more mature, especially in samples W–12o and W–13o (Table III.2), which originate from carbonate reservoirs in the eastern part of the research area.

The sterane isomerisation ratios (20S/(20S+20R); Table III.2) and $Rc_{(MPI\ 1)}$% values (Table III.3) show an increasing depth trend in wells W–1 to W–7 (W–1o to W–7o; Fig. III.1; Table III.1) in the central part of the study area, which could indicate that (i) oils (W–8o to W–12o; Tables III.2 and 3) experienced vertical migration, and (ii) source rocks maturity is greater in areas of W–13 well (W–13o; Table III.3).

3.5.3.2. Biomarker and non-biomarker indices

In the shallow boreholes, the stable carbon isotope composition in the hydrocarbon fraction of the Tard Clay follows and stretches along the marine line, as proposed by Sofer (1984; Fig. III.10a). In the deep well W–12, the $\delta^{13}C$ values suggest a greater contribution of terrestrial organic matter (e.g. land plants as evidenced by the Ol/(Ol+H); Table III.5), which could be the result of the proximity of the paleo-shoreface. In contrast, the $\delta^{13}C$ values of the oils point to a dominant marine organic matter input (Fig. III.10a).

Compound-specific stable carbon isotope analysis of *n*-alkanes is an important approach in correlation studies (e.g. Bjorøy et al., 1994; Cheng et al., 2015; Pedentchouk and Turich, 2017). Isotope patterns of *n*-alkanes are different between oil samples and extracts from Eocene rocks; however, there is an apparent fit between oil and Tard Clay core samples, with both sample sets showing a distinct V-shape pattern (Fig. III.10b), which also indicates that the mixing of different oils can be ruled out in the present study. The *n*-alkanes in crude oils are slightly depleted in ^{13}C, which could be an effect of the thermal maturation (e.g. Bjorøy et al., 1992; Clayton, 1991; Rooney et al., 1998; Schoell, 1984). The variations in the $\delta^{13}C$ values are within 2‰, indicating a positive correlation between the sample sets (Sofer, 1984) and the stable carbon isotope composition of individual biological markers allows the identification of specific sources (Hayes et al., 1987). Bechtel et al. (2013), Mayer et al. (2018) and Sachsenhofer et al. (2019) studied Lower Oligocene source rock intervals in the Alpine Foreland Basin, western Black Sea, and along the Carpathians, and observed a very specific V-shaped stable carbon isotope pattern in organic matter rich sediments deposited during nannoplankton zones NP 21, NP 22 and the lowermost part of NP 23 coeval with the Buda Marl and Tard Clay formations in the Hungarian Palaeogene Basin (Fig. III.2).

Despite the positive correlation, confirmed by compound-specific stable carbon isotope, the source-related biomarker parameters indicate subtle differences between the crude oils and Tard Clay. The most obvious differences concern higher DBT/P values and higher sterane to hopane ratios in crude oils compared to extracts from the Tard Clay in the deep well W–12 (Tables III.3 and 5). Higher DBT/P values may reflect variations in the amount of free H_2S as a result of varying iron availability, whereas higher sterane to hopane ratios and the V-shape pattern of the *n*-alkane isotope may express (chemoautotroph) bacterial activity due to water column stratification, as already detected within the Oligocene Tard Clay and Schöneck Formation by Bechtel et al. (2012) and Schulz et al. (2002). Water column stratification is suggested by high pregnanes concentrations, sulphur aromatic compounds and the occurrence of (low amounts of) gammacerane (Figs. III.5b and 7). Bechtel et al. (2012) and Ozsvárt et al. (2016) revealed different depositional environments, characterised by varying salinity and the occurrence of bottom water anoxia during the accumulation of the Tard Clay. These conditions are favourable for both the activity of sulphate reducing bacteria and the incorporation of sulphur phases into organic compounds, resulting in variable content of sulphur aromatic compounds in crude oils. Thus, the differences in molecular composition between the crude oils and Tard Clay extracts are likely caused by variations in the source facies described by Bechtel et al. (2012) and Ozsvárt et al. (2016).

The Tard Clay is the most apparent source for the accumulated oils. However, based on the V-shape compound-specific carbon isotope pattern (Fig. III.10b), which suggest deposition of the source rock during NP21 to NP23 (Sachsenhofer et al., 2019), a contribution from the Buda Marl (NP19–21; Fig. III.2) cannot be excluded. It is reasonable to assume that during the Eocene-Oligocene transition the continuous deepening of the Hungarian Palaeogene Basin (Nagymarosy et al., 1986) resulted in conditions favourable for organic matter enrichment. Within this context, it is important to note that Buda Marls in well W–9 contain a maximum of 2.7 wt% TOC (Fig. III.3) and are characterised by a fair petroleum potential (Fig. III.11b). Therefore, detailed organic geochemical studies of the Buda Marls are highly recommended.

3.6. Conclusion

The previously considered but hypothetical model of the petroleum system in the Hungarian Palaeogene Basin has been clarified in this study. The detailed organic geochemical investigation of the Upper Eocene and Lower Oligocene source rocks and accumulated oils in the Hungarian Palaeogene Basin led to the following conclusions.

(1) The sediments of the Kosd, Buda Marl and Tard Clay formations are identified as hydrocarbon-generating source rocks. In contrast, the involved rocks of the Kiscell Clay Formation are interpreted as non-source rocks. The spatial distribution and Rock-Eval characteristics of the former formations indicate diverse petroleum potential along the study area.

(2) The molecular composition of accumulated crude oils determines the Tard Clay as the most probable source rock. Minor differences in source-related biomarker parameters are assumed to be caused by vertical and lateral variations in the source facies.

(3) Considering the maturity parameters and the common V-shape pattern in the compound-specific carbon isotope profile of *n*-alkanes in sediment extracts, deposited during NP21 to NP23, a contributing source from the Buda Marl is assumable. Therefore, detailed organic geochemical studies of the Buda Marls are highly recommended to explore the significance of these findings.

IV. CHAPTER

Reservoir heterogeneity of an Eocene mixed siliciclastic-carbonate succession, northern Pannonian Basin

Sándor Körmös

University of Szeged, Department of Mineralogy, Geochemistry and Petrology, Egyetem u. 2, H-6722 Szeged, Hungary; MOL Plc, Október huszonharmadika u. 18, H-1117 Budapest, Hungary

email address: sandor.kormos@geo.u-szeged.hu

Andrea Varga

University of Szeged, Department of Mineralogy, Geochemistry and Petrology, Egyetem u. 2, H-6722 Szeged, Hungary

email address: raucsikvarga@geo.u-szeged.hu

Béla Raucsik

University of Szeged, Department of Mineralogy, Geochemistry and Petrology, Egyetem u. 2, H-6722 Szeged, Hungary

email address: raucsik@geo.u-szeged.hu

Georgina Lukoczki

University of Kentucky, Kentucky Geological Survey, 504 Rose Street, Lexington, KY 40502, United States of America

email address: gina.lukoczki@uky.edu

Balázs Géza Radovics

MOL Plc, Október huszonharmadika u. 18, H-1117 Budapest, Hungary

email address: BGRadovics@mol.hu

Nikoletta Papp

University of Szeged, Department of Mineralogy, Geochemistry and Petrology, Egyetem u. 2, H-6722 Szeged, Hungary

email address: nikoletta.papp@geo.u-szeged.hu

István Futó

Insitute for Nuclear Research, Isotope Climatology and Environmental Research Centre, Bem tér 18/c, H-4026 Debrecen, Hungary

email address: futo.istvan@atomki.hu

Félix Schubert

University of Szeged, Department of Mineralogy, Geochemistry and Petrology, Egyetem u. 2, H-6722 Szeged, Hungary

email address: schubert@geo.u-szeged.hu

Submitted to ***Marine and Petroleum Geology***

Reservoir heterogeneity of an Eocene mixed siliciclastic-carbonate succession, northern Pannonian Basin

by: Sándor Körmös, Andrea Varga, Béla Raucsik, Georgina Lukoczki, Balázs Géza Radovics, Nikoletta Papp, István Futó, Félix Schubert

Abstract

The quality of any reservoir is strongly controlled by diagenetic processes, especially of those that are comprised of mixed siliciclastic-carbonate sequences. An Eocene mixed siliciclastic-carbonate sequence forms reservoirs with diverse reservoir quality in the Hungarian Palaeogene Basin, which is found within the Pannonian Basin. Late Eocene transgression established extensive shallow-marine depositional environments strongly controlling the early diagenetic processes. Drill cores and cuttings were selected from several boreholes, representing a wide range of lithofacies to reveal the cause for reservoir heterogeneity. Petrographic, stable isotope and fluid inclusion analyses were performed to identify the diagenetic processes that controlled the porosity evolution of the reservoir.

The early diagenetic calcite neomorphism caused lateral homogeneity, whereas the early meteoric water incursion enhanced reservoir properties via the development of dissolution pores, which in turn resulted in vertical reservoir heterogeneity. The deterioration of porosity started in the eogenetic realm by kaolinite formation and continued during mesodiagenesis as burial calcite, quartz, dolomite and minor illite cement precipitated in remaining pore spaces. Petrographic evidence, such as kaolinite transformation into dickite and fluid inclusion homogenisation temperatures highlight the role of temperature increase with burial, the effect of changing fluid chemistry during the evolution of the basin is documented by the chemical zonation of dolomite, the variation in salinities of the fluids enclosed fluid inclusions, as well as recurrent and prolonged periods of cementation with calcite, quartz and dolomite. Mesogenetic processes were accompanied by hydrocarbon emplacement and the formation of late-stage pyrite. The propagation and cementation of faults first contributed to increase and later to reduce fluid flow, respectively. These steps collectively resulted in a heterogeneous reservoir, characteristic of the Eocene sequence in the Hungarian Palaeogene Basin.

4.1. Introduction

Clastic and carbonate reservoirs have been extensively investigated over the last century and the findings have been summarized in numerous special publications (e.g., Burley and Worden, 2003; Flügel, 2004; Lucia, 2007; Pettijohn et al., 1973; etc.). However, mixed siliciclastic-carbonate deposits earned less attention until recent years (e.g., Chiarella et al., 2017; Du et al., 2022; Feng et al., 2013; Mansurbeg et al., 2009; Palermo et al., 2008). In such deposits, carbonate and siliciclastic constituents act differently during diagenesis, which results in remarkable lateral and vertical reservoir heterogeneity. These mixed sediments may undergo a more extensive porosity loss compared to pure siliciclastic ones due to more pronounced compaction and cementation in the former (Mansurbeg et al., 2009). However, the dissolution of carbonate grains may enhance the reservoir capacity in a mixed siliciclastic-carbonate strata (Feng et al., 2013). This special type of sedimentary rock may host high-quality reservoirs, such as the Rogenstein Member of Lower Buntsandstein Formation in western Europe (Palermo et al., 2008) or the Shahejie Formation in the Bohai Bay Basin in China (Du et al., 2022).

In the Pannonian Basin, there are six known petroleum systems. The Palaeogene petroleum system of the Hungarian Palaeogene Basin, located in the north-central part of Hungary, is one of the most complex of these petroleum systems (Fig. IV.1a; Dolton 2006). The studied area is in the south-central part of the Hungarian Palaeogene Basin where several exploration and development wells were drilled in recent years. The wells penetrated more than two thousand meters of Neogene and Palaeogene sediments to reach the Mesozoic basement. The selected wells, W–1, W–7, W–9, W–14 and W–15 (Fig. IV.1b), penetrated Eocene mixed siliciclastic-carbonate hydrocarbon reservoirs with variable reservoir quality. Available reports point out the difficulty of production from these reservoirs (Boncz, 2013; Radovics et al., 2017). Diagenetic processes fundamentally influence rock characteristics that in turn constrain the volume in place estimation or long-term production capability of the reservoir, among others. Diagenesis also controls reservoir heterogeneity, causing compartmentalisation or, in a worst case, shortens the duration of production. Therefore, it is crucial to understand the diagenetic history of a heterogeneous mixed siliciclastic-carbonate system to be able to predict the reservoir quality. To maintain favourable production capacity, a detailed investigation of diagenetic processes characterising the Eocene mixed siliciclastic-carbonate reservoir rocks and their surroundings is needed as prerequisite for appropriate reservoir description. Thus, the goal of this study is to enhance the understanding of the diagenetic processes that control the quality of the mixed siliciclastic-carbonate reservoirs in the Hungarian Palaeogene Basin. To achieve this goal, optical petrography, qualitative and semi-quantitative analysis of the mineral phases, stable isotope and fluid inclusion analyses were performed, which revealed how the depositional environment controlled early diagenetic processes, and how the thermal history of the basin, together with the chemical evolution of fluids that migrated in the basin during mesogenesis, resulted in the complex reservoir characteristics encountered today.

4.2. Geological setting

The study area is located in the south-central part of the Hungarian Palaeogene Basin (Fig. IV.1). The rocks of this basin overlie the pre-Cenozoic basement rocks that comprise the Mid-Hungarian Zone (Kovács and Haas, 2010). The Hungarian Palaeogene Basin was formed in a retro-arc flexural foreland basin, where the paleo-depositional facies were reconstructed to have migrated east-northeastward during the Cenozoic (Tari et al., 1993; Kováč et al., 2016). The tectonic evolution of the Hungarian Palaeogene Basin was controlled by normal faulting and strike-slip movements (Palotai, 2013 and references therein). The Palaeogene Basin as a term includes all sedimentary sequences related to the depositional cycle from the Eocene to the Early Ottnangian (Sztanó and Tari, 1993).

The pre-Cenozoic basement of the research area is composed of Mesozoic rocks from different structural mega-units. The western part of the basement is comprised of Ladinian to Norian platform carbonates (Haas and Kovács, 2012) very similar to those of the Buda Hills (Transdanubian Range Unit). In the east, besides the Ladinian to Norian platform carbonates, a deep marine Middle to Upper Jurassic sedimentary succession and magmatites (Pelikán, 2005) are also reported showing pronounced affinity to the sequence of the Bükk Mountains (Bükk Unit).

In this area, the Alpine orogeny culminated in the exhumation of the Mesozoic strata during the Late Cretaceous and led to continental denudation that lasted until the Late Eocene (Haas and Kovács, 2012). Thus, the Palaeogene sediments overlie the Mesozoic basement on top of a regional unconformity (Fig. IV.2). The sedimentary succession starts with terrigenous conglomerate, breccia and variegated claystone (Bauer et al., 2016). The Kosd Formation reflects the development of a lagoonal environment (Gidai, 1978; Less, 2005), preserving the sign of

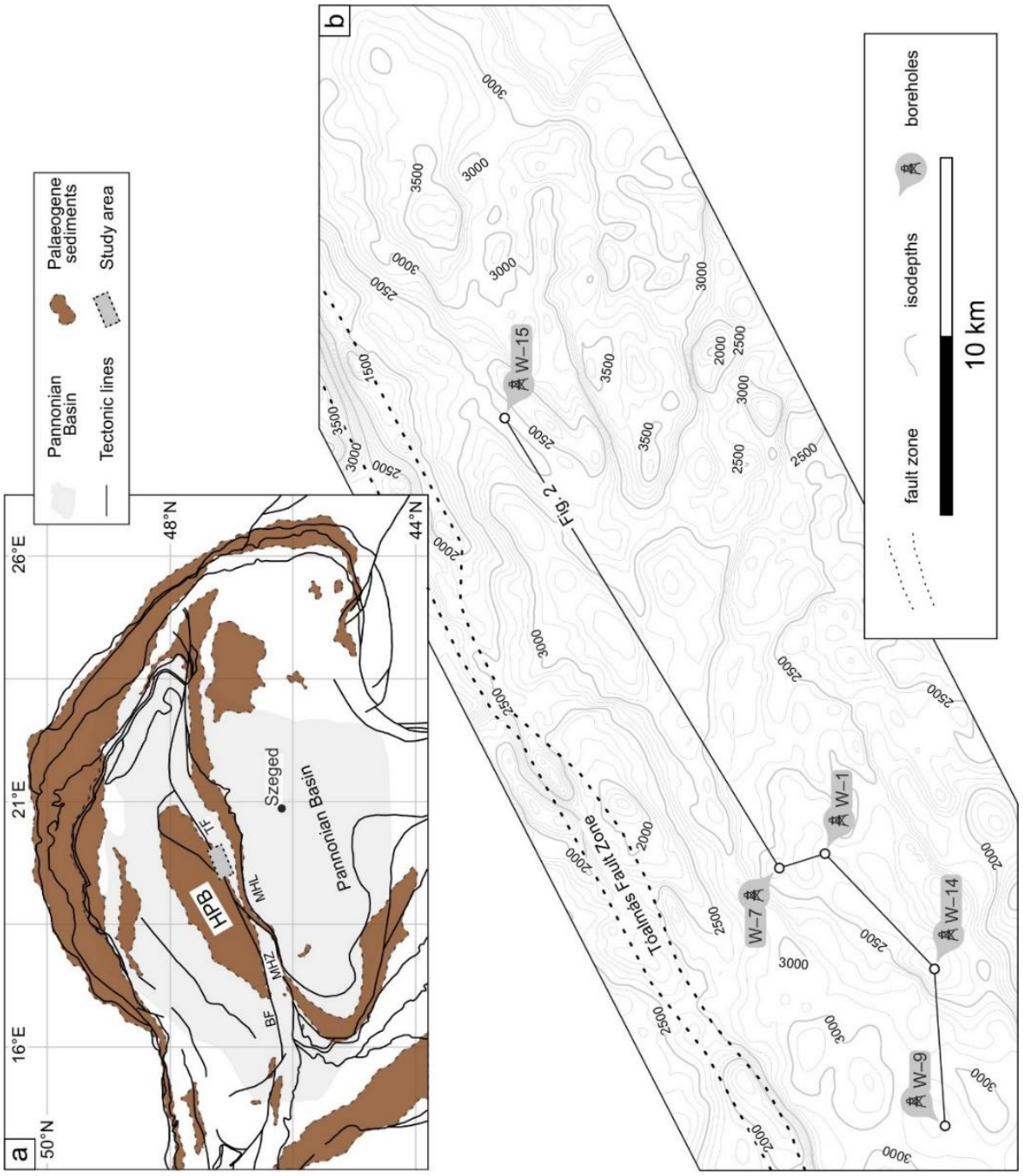

Fig. IV.1. Map of the study area. **a)** Regional setting of the Hungarian Palaeogene Basin. **b)** Map showing the top of the pre-Cenozoic basement in the study area (modified after Boncz, 2013; Kováč et al., 2016; Ozsvárt et al., 2016; Palotai, 2013; Schmid et al., 2008). Values, printed on isodepths, represent depths in metre below sea level. HPB – Hungarian Palaeogene Basin, BF – Balaton Fault, MHZ – Mid-Hungarian Zone, MHL – Mid-Hungarian Line, TF – Tóalmás Fault, W–1 to W–15 are the studied boreholes.

the Priabonian transgression (Figs. IV.2b and c; Báldi and Báldi-Beke, 1985). The coal-bearing upper part of the Kosd Formation includes pelitic sediments with variable carbonate content (Gidai, 1978; Less, 2005; Körmös et al., 2020). The shelf deposits of the Szépvölgy Limestone Formation overlie the Kosd Formation (Fig. IV.2a; Kázmér, 1985). Extended periods of subsidence resulted in the deposition of the Buda Marl Formation (Fig. IV.2a), containing marl and calcareous marl, allodapic limestones and calcareous turbidites deposited during the Eocene–Oligocene transition under oxygen-depleted conditions (Less, 2005; Nagymarosy and Báldi-Beke, 1988; Ozsvárt et al., 2016).

The Buda Marl Formation is covered by the Tard Clay Formation (Fig. IV.2a), which accumulated in a euxinic basin, and was later filled up from the west (according to the present position; Fodor et al., 1994) by prograding siliciclastic deltas. The Tard Clay Formation contains laminated and massive shale and sandstone (Brukner-Wein et al., 1990). The overlying sediments accumulated in a deep bathyal, well-oxygenated depositional environment (Báldi and Báldi-Beke, 1985), comprising the Kiscell Clay Formation (Fig. IV.2a), which is characterised by intercalations of siltstones and turbiditic sandstone bodies (Less, 2005; Milota et al., 1995).

The Palaeogene succession ends by interfingering heteropic sediments, including the shallow sublittoral Törökbálint Sandstone Formation, the deep sublittoral–shallow bathyal Szécsény Schlier Formation and the deep sublittoral Eger Formation (Fig. IV.2a; Kercsmár et al., 2015). The littoral–sublittoral Budafok Formation covers the Törökbálint Sandstone, which is laterally intercalated with the upper part of the Szécsény Schlier Formation (Fig. IV.2a; Sztanó and Tari, 1993). The latter grades eastwards into the shallow marine Pétervására Sandstone Formation, composed of several coast-parallel facies units (Fig. IV.2a; Sztanó and Tari, 1993). Gradual uplift in late Eggenburgian time resulted in subaerial exposure and the deposition of the Zagyvapálfalva Formation (Fig. IV.2a) in a coastal plain setting. The Gyulakeszi Rhyolite Tuff covers the eroded surface of the Palaeogene to Eggenburgian formations (Fig. IV.2a; Nagymarosy, 2012). The sedimentary sequence of the Hungarian Palaeogene Basin is covered by thick Neogene sediments (Fig. IV.2a).

4.3. Samples and analytical methods

4.3.1. Samples

Boreholes, including W–1, W–7, W–9, W–14 and W–15, were drilled by MOL Plc. during the last decades (for locations see Fig. IV.1). In total, 200 m of drill core and 2200 m of drill cuttings were collected to characterise the diagenetic evolution of the Eocene mixed siliciclastic-carbonate sequence. The selected drill cores and drill cuttings represent a wide range of lithofacies (Figs. IV.2b and c).

4.3.2. Analytical methods

A total of 50 representative drill core samples were impregnated with blue epoxy prior to thin section preparation. Thin sections made of these samples and an additional 24 covered archive thin sections were studied using an Olympus BX41 and a Brunel SP300P polarisation microscope for petrographic and modal analyses. The Gazzi-Dickinson point-counting method (Ingersoll et al., 1984) was used for modal analysis of sandstones considering at least 400 points. Dott (1964) and Mount (1985) classifications were followed for the discrimination of sandstones. Petrographic descriptions of grain and matrix content were performed by visual comparison of percentage (Folk, 1951), roundness (Powers, 1953) and sorting charts (Harrel, 1984; Jerram, 2001). Representative samples were selected and stained with a solution of

alizarin red-S and potassium ferricyanide to distinguish non-ferroan and ferroan calcite and dolomite (Dickson, 1965).

A Reliotron VII cold-cathode cathodoluminescence (CL) device assembled on an Olympus BX43 polarising microscope equipped with an Olympus DP73 digital camera was used for CL microscopy of thin sections to further characterise the authigenic minerals. The operating settings were 7 kV accelerating voltage and 670 μA beam current.

X-ray powder diffraction measurements were performed for qualitative and semi-quantitative analysis of the mineral phases in sandstone and siltstone samples. A total of 10 representative bulk samples were taken and ground in an agate mortar to ~10 μm grain size. Before separation of the clay (grain size of <2 μm) fraction, calcium-carbonate content of the samples was digested by 10 vol.% acetic acid solution at room temperature and decanted repeatedly until pH 6 was reached. Subsequently, the clay fraction was separated by repeated ultrasonic deflocculation and gravitational settling. Oriented clay specimens were made by pipetting on glass slides and drying at 50 °C. Both the homogenised bulk samples and air-dried clay specimens were measured on standard sample holders using a Rigaku Ultima IV X-ray diffractometer (CuKα radiation, Bragg-Brentano geometry, secondary graphite monochromator, proportional counter, divergence and detector slits of 2/3°). Thereafter, in order to detect swelling phases, the clay specimens were solvated by ethylene-glycol at 60 °C for 16 hours and measured. As next steps, the specimens were heat-treated (at 350 °C and 550 °C) and measured. The random bulk samples were measured scanned at 50kV/40mA with 3–70° 2Θ diffraction angle range, step-scan 0.05° 2Θ and 1°/min scan speed. The oriented clay specimens (air-dried, ethylene-glycolated and heat-treated) were measured at 45kV/35mA, from 3° to 50° 2Θ with a goniometer step-width of 0.1° 2Θ and 1°/min step rate. Polytypism of the clay minerals were established using random clay specimens on 'zero background' Si sample holder with 15–60° 2Θ scan range, 0.02° 2Θ step size and 0.5°/min scan speed. Qualitative interpretation of the samples was done using the International Centre for Diffraction Data database of Rigaku PDXL 1.8 software. Semi-quantitative compositions of the bulk samples were determined by the reference intensity ratio method. The semi-quantitative composition of the clay fraction was estimated by the integrated area of the conventionally used basal reflections and correction factors of Poppe et al. (2001).

Scanning electron microscopy was applied for the characterisation of pore-filling minerals. Fifteen freshly broken, approximately 1 cm3 rock fragments and thin sections were gold coated and analysed by a Hitachi S-4700 field emission scanning electron microscope combined with a Bruker (former Röntec) QX2 energy dispersive X-ray fluorescence spectrometer. The analysis was carried out at 20 kV acceleration voltage and 9 μA beam current.

Stable carbon and oxygen isotope measurements of 25 representative samples of mold-filling and vein-forming calcite and bulk rock carbonates were performed on hand-drilled powders. The pulverized samples were solvent extracted, using 20 ml chloroform, acetone then ethanol in two runs, to avoid contamination caused by solid bitumen and oil stain. Milli-Q water was used to flush the calcite and rock powders, and those were dried in an oven at 60 °C. The samples were analysed using a continuous flow technique with the H_3PO_4 digestion method (Spötl and Vennemann, 2003). The isotope ratios of CO_2, generated by acid reaction, were measured using a Thermo Finnigan DELTA plus XP IR mass spectrometer through a GasBench interface. Stable isotope ratios are expressed relative to the Vienna Pee Dee Belemnite standard (V-PDB) in delta notation ($\delta = [R_{sample}/R_{standard} - 1) \times 1000$; Coplen, 2011), where R is ($^{13}C/^{12}C$) or ($^{18}O/^{16}O$). The delta notation is reported in per mil (‰). The analytical error during the measurements was better than 0.1‰.

For the fluid inclusion (FI) study, representative samples containing authigenic minerals (calcite, dolomite and quartz) were chosen, including one cm-sized pore-filling and one fracture-

filling calcite sample, three sandstone samples (two arenites and one wacke), one siltstone drill core sample, and one sample made from drill cuttings. A total of seven double-polished 50 to 80 μm thick sections were prepared according to Shepherd et al. (1985). For cutting the samples a low-speed saw was used to avoid thermal or mechanical damage of FIs. Fluid inclusion petrography, microthermometry, UV-fluorescence and Raman microspectroscopy were performed on these thick sections.

Fluid inclusion assemblages (FIAs) were characterised following the instructions of Goldstein and Reynolds (1994). Linkam MDSG-600 and THMSG-600 heating-freezing stages mounted on an Olympus BX41 polarizing microscope were used for microthermometry. Synthetic FIs were measured for calibration purposes at –56.6 °C, 0.0 °C and 374.0 °C. The accuracy of the measurements was ±0.2 °C below 100 °C and ±1.0 °C above 100 °C. Fluid inclusions that show petrographic evidence of necking down were left out of measurements. To avoid stretching of aqueous FIs caused by freezing of the liquid phase, heating analyses were performed before freezing. A stepwise 1 °C heating rate was applied for accurate observation of phase changes while crosschecking the FIs. Terms and symbols suggested by Diamond (2003) were used during the study. The temperatures of homogenisation (T_h) and final ice melting (T_m(Ice)) were determined by the cycling method (Goldstein and Reynolds, 1994). Volume fractions of the vapour and liquid phases (φ_V) were estimated at room temperature. Salinity values of aqueous inclusions (AI) were calculated by final ice-melting temperatures and reported in mass percent (mass%) of NaCl equivalent (Bodnar, 1993; Bakker, 2003). In the present study, methane was detected in the vapour phase of some fluid inclusions, but methane hydrate was not observed upon cooling to –160 °C. Therefore, the reported salinities are assumed as maximum salinity values (e.g., Fall et al., 2011; Ou et al., 2015) because the concentration of the gaseous hydrocarbons in the AI could not be determined.

UV-fluorescence micro-spectroscopy was utilized to characterise the hydrocarbon-bearing FIs (HCFI). An Olympus BX41 polarizing microscope equipped with a 100 W high-pressure Hg lamp and an Olympus U-MNU-2 filter set for ultraviolet (360–370 nm) and Olympus U-MWBV2 filter set for blue-violet (400–440 nm) excitation was used for analysis. The spectra were recorded by an Ocean Optics QE PRO spectrometer connected through a QP115-025-XSR optical fibre to the microscope. For optimization of signal to noise ratio, the spectra were recorded during 1500 msec, using three times spectrum averaging and two times boxcar width on a spot of 2 μm diameter. Dark and white backgrounds were acquired at every crystal hosting HCFI to avoid colour-shifting caused by the refraction of the host mineral. The comparison between different petroleum types was done by the transformation of each spectrum to XYZ chromaticity coordinates and was plotted on CIE-1931 (Commission Internationale d'Eclairage) chromaticity chart (Smith and Guild, 1931).

Raman spectroscopy was applied to identify the volatile phases of the FIs. The measurements were carried out on a Thermo Scientific DXR confocal Raman microscope. A frequency-doubled diode-pumped solid-state Nd-YAG 532 nm wavelength laser with a 100x objective lens at 5 mW laser power was used. The spectral resolution of the instrument was 2 cm-1, while the spatial resolution was 3–4 μm3. Acquisition time was set to 1500 msec for obtaining the best signal to noise ratio. The Raman shifts were compared to the results of Frezzotti et al. (2012) for qualitative results.

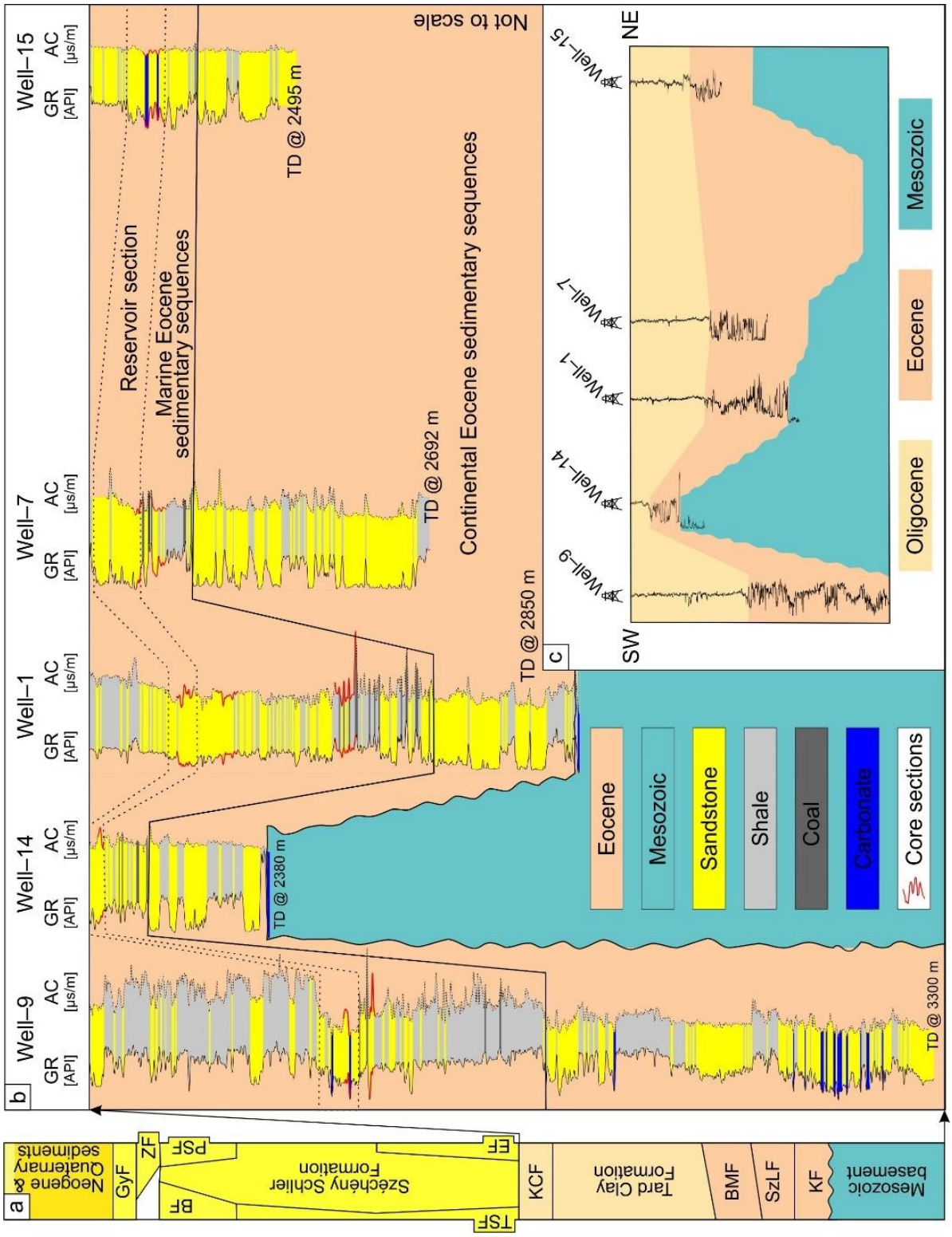

Fig. IV.2. Schematic stratigraphic diagrams of the study area. a) Interpreted lithostratigraphic chart of the Hungarian Palaeogene Basin and stratigraphic section along the investigated boreholes (for locations see Fig. IV.1) based on well logs **b)** gamma ray and acoustic, the top level of the section flattened along the top of the Eocene, and **c)** gamma ray log, levelled out along the top of the Oligocene. Red curves indicate cored intervals studied. KF – Kosd Formation, SzLF – Szépvölgy Limestone Formation, BMF – Buda Marl Formation, KCF – Kiscell Clay Formation, TSF – Törökbálint Sandstone Formation, EF – Eger Formation, BF – Budafok Formation, PSF – Pétervására Sandstone Formation, ZF – Zagyvapálfalva Formation, GyF – Gyulakeszi Formation, GR – gamma ray log, AC – acoustic log, TD – total depth.

4.4. Results

4.4.1. Mineralogy of the Eocene sediments

The mineralogical composition of the bulk rock samples is characterised by variable amounts of quartz, 10 Å phases (illite±mica), calcite, and 7 Å phase (kaolin-group minerals) as major components (Table IV.1). In some samples, the calcite and the 7 Å phase can be detected only in trace amounts. Besides these, potassium feldspar, plagioclase, dolomite and pyrite also occur in trace amounts. In a few samples, dolomite and pyrite were each measured to comprise up to 5–10% of the sample.

Table IV.1. Semi-quantitative mineralogical composition of selected samples from W–1 well.

	Bulk rock								Clay (<2 μm-sized) fraction						
	qtz	pl	kfp	cal	dol	10Å	7Å	pyr	ill/sm	10Å	$PT_{10Å}$	7Å	$PT_{7Å}$	qtz	pyr
	[%]								[%]			[%]		[%]	
Sst	40–50	–	–	30–40	–	10–20	5–10	tr	–	65	$2M_1$	35	dck>kln	tr	tr
	50–60	–	–	10–20	tr	10–20	tr	tr	–	73	$2M_1$	27	kln>dck	tr	tr
Sltst	20–30	–	–	5–10	tr	50–60	5–10	tr	tr	72	$2M_1$	28	dck>kln	tr	tr
	40–50	–	tr	tr	tr	40–50	tr	tr	–	88	$2M_1$	12	dck>kln	tr	tr
	40–50	tr	–	tr	tr	40–50	tr	tr	tr	74	$2M_1$	26	dck>kln	tr	tr
	60–70	tr	–	5–10	tr	10–20	tr	tr	tr	79	$2M_1$	21	dck≈kln	tr	tr
	60–70	tr	–	–	–	10–20	5–10	tr	tr	29	$2M_1$	71	dck≈kln	tr	tr
	30–40	tr	–	–	–	40–50	5–10	5–10	tr	70	$2M_1$	30	dck>kln	tr	tr
	40–50	tr	–	5–10	5–10	20–30	tr	tr	tr	82	$2M_1$	18	dck≈kln	tr	tr
	20–30	tr	–	tr	tr	50–60	5–10	tr	tr	80	$2M_1$	20	kln>dck	tr	tr

Sst – sandstone, Sltst – siltstone, qtz – quartz, pl – plagioclase feldspar, kfp – K-feldspar, cal – calcite, dol – dolomite, 10Å – 10 Ångström phase (illite±mica), 7Å – 7 Ångström phase (kaolin-group minerals), ill/sm – highly swelling mixed-layer illite/smectite, pyr – pyrite, PT10Å – polytypes of the 10 Ångström phase, PT7Å – polytypes of the 7 Ångström phase, kln>dck – kaolinite is more abundant than dickite, dck>kln – dickite is more abundant than kaolinite, dck≈kln – not possible to distinguish which polytype is more abundant, tr – trace amount. Percentage values for the 10Å and 7Å phases in the clay fraction express possible maximum amounts.

The clay (<2 μm-sized) fractions of siltstone and sandstone samples are generally predominated by 10 Å phases (illite±mica). Nevertheless, the 7 Å phase is also an important component and it is the major clay mineral in one studied sample. The illite±mica is represented by the 2M1 polytype. As for the kaolin polytypes, in some samples, kaolinite prevails over dickite but mostly dickite predominates over kaolinite. Besides these, minor mixed-layer illite/smectite is also present in most samples and, due to its very limited abundance, it cannot be quantified in a satisfactory manner. Trace amounts of quartz and pyrite are also identified in all analysed samples (Table IV.1).

4.4.2. Petrography of the Eocene sedimentary rocks

The investigated core samples contain consolidated siltstones, sandstones and conglomerates (Supplementary Fig. 1). Siltstones are generally medium grey, interbedded with light grey sandstones, showing flaser-to-wavy-beddings, which are often destroyed by bioturbation. Besides the wavy-bedding, slumps also occur. The flaser-to-wavy-bedded siltstones are inter-

rupted by erosional scour surfaces. Sandstones are fine-to-medium-grained, thin-to-thick-bedded, structureless and dominated by the alternation of light grey, calcareous and brownish grey, crude oil-impregnated lithotypes. Conglomerates are grain-supported and oligomictic, containing metamorphic and carbonate granules and pebbles.

4.4.2.1. Framework grains of the sandstones

The framework of the samples is built up of quartz (51–99%), feldspar (0–5%) and lithic fragments (1–49%; Fig. IV.3). The results of point counting are presented in Supplementary Table 4. The grains are angular to sub-rounded and show low to medium sphericity. The range of the grain size is typically between the coarse silt and medium sand and it is locally coarse-grained. The samples are poorly to moderately sorted and contain up to 30% of the argillaceous and calcareous matrix. The representative textures are presented in Fig. 4. The sandstones are classified as quartz and lithic arenites and wackes (Fig. IV.3a; Dott; 1964). Based on the high proportion of calcareous matrix, the wackes are further categorised as sandy micrite and micritic sandstone (Fig. IV.3b; Mount; 1985).

Detrital quartz grains dominantly are monocrystalline, and rarely show undulose extinction (>5°). Polycrystalline quartz grains are present in lower quantities and the boundary between the crystals within the grains is straight or sutured. As the grain size decreases the proportion of monocrystalline quartz grains increases in the samples. Feldspars are not common but potassium feldspar and plagioclase locally occur. In most cases, feldspars are replaced by calcite and clay minerals. Lithic grains are also important constituents and are dominated by metamorphic grains. Besides these, minor amounts of carbonate, chert, mudstone/shale, sandstone and volcanic (*cf.* Ingersoll et al., 1984) rock fragments are also present in the samples.

Besides the detrital framework grains, up to mm-sized detrital muscovite and locally, up to three-millimetre-long elongated metamorphic granules are present in the samples. Mica flakes are common in the very fine-to-fine-grained sandstones and form a major component of those samples. The sandstones are rich in fossils preserved in varying degrees, including nummulites, miliolid foraminifers, molluscs, brachiopods, echinoids, red algae and bryozoans (Figs. IV.4–6; Supplementary Figs. 1 and 2). In some cases, the skeletal grains are identified based on their micritic envelopes and are replaced by pyrite, kaolinite and ferroan calcite. Accessories, such as heavy minerals, including rutile and tourmaline, occur in the sandstones and siltstones.

The framework grains in the wackes float in the calcareous matrix (microspar), or are in tangential contact, whereas, in the arenites tangential to long and concavo-convex contacts also occur (Fig. 4). Micas are commonly bent and the flakes are split apart (Supplementary Fig. 2e). The rigid quartz grains squeeze and break bioclasts (Fig. IV.4a). Micro-stylolites, when present, either cross-cut the samples over several centimetres or cease within a few millimetres (Supplementary Figs. 2a and b). Besides these, further evidence of pressure solution, such as dissolution pits, are also documented in detrital quartz grains (Fig. IV.7). In some samples, mica flakes, elongated pebbles and fossil fragments are oriented parallel along their long axis.

4.4.2.2. Diagenetic minerals

Authigenic minerals occur as grain coatings, replacement and pore-filling phases, including illite/smectite, pyrite, calcite, dolomite, quartz and kaolin minerals. Table IV.2 summarizes the occurrence of diagenetic minerals in the different lithotypes.

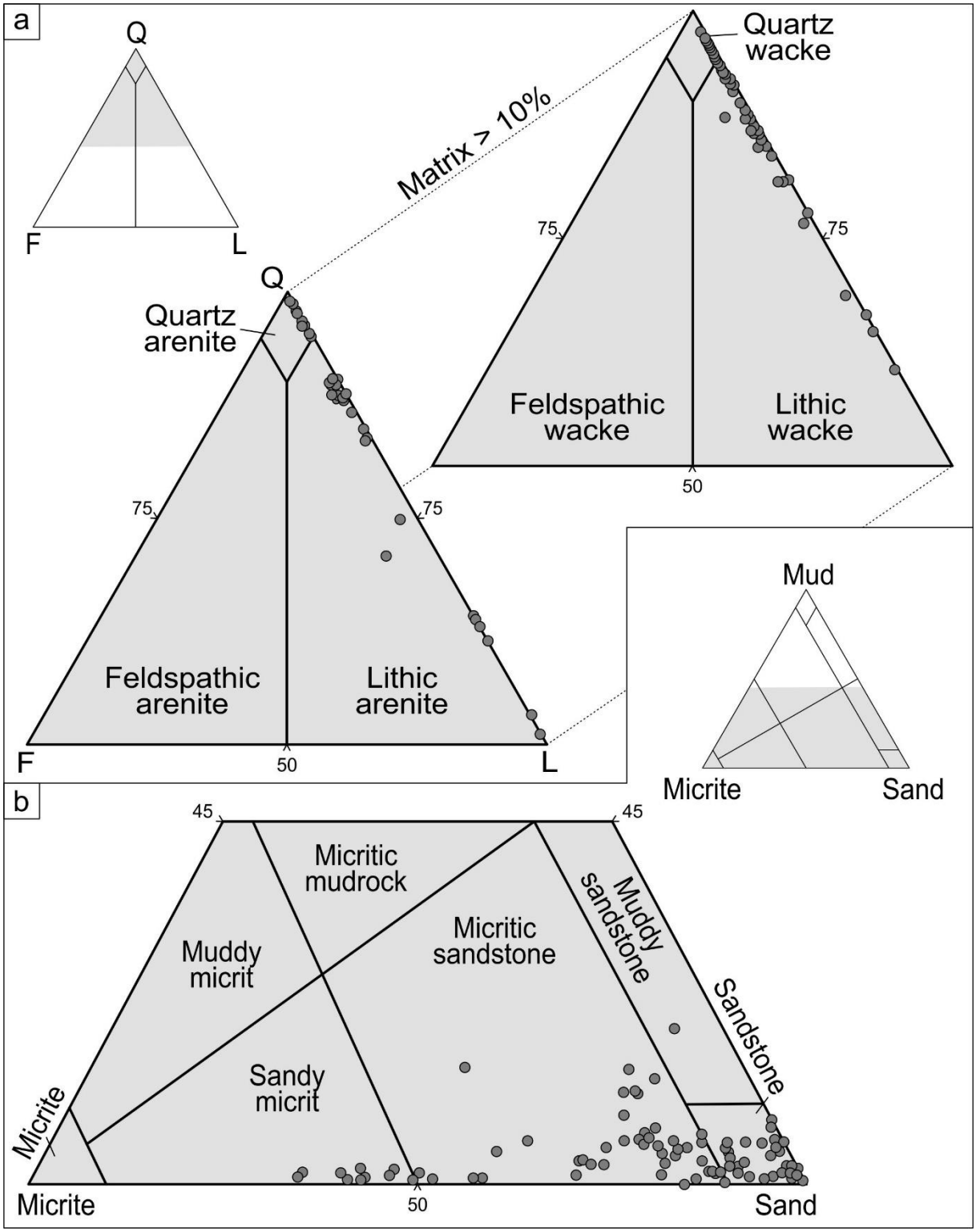

Fig. IV.3. Modal composition and classification of the sandstones. **a)** Framework grain composition (modified after Dott, 1964). **b)** Normalised composition of the mud, micrite and sand fraction (modified after Mount, 1985). Q – quartz grains, F – feldspar grains, L – lithic fragments.

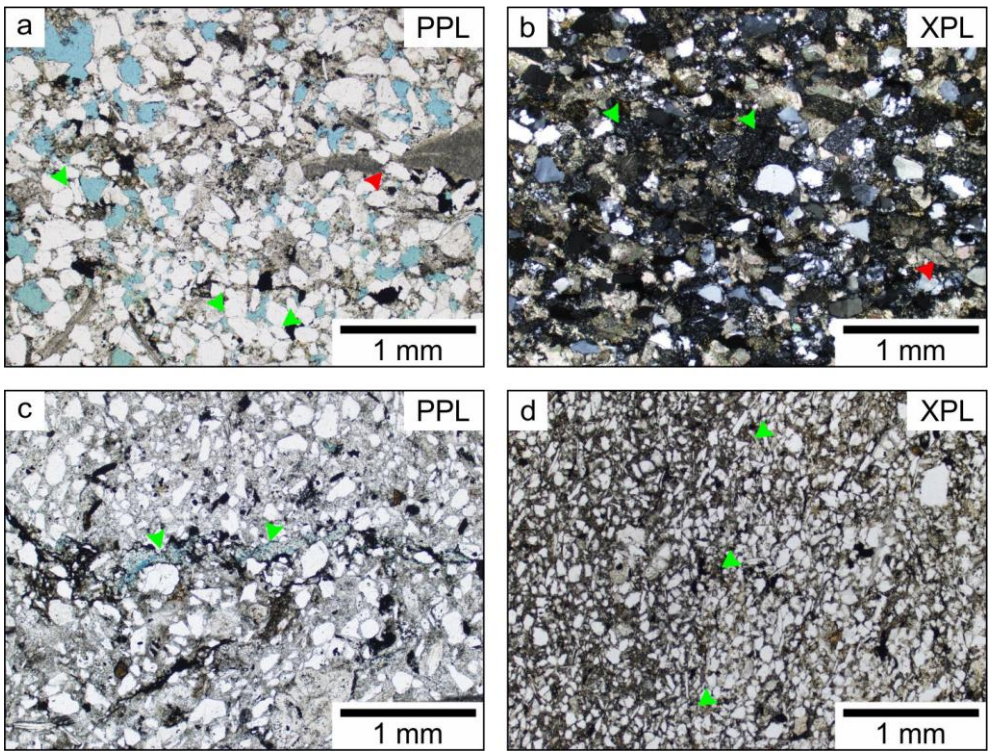

Fig. IV.4. Petrographic and textural features of arenites and wackes. **a)** Texture of an arenite in plane-polarized light (PPL; W–1; 2462.1 m MD), showing oversized pores, filled with blue epoxy, and the tangential to long and concavo-convex contacts between framework grains (green arrows), as well as fossil fragments separated by quartz grains (red arrow). **b)** Texture of an arenite in cross-polarized light (XPL; W–14; 2182.0 m MD). Framework grains include quartz grains, volcanic (green arrows) and carbonate (red arrow) rock fragments. **c)** Texture of a wacke (W–1; 2461.8 m MD). Framework grains float in the calcareous matrix and a dissolution pore cross-cut the section along with a micro-stylolite (green arrow). **d)** Microphotograph showing the transition (green arrows) from wacke to arenite (W–14; 2109.0 m MD) as indicated by the decrease in the proportion of the matrix from left to right.

Table IV.2. The occurrence of the diagenetic minerals in the investigated lithotypes.

	Conglomerate	Arenite	Wacke		Siltstone
			Argillaceous matrix	Calcareous matrix	
Calcite					
spar	✓	✓	✓	✓	✓
fracture-filling	✓	✓	✓	✓	✓
Dolomite					
rhomb		✓	✓		
pore-filling saddle-like		✓	✓		✓
Quartz					
overgrowth/outgrowth		✓	✓		
pore-filling	✓	✓	✓		✓
Illite		✓	✓	✓	✓
Kaolin minerals	✓	✓	✓		✓
Pyrite					
framboidal		✓	✓	✓	✓
euhedral		✓	✓		

4.4.2.2.1. Calcite

Calcite occurs either as a pervasive ferroan microspar (Fig. IV.4c), showing dull orange CL in the wackes, embaying the framework grains, or it forms up to medium-and-coarse-crystalline elongated, drusy, equant and blocky ferroan calcite spar in the sandstones. The coarse spar locally embays multiple grains, forming a poikilotopic fabric (Figs. IV.5a–b) or heals cm-wide fractures (labelled later as Cal_{FF}, see section 4.3.1.; Supplementary Fig. 2d). Drusy mosaics or locally single euhedral crystals of calcite occlude the chambers of well-preserved bioclasts and oversized pores (labelled later as Cal_{EU}, see section 4.3.1.; Fig. IV.5c). Equant spar seals partially the intergranular pores, molds and locally develop in equidistance in the molds of fossil fragments (labelled later as Cal_{EQ}, see section 4.3.1.; Fig. IV.5c). The calcite spars are characterised by distinct CL features and show bright and dull orange luminescence with locally developed zoning, but non-luminescent sparry calcite also exists (Figs. IV.5a–b). Locally, the CL-zoned calcite also shows zoning under UV and blue-light irradiation (Fig. IV.6a). Furthermore, the zoning in the ferroan calcite is also highlighted by carbonate staining, colouring the calcite to purple and then blue towards the centre of the pore indicating varying Fe content (Fig. IV.5d; Supplementary Fig. 2c). The calcite spars show a rather patchy occurrence. Framework grains, especially quartz grains are corroded by the ferroan sparry calcite, showing pitted margins and embayments (Fig IV.5a; Supplementary Fig. 2g), and volcanic rock fragments are partially replaced by ferroan calcite. Furthermore, the ferroan spar engulfs overgrowths of quartz crystals (Supplementary Fig. 2e). Ferroan calcite also preserves embayments that are partially filled with kaolinite (Supplementary Fig. 2f), but the fracture-filling calcite grows over kaolinite (Fig. 5e). The skeletal grains are highlighted by micritic envelopes. Most preserved bioclasts stained purple or blue while brachiopod fragments stained pink (Fig. IV.5f; Supplementary Fig. 2c).

4.4.2.2.2. Dolomite

Dolomite forms finely crystalline (30–70 μm) planar subhedral to euhedral (*Dol1*), as well as medium crystalline (up to 250 μm) nonplanar textures (*Dol2*; Fig. IV.6). The latter is occasionally characterised by curved crystal faces. Regardless of texture, the dolomite crystals locally show a brownish colouration in transmitted light (Fig. IV.6b), especially around the cleavage planes and outer rims. The brown colouration of dolomite is common where the crystals are associated with pyrite. All dolomites are non-cathodoluminescent (Figs. IV.6c–d). Locally, the dolomite may display zonation under UV and blue-light irradiation (Fig. IV.6a). The edges of the planar and nonplanar dolomite are stained turquoise, whereas the entirety of the nonplanar crystals stain turquoise was also observed (Fig. IV.6e; Supplementary Fig. 2d). The planar dolomite crystals contain a rim of fluid inclusions in the otherwise inclusion-poor crystals. Furthermore, less typically, spots of ferroan calcite and framboidal to euhedral pyrite also occur within the planar dolomite (Figs. IV.6c, f). The planar dolomite occludes primary and secondary pores, is partially engulfed by calcite, pyrite, kaolinite and quartz crystals (Figs. IV.6–7; Supplementary Figs. 2f and 3e, h) and also appears as a replacive phase scattered throughout the samples. The nonplanar dolomite crystals either fill intergranular pores or clog the chambers of preserved fossils (Fig. IV.6d; Supplementary Fig. 3c).

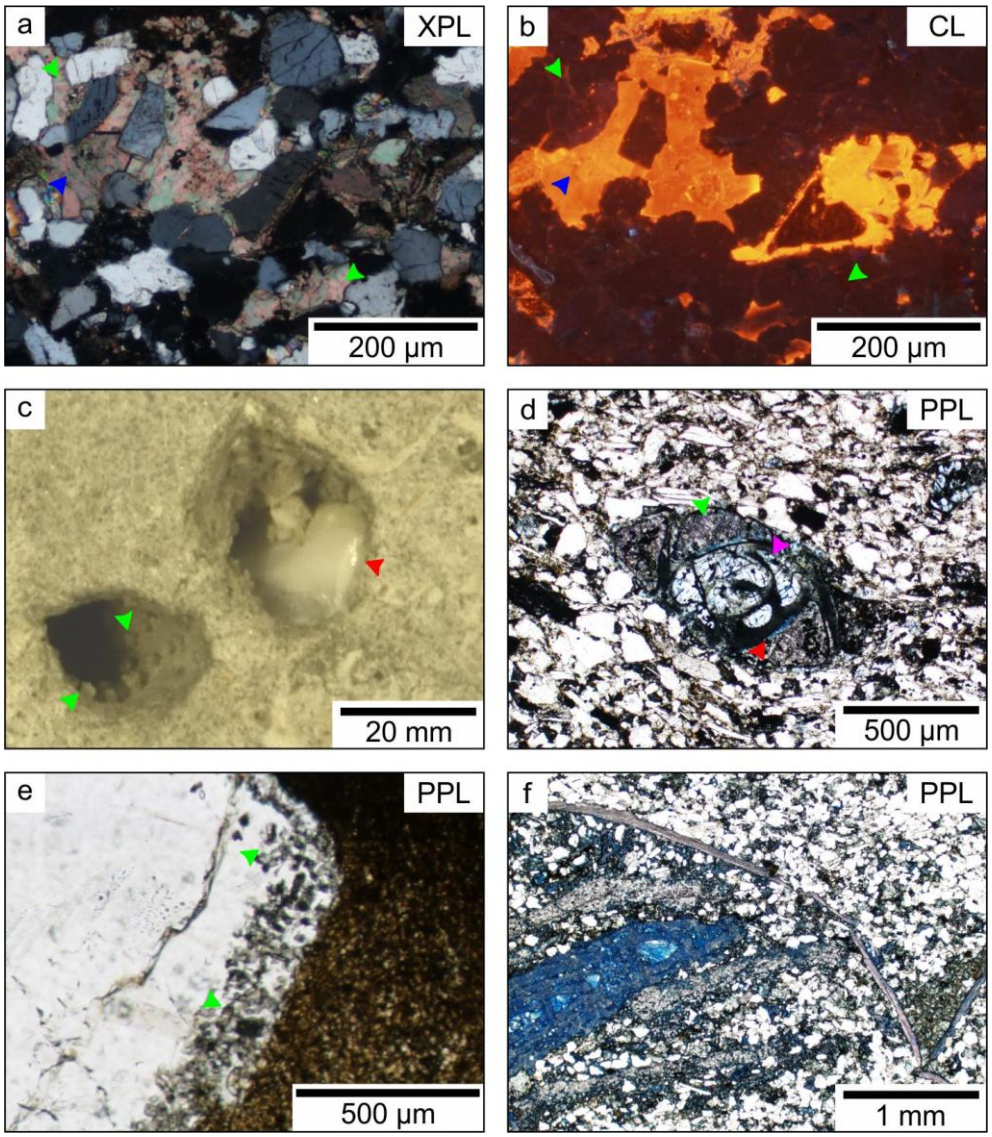

Fig. IV.5. Photomicrographs of calcite cement. **a)** and **b)** Poikilotopic calcite cemented arenite (W–9; 2811.0 m MD). Green arrows point to non-luminescing calcite, whereas the blue arrow marks an orange luminescent one. **c)** Single coarse crystal (red arrow) partially fills a moldic pore and calcite crystals (green arrows) sit in equidistance on the wall of a moldic pore (W–1; 2459.9 m MD). **d)** The outer chambers of a miliolid foraminifer are filled by purple-stained calcite (green arrow), which embays pyrite framboids. Towards the central chamber, which is clogged by non-ferroan dolomite (pink arrow), a rim of blue-stained calcite is also present along the margin of dolomite (red arrow; W–1; 2603.4 m MD). **e)** Fracture-filling coarse-crystalline calcite with well-developed crystal facets embays kaolinite (green arrows; W–15; 2350.5 m MD). **f)** Pink-stained bioclast fragments (brachiopods) and blue-stained skeletal grain (nummulite) in an arenite (W–15; 2354.5 m MD).

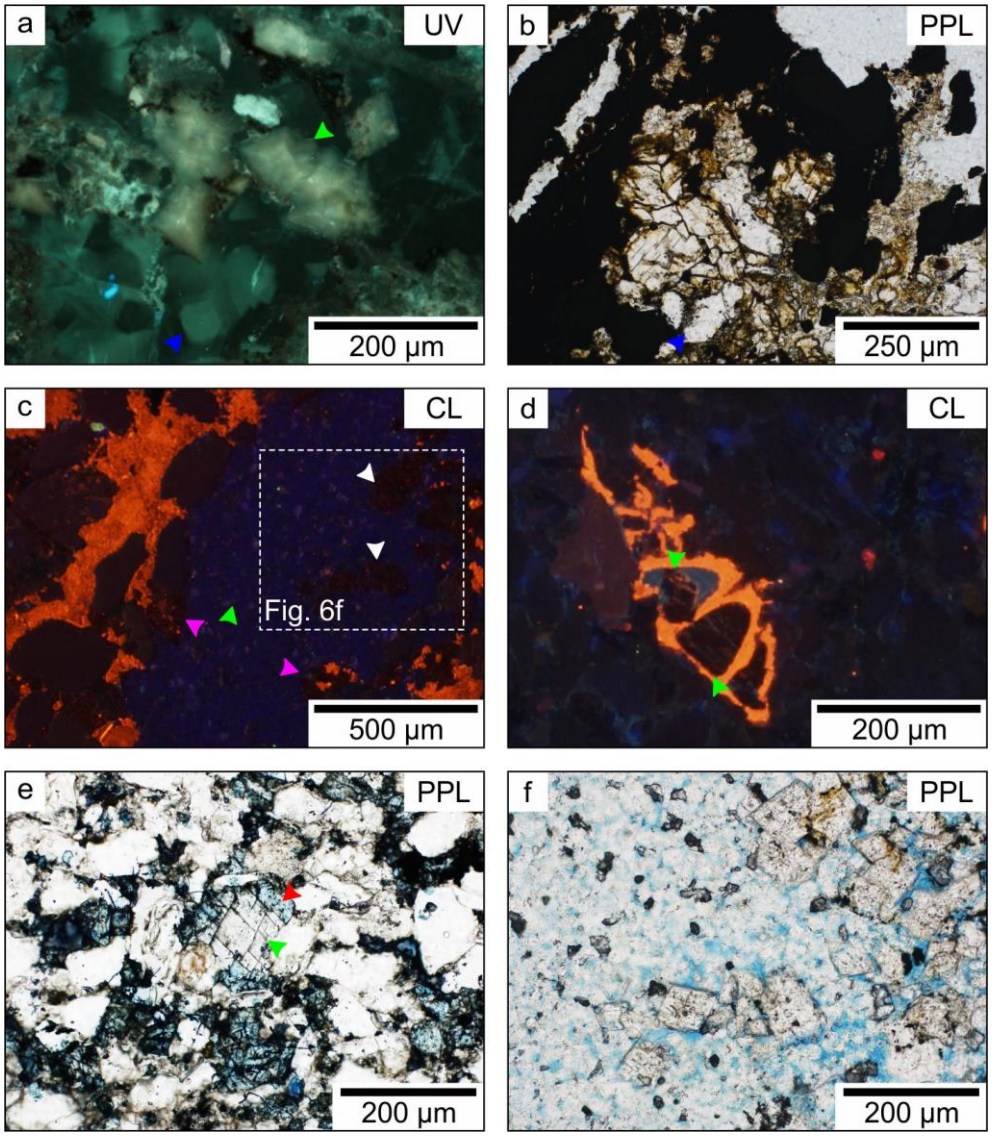

Fig. IV.6. Photomicrographs of dolomite phases. **a)** Zoned dolomite (green arrow) and calcite (blue arrow) under UV-light irradiation (W–15; 2358.0 m MD). **b)** Medium-crystalline non-planar dolomite crystals surrounded by opaque minerals and solid bitumen. Dolomite shows brown colouration along cleavage planes (W–7; 2460.2 m MD). **c)** Blue-luminescing kaolinite (green arrow) and non-luminescent dolomite (pink and white arrows) fill an oversized pore. Orange-luminescing calcite replaces non-luminescent detrital quartz grains. Non-luminescent dolomite partially replaces luminescing calcite (pink arrow; W–1; 2455.3 m MD). **d)** Orange-luminescing skeletal grain is filled by non-luminescent dolomite (green arrow; W–9; 2810.5 m MD). **e)** Turquois-stained ferroan dolomite (red arrow) grows over non-stained planar euhedral dolomite rhomb (green arrow; W–15; 2354.5 m MD). **f)** Planar euhedral-subhedral dolomite rhombs embayed by kaolinite. Dolomite hosts subhedral pyrite crystals and shows brownish colouration (W–1; 2455.3 m MD).

4.4.2.2.3. Quartz

Quartz cement occurs as syntaxial overgrowth, outgrowth (Fig. IV.7a) and it heals microfractures in detrital quartz grains. Quartz cement is less common in calcite cemented samples. Over- and outgrowths partially or completely occlude the intergranular pores in sandstones and siltstones. The overgrowths form up to 100 µm-wide rims around the quartz grains. Moreover, up to 200-µm-sized outgrowths are also present in some samples. The authigenic quartz is non-cathodoluminescent. Large overgrowths engulf authigenic dolomite rhombs (Fig. IV.7a). A thin coat of clay minerals and iron oxyhydroxides cover the crystal facets (Fig. IV.7b; Supplementary Figs. 3g, h) and locally highlight the boundaries between quartz grains in densely packed lithologies.

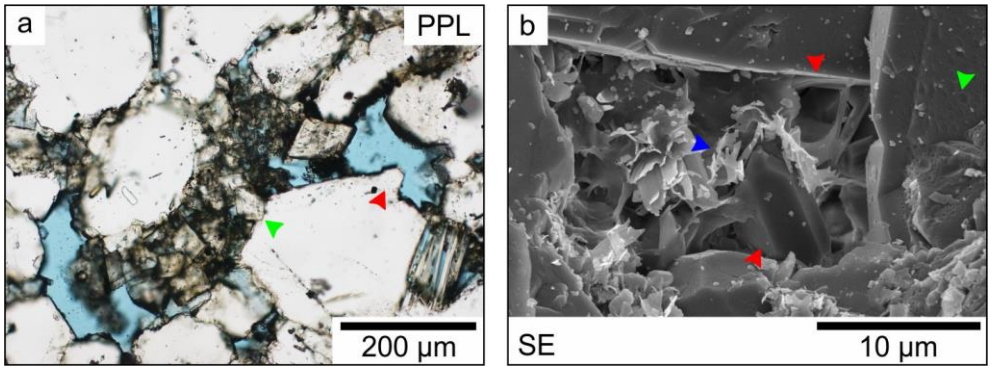

Fig. IV.7. Photomicrographs of quartz cement. **a)** Quartz cement forms syntaxial overgrowths and outgrowths (red arrow) pointing towards pores, filled with blue epoxy. Planar euhedral dolomite rhomb (green arrow) abuts against quartz overgrowth (W–1; 2455.3 m MD). **b)** Illite flakes (blue arrow) cover euhedral quartz crystals (red arrows) in a secondary electron image (SE). Dissolution pits are marked by green arrows (W–9; 2809.5 m MD).

4.4.2.2.4. Illite

Illite flakes and filaments occur in the samples as mineral coatings (Fig. IV.7b), covering the authigenic quartz and kaolin group minerals. Illite shows black and brown colouration in transmitted light.

4.4.2.2.5. Kaolin minerals

Individual kaolin crystals are less than 2 µm thick and form vermicular aggregates (Fig. IV.8a). The stacked booklets of pseudohexagonal crystals are up to 40 µm thick. Besides the vermiform kaolin, up to 6-µm-thick blocky crystals are also present in the samples and preserve the original stacking pattern (Fig. IV.8a). Kaolin is white or shows brownish to blackish colouration in transmitted light, and a bright, deep blue CL (Figs. IV.6c, f). Booklet-like piles of kaolin are locally associated with muscovite and fill the space between split flakes (Fig. IV.8b). Kaolin piles are also linked to intragranular pores of feldspar grains or argillaceous rock fragments (Figs. IV.8c–d). Furthermore, the stacked booklets also clog the chambers of fossils (Fig. 8e). More commonly, vermicular kaolin exists in between framework grains, occluding intergranular and oversized pores completely or partially. Moreover, kaolin also sits on the wall of ferroan calcite (Supplementary Fig. 2f) and calcite-filled fractures (Fig. IV.5e). Occasionally, neoform kaolin is present in the embayments of detrital quartz grains. Kaolin crystals surround pyrite framboids and dolomite rhombs (Fig. IV.6f), or it is engulfed by

quartz overgrowth, outgrowth (Fig. IV.8f) and ferroan calcite (Fig. IV.5e). Kaolin crystals are densely stacked in association with argillaceous debris squeezed into rigid framework grains (Figs. IV.8c–d).

4.4.2.2.6. Pyrite

Pyrite occurs as framboidal aggregates, sized up to 50 μm, and locally mm-sized single crystals or nodules made up of anhedral-to-euhedral crystals. Spherical aggregates are either associated with bioclasts (Fig. IV.9a), develop within chambers pre-dating calcite, or replace skeletal grains, forming ghosts after the original fossils. Furthermore, framboids occur between the framework grains, appear floating in the calcareous matrix (Fig. IV.9b) or sit on the edge of detrital grains. The subhedral to euhedral crystals are common along dissolution seams together with solid bitumen (Fig. IV.9c), and form rims and nodules along framework grains, especially quartz grains (Fig. IV.9d) and lithic fragments, and accessory minerals such as rutile. Pyrite crystals consume dolomite (Supplementary Fig. 3h) and less typically occur as inclusions in planar dolomite rhombs (Fig. IV.6f). Pyrite is locally surrounded by brownish iron oxyhydroxide phases (Figs. IV.6b, f), which typically also cover framework grains.

4.4.2.3. Porosity

Blue epoxy impregnated thin sections reveal that the partial or complete dissolution of detrital intra- and extrabasinal grains control the intergranular and intragranular porosity (Fig. IV.4a; Supplementary Figs. 3a, e and f). Moldic pores are also present preserving the shape of the fossil fragments (Fig. IV.5c; Supplementary Fig. 1d). The size of the pores is typically more than two times greater than the diameter of the framework grains. These oversized pores ensure the interconnectedness of pores throughout the sandstones regardless of the abundance of the matrix. Authigenic minerals, such as ferroan calcite and kaolin crystals, and dolomite often occlude the pores but intercrystalline pores between the cement crystals remain (Fig. IV.6f). Fracture porosity also exists either as open or partially healed fractures. The outlined hybrid porosity varies even at the microscale and shows considerable heterogeneity in the spatial characteristics of the pore system. Even though the porosity of sandstones is dominated by secondary porosity, primary porosity is also preserved, such as intraskeletal pores.

4.4.3. Fluid inclusion petrography and microthermometry

Representative samples, including centimetre-sized euhedral calcite in an oversized pore, centimetre-thick fracture-filling calcite, as well as samples of arenite, wacke, siltstone and drill cuttings were selected for detailed FI study. These samples contain authigenic minerals, such as calcite, dolomite and quartz that host numerous FIs of suitable size. The results of the FI studies are summarized in Table IV.3.

4.4.3.1. Calcite

Numerous FIs are present in the various bright to dull orange-luminescing ferroan calcite crystals, including euhedral calcite (Cal_{EU}) that fills oversized pores, equant calcite spar that fills the chambers of preserved bioclasts or intragranular pore spaces (Cal_{EQ}), and fracture-filling calcite (Cal_{FF}).

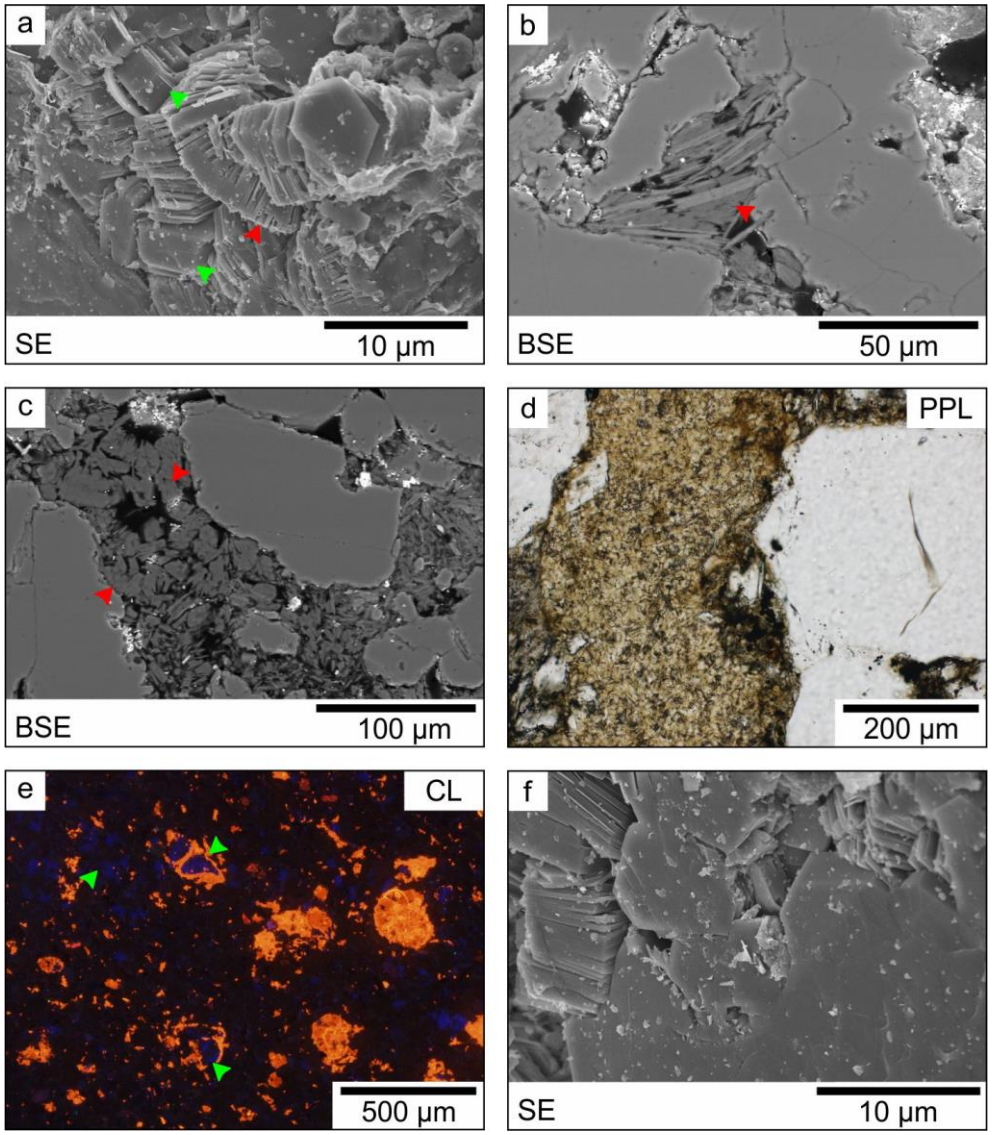

Fig. IV.8. Photomicrographs of kaolin cement. **a)** Stacked booklets of pseudohexagonal kaolin crystals. The red arrow points to a less than 2-µm-thick crystal, whereas the green arrows mark the thicker blocky crystals (W–9; 2810.0 m MD). **b)** Backscattered electron (BSE) image of booklet-like piles of kaolin (red arrow) that are associated with muscovite and fill the space between split flakes (W–1; 2455.3 m MD). **c)** Kaolin crystals (red arrows) replacing framework grain (W–1; 2455.3 m MD). **d)** Densely stacked kaolin in association with argillaceous debris squeezed into rigid framework grains (W–7; 2460.2 m MD). **e)** Blue-luminescing kaolinite (green arrows) fills chambers of orange-luminescing fossils and forms nest in intergranular pores (W–14; 2109.0 m MD). **f)** Syntaxial quartz overgrowths embay kaolin crystals (W–9; 2810.0 m MD).

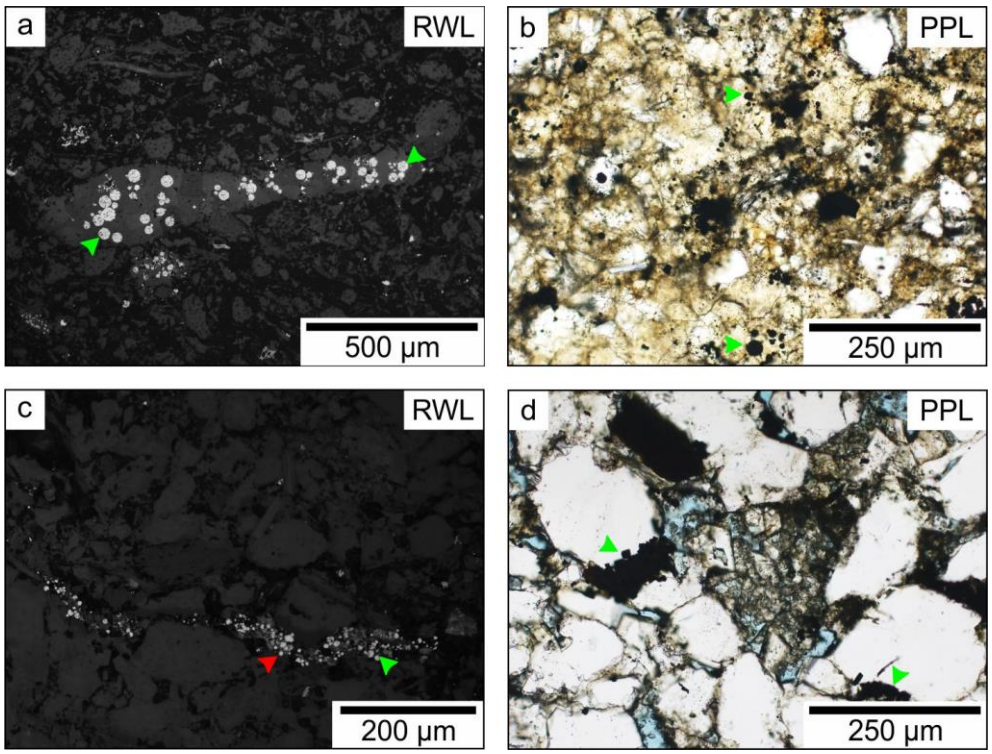

Fig. IV.9. Photomicrographs of authigenic pyrite. **a)** Pyrite framboids (green arrows) sit within a fossil in reflected white light (RWL; W–1; 2603.1 m MD). **b)** Pyrite framboids (green arrows) engulfed by calcite spars in a wacke (W–1; 2461.8 m MD). **c)** Pyrite crystals associated with micro-stylolite (W–1; 2504.0 m MD). **d)** Euhedral pyrite crystal aggregates (green arrows) replacing quartz grains (W–1; 2455.3 m MD).

4.4.3.1.1. Euhedral calcite (Cal_{EU})

The euhedral calcite hosts primary FIs, forming planes along crystal-growth zones. The FIs are sized up to 50 µm and have shapes of negative crystal and rounded forms as well. The inclusions are colourless and non-fluorescent two-phase (L_{aq}+V) with $\varphi_V \approx 0.1–0.2$ at room temperature and are interpreted as primary aqueous inclusions (AIs). Raman microspectroscopy indicates the presence of gaseous hydrocarbons, methane and ethane, in the vapour phase of some AIs (Fig. IV.10). The homogenisation occurs into the liquid phase ($L_{aq}+V \rightarrow L_{aq}$), the T_h varies in a narrow range from 129 °C to 137 °C (n=85; Fig. IV.11). The T_m(Ice) ranges between −3.4 °C and −2.5 °C (n=85; Fig. IV.12), indicating a range of salinity between 4.2 mass% and 5.6 mass% NaCl equivalent. No visual changes were observed in AIs while cooling them to –160 °C, indicating the lack of a clathrate phase.

4.4.3.1.2. Equant calcite (Cal_{EQ})

The inclusions form groups either in the core of the equant sparry calcite or are present throughout the entire calcite crystal, which argues for primary origin. The inclusions are sized up to 11 µm and contain colourless liquid and vapour phases with $\varphi_V \approx 0.1–0.2$ at room temperature. The FIs are non-fluorescent and are defined as aqueous inclusions. The fluids homogenise into the liquid phase ($L_{aq}+V \rightarrow L_{aq}$) with T_h varying between 126 °C and 141 °C (n=35; Fig. IV.11). The T_m(Ice) ranges between −3.1 °C and −2.8 °C (n=17; Fig. IV.12), indicating a range of salinity between 4.7 mass% and 5.1 mass% NaCl equivalent. A decrease in T_h across a single spar towards the edge is apparent in these FIAs, but the values of T_m(Ice) do not show similar variation.

Table IV.3. Petrographic and microthermometric characteristics of the studied FIAs.

Mineral phase	Genetic origin	Size	Colour in transmitted light	Colour under UV-light irradiation	Composition	Vapour phase ratio	Homogenisation process	T_h	T_m(Ice)	salinity
		[μm]						[°C]		[mass%]
Cal_{EU}	primary	<50	colourless	non-fluorescent	L_{aq}+V	$\varphi_V \approx 0.1–0.2$	L_{aq}+V→L_{aq}	129–137	–3.4– –2.5	4.2–5.6
Cal_{EQ}	primary	<11	colourless	non-fluorescent	L_{aq}+V	$\varphi_V \approx 0.1–0.2$	L_{aq}+V→L_{aq}	126–141	–3.1– –2.8	4.7–5.1
	secondary	<10	colourless	non-fluorescent	L_{aq}+V	$\varphi_V \approx 0.2$	L_{aq}+V→L_{aq}	115–146	–5.2– –1.6	2.7–8.1
		<5	colourless	yellowish-orange	L_{hc}+V	$\varphi_V \approx 0.1–0.2$	L_{hc}+V→L_{hc}	105–142		
Cal_{FF}	primary	<25	colourless	non-fluorescent	L_{aq}+V	$\varphi_V \approx 0.2$	L_{aq}+V→L_{aq}	105–126	–2.1– –1.3	2.2–3.6
		<13	colourless	bluish	L_{hc}+V	$\varphi_V \approx 0.1–0.2$	L_{hc}+V→L_{hc}	103–123		
Dol1	primary	<19	colourless	non-fluorescent	L_{aq}+V	$\varphi_V \approx 0.2–0.3$	L_{aq}+V→L_{aq}	105–142	–5.5– –0.6	1.2–8.5
Qtz	primary	<17	colourless	non-fluorescent	L_{aq}+V	$\varphi_V \approx 0.2–0.3$	L_{aq}+V→L_{aq}	110–136	–3.4– –1.5	2.6–5.6
	secondary	<10	colourless	non-fluorescent	L_{aq}+V	$\varphi_V \approx 0.2$	L_{aq}+V→L_{aq}	120–129	–2.2– –0.9	1.6–3.7
		<5	colourless	bluish-green	L_{hc}+V L_{aq}+L_{hc}+V L_{hc}+V+S_{bit}	$\varphi_V \approx 0.1–0.2$ $\varphi_S \approx 0.1–0.2$	L_{hc}+V→L_{hc} L_{hc}+V+S_{bit}→L_{hc}+S_{bit}	117–130		

Cal_{EU} – euhedral calcite, Cal_{EQ} – equant sparry calcite, Cal_{FF} – fracture-filling calcite, Dol1 – planar dolomite, Qtz – quartz.

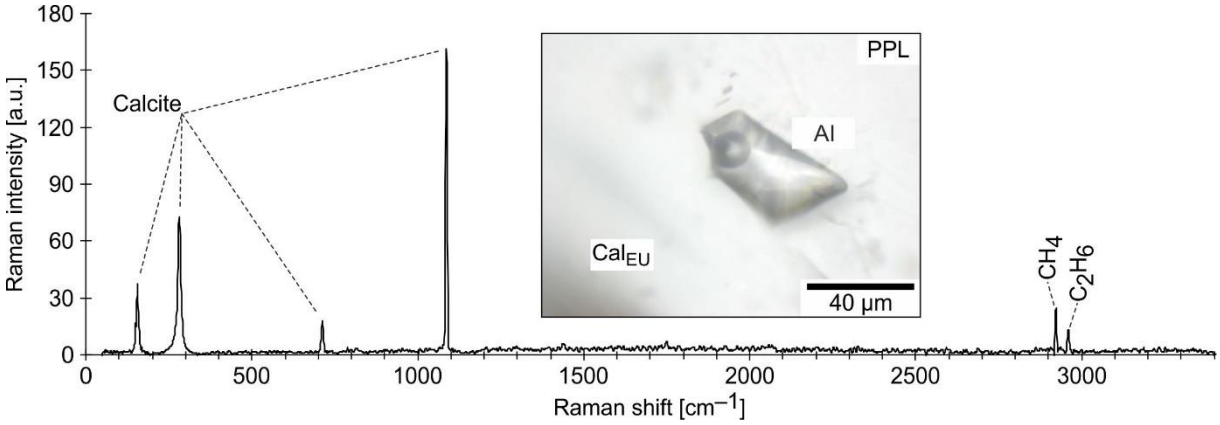

Fig. IV.10. Representative Raman spectrum of the vapour phase within an aqueous inclusion (AI) assemblage of euhedral calcite (Cal_{EU}).

Secondary FIAs are also present in the equant sparry calcite sample. FIs form trails and cross-cut several calcite crystals. The FIs are up to 10 µm in size, are colourless in plane-polarized light, and have a yellowish-orange fluorescence in UV-light irradiation (Fig. IV.13). Groups of fluorescent FIs, containing a maximum of five inclusions, also exist in these spars with a maximum FI size of 10 µm. These inclusions are interpreted as HCFIs and are two-phase inclusions (L_{hc}+V; $\varphi_V \approx 0.1–0.2$) and homogenise into the liquid phase (L_{hc}+V→L_{hc}) between 105 °C and 142 °C (n=37; Fig. IV.11). Two-phase, colourless aqueous FIs of up to 5 µm size (L_{aq}+V; $\varphi_V \approx 0.2$) also occur within these FIAs. These aqueous FIs homogenise into the liquid phase (L_{aq}+V→L_{aq}), and the T_h varies from 115 °C to 146 °C (n=16; Fig. IV.11). The T_m(Ice) ranges between −5.2 °C and −1.6 °C (n=16; Fig. IV.12), indicating a range of salinity between 2.7 mass% and 8.1 mass% NaCl equivalent. The intense fluorescence of the co-occurring HCFIs prevented the application of Raman microspectroscopy to determine the gaseous hydrocarbons in the vapour phase.

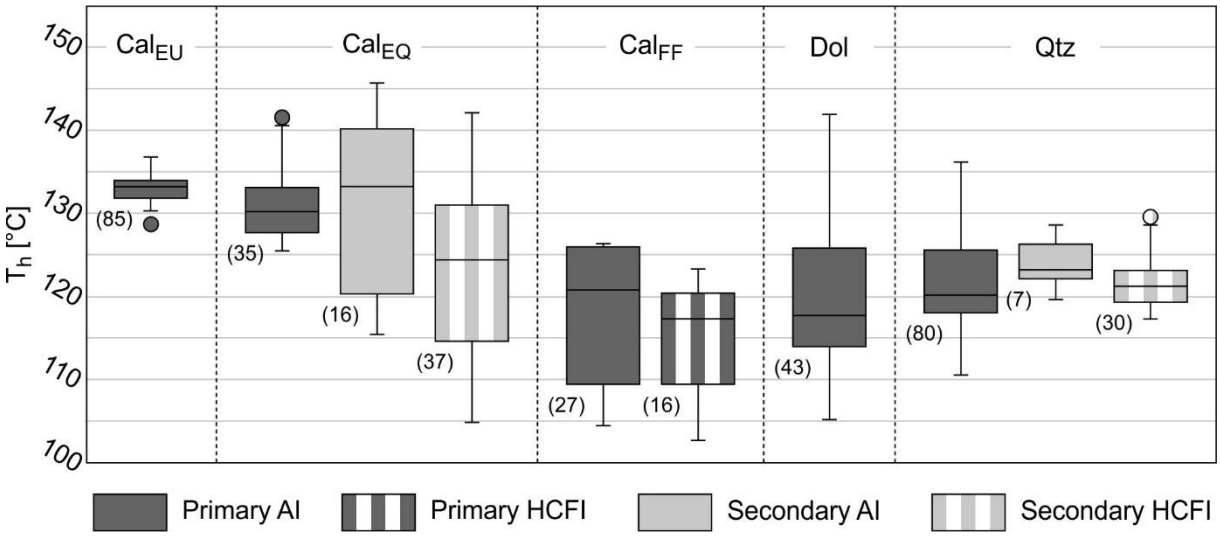

Fig. IV.11. Box-plot of the homogenisation temperatures (T_h). The numbers in brackets correspond to the number of analysed FIs. Cal_{EU} – euhedral calcite, Cal_{EQ} – equant calcite, Cal_{FF} – fracture-filling calcite, Dol – planar dolomite, Qtz – quartz.

4.4.3.1.3. Fracture-filling calcite (Cal_{FF})

Fracture-filling blocky calcite hosts FIs that form planes along growth zones. The primary FIs are up to 25 µm in size and are characterised by rounded and negative crystal shapes. The inclusions are colourless in plane-polarized light and show bluish epifluorescence (Fig. IV.13). The HCFIs are two-phase (L_{hc}+V) with $\varphi_V \approx 0.1–0.2$ at room temperature. These inclusions homogenise to the liquid phase ($L_{hc}+V \rightarrow L_{hc}$) between 103 °C and 123 °C (n=27; Fig. IV.11). No visual changes were observed in HCFIs while cooling them to –160 °C. Cogenetic colourless two-phase AIs (L_{aq}+V; $\varphi_V \approx 0.2$), with a maximum of 13 µm diameter, are also present in FIAs. Raman microspectroscopy of the aqueous FIs was hindered because of the intense fluorescence of the HCFIs. The homogenisation occurs in the liquid phase ($L_{aq}+V \rightarrow L_{aq}$) and the T_h varies from 105 °C to 126 °C (n=16; Fig. IV.11). The T_m(Ice) ranges between −2.1 °C and −1.3 °C (n=16; Fig. IV.12), indicating a range of salinity between 2.2 mass% and 3.6 mass% NaCl equivalent.

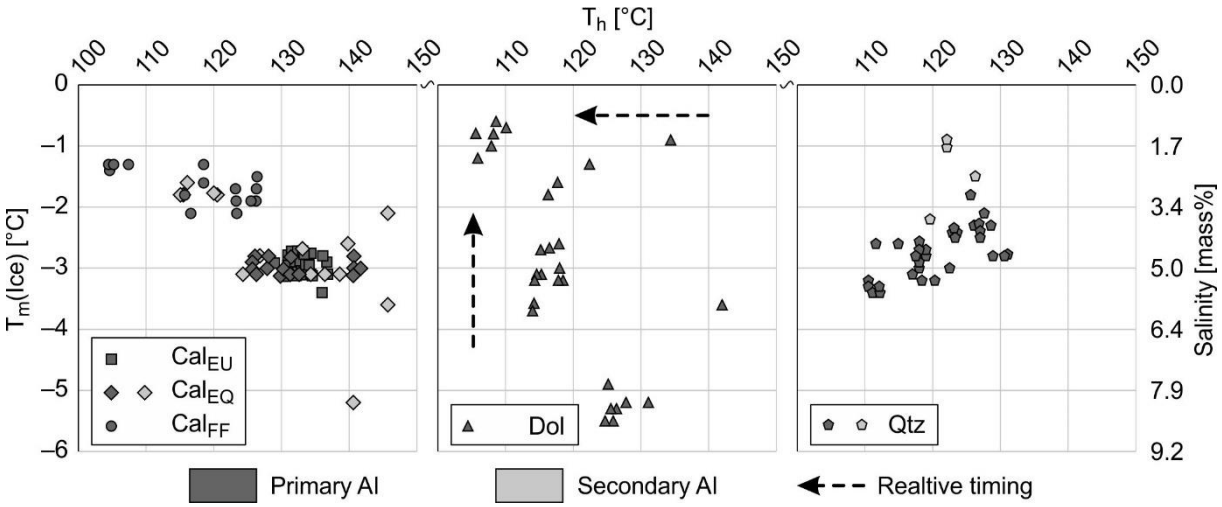

Fig. IV.12. Cross-plot of homogenisation temperatures (T_h) vs. final ice melting temperatures (T_m(Ice) of the analysed aqueous fluid inclusion assemblages. Arrows, representing the relative timing of FI entrapments, point to younger FIs. Cal_{EU} – euhedral calcite, Cal_{EQ} – equant calcite, Cal_{FF} – fracture-filling calcite, Dol – planar dolomite, Qtz – quartz.

4.4.3.2. Dolomite

Planar subhedral-to-euhedral rhombs (*Dol1*) in the sandstones contain FIs. Primary FIAs developed across the crystal outwards from the core. The FIs are sized up to 19 µm and are generally characterised by negative crystal shapes. At room temperature, in plane-polarized light, the inclusions consist of colourless liquid and vapour phase (L_{aq}+V; $\varphi_V \approx 0.2–0.3$). The primary FIs homogenised in the liquid phase ($L_{aq}+V \rightarrow L_{aq}$) and T_h values fall between 105 °C and 142 °C (n=43; Fig. IV.11). The T_m(Ice) varies from −5.5 °C to −0.6 °C (n=30; Fig. IV.12), indicating a rather broad salinity range between 1.2 mass% and 8.5 mass% NaCl equivalent. The distribution of the T_h and T_m(Ice) display a distinct spatial trend in these FIAs (Fig. IV.12): the T_h decreases from a maximum of 142 °C in the core to a minimum of 106 °C towards the rim of the crystal, whereas the T_m(Ice) increases from a minimum of −5.5 °C in the core to a maximum of −2.2 °C towards the edge.

4.4.3.3. Quartz

Authigenic quartz occurs as syntaxial overgrowth, outgrowth and as healed microfractures in detrital quartz grains in the sandstones and siltstones. Fluid inclusion assemblages occur along the dust rims in overgrowths, forming groups in pore-filling quartz and along with healed microfractures.

Primary FIAs along the dust rims are sized up to 17 μm and their shapes vary among negative crystal shaped, rounded and amoeboid forms. These inclusions are liquid dominant ($\varphi_V \approx 0.2$–0.3) and contain non-fluorescent, colourless fluid and vapour phases ($L_{aq}+V$). The homogenisation occurs into the liquid phase ($L_{aq}+V \rightarrow L_{aq}$) with T_h varying from 110 °C to 136 °C (n=80; Fig. IV.12). The T_m(Ice) ranges between −3.4 °C and −1.5 °C (n=38; Fig. IV.13), indicating a range of salinity between 2.6 mass% and 5.6 mass% NaCl equivalent.

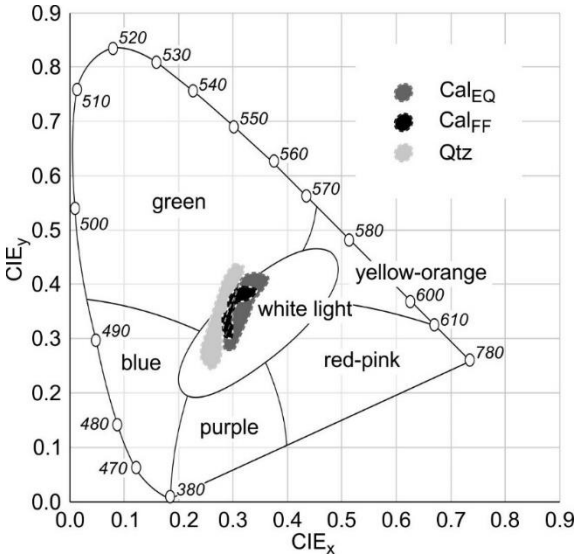

Fig. IV.13. Fluorescence colours of the hydrocarbon-bearing inclusions plotted on a CIE-1931 diagram (Smith and Guild, 1931) for visual comparison. Numbers presented along the colour envelope correspond to wavelengths in nanometres.

Secondary FIAs fluoresce intensely with bluish-green colour under UV epi-illumination (Fig. IV.14) and are interpreted as HCFIs. The HCFIs are either colourless or brownish in transmitted light regardless of fluorescence colour. The inclusions are characterised by rounded and irregular shapes and range in size up to 10 μm. The HCFIs are dominantly two-phase ($L_{hc}+V$; $\varphi_V \approx 0.1$–0.2) inclusions. Locally one-phase (L_{hc}) and three-phase ($L_{aq}+L_{hc}+V$) HCFIs are also present. Occasionally brownish black to opaque solid bitumen occurs in some two-phase ($L_{hc}+V+S_{bit}$) HCFIs. The volume fraction of the bitumen phase varies in a wide range ($\varphi_S \approx 0.01$–0.2) and is interpreted as an accidentally captured phase. Phase transition of the bitumen did not occur upon heating to 200 °C. Similarly, no visual changes occurred in HCFIs while cooling them to –160 °C. The two-phase inclusions undergo homogenisation to the liquid phase ($L_{hc}+V \rightarrow L_{hc}$) and the T_h of HCFIs is between 117 °C and 130 °C (n=28; Fig. IV.12). The three-phase HCFIs homogenise to two-phase inclusions ($L_{hc}+V+S_{bit} \rightarrow L_{hc}+S_{bit}$) and the T_h ranges from 119 °C to 121 °C (n=2; Fig. IV.12). Spatially rare cogenetic, up to 7 μm-diameter, two-phase colourless aqueous FIs ($L_{aq}+V$; $\varphi_V \approx 0.2$) also occur within these FIAs. The aqueous FIs homogenise into liquid phase ($L_{aq}+V \rightarrow L_{aq}$) and the T_h varies from 120 °C to 129 °C (n=7; Fig. IV.12). The T_m(Ice) ranges between −2.2 °C and −0.9 °C (n=4; Fig. IV.13), indicating a range of salinity between 1.6 mass% and 3.7 mass% NaCl equivalent.

4.4.4. Stable carbon and oxygen isotope composition

The stable carbon and oxygen isotope compositions of the investigated samples are listed in Table IV.4. The $\delta^{13}C$ and $\delta^{18}O$ values of the euhedral calcite vary from 0.34 ‰ to 1.61‰ and from –12.90‰ to –11.89‰, respectively. The fracture-filling calcite is characterised by –0.54‰ to –0.49‰ for $\delta^{13}C$, and –11.50‰ to –10.59‰ for $\delta^{18}O$ values. The $\delta^{13}C$ of the bulk rock samples is between –3.83‰ and 1.00‰, and the $\delta^{18}O$ ranges from –15.42‰ to –9.52‰ (Fig. IV.14).

Table IV.4. The stable carbon ($\delta^{13}C$) and oxygen ($\delta^{18}O$) isotope compositions of the investigated samples.

Sample type	Carbonate cement phase	$\delta^{13}C$	$\delta^{18}O$
		[‰; V-PDB]	
Wacke	Fe-Cal with Dol1	0.16	–12.38
		0.20	–10.19
		0.20	–12.66
		0.74	–11.34
		0.08	–12.52
		–0.02	–12.90
Arenite	Fe-Cal with Dol1	0.06	–9.52
		1.00	–15.42
		0.54	–14.48
	Fe-Cal and Dol2	–0.34	–9.98
		–0.24	–10.36
Sandstone with gravel	Fe-Cal and Dol1/Dol2	–2.77	–10.08
		–2.39	–9.93
Siltstone	Fe-Cal with Dol1/Dol2	–3.56	–14.98
		–3.83	–12.99
Calcite	Euhedral	1.61	–12.18
		1.13	–12.90
		0.34	–12.07
		1.13	–11.89
		0.94	–12.67
	Fracture-filling	–0.54	–11.50
		–0.49	–10.59

Fe-Cal – ferroan calcite, Dol1 – planar dolomite, Dol2 – nonplanar dolomite.

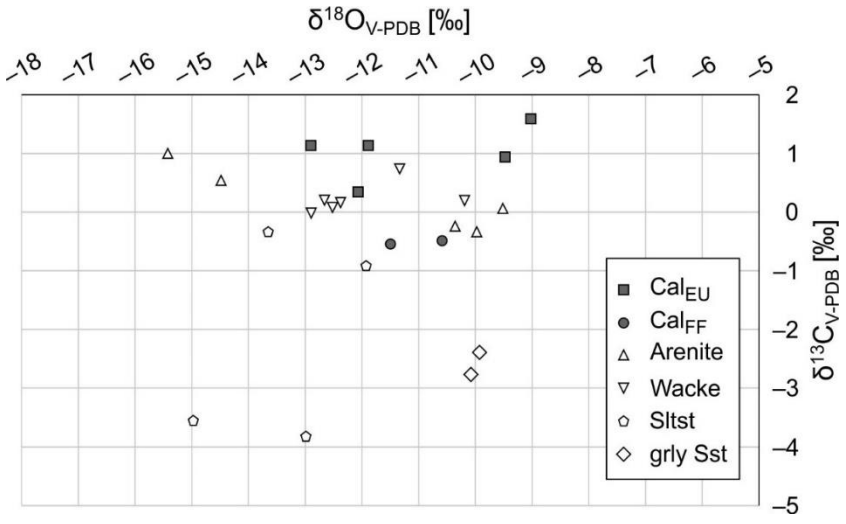

Fig. IV.14. Cross-plot of the stable carbon ($\delta^{13}C$) and oxygen ($\delta^{18}O$) isotope compositions of the investigated samples. Cal_{EU} – euhedral calcite, Cal_{FF} – fracture-filling calcite, Sltst – siltstone, grly Sst – sandstone with gravel.

4.5. Discussion

The paragenetic sequence was reconstructed based on textural relationships between diagenetic minerals, as well as fluid inclusion and stable carbon and oxygen isotope data. The paragenesis is summarized in Fig. IV.15 and the processes are explained in the following sections.

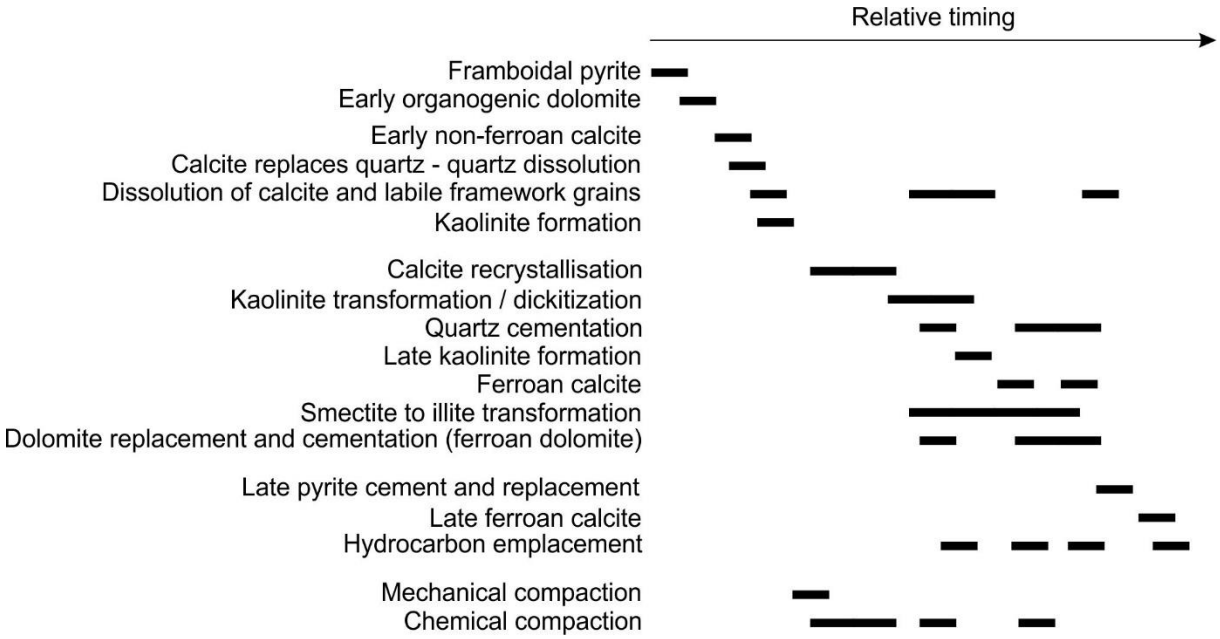

Fig. IV.15. Reconstructed paragenetic sequence of the south-central part of Hungarian Palaeogene Basin.

4.5.1. Control of depositional environment on early diagenetic processes

The Eocene sedimentary sequence in the study area records the transition from a continental to a lagoonal depositional environment (Gidai, 1978; Less, 2005), recording the first signs of the Priabonian transgression (Báldi and Báldi-Beke, 1985), which process fundamentally controls the fabric, texture, as well as the initial porosity and permeability of the accumulating sediments. The coal-bearing upper part of the Kosd Formation accumulated in a marine delta and is intercalated with sandstone and siltstone (Fig. IV.2), containing miliolid foraminifers (Körmös et al., 2020), indicating low-energy environments with varying sea-level. The Kosd Formation is followed by the shelf deposits of the biogenic Szépvölgy Limestone Formation (Kázmér, 1985), which occurs in the NE part of the study area, in the Well–15 (Fig. IV.2b), suggesting a continuous basin development. Even though the biogenic Szépvölgy carbonate is not present in the SW part of the study area, the preserved bioclasts (Figs. IV.4a, IV.5d, f, IV.6d, IV.8e, IV.9a; Supplementary Fig. 2c) in the studied sandstones are marine benthic (e.g., nummulites and miliolid foraminifers), sessile, attached (e.g., brachiopods), filter-feeding (e.g., bryozoans), grazer or burrower (e.g., echinoids) organisms and indicate photic zone (e.g., red algae) of the water column in a sandy shelf area (*cf.,* Scholle and Ulmer-Scholle, 2003). Sediments rich in intra-basinal carbonate grains (e.g., bioclasts) are prone to exhaustive carbonate cementation, reducing the initial depositional porosity and permeability.

The mineralogical composition of the rock components is a fundamentally important control on what mineralogical and chemical reactions play out during diagenesis. In clastic rocks, the tectonostratigraphy, i.e., the hinterland determines the source of the detrital material. From the

Late Cretaceous, the regional orogenic uplift led to subaerial exposure of the Mesozoic strata, including sedimentary and magmatic sequences, abundant in feldspar (e.g., Szarvaskő-Mónosbél Nappe in the Bükk Unit), and as a consequence, significant denudation occurred (Less, 2005; Haas and Kovács, 2012). The gradual north-eastward trending of the Eocene transgression reached the study area during the Bartonian and Priabonian (Báldi and Báldi-Beke, 1985; Báldi-Beke, 2003a, 2003b), allowing the accumulation of sediments with varying feldspar content. The widespread occurrence of kaolinite on the erosional surfaces in the hinterland (Viczián, 1987, 1995) and the stacked booklets, clogging the chambers of fossils (Fig. IV.8e) emphasize the importance of chemical weathering of a feldspar-bearing source that resulted in the accumulation of detrital kaolin minerals.

4.5.2. Bacterial sulphate reduction and organogenic dolomite

The presence of densely packed framboidal pyrite aggregates within the chamber of bioclasts and around their test (Figs. IV.9a) indicates locally reducing conditions during formation due to the oxidation of organic matter that was incorporated within skeletal structures. Moreover, the framboids, floating in the calcareous matrix (microspar; Fig. IV.9b) suggest the presence of sulphate-rich marine pore waters, the availability of reactive iron and the activity of sulphate-reducing bacteria (Sweeney and Kaplan, 1973; Gong et al., 2008). In some cases, planar dolomite rhombs enclose pyrite framboids, which may imply the localised occurrence of organogenic dolomite formation (Baker and Kastner, 1981; Morad et al., 2000). Organogenic dolomite is typically very finely crystalline and is interpreted to form when marine and meteoric waters mix and the sulphate ions are removed by the bacterial reduction in the bacterial sulphate-reducing zone (Petrash et al. 2017). However, the larger sizes of the dolomite rhombs in this study together with the >100 °C homogenisation temperatures suggest that, if present, organogenic dolomite only served as nucleation sites for the later, high-temperature ones. Bacterial sulphate reduction and the formation of potentially organogenic dolomite nuclei are interpreted to have taken place in a marine palaeoenvironment.

4.5.3. Origin of the microspar matrix

The high volume occupied by intergranular calcareous matrix (microspar) in the wackes (Figs. IV.4c), the absence of authigenic minerals other than those formed in the bacterial sulphate-reduction zone, and the lack of framework grain rearrangement features indicate an early, near-surface origin of the microspar, likely as intergranular micrite matrix that underwent crystal enlargement (*cf.*, Bathurst, 1975). The ferroan character of the microspar may indicate suboxic conditions in the bottom waters but the values of $\delta^{13}C$ (–0.02 to +0.74; Table IV.4) and the preserved bioclast assemblage argue for a precursor carbonate mud that accumulated in well-oxygenated water (Morad, 1998). Furthermore, under suboxic conditions, the available ferrous iron is typically incorporated into minerals, such as pyrite, in the bacterial sulphate-reduction zone. Nevertheless, the later precipitated calcite below the sediment-water interface may locally show ferroan character but it is generally Fe-poor. The ferroan nature of the calcite is thus more likely the result of recrystallisation (neomorphism) in a subsequent diagenetic phase.

4.5.4. Early kaolinization

Dissolution and alteration of silicates, especially the kaolinization of feldspar and mica (Fig. IV.8b–c) are common processes in the presence of low ionic strength meteoric waters (Worden and Burley, 2003). In shallow marine environments, the shelf is exposed to the

freshwater influx and meteoric recharge during sea-level lowstand (Worden and Morad, 2003 and references therein). The $\delta^{18}O$ values of the wackes (avg. –12.0‰ V-PDB; Table IV.4) support the presence of meteoric or mixed marine-meteoric pore water during calcite precipitation. Assuming 30 °C surface ocean temperature (Tindall et al., 2010) during early calcite formation, the calcite-water oxygen isotope fractionation equation (O'Neil et al., 1969) reveals a porewater characterised by an average $\delta^{18}O_{V\text{-}SMOW}$-value of –8.3‰. Considering the negligible land-covering ice-volume during the Palaeogene, and the $\delta^{18}O_{V\text{-}SMOW}$ composition of surface seawater in the shallow coastal areas (–4.0‰; Zhou et al., 2020) during the early Eocene, it supports the influence of meteoric pore water. Thus, we interpret this mixed, low-ionic-strength water as the diagenetic agent responsible for the kaolinization process. However, the occurrence of intergranular pore-filling (Fig. IV.6f) and fracture-clogging kaolinite (Fig. IV.5e), as well as kaolinite co-occurring with relatively high-temperature dolomite (T_h > 100 °C) indicate multiphase kaolinization. Moreover, kaolinite sitting on the edge of pitted quartz grains (Fig. IV.6c) and at the embayed contact of quartz and calcite (Figs. IV.5a; Supplementary Fig. 2f) may indicate multiple dissolution phases as well. The open-packing texture and the irregular pitted margins of detrital quartz and calcite elsewhere were interpreted to represent the result of localised quartz dissolution during early carbonate diagenesis (e.g., Worden et al. 2020). Textural observations suggest calcite replacement of quartz grains in the studied samples pointing to a similar process affecting the Eocene succession of the Hungarian Paleogene Basin. Therefore, some kaolinite may have accumulated in pore spaces that were created by the dissolution of quartz grains or by the later dissolution of quartz-replacing carbonates.

4.5.5. Burial calcite cementation and neomorphism

Besides the microspar in the matrix of the sandstone, calcite is also present as equant blocky, poikilotopic, drusy and fracture-filling cement (Fig. IV.5; Supplementary Figs. 2e–h, 3a, b, d and f), indicating a wide range of diagenetic conditions during burial history. The patchy occurrence of the poikilotopic and equigranular blocky calcite highlights the process of burial recrystallisation (Saigal and Bjørlykke, 1987), whereas the drusy nature of the calcite crystals supports an origin by direct precipitation (Morad, 1998). The fossil fragments that are stained purple to pale blue (Figs. IV.5f) also imply recrystallisation (dissolution and re-precipitation) of the precursor skeletons originally composed of high-magnesian calcite (*cf.*, Richter and Füchtbauer, 1978). The stable carbon isotope values of the cm-sized euhedral mold-, oversized pore- and fracture-filling calcite are close to 0‰ (–0.54 to 1.61‰; Table IV.4). Bulk rock $\delta^{13}C$ values are also near 0‰ (–0.34 to 1.00‰; Table IV.4), which is thought to reflect a marine bioclastic source (Morad, 1998). These values together with petrographic observations, such as neomorphism of carbonate mud and recrystallisation of skeletal grains support burial recrystallisation. The negative values close to –3‰ (–2.39 to –3.83‰; Table IV.4) suggest that decarboxylation during thermal alteration of the organic matter was contributing to the dissolved carbon content (Morad, 1998). Marine $\delta^{13}C$ values are also supported by the presence of marine skeletal fragments, whereas the effect of organic matter diagenesis is supported by the presence of coal measures in the siltstones (Körmös et al., 2020), and solid bitumen associated with sandstones (Supplementary Fig. 2a, b). The T_h of the primary aqueous FIs, trapped in equant calcite, is above 100 °C (Fig. IV.11) and proves that equant calcite precipitation occurred during deep burial mesodiagenesis. In some cases, the primary aqueous FIs, enclosed in equant calcite, are characterised by decreasing T_h towards the edges of the crystals, which reflects a cooling trend during precipitation likely during Pliocene uplift (Nagymarosy and Hámor, 2012).

4.5.6. Fracture-filling calcite cementation

Petrographic and geochemical data suggest that the various calcite cement types, such as equant, euhedral and the fracture-filling calcite formed under various conditions, even though the stable oxygen isotope composition of the euhedral calcite and sandstones-hosted equant calcite is identical (Fig. IV.14; Table IV.4). Based on the $\delta^{18}O$ of the equant calcite, the corresponding fluid inclusion T_h and the calcite-water oxygen isotope fractionation equation (O'Neil et al., 1969) suggest that the mineralizing fluid was a basinal brine characterised by a minimum $\delta^{18}O_{V\text{-}SMOW}$ value of 3.1‰.

The fracture-filling calcite is slightly depleted in ^{16}O (Fig. IV.14) and hosts primary aqueous FIs with lower T_h values (Fig. IV.11) compared to the equant and euhedral calcites. Consequently, the source formation water is characterised by $\delta^{18}O_{V\text{-}SMOW}$ values between 3.9‰ and 5.9‰ (Fig. IV.16), slightly higher than those of the euhedral calcite, 4.1‰ and 5.1‰ (Fig. IV.16). The higher $\delta^{18}O_{V\text{-}SMOW}$ and lower T_h values suggest that fracture-filling calcite postdates the euhedral one. The timing of the formation of this calcite is estimated based on the presence of primary HCFIs to have occurred sometime during the last six million years since the source rocks of the area reached the oil window within this period (Milota et al., 1995). A genetic relation of this calcite with hydrocarbon-bearing fluids is further supported by their $\delta^{13}C_{V\text{-}PDB}$ values (–0.5‰; Table IV.4), indicating that the migrating fluids contained dissolved carbon likely originating from thermal maturation of the organic matter at least to some extent.

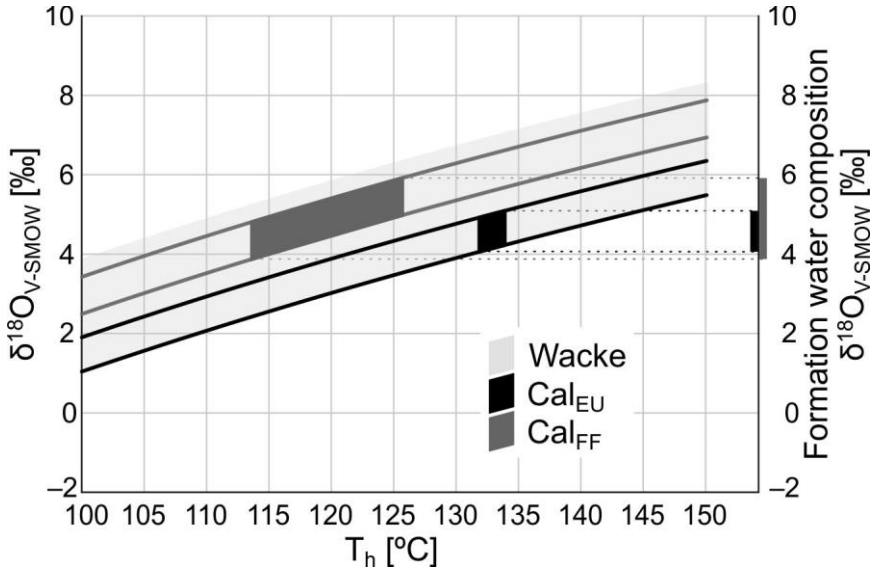

Fig. IV.16. Formation water composition, $\delta^{18}O_{V\text{-}SMOW}$ is based on homogenisation temperatures (T_h) of FIs and stable oxygen isotope ($\delta^{18}O_{V\text{-}PDB}$) of selected carbonate phases based on O'Neil et al., 1969., Cal_{EU} – euhedral calcite, Cal_{FF} – fracture-filling calcite.

4.5.7. Burial dissolution and kaolinite cementation

The presence of oversized and moldic pores (Fig. IV.5c; Supplementary Figs. 1d and 3a) in the sandstones that otherwise show evidence for mechanical and chemical compaction suggest burial (post-compaction) dissolution of the labile framework grains and bioclasts. This dissolution event indicates the incursion of low-pH or low-ionic-strength formation water, which dissolved the unstable framework grains. This fluid could have entered the formation either with a considerable hydraulic head (e.g., Mansurberg et al., 2020), including vertical and lat-

eral communication (e.g., Mádl-Szőnyi et al., 2019) or could have been generated by the process of organic matter maturation (e.g., Morad, 1998). The presence of dense kaolinite replacing ductile grains with no visible intercrystalline porosity (Fig. IV.8d) and the continuous thermal maturation of the organic matter within the research area (Körmös et al., 2021) support the deep burial origin of the kaolinite filling some of these pores. Kaolinite is also present along dissolution pores partially cemented by medium crystalline ferroan calcite, showing pitted margins (Supplementary Fig. 2f) and, hence postdating it. Furthermore, the fracture-filling calcite embays kaolinite booklets (Fig. IV.5e). The presence of kaolinite and the embaying fracture-filling calcite with well-developed crystal facets suggest that the fracture system conducted chemically diverse fluids. The heterogeneous nature of the pore system, e.g., the occurring intercrystalline, oversized and biomoldic pores, points to a vital role of dissolution in reservoir quality enhancement. The observed coarse crystal size of kaolinite may reveal a slow formation at a lower level of supersaturation (McKay et al., 1995) and supports the subsequent changes in water chemistry, such as the effective concentration of elements and Eh-pH conditions. Based on mineralogical (Table IV.1) and petrographic (Fig. IV.8a) observations the textural features of kaolin crystals indicate a transformation into dickite (Morad et al., 1994) in a temperature range between 80 and 130 °C (Ehrenberg et al., 1993).

4.5.8. Quartz cementation

Syntaxial overgrowth and outgrowth of quartz crystals occur in the arenites. However, the lack of these quartz cements in the wackes suggests that the presence of pervasive calcite hampered quartz formation. An internal source for the silica for these cements is suggested by the evidence of pressure solution (e.g., stylolites, Fig. IV.8f; Supplementary Fig. 2a, b; e.g., Barclay and Worden, 2000). The alteration of feldspar grains (e.g., Worden and Morad, 2003) and the progressive transformation of smectite to illite (see later; e.g., McKinley et al., 2003) possibly also contributed to the source of the quartz cement. The T_h of primary aqueous FIs along the dust rims suggests a temperature range of fluid entrapment between 110 and 136 °C (Fig. IV.11). This range of minimum trapping temperature (*cf.*, Goldstein and Reynolds, 1994) corresponds well with the proposed thermal conditions of the kaolinite to dickite transformation (Ehrenberg et al., 1993), which likely accompanied quartz cementation under similar chemical conditions.

4.5.9. Illitisation

Locally the authigenic quartz and kaolin crystals are covered by illite and illite/smectite flakes (Fig. IV.7b) suggesting a diagenetic origin of the illite and illite/smectite. Illite is a product of progressive transformation of the pre-existing smectite *via* mixed-layer illite/smectite intermediate stages. Smectite to illite transformation occurs at a temperature greater than 70–90 °C (e.g., Boles and Franks, 1979; Morad et al., 2000) further supporting that the succession reached burial depths and corresponding temperatures in excess of 70–90 °C (*cf.*, T_h in quartz, Fig. IV.11). Another possible source for illite is feldspar alteration (Morad et al., 2000; Worden and Burley, 2003), as indicated by the lack of feldspar (Fig. IV.3a) and the presence of kaolinite (Fig. IV.8), a likely product of feldspar alteration. Nevertheless, the low amount of illite and mixed-layer illite/smectite (Table IV.1) suggest that most potassium feldspar grains in the sediments were altered during earlier stages of diagenesis and were not available to supply adequate amounts of material to form larger quantities of illite and illite/smectite.

4.5.10. Burial dolomitization and thermochemical sulphate reduction

Even though an early-formed, potentially organogenic core is assumed to have served as nucleation sites for later dolomite growth, textural observations and fluid inclusion data indicate that the bulk of the replacive and cement dolomites formed during relatively late, high-temperature diagenetic processes. For example, planar dolomite crystals are embayed by syntaxial quartz overgrowths (Fig. IV.7a; Supplementary Fig. 3) and kaolin crystals (Fig. IV.6f). The T_h of primary aqueous FIs enclosed in planar dolomite rhombs (105–142 °C; Fig. IV.11) indicates formation at elevated temperatures. Elevated formation temperatures (min. 60–80 °C) are also supported by the locally occurring saddle dolomite (Fig. IV.6b; e.g., Spötl and Pitman, 1998). The Mg^{2+} for these dolomites might be supplied by the alteration of clay minerals. For example, the transformation of smectite to illite, which occurs in the same temperature range in which these dolomites formed, releases a considerable amount of Mg^{2+} and Fe^{2+} that could be taken up by dolomite (Boles and Franks, 1979). Furthermore, the alteration of clay intraclasts may have contributed to Eh-pH conditions favourable for dolomite formation (e.g., Barclay and Worden, 2000). Locally appearing calcite inclusions within dolomite crystals (Fig. IV.7h) suggest the replacive origin of some of the dolomite. The changes in pore-fluid chemistry, e.g., the effective concentration of elements, is further documented by the chemical variation in the internal cement of well-preserved bioclasts, including purple-stained calcite in the outer chamber with a rim of blue-stained calcite and non-ferroan dolomite in the central chamber (Fig. IV.5d). All these show the availability of reactive Fe^{2+} and Mg^{2+} during progressive diagenetic evolution. The chemical zonation, documented by fluorescence and carbonate staining (Figs. IV.6a, e) along with the decreasing trend in the T_h and T_m(Ice) of AIs in the planar dolomite rhombs (Fig. IV.13) document the chemical evolution of the parent fluid and the incorporation of Fe^{2+}. As the petrographic observations suggest, dolomite at least partially replaced (ferroan) calcite, suggesting, at least locally, another internal source of Fe^{2+} for ferroan dolomite formation, besides the supplied cations by the alteration of clay minerals. This process also enhanced porosity since dolomite has a smaller molar volume than calcite (Warren, 2000). Calcite and dolomite cements occur in approximately equal amounts in some arenites, including pebbly sandstones (Table IV.4), but their crystal size did not allow mineral-selective stable isotope analyses. Nevertheless, the bulk $\delta^{13}C$ values (–0.24 to –3.83‰; Table IV.4), suggest that besides the reorganization of the marine bioclastic carbon source (i.e., dissolution of bioclast supplying material for carbonate cementation), decarboxylation during thermal alteration of the organic matter may also have contributed to the dissolved carbon content of the mineralizing fluids (Morad, 1998).

Besides the eogenetic pyrite framboids, pyrite crystals are associated with solid bitumen and pyrite also locally replaced quartz grains and planar dolomite rhombs (Figs. IV.9c, d; Supplementary Fig. 3h). The presence of solid bitumen suggests a mesogenetic origin since hydrocarbon generation started six million years ago (Milota et al., 1995), ca. 35 Ma after the deposition of the host sediments. Moreover, the cogenetic HCFIs and AIs hosted in quartz minerals also document a hydrocarbon-bearing fluid migration at elevated temperatures, further supporting the burial origin of these pyrite aggregates. This temperature range (115–130 °C) is favourable for thermochemical sulphate reduction (Machel, 2001) but sulphate phases are not known in the research area. Therefore, hydrocarbons likely served as the source for H_2S generation either as a result of thermal maturation or H_2S reacted with saturated hydrocarbons forming elemental sulphur, which was later reduced. In high-temperature diagenetic conditions, sulphur acts as an active oxidizing agent for hydrocarbons, producing H_2S, solid bitumen and NSO compounds among others (Orr, 1977). Therefore, in the presence of metal cations, e.g., Fe^{2+}, pyrite forms on nucleation sites of eogenetic pyrite framboids (Machel, 2001).

4.5.11. Mineralizing fluid evolution during the late mesogenesis

Fluid inclusion analyses, stable oxygen isotope and detailed petrography revealed that cement minerals formed at elevated temperatures, but the source fluid chemistry differs significantly. Based on FI microthermometry the FIAs have not been subjected to thermal re-equilibration (*cf.*, Goldstein and Reynolds, 1994; Fig. IV.12), and the chemical zonation of the dolomite also rules out this process (e.g., Mazzulo, 1992).

The T_h values of the cement minerals (Fig. IV.11) considerably overlap. Comparing these results with the petrographic observations, a prolonged period with substantial changes in fluid chemistry characterise the evolution of pore fluids that control dissolution and precipitation processes. In some cases, a decreasing trend in the T_h values can be observed towards the younger growth zones (e.g., equant calcite spar and dolomite rhomb). However, the salinity of the enclosed fluids was not following the same trend in the equant calcite spars. On the contrary, obvious changes in the salinity were recorded by dolomite rhombs, following the trend of T_h, and also documented in chemical zonation (Figs. IV.6e, IV.12). The high salinity values, recorded by AIs are typical of basinal brines in the Hungarian Palaeogene Basin (Kovács and Gyuricza, 2014). The descending trend in salinity is either the result of mixing with meteoric water present at the basin margin with an elevated hydraulic head (e.g., Khalifa et al., 2017; Poros et al., 2012) or indicate the changes in water chemistry (e.g., the effective concentration of elements evolving with progressive diagenetic processes) of the basinal fluids. The calculated $\delta^{18}O_{V\text{-}SMOW}$ values of formation water (Fig. IV.16) are consistent with brines described in sedimentary basins (e.g., Khalifa et al., 2017) ruling out the role of meteoric water during dolomite formation. The chemical zonation (Figs. IV.6a, e) indicates the variations in the concentrations of Fe^{2+} and Mg^{2+} during precipitation (Morad, 1998). The salinity values, preserved in quartz crystals hosted AIs along dust rims, show an opposite relation compared to dolomite (Fig. IV.12). The T_m(Ice) values increase with rising homogenisation temperatures, indicating less saline formation water. Quartz postdates dolomite and a recurrent and prolonged period of cementation can be reconstructed, in which the burial depth and temperature have a critical role on the source fluid in as much as the effective concentration of the dissolved elements, Eh-pH conditions follow the changes of salinity.

The carbonate minerals are characterised by retrograde solubility during progressive burial (Morad et al., 2000), resulting in carbonate precipitation due to a decrease in dissolved CO_2 in the pore-fluid. Organic matter-bearing mudstones are present along the basin (Fig. IV.2; Körmös et al., 2021) and the transformation of smectite to illite releases a considerable amount of Mg^{2+} and Fe^{2+} (Boles and Franks, 1979) together with CO_2 as a by-product of thermal alteration of the organic matter. The dewatering of mudstone and the expulsion of CO_2 contribute to the development of the pore system by the acidic nature of the fluid front and may also be responsible for the quartz and carbonate cementation (Morad et al., 2000). The $\delta^{13}C_{V\text{-}PDB}$ values of dolomite cemented samples (Table IV.2) highlight the contribution of decarboxylation during thermal alteration of the organic matter to the dissolved carbon content (Morad, 1998), supporting the previous assumption.

4.5.12. Hydrocarbon migration

The cogenetic AIs and HCFIs in equant and fracture-filling calcite as well as in quartz mineral phase(s) indicate that hydrocarbons migrated together with the basinal brines. Besides the HCFIs studied here, Körmös et al. (2019) and Körmös (2017) reported aromatic hydrocarbons, methane and CO_2, liberated from FIs trapped in bulk samples (drill cuttings) of the Kosd Formation. However, mineral selective analyses were not performed and the tightly held fluids probably also contributed to their results (*cf.*, Volk and George, 2019). Nevertheless, methane was detected in AIs entrapped in euhedral calcite (Fig. IV.10). Based on the above

observations, methane saturation is assumed (*cf.*, Munz, 2001) and the aqueous phase may represent the H_2O–NaCl–CH_4 ± CO_2-system, which was concluded by Poros et al. (2012) in the Buda Hills, another part of the Hungarian Palaeogene Basin.

The fluorescence colour of HCFIs ranges from yellowish to bluish colours under UV excitation (Fig. IV.13). These observations correspond well with previous findings (Bauer et al., 2016). Aromatic hydrocarbons and polar compounds enclosed within FIs are responsible for the fluorescence properties (e.g., Stasiuk and Snowdon, 1997). Stasiuk and Snowdon (1997) demonstrated the correlation between fluorescence and API gravities of the trapped liquids in FIs; heavy oils show emission at higher wavelengths than lighter oils. That suggests a wide range of composition of the entrapped hydrocarbons. However, the intra- and intermolecular interactions make the interpretation of the fluorescent spectra difficult (Bertrand et al., 1986). The polar compounds preferentially adsorb onto charged mineral surfaces and inclusion oils. Thus, when captured in minerals, inclusion oils generally contain a higher proportion of polar compounds and, therefore, show a red shift relative to the associated reservoir oils (e.g., Han et al., 2022; Nedkvitne et al., 1993; Stasiuk and Snowdon, 1997). Considering the paragenetic sequence and the UV fluorescence of hydrocarbon-bearing FIAs, the equant calcite presumably trapped heavier oils, containing more polar compounds than the postdating counterparts (quartz and fracture-filling calcite). Besides the chemical composition, the thermal maturity of the inclusion oil may also affect the fluorescence properties. George et al. (2001) confirmed that blue-fluorescing HCFIs have molecular maturity anywhere in the oil window, making the maturity assumption of the investigated HCFIs controversial. Nevertheless, consequential differences in maturity are not expected because the thermal maturity of the crude oils and source rocks in the study area are in a narrow range (Körmös et al., 2021). The most probable explanation of the blue shift in UV fluorescence properties is phase separation or gas washing during or preceding trapping (Bourdet et al., 2014; Ping et al., 2019) since oil and gas generating source rocks are present in the Hungarian Palaeogene Basin (Körmös et al., 2020; 2021). Based on the above discussion, the hydrocarbon emplacement is interpreted to have occurred during a prolonged period under varying conditions, as indicated by the presence of primary HCFIs enclosed in a variety of host minerals, and the range of fluorescence colours likely represents at least a two-stage hydrocarbon charge events.

4.6. Conclusion

Detailed investigation of an Eocene mixed siliciclastic–carbonate succession in the Pannonian Basin led to the following conclusions. The shallow-marine depositional environment controlled the eogenetic processes. The sandy carbonate shelf provided suitable conditions for bacterial sulphate reduction. Extensive calcite cementation and neomorphism resulted in the loss of reservoir quality and lateral homogeneity. Whereas, the meteoric water incursion during sea-level lowstand at shallow burial enhanced the reservoir properties by the development of intragranular and intergranular porosity and also resulted in important vertical heterogeneity. Kaolinite formation and conversion into dickite during burial diagenesis on the one hand increased secondary porosity since it consumed feldspar and clay intraclasts but on the other hand partly reduced permeability as kaolinite clogged some of the pore spaces. Besides kaolinization, chemical compaction during increasing burial provided a sufficient source of silica for quartz cementation. The earlier alteration of feldspar resulted in a lack of potassium supply for late-diagenetic illite formation. Alteration of the basin-wide mudstones and the progressive transformation of smectite *via* mixed-layer illite/smectite to illite released a considerable amount of Mg^{2+} and Fe^{2+} for dolomite formation. Dolomite replacement may have locally improved porosity. Hydrocarbon emplacement with accompanying late pyrite formation further deteriorated porosity. The tectonostratigraphic evolution of the study area, i.e., propagation and cementation of the fault system by late ferroan calcite, contributed to improving

and reducing the lateral and vertical fluid flow. These steps collectively resulted in a heterogeneous reservoir, characterising the Eocene lithology in the Hungarian Palaeogene Basin.

V. CHAPTER

Conclusion

This study focused on the south-central part of the Hungarian Palaeogene Basin, where several boreholes were drilled during the last decades. These wells explored Eocene mixed siliciclastic-carbonate sequences, forming hydrocarbon reservoirs and penetrated coal-bearing sequences of the Kosd Formation beneath the Oligocene source rocks. The aims were to enhance the understanding of the depositional environment and organic matter sources of the coal-bearing Kosd Formation and estimate the hydrocarbon potential of deep Eocene Kosd coal. Moreover, intended to advance knowledge of the petroleum system by characterising the maturity and source rock potential of the Upper Eocene (Kosd and Buda Marl formations) and Oligocene (Tard Clay and Kiscell Clay formations) succession, and determine the source rock facies of crude oils produced in several oil fields in the Hungarian Palaeogene Basin. Besides them, addressed the correlation of these crude oils to the source rock formation. Furthermore, designed to call attention on the specific diagenetic processes that determine the quality of the Eocene mixed siliciclastic-carbonate reservoirs and their surroundings in the Hungarian Palaeogene Basin.

The investigation of coal measure of the Eocene Kosd Formation in the northern Pannonian Basin has yielded important new results regarding the depositional environment, organic matter source and hydrocarbon potential of the coal-bearing sequences. The thorough organic geochemical research of the Upper Eocene coal-bearing Kosd Formation is concluded as the followings. The coal measure of the Eocene Kosd Formation evolved in a marine deltaic environment. The accumulation of peat-forming vegetation in a low-lying, rheotrophic mire was affected by fluctuations of the water table. The slightly alkaline conditions and depletion in dissolved oxygen noted in the sediments promoted the reduction of sulphates by sulphate-reducing bacteria and bacterial decomposition of plant remains. In addition to the high sulphur contents observed (max. 8.8 wt%), the orange-brown fluorescence colour of vitrinite and its strong swelling during pyrolysis are typical indicators of marine-influenced coals. The peat-forming flora was dominated by land plants with varying contributions of algae and aquatic macrophytes. Similar to other Eocene coal seams, angiosperms predominated over gymnosperms. An upward increase in the relative contribution of gymnosperms (e.g., Cupressaceae) to the biomass was observed at depth between 2599.0 and 2604.4 m. The organic matter in the paleomire was highly reworked by microbial processing. The dense flourishing vegetation established a CO_2-limited environment forcing aquatic plants to utilise HCO_3^- during photosynthesis. Vitrinite reflectance, Tmax, and biomarker indices denote that organic matter in the Kosd Formation (as identified in deep borehole W–1) is thermally mature and suggests that the Kosd coal reached high-volatile bituminous rank in the research area. This is higher than the rank of the sub-bituminous coal in the shallow Kosd coalfield of the North Hungarian Mountains. This advanced maturity influenced the molecular and isotopic composition of hydrocarbons. Rock-Eval pyrolysis results indicate that the coaly samples studied are gas- and oil-prone and have reached the maturity threshold for first gas generation and the onset of oil expulsion.

The previously considered but hypothetical model of the petroleum system in the Hungarian Palaeogene Basin has been clarified in this study. The detailed organic geochemical investigation of the Upper Eocene and Lower Oligocene source rocks and accumulated oils in the Hungarian Palaeogene Basin led to the following conclusions. The sediments of the Kosd, Buda Marl and Tard Clay formations are identified as hydrocarbon-generating source rocks. In contrast, the involved rocks of the Kiscell Clay Formation are interpreted as non-source rocks. The spatial distribution and Rock-Eval characteristics of the former formations indicate

diverse petroleum potential along the study area. Molecular parameters of crude oil samples indicate a shaly source rock deposited in a marine/brackish environment. Salinity stratification, causing the development of oxygen-depleted conditions, is likely. Aquatic biomass, including algae, dino-flagellates and chemoautotrophic bacteria, dominates the accumulated organic matter. Minor angiosperm-dominated organic matter is transported into the basin from the shoreline. The molecular composition of accumulated crude oils determines the Tard Clay as the most probable source rock. Minor differences in source-related biomarker parameters are assumed to be caused by vertical and lateral variations in the source facies. Considering the maturity parameters and the common V-shape pattern in the compound-specific carbon isotope profile of *n*-alkanes in sediment extracts, deposited during nannoplankton zones NP21 to NP23, a contributing source from the Buda Marl is assumable. Therefore, detailed organic geochemical studies of the Buda Marls are highly recommended to explore the significance of these findings.

The reconstructed diagenetic evolution of the Eocene mixed siliciclastic-carbonate succession in the Pannonian Basin has pointed to specific diagenetic processes that determine the reservoir quality. Detailed investigation of an Eocene mixed siliciclastic-carbonate succession in the Pannonian Basin led to the following conclusions. The shallow-marine depositional environment controlled the eogenetic processes. The sandy carbonate shelf provided suitable conditions for bacterial sulphate reduction. Extensive calcite cementation and neomorphism resulted in the loss of reservoir quality and lateral homogeneity. Whereas, the meteoric water incursion during sea-level lowstand at shallow burial enhanced the reservoir properties by the development of intragranular and intergranular porosity and also resulted in important vertical heterogeneity. Kaolinite formation and conversion into dickite during burial diagenesis on the one hand increased secondary porosity since it consumed feldspar and clay intraclasts but on the other hand partly reduced permeability as kaolinite clogged some of the pore spaces. Besides kaolinization, chemical compaction during increasing burial provided a sufficient source of silica for quartz cementation. The earlier alteration of feldspar resulted in a lack of potassium supply for late-diagenetic illite formation. Alteration of the basin-wide mudstones and the progressive transformation of smectite *via* mixed-layer illite/smectite to illite released a considerable amount of Mg^{2+} and Fe^{2+} for dolomite formation. Dolomite replacement may have locally improved porosity. Hydrocarbon emplacement with accompanying late pyrite formation further deteriorated porosity. The tectonostratigraphic evolution of the study area, i.e., propagation and cementation of the fault system by late ferroan calcite, contributed to improving and reducing the lateral and vertical fluid flow. These steps collectively resulted in a heterogeneous reservoir, characterising the Eocene lithology in the Hungarian Palaeogene Basin.

Summary

The Neogene Pannonian Basin formed part of the Central Paratethys and is underlain by the Eocene and Oligocene sediments of the Hungarian Palaeogene Basin (Tari et al., 1993). In the Pannonian Basin, there are six known hydrocarbon systems and the Palaeogene hydrocarbon system belongs to the Hungarian Palaeogene Basin (Dolton, 2006), which is located in the north-central part of Hungary. The Hungarian Palaeogene Basin is interpreted as a retro-arc flexural foreland basin, where the depositional facies migrated towards the east-northeast according to the present position (Tari et al., 1993; Kováč et al., 2016). The tectonic evolution has been related to normal faulting and strike-slip regimes (Palotai, 2013 and references therein). The term Palaeogene Basin comprises all sedimentary sequences, forming a single cycle from the Eocene to the Early Ottnangian (Sztanó and Tari, 1993).

The Palaeogene sediments are unconformably overly the Mesozoic basement. The generalized lithostratigraphy begins with sediments showing a continuous upward transition from a terrigenous to a lagoonal environment, the Eocene Kosd Formation (Gidai, 1978; Less, 2005). The Kosd Formation is followed by the shelf deposits of the Szépvölgy Limestone Formation (Kázmér, 1985). The continued subsidence and the east-northeast trending of the depositional facies caused the deposition of the Buda Marl Formation under oxygen-depleted conditions (Less, 2005; Nagymarosy and Báldi-Beke, 1988; Ozsvárt et al., 2016). The sediments of the Tard Clay Formation accumulated in a euxinic basin (Báldi, 1984, Bechtel et al., 2012) then the Kiscell Clay Formation settled down in a well-oxygenated depositional environment (Báldi and Báldi-Beke, 1985). The sedimentary sequence of the Hungarian Palaeogene Basin is covered by thick Neogene sediments.

In the last few decades, several hydrocarbon reservoirs have been discovered in the Hungarian Palaeogene Basin. Hydrocarbons were detected in the fractured and weathered Mesozoic basement rocks in the research area. The basal conglomerate and breccia and the sandstone sequence of the Kosd Formation also form reservoirs and host substantial amounts of hydrocarbons. The karstified Szépvölgy Limestone and turbidite sandstone bodies within the Kiscell Clay Formation and the clastic sediments of the Miocene formations also serve as targets of exploration activities (Dolton, 2006). The reservoirs were discovered along with various structural, stratigraphic and combination trap types within the study area (Kokai, 1994; Dolton, 2006).

Fine-grained, organic matter-rich sediments within the Eocene and Oligocene succession were recognized as potential source rocks (e.g., Badics and Vető, 2012; Bechtel et al., 2012; Brukner-Wein et al., 1990; Milota et al., 1995). It is widely accepted that the Lower Oligocene Tard Clay Formation provides the most important source rocks (Bechtel et al., 2012; Brukner-Wein et al., 1990; Hertelendi and Vető, 1991; Milota et al., 1995). However, the Late Eocene Buda Marl Formation (Sachsenhofer et al., 2018a, 2018b) and Late Oligocene Kiscell Clay Formation (Milota et al., 1995) were also considered as potential source rocks.

Boreholes, drilled in the early 2000s in the south-central part of the Hungarian Palaeogene Basin, penetrated Eocene mixed siliciclastic-carbonate sequence, forming hydrocarbon reservoirs and coal-bearing sequences of the Kosd Formation beneath the Oligocene source rocks. The Oligocene source rocks have been investigated by several authors (e.g., Badics and Vető, 2012; Bechtel et al., 2012; Milota et al., 1995; Sachsenhofer et al., 2018a, 2018b), but the Eocene Kosd Formation remained largely uninvestigated. Comprehensive organic geochemical studies have only been performed on sediments of the Tard Clay Formation (Bechtel et al., 2012), whereas in-depth investigations are still missing for the Kosd, Buda Marl and Kiscell Clay formations. Furthermore, the detailed analysis of crude oils and thorough oil-to-source rock correlation are also absent. Besides the missing organic geochemical analyses of the potential source rocks and oil-to-source rock correlation, the Eocene mixed siliciclastic-

carbonate reservoir section also waits for detailed investigation. These reservoirs are characterised by diverse reservoir quality. The initial high production capacity of the reservoirs can only be maintained by multiple workover activities (Radovics et al., 2017). To maintain favourable production capacity, a detailed investigation of diagenetic processes characterising the Eocene mixed siliciclastic-carbonate reservoir rocks and their surroundings is needed as a prerequisite for appropriate reservoir description.

This study focuses on the southern-central part of the Hungarian Palaeogene Basin. The aims are to (i) enhance the understanding of the depositional environment and organic matter sources of the coal-bearing Kosd Formation, (ii) estimate the hydrocarbon potential of deep Eocene Kosd coal, moreover, (iii) advance knowledge of the petroleum system by characterising the maturity and source rock potential of the Upper Eocene (Kosd and Buda Marl formations) and Oligocene (Tard Clay and Kiscell Clay formations) succession, (iv) determine the source rock facies of crude oils produced in several oil fields in the Hungarian Palaeogene Basin, (v) correlate these crude oils to the source rock formation, furthermore, (vi) call attention on specific diagenetic processes that determine the quality of the Eocene mixed siliciclastic-carbonate reservoirs and their surroundings in the Hungarian Palaeogene Basin.

The investigation of the coal measure of the Eocene Kosd Formation in the northern Pannonian Basin has yielded important new results regarding its depositional environment, organic matter source and hydrocarbon potential:

T1 The coal measure evolved in a marine deltaic environment. The accumulation of peat-forming vegetation in a low-lying, rheotrophic mire was affected by fluctuations of the water table. Slightly alkaline conditions and the depletion in dissolved oxygen noted in the sediments promoted the reduction of sulphates by sulphate-reducing bacteria and bacterial decomposition of plant remains. In addition to the high sulphur contents observed (max. 8.8 wt%), the orange-brown fluorescence colour of vitrinite and its strong swelling during pyrolysis are typical indicators of marine-influenced coals.

T2 The peat-forming flora was dominated by land plants with varying contributions of algae and aquatic macrophytes. Similar to other Eocene coal seams, angiosperms predominated over gymnosperms. An upward increase in the relative contribution of gymnosperms (e.g., Cupressaceae) to the biomass is observed at a depth between 2599.0 and 2604.4 m. The organic matter in the paleomire was highly reworked by microbial processing. Dense flourishing vegetation established a CO_2-limited environment forcing aquatic plants to utilise HCO_3^- during photosynthesis.

T3 Vitrinite reflectance, Tmax, and biomarker indices denote that organic matter in the Kosd Formation (as identified in deep borehole W–1) is thermally mature and suggests that the Kosd coal reached the high-volatile bituminous rank in the research area. This is higher than the rank of the sub-bituminous coal in the shallow Kosd coalfield of the North Hungarian Mountains. This advanced maturity influenced the molecular and isotopic composition of hydrocarbons. Rock-Eval pyrolysis results indicate that the coaly samples studied are gas- and oil-prone and have reached the maturity threshold for first gas generation and the onset of oil expulsion.

The previously considered but hypothetical model of the petroleum system in the Hungarian Palaeogene Basin has been clarified in this study. The detailed organic geochemical investigation of the Upper Eocene and Oligocene source rocks and accumulated oils in the Hungarian Palaeogene Basin led to the following conclusions:

T4 The sediments of the Kosd, Buda Marl and Tard Clay formations are identified as hydrocarbon-generating source rocks. In contrast, the involved rocks of the Kiscell Clay Formation

are interpreted as non-source rocks. The spatial distribution and Rock-Eval characteristics of the former formations indicate diverse petroleum potential along the study area.

T5 Molecular parameters of crude oil samples indicate a shaly source rock deposited in a marine/brackish environment. Salinity stratification, causing the development of oxygen-depleted conditions, is likely. Aquatic biomass, including algae, dino-flagellates and chemo-autotrophic bacteria, dominates the accumulated organic matter. Minor angiosperm-dominated organic matter is transported into the basin from the shoreline.

T6 The molecular composition of accumulated crude oils determines the Tard Clay as the most probable source rock. Minor differences in source-related biomarker parameters are assumed to be caused by vertical and lateral variations in the source facies. Considering the maturity parameters and the common V-shape pattern in the compound-specific carbon isotope profile of *n*-alkanes in sediment extracts, deposited during nannoplankton zones, NP21 to NP23, a contributing source from the Buda Marl is assumable. Therefore, detailed organic geochemical studies of the Buda Marls are highly recommended to explore the significance of these findings.

The detailed investigation of an Eocene mixed siliciclastic–carbonate succession in the northern Pannonian Basin resulted in the following conclusions:

T7 The shallow-marine depositional environment controlled the eogenetic processes. The sandy carbonate shelf provided suitable conditions for bacterial sulphate reduction. Extensive calcite cementation and neomorphism resulted in the loss of reservoir quality and lateral homogeneity. Whereas, the meteoric water incursion during sea-level lowstand during shallow burial enhanced the reservoir properties by the development of intragranular and intergranular porosity and also resulted in important vertical heterogeneity. Kaolinite formation and conversion into dickite during burial diagenesis on the one hand increased secondary porosity since it consumed feldspar and clay intraclasts but on the other hand partly reduced permeability as kaolinite clogged some of the pore spaces. Besides kaolinization, chemical compaction during increasing burial provided a sufficient source of silica for quartz cementation. The earlier alteration of feldspar resulted in a lack of potassium supply for late-diagenetic illite formation. The progressive transformation of smectite *via* mixed-layer illite/smectite to illite in the basin-wide mudstones released a considerable amount of Mg^{2+} and Fe^{2+} for dolomite formation. Dolomite replacement may have locally improved porosity. Hydrocarbon emplacement with accompanying late pyrite formation further deteriorated porosity. The tectonostratigraphic evolution of the study area, i.e., propagation and cementation of the fault system by late ferroan calcite, contributed to improving and reducing the lateral and vertical fluid flow. These steps collectively resulted in a heterogenic reservoir, characterising the Eocene lithology in the Hungarian Palaeogene Basin.

Összegzés

A doktori kutatásomban a Központi-Paratethys Észak-magyarországi területén, az úgynevezett Észak-magyarországi Paleogén-medencében feltárt szénhidrogén rendszer vizsgálatával foglalkoztam. A kutatási terület az Észak-magyarországi Paleogén-medence középső részén helyezkedik el. A Paleogén-medence kialakulása egy ív-mögötti medence előterében történt, amelyben az üledékképződési környezetek kelet-északkelet irányban vándoroltak (Tari és mtsai., 1993; Kováč és mtsai., 2016). A medence fejlődését intenzív lemeztektonikai események kísérték (Palotai, 2013), amelyek meghatározzák mind a fluidumok migrációját, mind a rezervoárok tárolókapacitását. A vizsgált medence általános földtani felépítésére jellemző, hogy a mezozoós aljzatra üledékhézaggal települ a paleogén összlet, amelynek kezdő tagja az eocén korú Kosdi Formáció. Ennek alsó részét szárazföldi, míg felső részét édes-, később csökkent sósvizű környezetben lerakódott kőzetek építik fel (Gidai, 1978; Less, 2005). Ennek a fedőjét a sekélytengeri karbonátrámpa kifejlődésű Szépvölgyi Mészkő Formáció üledékei alkotják (Kázmér, 1985). Ezt a medence fáciesű Budai Márga Formáció, a mély szublitorális Tardi Agyag Formáció és a sekély szublitorális Kiscelli Agyag Formáció üledékes kőzetei követik (Báldi, 1984; Báldi és Báldi-Beke, 1985; Bechtel és mtsai., 2012; Less, 2005; Nagymarosy és Báldi-Beke, 1988; Ozsvárt és mtsai., 2016). A paleogén korú üledékeket jelentős vastagságú neogén korú képződmények zárják.

Az utóbbi néhány évtizedben számos szénhidrogén-kutató fúrás mélyült az Észak-magyarországi Paleogén-medence területén, amelyek nagy vastagságban tártak fel szervesanyagban gazdag paleogén korú finomtörmelékes kőzeteket (pl., Badics és Vető, 2012; Bechtel és mtsai., 2012; Brukner-Wein és mtsai., 1990; Hertelendi és Vető, 1991; Milota és mtsai., 1995; Sachsenhofer és mtsai., 2018a, 2018b) és sziliciklasztos, karbonátos, valamint kevert sziliciklasztos és karbonátos szénhidrogéntároló képződményeket (Dolton, 2006; Kokai, 1994).

Doktori kutató munkámban az Észak-magyarországi Paleogén-medence szénhidrogén rendszerének vizsgálatát és az eddigi ismeretanyag pontosítását tűztem ki célul, hogy (1) feltárjam, az eddig részletesen nem vizsgált Kosdi Formáció szén-tartalmú összletének eredetét, beleértve a felhalmozódott szervesanyag prekurzor vegetációját, valamint életterét, (2) meghatározzam a barnakőszén szénhidrogén generáló kapacitását. Ezenfelül kiemelt figyelmet fordítottam a szénhidrogénrendszer egyes elemeinek pontosítására, hogy (3) részmedence-léptékben bemutassam a szervesanyagban gazdag paleogén korú finomtörmelékes kőzetek szénhidrogén generáló potenciálját, (4) megállapítsam mind a hagyományos, mind a nem-hagyományos szénhidrogén tárolókból termelt fluidumok eredetét, valamint (5) biomarkerek alapján korreláljam a kőolajat és annak anyakőzetét. A kevert sziliciklasztos és karbonátos tárolókőzeteket jellemző és a kitermelést megnehezítő rezervoár-heterogenitásának feltárása érdekében (6) ismertessem a tárolókőzet és környezetének diagenetikus fejlődéstörténetét.

Az Észak-magyarországi Paleogén-medence központi részén fekvő eocén korú Kosdi Formáció szén-tartalmú összletének vizsgálata során az alábbi új tudományos eredmények születtek a felhalmozódási környezet, a prekurzor szervesanyag és a szénhidrogén potenciál tekintetében:

A szenes összlet alacsonyan fekvő reotróf lápban, tengeri deltai környezetben halmozódott fel, amelyre a talajvízszint ingadozása jelentős hatással volt. A lápban kialakult enyhén lúgos kémhatás és az oldott oxigén tartalom csökkenése megfelelő környezeti körülményeket biztosított a szulfátredukáló baktériumok élettevékenységének és a növényi maradványok bakteriális lebontásának. A magas kéntartalom (max. 8,8 tömeg%) mellett, a vitrinit narancssárga-barna fluoreszcens színe és a pirolízis során tapasztalt jelentős mértékű duzzadás a tengeri környezetben történt felhalmozódást bizonyítja.

A tőzegképző flórát a magasabbrendű szárazföldi növények uralták, a moszatok és vízi makrofiták változó mértékű megjelenése mellett. Az eocén korú széntelepekhez hasonlóan a zárvatermők domináltak a nyitvatermőkkel szemben. Mindazonáltal a vizsgált rétegsorban a nyitvatermők (pl. Cupressaceae) fokozatosan növekvő hozzájárulása figyelhető meg, az a normál rétegződést feltételezve a fiatalabb üledékek szervesanyagában dúsul. A leülepedett szervesanyagot je-lentősen átdolgozta a mikrobiális tevékenység. A sűrű, virágzó növényzet CO_2-korlátozott környezetet hozott létre, amely a vízi növényeket a HCO_3^- felhasználására késztette azok fotoszintézis során.

A vitrinit reflexió, Tmax és biomarker indexek azt jelzik, hogy a Kosdi Formáció szervesanyaga (a W–1 mélyfúrásban) termikusan érett, a vizsgált területen a szenes összlet elérte a nagy illékonyságú bitumenes kőszén állapotot. Ez magasabb, mint az Észak-magyarországi-középhegység sekély Kosdi szénmezőjében feltárt szubbitumenes kőszén esetében. Ez az előrehaladott termikus érettség befolyásolta a szénhidrogének molekuláris és stabil izotópos összetételét. A Rock-Eval pirolízis eredményei azt mutatják, hogy a vizsgált kőszénminták gáz-és-olaj-generálására alkalmasak, és elérték az első gázképződés és az olajkiszorítás kezdetének érettségi küszöbét.

Az Észak-magyarországi Paleogén-medence hipotetikus szénhidrogén rendszerének modelljét a kutatási eredményeim pontosítják. A magas szervesanyag tartalmú finomtörmelékes kőzetek és a termelt kőolaj részletes szerves geokémiai vizsgálata alapján a Kosdi, Budai Márga és Tard Agyag formációk szervesanyagban gazdag üledékei tekinthetők anyakőzetnek. Ezzel szemben a Kiscelli Agyag Formáció kőzeteit nem lehet anyakőzetként értelmezni. A képződmények térbeli eloszlása és azok Rock-Eval jellemzői változatos szénhidrogén-generáló potenciálra utalnak a vizsgált területen.

A kőolajminták molekuláris összetétele alapján azok eredeti szervesanyaga tengeri és/vagy brakkvízi környezetben leülepedett agyagos kőzetben halmozódott fel. A sótartalom különbség miatt kialakult vízrétegződés valószínűsíthető, ami oxigénhiányos állapot kialakulását eredményezte. A szervesanyagot a vízi biomassza uralta, beleértve az algákat, dinoflagellátokat és kemoautotróf baktériumokat. Kisebb mennyiségű, zárvatermő domináns magasabb rendű növényi szervesanyag a partvonal felől került a medencébe.

A felhalmozódott kőolajok, azok biomarker összetételük alapján a Tardi Agyag Formáció képződményeivel mutanak rokonságot. Az őskörnyezet rekonstrukció során feltárt enyhébb eltérések a forráskőzet litofáciesének vertikális és horizontális változékonyságára mutatnak rá. Amennyiben figyelembe vesszük a vizsgált kőzetek termikus érettségét és a nanoplankton, NP21 és NP23 zónában felhalmozódott üledékek komponens-specifikus (*n*-alkán) szénizotópos összetételre jellemző V-alakú mintázatot, akkor feltételezhető, hogy a Budai Márga Formáció üledékei is hozzájárulhattak a felhalmozódott szénhidrogénekhez. Ezért a Budai Márga Formáció részletes szerves geokémiai vizsgálata kifejezetten ajánlott ezen megfigyelések jelentőségének feltárása érdekében.

Az Észak-magyarországi Paleogén-medence területén található kevert sziliciklasztos és karbonátos kőzetek tárolóképességét meghatározó diagenetikus folyamatok vizsgálata alapján a kőzetegyüttes felhalmozódási környezete alapvetően meghatározza az eogenetikus folyamatokat. A homokos és karbonátos self biztosította a szükséges környezeti feltételeket a bakteriális szulfátredukcióhoz. A kiterjedt koradiagenetikus kalcitcementáció és a neomorfizmus a kőzetegyüttes tározó képességének csökkenéséhez és laterális homogenitásának kialakulásához vezetett. A sekélybetemetődés során a tengerszint kisvízállása mellett az összleten keresztül migráló csapadékvíz a szemcsénbelüli és szemcseközi porozitás kialakításával javította annak tároló kapacitását, és jelentős vertikális heterogenitást eredményezett. A kaolinitképződés és a betemetődéshez kapcsolódó kaolinit-dickit átalakulás egyrészt növelte a másodlagos porozitást, a vázépítő földpát és agyag intraklasztok oldódása révén, másrészt

részben csökkentette a kőzet permeabilitását, mivel a kaolinit eltömítette a pórustér egy részét. A kémialag instabil vázépítőszemcsék átalakulása mellett a növekvő betemetődési mélységgel bekövetkezett kémiai kompakció elegendő kova forrást biztosított a kvarccementációhoz. A földpát szemcsék kora- és sekélydiagenetikus átalakulása a késődiagenetikus illitképződést korlátozata. A medenceléptékben megjelenő finomtörmelékes kőzetek szmektit tartalmának fokozatos átalakulása – kevert szerkezetű illit/szmektit ásványokon kersztül – illitté jelentős mennyiségű kationt, Mg^{2+} és Fe^{2+} biztosított a dolomitképződéshez. A dolomit helyettesítés lokálisan növelte, míg a szénhidrogén migrációt követő késő diagenetikus piritképződés rontotta a kőzetek porozitását. A vizsgált terület horizontális és vertikális fluidumáramlási tulajdonságait a törésrendszer kialakulása és annak fejlődése fokozta, míg a törések cementációja – vastartalmú kalcittal – csökkentette azt. Ezen diagenetikus események együttesen eredményezték azt a tározó heterogenitást, amely az Észak-magyarországi Paleogén-medence eocén korú kevert sziliciklasztos és karbonátos összletét jellemzi.

Acknowledgements

First and foremost I am extremely grateful to my supervisor Dr. ***Félix Schubert*** for his continuous support. The time we spent discussing research topics was invaluable and granted me progression as an early researcher. I would also like to express my sincere gratitude to Prof. Dr. ***Reinhard Sachsenhofer*** for providing me with the opportunity to perform part of my doctoral study in the Chair of Petroleum Geology, Montanuniverstät Leoben, Austria. Their immense knowledge and plentiful experience have encouraged me all the time during my academic research and daily life.

I would like to say special thanks to Dr. ***Achim Bechtel***, Dr. ***Andrea Varga***, Dr. ***Béla Raucsik***, Dr. ***Georgina Lukoczki***, dr. ***Katalin Milota*** and ***Balázs Géza Radovics*** for their suggestions and guidance during our joint research. Our collaboration has led to my Ph.D. dissertation.

I would like to offer my thanks to Prof. Dr. ***Tivadar M.Tóth***, head of the Doctoral School of Geosciences, University of Szeged, Hungary for the opportunity to undertake my studies at the Department of Mineralogy, Geochemistry and Petrology, University of Szeged, Hungary.

All members of the ***Chair of Petroleum Geology, Montanuniversität Leoben*** (head of the department is Prof. Dr. Reinhard Sachsenhofer) and the ***Department of Mineralogy, Geochemistry and Petrology*****, University of Szeged** (head of the department is Prof. Dr. Tivadar M.Tóth) deserve my special thanks. Besides the above-mentioned colleagues, Prof. Dr. ***Doris Groß***, Dr. ***Magdalena Pup***, ***Stephen Ajuaba*** and ***Nobis Günter*** should be mentioned namely for their assistance.

I gratefully acknowledge MOL Plc. for granting the availability of samples analysed and permission for submitting the original manuscripts. My doctoral study was supported by the Ernst Mach scholarship, Stiftung Aktion Österreich-Ungarn (ICM-2018-12611) and Campus Mundi scholarship, Tempus Public Foundation (CM-SMR-421662-2020). This work was sponsored by the National Research, Development and Innovation Fund, Cooperative Doctoral Programme (975153), New National Excellence Program (UNKP-21-4-SZTE-491) and Hungarian Scientific Research Fund (K-138919) Ministry for Innovation and Technology, Hungary. The University of Szeged Open Access Fund (4665; 5057 and 5860) financed the publications.

Last but not least, I owe my wife, ***Nikoletta Papp*** a warm thanks for her patience and support, which I needed during my doctoral research.

References

van Aarssen, B.G.K., Hessels, J.K.C., Abbink, O.A., de Leeuw, J.W., 1992. The occurrence of polycyclic sesqui-, tri-, and oligoterpenoids derived from a resinous polymeric cadinene in crude oils from southeast Asia. Geochim. Cosmochim. Acta 56, 1231–1246. https://doi:10.1016/0016-7037(92)90059-r.

Aichner, B., Herzschuh, U., Wilkes, H., 2010. Influence of aquatic macrophytes on the stable carbon isotopic signatures of sedimentary organic matter in lakes on the Tibetan Plateau. Org. Geochem. 41, 706–718. https://doi.org/10.1016/j.orggeochem.2010.02.002.

Alexander, G., Hazai, I., Grimalt, J., Albaigés, J., 1987. Occurrence and transformation of phyllocladanes in brown coals from Nograd Basin, Hungary. Geochim. Cosmochim. Acta 51, 2065–2073. https://doi:10.1016/0016-7037(87)90256-0.

Alexander, R., Bastow, T.P., Fisher, S.J., Kagi, R.I., 1995. Geosynthesis of organic compounds: II. Methylation of phenanthrene and alkylphenanthrenes. Geochim. Cosmochim. Acta 59, 4259–4266. https://doi:10.1016/0016-7037(95)00285-8.

Alexander, R., Kagi, R., Noble, R., 1983. Identification of the bicyclic sesquiterpenes drimane and eudesmane in petroleum. J. Chem. Soc., Chem. Commun. 5, 226–228. https://doi:10.1039/c39830000226.

Alexander, R., Kagi, R. I., Noble, R., Volkman, J. K., 1984. Identification of some bicyclic alkanes in petroleum. Org. Geochem. 6, 63–72. https://doi:10.1016/0146-6380(84)90027-5.

Aquino Neto, F.R., Trendel, J.M., Restlé, A., Connan, J., Albrecht, P., 1983. Occurrence and formation of tricyclic terpanes in sediments and petroleums. in: Bjorøy, M., Albrecht, P., Cornford, C., de Groot, K., Eglinton, G., Galimov, E., Leythaeuser, D., Pelet, R., Rullkötter, J., Speers, G. (Eds.), Advances in Organic Geochemistry 1981. Wiley, Chichester, pp. 659–667.

ASTM International, 2015. ASTM D2797/D2797M-11a: Standard practice for preparing coal samples for microscopical analysis by reflected light. ASTM International, West Conshohocken, Pennsylvania, 5 p. https://doi.org/10.1520/d2797_d2797m-11a.

ASTM International, 2018. ASTM D3174-12: Standard test method for ash in the analysis smple of coal and coke from coal. ASTM International, West Conshohocken, Pennsylvania, 6 p. https://doi.org/10.1520/d3174-12r18.

Badics, B., Vető, I., 2012. Source rocks and petroleum systems in the Hungarian part of the Pannonian Basin: The potential for shale gas and shale oil plays. Mar. Petrol. Geol. 31, 53–69. https://doi:10.1016/j.marpetgeo.2011.08.015.

Báldi, T., 1984. The terminal Eocene and Early Oligocene events in Hungary and the separation of an anoxic, cold Paratethys. Eclogae Geol. Helv. 77, 1–27.

Báldi, T., Báldi-Beke, M., 1985. The evolution of the Hungarian Paleogene Basins. Acta Geol. Hung. 28, 5–28.

Báldi-Beke, M., 2003a. A dunántúli eocén kőszénösszletek fedőképződményeinek rétegtana és paleoökológiája nannoplankton alapján (Stratigraphy and palaeoecology of the formations overlying the Middle Eocene coal sequence based on nannofossils - (Transdanubia, Hungary)). Bull. Hu. Geol. Soc. 133, 325–343. (in Hungarian with English abstract)

Báldi-Beke, M. 2003b. A magyarországi eocén transzgressziók ideje: a nannoplankton biosztratigráfiai és magnetosztratígráfiai eredmények együttes értékelése (Time of the Eocene

transgressions in Hungary: evaluation of the nannoplankton biostratigraphy and magnetostratigraphy). Bull. Hu. Geol. Soc. 133, 437–440. (in Hungarian with English abstract)

Baker, P.A., Kastner, M., 1981. Constraints on the Formation of Sedimentary Dolomite. Science, 213, 214–216. https://doi.10.1126/science.213.4504.214.

Bakker, R.J., 2003. Package FLUIDS 1. Computer programs for analysis of fluid inclusion data and for modelling bulk fluid properties. Chem. Geol. 194, 3–23. https://doi.10.1016/s0009-2541(02)00268-1.

Barclay, S.A., Worden, R.H., 2000. Geochemical modelling of diagenetic reactions in a subarkosic sandstone. Clay Min., 35, 57–67. https://doi.10.1180/000985500546729.

Bauer, M., M.Tóth, T., Raucsik, B., Garaguly, I., 2016. Petrology and paleokarst features of the Gomba hydrocarbon reservoir (central Hungary). Centr. Eur. Geol. 59, 28–59. https://doi.org/10.1556/24.59.2016.003.

Bechtel, A., Gratzer, R., Linzer, H.-G., Sachsenhofer, R.F., 2013 Influence of migration distance, maturity and facies on the stable isotopic composition of alkanes and on carbazole distributions in oils and source rocks of the Alpine Foreland Basin of Austria. Org. Geochem. 62, 74–85.

Bechtel, A., Gratzer, R., Sachsenhofer, R.F., Gusterhuber, J., Lücke, A., Püttmann, W., 2008. Biomarker and carbon isotope variation in coal and fossil wood of Central Europe through the Cenozoic. Palaeogeogr. Palaeoclimatol. Palaeoecol. 262, 166–175. https://doi:10.1016/j.palaeo.2008.03.005.

Bechtel, A., Hámor-Vidó, M., Gratzer, R., Sachsenhofer, R.F., Püttmann, W., 2012. Facies evolution and stratigraphic correlation in the early Oligocene Tard Clay of Hungary as revealed by maceral, biomarker and stable isotope composition. Mar. Pet. Geol. 35, 55–74. https://doi.10.1016/j.marpetgeo.2012.02.017.

Bechtel, A., Hámor-Vidó, M., Sachsenhofer, R.F., Reischenbacher, D., Gratzer, R., Püttman, W., 2007. The middle Eocene Márkushegy subbituminous coal (Hungary): Paleoenvironmental implications from petrographical and geochemical studies. Int. J. Coal Geol. 72, 33–52. https://doi.org/10.1016/j.coal.2006.12.008.

Bechtel, A., Hámor-Vidó, M., Gratzer, R., Sachsenhofer, R.F., Püttmann, W., 2012. Facies evolution and stratigraphic correlation in the early Oligocene Tard Clay of Hungary as revealed by maceral, biomarker and stable isotope composition. Mar. Pet. Geol. 35, 55–74. https://doi:10.1016/j.marpetgeo.2012.02.017.

Bechtel, A., Sachsenhofer, R.F., Markic, M., Gratzer, R., Lücke, A., Püttmann, W., 2003. Paleoenvironmental implications from biomarker and stable isotope investigations on the Pliocene Velenje lignite seam (Slovenia). Org. Geochem. 34, 1277–1298. https://doi.org/10.1016/s0146-6380(03)00114-1.

Behar, F., Beaumont, V., De B. Penteado, H.L., 2001. Rock-Eval 6 Technology: Performances and Developments. Oil Gas Sci. Technol. 56, 111–134. https://doi.10.2516/ogst:2001013.

Beke, B., Szőcs, E., Hips, K., Schubert, F., Petrik, A., Milovský, R., Fodor, L., 2021. Evolution of deformation mechanism and fluid flow in two pre-rift siliciclastic deposits (Pannonian Basin, Hungary). Glob. Planet. Change 199, 103434. https://doi.org/10.1016/j.gloplacha.2021.103434.

Berner, R.A., 1982. Burial of organic carbon and pyrite sulfur in the modern ocean: its geochemical and environmental significance. Am. J. Sci. 282, 451–473. https://doi.org/10.2475/ajs.282.4.451.

Berner, R.A., 1984. Sedimentary pyrite formation: an update. Geochim. Cosmochim. Acta 48, 605–615. https://doi.org/10.1016/0016-7037(84)90089-9.

Bertrand, P., Pittion, J.-L., Bernaud, C., 1986. Fluorescence of sedimentary organic matter in relation to its chemical composition. Org. Geochem. 10, 641–647. https://doi.10.1016/0146-6380(86)90061-6.

Bingham, E.M., McClymont, E.L., Väliranta, M., Mauquoy, D., Roberts, Z., Chambers, F.M., Evershed, R. P., 2010. Conservative composition of n-alkane biomarkers in Sphagnum species: Implications for palaeoclimate reconstruction in ombrotrophic peat bogs. Org. Geochem. 41, 214–220. https://doi:10.1016/j.orggeochem.2009.06.010.

Bjorøy, M., Hall, K., Gillyon, P., Jumeau, J., 1991. Carbon isotope variations in n-alkanes and isoprenoids of whole oils. Chem. Geol. 93, 13–20. https://doi:10.1016/0009-2541(91)90061-u.

Bjorøy, M., Hall, P.B., Hustad, E., Williams, J.A. 1992. Variation in stable carbon isotope ratios of individual hydrocarbons as a function of artificial maturity. Org. Geochem. 19, 89–105. https://doi:10.1016/0146-6380(92)90029-w.

Bjorøy, M., Hall, P.B., Moe, R.P., 1994. Stable carbon isotope variation of *n*-alkanes in Central Graben oils. Org. Geochem. 22, 355–381. https://doi:10.1016/0146-6380(94)90114-7.

Blair, N., Leu, A., Muñoz, E., Olsen, J., Kwong, E., Des Marais, D., 1985. Carbon isotopic fractionation in heterotrophic microbial metabolism. Appl. Environ. Microbiol. 50, 996–1001. https://doi.10.1128/aem.50.4.996-1001.1985.

Blumer, M., Mullin, M.M., Thomas, D.W., 1963. Pristane in zooplankton. Science 140, 974. https://doi.org/10.1126/science.140.3570.974.

Bodnar, R.J., 1993. Revised equation and table for determining the freezing point depression of H2O-NaCl solutions. Geochem. Cosmochim. Acta 57, 683–684. https://doi.org/10.1016/0016-7037(93)90378-a.

Boles, J.R., Franks. S.G., 1979. Clay diagenesis in Wilcox sandstones of southwest Texas: implications of smectite diagenesis on sandstone cementation. J. Sediment. Petrol. 49, 55–70. https://doi.10.1306/212f76bc-2b24-11d7-8648000102c1865d.

Boncz, L. (Ed.), 2004. Final report of the hydrocarbon exploration activities in the area of 103. Gödöllő vol. I–II. MOL Plc., Szolnok. MGSH Geological Data Store, T.21172, Budapest. (in Hungarian)

Boncz, L. (Ed.), 2013. Final report of the hydrocarbon exploration activities in the area of 138. Monor vol. I–II. MOL Plc., Szolnok. MGSH Geological Data Store, T.22781, Budapest. (in Hungarian)

Bordenave, M.L., Espitalié, J., Leplat, P., Oudin, J.L., Vandenbroucke, M., 1993. Screening techniques for source rock evaluation. in: Bordenave, M.L. (Ed.), Applied petroleum geochemistry, Éditions Technip, Paris, pp. 217–278.

Bourdet, J., Burruss, R.C., Chou, I.M., Kempton, R., Liu, K., Hung, N.V., 2014. Evidence for a palaeo-oil column and alteration of residual oil in a gas-condensate field: Integrated oil inclusion and experimental results. Geochim. Cosmochim. Acta 142, 362–385. ttps://doi.org/10.1016/j.gca.2014.07.022.

Bray, E.E., Evans, E.D., 1961. Distribution of n-paraffins as a clue to recognition of source beds. Geochim. Cosmochim. Acta 22, 2–15. https://doi.org/10.1016/0016-7037(61)90069-2.

Brukner-Wein, A., Hetényi, M., Vető, I., 1990. Organic geochemistry of an anoxic cycle: a case history from the Oligocene section, Hungary. Org. Geochem. 15, 123–130. https://doi.org/10.1016/0146-6380(90)90077-d.

Burley, S.D., Worden, R.H., 2003. Sandstone diagenesis: recent and ancient, first ed. Blackwell Publishing, Malden, Oxford, Melbourne, Berlin.

Calder, J.H., Gibling, M.R., Mukhopadhyay, P.K, 1991. Peat formation in a Westphalian B piedmont setting, Cumberland basin, Nova Scotia: implications for the maceral-based interpretation of rheotropic and raised paleomires. B. Soc. Geol. Fr. 162, 283–298.

Carr, A.D., 2000. Suppression and retardation of vitrinite reflectance: Part 1. Formation and significance for hydrocarbon generation. J. Petrol. Geol. 23, 313–343. https://doi.org/10.1111/j.1747-5457.2000.tb01022.x.

Casagrande, D.J., 1987. Sulphur in peat and coal, in: Scott, A.C. (Ed.), Coal and coal-bearing strata: recent advances. Geol. Soc., London, Special Publications 32, pp. 87–105. https://doi.10.1144/gsl.sp.1987.032.01.07.

Cheng, P., Xiao, X.M., Gai, H.F., Li, T.F., Zhang, Y.Z., Huang, B.J., Wilkins, R.W.T., 2015. Characteristics and origin of carbon isotopes of *n*-alkanes in crude oils from the western Pearl River Mouth Basin, South China sea. Ma. Pet. Geol. 67, 217–229. https://doi.10.1016/j.marpetgeo.2015.05.028.

Chiarella, D., Longhitano, S.G., Tropeano, M., 2017. Types of mixing and heterogeneities in siliciclastic-carbonate sediments. Mar. Pet. Geol. 88, 617–627. https://doi.org/10.1016/j.marpetgeo.2017.09.010.

Clayton, C.J., 1991. Effect of maturity on carbon isotope ratios of oils and condensates. Org. Geochem. 17, 887–899. https://doi:10.1016/0146-6380(91)90030-n.

Cloern, J.E., Canuel, E.A., Harris, D., 2002. Stable carbon and nitrogen isotope composition of aquatic and terrestrial plants of the poppe

San Francisco Bay estuarine system. Limnol. Oceanogr. 47, 713–729. https://doi.10.4319/lo.2002.47.3.0713

Close, H.G., 2019. Compound-specific isotope geochemistry in the ocean. Annu. Rev. Mar. Sci. 11, 27–56. https://doi:10.1146/annurev-marine-121916-063634.

Collister, J.W., Lichtfouse, E., Hieshima, G., Hayes, J.M., 1994. Partial resolution of sources of n-alkanes in the saline portion of the Parachute Creek Member, Green River Formation (Piceance Creek Basin, Colorado). Org. Geochem. 21, 645–659. https://doi:10.1016/0146-6380(94)90010-8.

Collister, J.W., Summons, R.E., Lichtfouse, E., Hayes, J.M., 1992. An isotopic biogeochemical study of the Green River oil shale. Org. Geochem. 19, 265–276. https://doi:10.1016/0146-6380(92)90042-v.

Connan, J., Cassou, A.M., 1980. Properties of gases and petroleum liquids derived from terrestrial kerogen at various maturation levels. Geochim. Cosmochim. Acta 44, 1–23. https://doi:10.1016/0016-7037(80)90173-8.

Coplen, T.B., 2011. Guidelines and recommended terms for expression of stable-isotope-ratio and gas-ratio measurement results. Rapid Commun. Mass Sp. 25, 2538–2560. https://doi.org/10.1002/rcm.5129.

Cortes, J.E., Rincon, J.M., Jaramillo, J.M., Philp, R.P., Allen, J., 2010. Biomarkers and compound-specific stable carbon isotope of n-alkanes in crude oils from Eastern Llanos Basin, Colombia. J. S. Am. Earth Sci. 29, 198–213. https://doi:10.1016/j.jsames.2009.03.010.

Cranwell, P.A., 1977. Organic Geochemistry of Cam Loch (Sutherland) sediments. Chem. Geol. 20, 205–221. https://doi.org/10.1016/0009-2541(77)90044-4.

Cranwell, P.A., Eglinton, G., Robinson, N., 1987. Lipids of aquatic organisms as potential contributors to lacustrine sediments—II. Org. Geochem. 11, 513–527. https://doi.org/10.1016/0146-6380(87)90007-6.

Dehmer, J., 1995. Petrological and organic geochemical investigation of recent peats with known environments of deposition. Int. J. Coal Geol. 28, 111–138. https://doi:10.1016/0166-5162(95)00016-x.

Diamond, L.W., 2003. Glossary: Terms and symbols used in fluid inclusion studies, in: Samson, I., Anderson, A., Marshall, D. (Eds.), Fluid inclusions: Analysis and Interpretation. Mineral. Assoc. Can., Québec, pp. 365–374.

Dickson, J.A.D., 1965. A modified staining technique for carbonates in thin section. Nature, 205, 587–587. https://doi:10.1038/205587a0.

Didyk, B.M., Simoneit, B.R.T., Brassell, S.C., Eglinton, G., 1978. Organic geochemical indicators of palaeoenvironmental conditions of sedimentation. Nature 272, 216–222. https://doi.org/10.1038/272216a0.

Diefendorf, A.F., Freeman, K.H., Wing, S.L., Graham, H.V., 2011. Production of n-alkyl lipids in living plants and implications for the geologic past. Geochim. Cosmochim. Acta 75, 7472–7485. https://doi:10.1016/j.gca.2011.09.028.

Diefendorf, A.F., Freimuth, E.J., 2017. Extracting the most from terrestrial plant-derived n-alkyl lipids and their carbon isotopes from the sedimentary record: A review. Org. Geochem. 103, 1–21. https://doi:10.1016/j.orggeochem.2016.10.016.

Diefendorf, A.F., Sberna, D.T., Taylor, D.W., 2015. Effect of thermal maturation on plant-derived terpenoids and leaf wax n-alkyl components. Org. Geochem. 89–90, 61–70. https://doi:10.1016/j.orggeochem.2015.10.006.

Diessel, C.F.K., 1992. Coal-bearing depositional systems. Springer-Verlag, Berlin.

Doković, N., Mitrović, D., Životić, D., Bechtel, A., Sachsenhofer, R.F., Matić, V., Glamočanin, L., Stojanović, K., 2018. Petrographical and organic geochemical study of the lignite from the Smederevsko Pomoravlje field (Kostolac Basin, Serbia). Int. J. Coal Geol. 195, 139–171. https://doi.org/10.1016/j.coal.2018.06.005.

Dolton, G.L., 2006. Pannonian Basin Province, Central Europe (Province 4808)—Petroleum geology, total petroleum systems, and petroleum resource assessment. U.S. Geological Survey Bulletin 2204–B. https://doi.org/10.3133/b2204b.

Dott, R.H., 1964. Wacke, graywacke and matrix - what approach to immature sandstone classification. J. Sediment. Petrol. 34, 625–632. https://doi.org/10.1306/74d71109-2b21-11d7-8648000102c1865d.

Du, X., Ye, M., Xie, X., Zhao, K., Jia, J., Du, X., 2022. Why is it easy to form high-quality reservoirs in a mixed siliciclastic-carbonate system? Evidence from diagenetic characteristics. J. Pet. Sci. Eng. 212, 110339. https://doi.org/10.1016/j.petrol.2022.110339.

Dzou, L.I.P., Hughes, W.B., 1993. Geochemistry of oils and condensates, K field, offshore Taiwan: a case study in migration fractionation. Org. Geochem. 20, 437–462. https://doi.org/10.1016/0146-6380(93)90092-p.

Eble, C.F., Greb, S.F., Williams, D.A, Hower, J.C, O'Keefe, J.M.K., 2019. Palynology, organic petrology and geochemistry of the Bell coal bed in Western Kentucky, Eastern Interior (Illinois) Basin, USA. Int. J. Coal Geol. 213, 103264. https://doi.org/10.1016/j.coal.2019.103264.

Eglinton, G., Hamilton, R.J., 1967. Leaf epicuticular waxes. Science 156, 1322–1335. https://doi.org/10.1126/science.156.3780.1322.

Ehrenberg, S.N., Aagaard, P., Wilson, M.J., Fraser, A.R., Duthie, D.M.L., 1993. Depth-dependent transformation of kaolinite to dickite in sandstones of the Norwegian continental chelf. Clay Miner. 28, 325–352. https://doi:10.1180/claymin.1993.028.3.01.

Ekweozor, C.M., Okogun, J.I., Ekong, D.E.U., Maxwell, J.R., 1979. Preliminary organic geochemical studies of samples from the Niger delta (Nigeria) I. Analyses of crude oils for triterpanes. Chem. Geol. 27, 11–28. https://doi:10.1016/0009-2541(79)90100-1.

Ekweozor, C., Strausz, O., 1983. Tricyclic terpanes in the Athabasca oil sands: their geochemistry. In: Bjorøy, M., Albrecht, P., Cornford, C., de Groot, K., Eglinton, G., Galimov, E., Leythaeuser, D., Pelet, R., Rullkötter, J., Speers, G. (Eds.), Advances in Organic Geochemistry 1981. Wiley, Chichester, pp. 746–766.

Ensminger, A., Joly, G., Albrecht, P., 1978. Rearranged steranes in sediments and crude oils. Tetrahedron Lett. 19, 1575–1578. https://doi.10.1016/s0040-4039(01)94608-8.

Espitalié, J., LaPorte, J.L., Madec, M., Marquis, F., Leplat, P., Paulet, J., Boutefeu, A., 1977. Méthode rapide de charactérisation des roches metres, de leur potential pétrolier et de leur degé d'évolution. Revue de l'Institut Français du Pétrole 32, 23–42. https://doi.org/10.2516/ogst:1977002.

Espitalié, J., Marquis, F., Barsony, I., 1984. Geochemical logging, in: Voorhees, K.J. (ed.), Analytical pyrolysis techniques and applications, Butterworths, London, pp. 276–304.

Fall, A., Tattitch, B., Bodnar, R.J., 2011. Combined microthermometric and Raman spectroscopic technique to determine the salinity of H2O–CO2–NaCl fluid inclusions based on clathrate melting. Geochim. Cosmochim. Acta, 75. 951–964. https://doi.10.1016/j.gca.2010.11.021.

Feng, J., Cao, J., Hu, K., Peng, X., Chen, Y., Wang, Y., Wang, M., 2013. Dissolution and its impacts on reservoir formation in moderately to deeply buried strata of mixed siliciclastic–carbonate sediments, northwestern Qaidam Basin, northwest China. Mar. Pet. Geol. 39, 124–137. https://doi.10.1016/j.marpetgeo.2012.09.002.

Ficken, K.J., Barber, K.E., Eglinton, G. 1998a. Lipid biomarker, δ13C and plant macrofossil stratigraphy of a Scottish montane peat bog over the last two millennia. Org. Geochem. 28, 217–237. https://doi:10.1016/s0146-6380(97)00126-5.

Ficken, K.J., Li, B., Swain, D.L., Eglinton, G., 2000. An n-alkane proxy for the sedimentary input of submerged/floating freshwater aquatic macrophytes. Org. Geochem. 31, 745–749. https://doi.org/10.1016/s0146-6380(00)00081-4.

Ficken, K.J., Street-Perrott, F.A., Perrott, R.A., Swain, D.L., Olago, D.O., Eglinton, G., 1998b. Glacial/interglacial variations in carbon cycling revealed by molecular and isotope stratigraphy of Lake Nkunga, Mt. Kenya, East Africa. Org. Geochem. 29, 1701–1719. https://doi.10.1016/s0146-6380(98)00109-0.

Flügel, E., 2004. Microfacies of carbonate rocks: analysis, interpretation and application, first ed. Springer-Verlag, Berlin, Heidelberg.

Freeman, K.H., Hayes, J.M., Trendel, J.M., Albrecht, P., 1990. Evidence from carbon isotope measurements for diverse origins of sedimentary hydrocarbons. Nature 343, 254–256. https://doi:10.1038/343254a0.

Fodor, L., Magyari, Á., Fogarasi, A., Palotás, K., 1994. Tertiary tectonics and Late Palaeogene sedimentation in the Buda Hills, Hungary. A new interpretation of the Buda Line. Bull. Hu. Geol. Soc. 124, 129–305. (in Hungarian with extended English summary)

Folk, R.L., 1951. A comparison chart for visual percentage estimation. J. Sediment Res. 21. 32–33. https://doi.org/10.1306/d4269413-2b26-11d7-8648000102c1865d.

Frezzotti, M.L., Tecce, F., Casagli, A., 2012. Raman spectroscopy for fluid inclusion analysis. J. Geochem. Explor. 112, 1–20. https://doi.org/10.1016/j.gexplo.2011.09.009.

George, S.C., Ruble, T.E., Dutkiewicz, A., Eadington, P.J., 2001. Assessing the maturity of oil trapped in fluid inclusions using molecular geochemistry data and visually-determined fluorescence colours. App. Geochem. 16, 451–473. https://doi.org/10.1016/S0883-2927(00)00051-2.

Gidai, L., 1978. A kósdi eocén képződmények rétegtani viszonyai (Conditions stratigraphiques des formations éocènes de Kósd). Bull. Hu. Geol. Soc. 108, 65–86. (in Hungarian with extended French summary)

Goldstein, R.H., Reynolds, T.J., 1994. Systematics of fluid inclusions in diagenetic minerals. Soc. Sediment. Geol., Tulsa. https://doi.org/10.2110/scn.94.31.

Gong, Y.-M., Shi, G.R., Weldon, E.A., Du, Y.-S., Xu, R., 2005. Pyrite framboids interpreted as microbial colonies within the Permian Zoophycos spreiten from southeastern Australia. Geol. Mag. 145, 95–103. https://doi.org/10.1017/s0016756807003974.

Goossens, H., de Leeuw, J.W., Schenck, P.A., Brassell, S.C., 1984. Tocopherols as likely precursors of pristane in ancient sediments and crude oils. Nature 312, 440–442. https://doi.org/10.1038/312440a0.

Grantham, P.J., Wakefield L.L., 1988. Variations in the sterane carbon number distributions of marine source rock derived crude oils through geological time. Org. Geochem. 12, 61–73. https://doi.org/10.1016/0146-6380(88)90115-5.

Grice, K., de Mesmay, R., Glucina, A., Wang, S., 2008. An improved and rapid 5Å molecular sieve method for gas chromatography isotope ratio mass spectrometry of *n*-alkanes (C_{8}–C_{30+}). Organic Geochemistry 39, 284–288.

Gross, D., Bechtel, A., Harrington, G.J., 2015. Variability in coal facies as reflected by organic petrological and geochemical data in Cenozoic coal beds offshore Shimokita (Japan) - IODP Exp. 337. Int. J. Coal Geol. 152, 63–79. https://doi:10.1016/j.coal.2015.10.007.

Haas, J., Kovács, S., 2012. Pelso composite unit, in: Haas, J. (Ed.), Geology of Hungary. Springer-Verlag, Berlin, pp. 21–81.

Hámor T., 1994. The occurrence and morphology of sedimentary pyrite. Acta Geol. Hung. 37, 153–181.

Hámor-Vidó, M., Hámor T., 2007. Sulphur and carbon isotopic composition of power supply coals in the Pannonian Basin, Hungary. Int. J. Coal Geol. 71, 425–227. https://doi.org/10.1016/j.coal.2006.11.002.

Han, Y., Noah, M., Lüders, V., Körmös, S., Schubert, F., Poetz, S., Horsfield, B., Mangelsdorf, K., 2022. Fractionation of hydrocarbons and NSO-compounds during primary oil migration revealed by high resolution mass spectrometry: insights from oil trapped in fluid inclusions, Int. J. Coal Geol. 254, 103974. https://doi.org/10.1016/j.coal.2022.103974.

Harrel. J., 1984. A visual comparator for degree of sorting in thin and plane sections. J. Sediment. Res. 54. 646–650. https://doi.org/10.2110/jsr.54.646.

Havelcová, M., Sýkorová, I., Trejtnarová, H., Šulc, A., 2012. Identification of organic matter in lignite samples from basins in the Czech Republic: Geochemical and petrographic properties in relation to lithotype. Fuel 99, 129–142. https://doi:10.1016/j.fuel.2012.03.025.

ten Haven, H.L., de Leeuw, J.W., Peakman, T.M., Maxwell, J.R., 1986. Anomalies in steroid and hopanoid maturity indices. Geochim. Cosmochim. Acta, 50, 853–855. https://doi:10.1016/0016-7037(86)90361-3.

ten Haven, H.L., de Leeuw, J.W., Rullkötter, J., Sinninghe Damsté, J.S., 1987. Restricted utility of the pristane/phytane ratio as a palaeoenvironmental indicator. Nature 330, 641–643. https://doi.org/10.1038/330641a0.

Hayes, J.M., 1993. Factors controlling 13C contents of sedimentary organic compounds: principles and evidence. Mar. Geol. 133, 111–126. https://doi.org/10.1016/0025-3227(93)90153-m.

Hayes, J.M., Freeman, K.H., Popp, B.N., Hoham, C.H., 1990. Compound-specific isotopic analyses: A novel tool for reconstruction of ancient biogeochemical processes. Org. Geochem. 16, 1115–1128. https://doi:10.1016/0146-6380(90)90147-r.

Hayes, J.M., Takigiku, R., Ocampo, R., Callot, H.J., Albrecht, P., 1987. Isotopic compositions and probable origins of organic molecules in the Eocene Messel shale. Nature 329, 48–51. https://doi:10.1038/329048a0.

Hertelendi, A., Vető, I., 1991. The marine photosynthetic carbon isotope fractionation remained constant during the Early Oligocene. Palaeogeogr. Palaeoclimatol. Palaeoecol. 83, 333–339. https://doi.org/10.1016/0031-0182(91)90059-z.

Holtvoeth, J., Whiteside, J.H., Engels, S., Freitas, F.S., Grice, K., Greenwood, P., Johnson, S., Kendall, I., Lengger, S.K., Lücke, A., Mayr, C., Naafs, B.D.A., Rohrssen, M., Sepúlveda, J., 2019. The paleolimnologist's guide to compound-specific stable isotope analysis – An introduction to principles and applications of CSIA for Quaternary lake sediments. Quaternary Sci. Rev. 207, 101–133. https://doi.org/10.1016/j.quascirev.2019.01.001.

Horváth, F., Bada, G., Windhoffer, G., Csontos, L., Dövény, P., Fodor, L., Grenerczy, G., Síkhegyi, F., Szafián, P., Székely, B., Tímár, G., Tóth, L., Tóth, T., 2005. Atlas of the present-day geodynamics of the Pannonian basin: Euroconform maps with explanatory text. http://geophysics.elte.hu/projektek/geodinamikai_atlasz_eng.htm (accessed on 5 August 2019).

Huang, W.Y., Meinshein, W.G., 1979. Sterols as ecological indicators. Geochim. Cosmochim. Acta 43, 739–745. https://doi.org/10.1016/0016-7037(79)90257-6.

Hughes, W.B., Holba, A.G., Dzou, L.I.P., 1995. The ratios of dibenzothiophene to phenanthrene and pristan to phytan as indicators of depositional environment and lithology of pe-

troleum source rocks. Geochim. Cosmochim. Acta 59, 3581–3598. https://doi.org/10.1016/0016-7037(95)00225-o.

Hussler, G., Connan, J., Albrecht, P., 1984. Novel families of tetra- and hexacyclic aromatic hopanoids predominant in carbonate rocks and crude oils. Org. Geochem. 6, 39–49. https://doi.org/10.1016/0146-6380(84)90025-1.

ICCP, 1998. The new vitrinite classification (ICCP System 1994). Fuel 77, 349–358. https://doi.org/10.1016/s0016-2361(98)80024-0.

ICCP, 2001. The new inertinite classification (ICCP System 1994). Fuel 80, 459–471. https://doi.org/10.1016/s0016-2361(00)00102-2.

Ingersoll, R.V., Bullard, T.F., Ford, R.L., Grimm, J.P., Pickle, J.D., Sares, S.W., 1984. The effect of grain size on detrital modes: a test of the Gazzi-Dickinson point-counting method. Int. J. Sediment Res. 54. 103–116. https://doi.org/10.1306/212f83b9-2b24-11d7-8648000102c1865d.

Jacob, J., Disnar, J.-R., Boussafir, M., Spadano Albuquerque, A.L., Sifeddine, A., Turcq, B., 2007. Contrasted distributions of triterpene derivatives in the sediments of Lake Caçó reflect paleoenvironmental changes during the last 20,000 yrs in NE Brazil. Org. Geochem. 38, 180–197. https://doi:10.1016/j.orggeochem.2006.10.007.

Jerram, D.A., 2001. Visual comparators for degree of grain-size sorting in two and three-dimensions. Comput. Geosci. 27. 485–492. https://doi.org/10.1016/s0098-3004(00)00077-7.

Karrer, W., Cherbuliez, E., Eugster, C.H., 1977. Konstitution und Vorkommen der organischen Pflanzenstoffe (exclusive Alkaloide) Ergänzungsband I. Birkhäuser Verlag, Basel und Stuttgart.

Kázmér, M., 1985. Microfacies pattern of the Upper Eocene limestones at Budapest, Hungary. Annales Universitatis Scientiarium Budapestinensis de Rolando Eötvös Nominatae Sectio Geologica 25, 139–152.

Kercsmár, Zs., Budai, T., Csillag, G., Selmeczi, I., Sztanó, O., 2015. Surface geology of Hungary. Explanatory notes to the Geological map of Hungary (1:500 000). Geological and Geophysical Institute of Hungary, Budapest.

Khalifa, M.A., Mansurbeg, H., Morad, D., Morad, S., Al-Aasm, I.S., Spirov, P., Ceriani, A., De Ros, L.F., 2017. Quartz and Fe-dolomite cements record shifts in formation-water chemistry and hydrocarbon migration in devonian shoreface sandstones, Ghadamis Basin, Libya. J. Sediment. Res. 88, 38–57. https://doi.10.2110/jsr.2017.66.

Khorasani, G.K., 1987. Novel development in fluorescence microscopy of complex organic mixtures: Application in petroleum geochemistry. Org. Geochem. 11, 157–168. https://doi.10.1016/0146-6380(87)90019-2.

Killops, S.D., Funnell, R.H., Suggate, R.P., Sykes, R., Peters, K.E., Walters, C., Woolhouse, A.D., Boudou, J.-P., 1998. Predicting generation and expulsion of paraffinic oil from vitrinite-rich coals. Org. Geochem. 29, 1–21. https://doi:10.1016/s0146-6380(98)00087-4.

Kiss, K. (Ed.), 1999. Final report of the hydrocarbon exploration activities in the area of 27. SW Hungarian Palaeogene Basin vol. I–II. MOL Plc., Szolnok. MGSH Geological Data Store, T.20132, Budapest. (in Hungarian)

Kokai, J., 1994. Exploration History and Future Possibilities in Hungary, in: Popescu, B.M. (Ed.), Hydrocarbons of Eastern Central Europe, Habitat, Exploration and Production History. Springer-Verlag, Berlin, pp. 147–173. https://doi:10.1007/978-3-642-77205-4_5.

Kováč, M., Plašienka, D., Soták, J., Vojtko, R., Oszczypko, N., Less, Gy., Ćosović, V., Fügenschuh, B., Králiková, S., 2016. Paleogene palaeogeography and basin evolution of the Western Carpathians, Northern Pannonian domain and adjoining areas. Global Planet. Change 140, 9–27. https://doi.org/10.1016/j.gloplacha.2016.03.007.

Kovács, Zs., Gyuricza, Gy., 2014. A complex research proposal for the Monor hydrocarbon concession area. Mining and Geological Survey of Hungary, Budapest (in Hungarian).

Kovács, S., Haas, J., 2010. Displaced South Alpine and Dinaridic elements in the mid-Hungarian zone. Cent. Eur. Geol. 53, 135–164. https://doi:10.1556/ceugeol.53.2010.2-3.3.

Körmös, S., Bechtel, A., Sachsenhofer, R.F., Radovics, B.G., Milota, K., Schubert, F., 2020. Petrographic and organic geochemical study of the Eocene Kosd Formation (northern Pannonian Basin): Implications for paleoenvironment and hydrocarbon source potential. Int. J. Coal Geol. 103555. https://doi:10.1016/j.coal.2020.103555.

Körmös, S., Sachsenhofer, R.F., Bechtel, A., Radovics, B.G., Milota, K., Schubert, F., 2021. Source rock potential, crude oil characteristics and oil-to-source rock correlation in a Central Paratethys sub-basin, the Hungarian Palaeogene Basin (Pannonian basin). Mar. Pet. Geol. 127. 104955. https://doi.10.1016/j.marpetgeo.2021.104955

Körmös, S., Steinbach, G., Schubert, F., 2019. Fluid inclusion chemostratigraphy on the Eocene Kosd Formation (Central Hungary), in: Pál-Molnár, E., Berkesi, M., Guzmics, T., Kiss, B.G., Cseresznyés, D., Spránitz, T., Gelencsér., O., Király. Cs., Liptai, N. (Eds.). European Current Research on Fluid Inclusions, A meeting dedicated to fluid and melt inclusions. Acta Mineralogica-Petrographica, pp. 66.

Kubacska, A., 1925. Daten zur Geologie der Umgebung des Nagyszál. Bull. Hung. Geol. Soc. 55, 327–332.

Kvaček, Z., 2010. Forest flora and vegetation of the European early Palaeogene – a review. Bull. Geosci. 85, 63–76. https://doi:10.3140/bull.geosci.1146.

Lafargue, E., Marquis, F., Pillot, D., 1998. Rock-Eval 6 applications in hydrocarbon exploration, production, and soil contamination studies. Revue de l'Institut Français du Pétrole 53, 421–437. https://doi.org/10.2516/ogst:1998036.

Laflamme, R.E., Hites, R.A., 1978. The global distribution of polycyclic aromatic hydrocarbons in recent sediments. Geochim. Cosmochim. Acta 42, 289–303. https://doi:10.1016/0016-7037(78)90182-5.

Lamb, A.L., Wilson, G.P., Leng, M.J., 2006. A review of coastal palaeoclimate and relative sea-level reconstructions using δ13C and C/N ratios in organic material. Earth-Sci. Rev. 75, 29–57. https://doi.org/10.1016/j.earscirev.2005.10.003.

Less, Gy., 2005. Palaeogene, in: Pelikán, P. (ed.), Geology of the Bükk mountains, Explanatory book of the geological map of the Bükk Mountains (1:50 000), Hungarian Geological Society, Budapest, pp. 204–210.

Li, R., Fan, J., Xue, J., Meyers, P.A., 2017. Effects of early diagenesis on molecular distributions and carbon isotopic compositions of leaf wax long chain biomarker n-alkanes: Comparison of two one-year-long burial experiments. Org. Geochem. 104, 8–18. https://doi:10.1016/j.orggeochem.2016.11.006.

Littke, R., Leythaeuser, D., Radke, M., Schaefer, R.G., 1990. Petroleum generation and migration in coal seams of the Carboniferous Ruhr Basin, northwest Germany. Org. Geochem. 16, 247–258. https://doi:10.1016/0146-6380(90)90045-2.

Lockheart, M.J., Van Bergen, P.F., Evershed, R.P., 1997. Variations in the stable carbon isotope compositions of individual lipids from the leaves of modern angiosperms: implications for the study of higher land plant-derived sedimentary organic matter. Org. Geochem. 26, 137–153. https://doi:10.1016/s0146-6380(96)00135-0.

Lucia, F.J., 2007. Carbonate reservoir characterisation, second ed. Springer, Berlin, Heidelberg, New York.

Mackenzie, A.S., 1984. Application of biological markers in petroleum geochemistry, in: Brooks, J., Welte, D.H. (Eds.), Advances in Petroleum Geochemistry. Academic Press, London, pp. 115–214. https://doi.org/10.1016/b978-0-12-032001-1.50008-0.

Mackenzie, A.S., Brassell, S.C., Eglinton, G., Maxwell, J.R., 1982. Chemical fossils: the geological fate of steroids. Science 217, 491–504. https://doi.org/10.1126/science.217.4559.491.

Mackenzie, A.S., Maxwell, J.R., 1981. Assessment of thermal maturation in sedimentary rocks by molecular measurements, in: Brooks, J. (Ed.), Organic maturation studies and fossil fuel exploration. Academic Press, London, pp. 239–254.

Mackenzie, A. S., Patience, R. L., Maxwell, J. R., Vandenbroucke, M., Durand, B., 1980. Molecular parameters of maturation in the Toarcian shales, Paris Basin, France–I. Changes in the configuration of acyclic isoprenoid alkanes, steranes, and triterpanes. Geochim. Cosmochim. Acta 44, 1709–1721. https://doi.org/10.1016/0016-7037(80)90222-7.

McKinley, J.M., Worden, R.H., Ruffell, A.H., Worden, R.H., Morad, S., 2003. Smectite in sandstones: a review of the controls on occurrence and behaviour during diagenesis, in: Worden, R.H., Morad, S. (Eds.), Clay mineral cements in sandstones, Blackwell Publishing Ltd. pp. 109–128. https://doi.10.1002/9781444304336.ch5.

Maclean, L.C.W., Tyliszczak, T., Gilbert, P.U.P.A., Zhou, D., Pray, T.J., Onstott, C., Southam, G., 2008. A high-resolution chemical and structural study of framboidal pyrite formed within a low-temperature bacterial biofilm. Geobiology 6, 471–480. https://doi.org/10.1111/j.1472-4669.2008.00174.x.

Mádl-Szőnyi, J., Czauner, B., Iván, V., Tóth, Á., Simon, S., Erőss, A., Bodor, P., Havril, T., Boncz, L., Sőreg, V., 2019. Confined carbonates – Regional scale hydraulic interaction or isolation? Mar. Pet. Geol. 107, 591–612. https://doi.10.1016/j.marpetgeo.2017.06.006.

Magoon, L.B., Dow, W.G., 1994. The petroleum system, in: Magoon, L.B., Dow, W.G. (Eds.), The petroleum system – from source to trap. AAPG Memoir 60., AAPG. Tulsa, Olahoma, USA, pp. 3–24. https://doi.org/10.1306/m60585c1.

Mansurbeg, H., Caja, M.A., Marfil, R., Morad, S., Remacha, E., Garcia, D., Martin-Crespo, T., El-Ghali, M.A.K., Nystuen, J.P., 2009. Diagenetic Eevolution and porosity destruction of turbiditic hybrid arenites and siliciclastic sandstones of foreland basins: Evidence from the Eocene Hecho Group, Pyrenees, Spain. J. Sediment. Res. 79, 711–735. https://doi.10.2110/jsr.2009.060.

Mansurberg, H., Morad, S., Al Suwaidi, M., Qurtas, S., Tveiten, O.G., Shahrokhizadeh, S., Harchegani, F.K., 2020. Meteoric-water incursion into marine turbiditic sandstones: Evidence from the Andrew Formation (Paleocene), UK Central Graben, North Sea. Mar. Pet. Geol. 118. 104428. https://doi.10.1016/j.marpetgeo.2020.104428.

Markič, M., Sachsenhofer, R.F., 1997. Petrographic composition and depositional environments of the Pliocene Velenje lignite seam (Slovenia). Int. J. Coal Geol. 33, 229–254. https://doi.org/10.1016/s0166-5162(96)00043-2.

Marynowski, L., Smolarek, J., Bechtel, A., Philippe, M., Kurkiewicz, S., Simoneit, B.R.T., 2013. Perylene as an indicator of conifer fossil wood degradation by wood-degrading fungi. Org. Geochem. 59, 143–151. https://doi.org/10.1016/j.orggeochem.2013.04.006.

Mayer, J., Sachsenhofer, R.F., Ungureanu, C., Bechtel, A., Gratzer, R., Sweda, M., Tari, G., 2018. Petroleum charge and migration in the Black Sea: Insights from oil and source rock geochemistry. J. Pet. Geol. 41, 337–350. https://doi.10.1111/jpg.12706.

Mazzullo, S.J., 1992. Geochemical and neomorphic alteration of dolomite: A review. Carbonates Evaporites 7, 21–37. https://doi.10.1007/bf03175390.

McKay, J.L., Longstaffe, F.J., Plint, A.G., 1995. Early diagenesis and its relationship to depositional environment and relative sea-level fluctuations (Upper Cretaceous Marshybank Formation, Alberta and British Columbia). Sedimentology 42, 161–190. https://doi.10.1111/j.1365-3091.1995.tb01276.x.

Mead, R., Xu, Y., Chong, J., Jaffé, R., 2005. Sediment and soil organic matter source assessment as revealed by the molecular distribution and carbon isotopic composition of n-alkanes. Org. Geochem. 36, 363–370. https://doi.org/10.1016/j.orggeochem.2004.10.003.

Meyers, P.A., 1997. Organic geochemical proxies of paleoceanographic, paleolimnologic, and paleoclimatic processes. Org. Geochem. 27, 213–250. https://doi:10.1016/s0146-6380(97)00049-1.

MGSH – Mining and Geological Survey of Hungary, Digital coal cadastre of Hungary. https://map.mbfsz.gov.hu/coal_cadastre/ (accessed on 13 January 2020).

Milota, K., Kovacs, A., Galicz, Z., 1995. Petroleum potential of the North Hungarian Oligocene sediments. Petrol. Geosci. 1, 81–87. https://doi:10.1144/petgeo.1.1.81.

Moldowan, J.M., Fago, F.J., Lee, C.J., Jacobson, S.R., Watt, D.S., Slougui, N.E., Jeganathan, A., Young, D.C., 1990. Sedimentary 24-n-propylcholestanes, molecular fossils diagnostic of marine algae. Science 247, 309–312. https://doi:10.1126/science.247.4940.309.

Monthioux, M., Landais, P., 1989. Natural and artificial maturation of coal: non-hopanoid biomarkers. Chem. Geol. 77, 71–85. https://doi.org/10.1016/0009-2541(89)90017-x.

Morad, S., 1998. Carbonate cementation in sandstones: distribution patterns and geochemical evolution. Sp. Pub. IAS. 26, 1–26. https://doi.org/10.1002/9781444304893.ch1.

Morad, S., De Ros, L.F., Nystuen, J.P., Bergan, M., 1998. Carbonate diagenesis and porosity evolution in sheet-flood sandstones: evidence from the Middle and Lower Lunde Members (Triassic) in the Snorre Field, Norwegian North Sea, in: Morad, S. (Ed.), Carbonate cementation in sandstones. Blackwell Science Ltd., Cambridge, pp., 53–85. https://doi.10.1002/9781444304893.ch3.

Morad, S., Ismail, H.N.B., De Ros, L.F., Al-Aasm, I.S., Serrhini, N.-E., 1994. Diagenesis and formation water chemistry of Triassic reservoir sandstones from southern Tunisia. Sedimentology 41, 1253–1272. https://doi.10.1111/j.1365-3091.1994.tb01452.x.

Morad, S., Ketzer, J.M., De Ros, L.F., 2000. Spatial and temporal distribution of diagenetic alterations in siliciclastic rocks: implications for mass transfer in sedimentary basins. Sedimentology 47, 95–120. https://doi:10.1046/j.1365-3091.2000.00007.x.

Morris, J.E., Hampson, G.J., Johnson, H.D., 2006. A sequence stratigraphic model for an intensely bioturbated shallow-marine sandstone: the Bridport Sand Formation, Wessex Basin, UK. Sedimentology, 53, 1229–1263, https://doi.org/10.1111/j.1365-3091.2006.00811.x.

Mortillaro, J.M., Passarelli, C., Abril, G., Hubas, C., Alberic, P., Artigas, L. F., Benedetti, M.F., Thiney, N., Moreira-Turcq, P., Perez, M.A.P., Vidal, L.O., Meziane, T., 2016. The fate of C4 and C3 macrophyte carbon in central Amazon floodplain waters: Insights from a batch experiment. Limnol. 59, 90–98. https://doi.10.1016/j.limno.2016.03.008.

Mount, J., 1985. Mixed siliciclastic and carbonate sediments: a proposed first-order textural and compositional classification. Sediment. 32. 435–442. https://doi.org/10.1111/j.1365-3091.1985.tb00522.x.

Munz, I.A., 2001. Petroleum inclusions in sedimentary basins: systematics, analytical methods and applications. Lithos 55, 195–212. https://doi.10.1016/s0024-4937(00)00045-1.

Murray, A.P., Summons, R.E., Boreham, C.J., Dowling, L.M., 1994. Biomarker and n-alkane isotope profiles for Tertiary oils: relationship to source rock depositional setting. Org. Geochem. 22, 521–542. https://doi:10.1016/0146-6380(94)90124-4.

Nagymarosy, A., 1983. Mono- and duospecific nannofloras in Early Oligocene sediments of Hungary. Palaeontology Proceedings B86, 273–283.

Nagymarosy, A., 2012. Hungarian Palaeogene Basin. In: Haas, J. (Ed.), Geology of Hungary. Springer, p. 83–102. https://doi:10.1007/978-3-642-21910-8.

Nagymarosy, A., 2013. Hungarian Palaeogene Basin, in: Haas, J. (Ed.), Geology of Hungary, Springer, pp. 83–102. https://doi:10.1007/978-3-642-21910-8.

Nagymarosy, A., Báldi-Beke, M., 1988. The position of the Paleogene Formations of Hungary in the standard Nannoplankton zonation. — Annales Universitatis Scientiarum Budapestinensis de Rolando Eötvös Nominatae Sectio Geologica 28, 3–25.

Nagymarosy, A., Báldi, T., Horváth, M., 1986. The Eocene/Oligocene boundary in Hungary. Dev. Palaentol. Stratigr. 113–116. https://doi:10.1016/s0920-5446(08)70103-1.

Nagymarosy, A., Hámor, G., 2012. Genesis and evolution of the Pannonian Basin, in: Haas, J. (Ed.), Geology of Hungary, 149–200. https://doi:10.1007/978-3-642-21910-8_3.

Nedkvitne, T., Karlsen, D.A., Bjørlykke, K., Larter, S.R., 1993. Relationship between reservoir diagenetic evolution and petroleum emplacement in the Ula Field, North Sea. Mar. Pet. Geol. 10. 255–270. https://doi.10.1016/0264-8172(93)90108-5.

Needham, S.J., Worden, R.H., McIlroy, D., 2005. Experimental production of clay rims by macrobiotic sediment ingestion and excretion processes. J. Sediment. Res. 75, 1028–1037. https://doi.org/10.2110/jsr.2005.078.

Némedi Varga, Z., 2010. Kőszénföldtan. A magyarországi kőszénelőfordulások áttekintésével és bibliográfiájával. Bíbor kiadó, Miskolc. (in Hungarian)

Nott, C.J., Xie, S., Avsejs, L.A., Maddy, D., Chambers, F.M., Evershed, R.P., 2000. n-Alkane distributions in ombrotrophic mires as indicators of vegetation change related to climate variation. Org. Geochem. 31, 231–235. https://doi.org/10.1016/s0146-6380(99)00153-9.

Nytoft, H.P., Samuel, O.J., Kildahl-Andersen G., Johansen, J.E., Jones, M., 2009. Novel C15 sesquiterpanes in Niger Delta oils: structural identification and potential application as new markers of angiosperm input in light oils. Org. Geochem. 40, 595–603. https://doi.org/10.1016/j.orggeochem.2009.02.003.

Odden, W., Barth, T., Talbot, M.R., 2002. Compound-specific carbon isotope analysis of natural and artificially generated hydrocarbons in source rocks and petroleum fluids from offshore Mid-Norway. Org. Geochem. 33, 47–65. https://doi:10.1016/s0146-6380(01)00127-9.

O'Leary, M.H., 1981. Carbon isotope fractionation in plants. Phytochemistry 20, 553–567. https://doi:10.1016/0031-9422(81)85134-5.

O'Neil, J.R., Clayton, R.N., Mayeda, T.K., 1969. Oxygen isotope

Orr, W.L., 1977. Geologic and geochemical controls on the distribution of hydrogen sulfide in natural gas, in: Campos, R., Gobi, J. (Eds.), Advances in Organic Geochemistry, Enadimsa, Madrid, pp. 571–597.

Otto, A., Walther, H., Püttmann, W., 1997. Sesqui- and diterpenoid biomarkers preserved in Taxodium-rich Oligocene oxbow lake clays, Weisselster basin, Germany. Org. Geochem. 26, 105–115. https://doi:10.1016/s0146-6380(96)00133-7.

Otto, A., Wilde, V., 2001. Sesqui-, di-, and triterpenoids as chemosystematic markers in extant conifers – A review. Bot. Rev. 67, 141–238. https://doi.org/10.1007/bf02858076.

Ou, W., Guo, H., Lu, W., Wu, X., Chou, I.-M., 2015. A re-evaluation of the effects of temperature and NaCl concentration on quantitative Raman spectroscopic measurements of dissolved CH4 in NaCl aqueous solutions: Application to fluid inclusion analysis. Chem. Geol. 417. 1–10. https://doi.10.1016/j.chemgeo.2015.09.018.

Ourisson, G., Albrecht, P., Rohmer, M., 1979. The hopanoids. Pure Appl. Chem. 51, 709–729.

Ozsvárt, P., Kocsis, L., Nyerges, A., Győri, O., Pálfy, J., 2016. The Eocene-Oligocene climate transition in the Central Paratethys. Palaeogeogr. Palaeoclimatol. Palaeoecol. 459, 471–487. https://doi:10.1016/j.palaeo.2016.07.034.

Palermo, D., Aigner, T., Geluk, M., Poeppelreiter, M., Pipping, K., 2008. Reservoir potential of a mixed carbonate / siliciclastic gas reservoir: the Lower Triassic Rogenstein in the Netherlands. J. Pet. Geol. 31, 61–96. https://doi.org/10.1111/j.1747-5457.2008.00407.x.

Palotai, M., 2013. Oligocene−Miocene tectonic evolution of the central part of the Mid-Hungarian Shear Zone. Doctoral dissertation, Eötvös Loránd University, Budapest.

Palotai, M., Csontos, L., 2010. Strike-slip reactivation of a Paleogene to Miocene fold and thrust belt along the central part of the Mid-Hungarian Shear Zone. Geol. Carpath. 61, 4833–493. https://doi.org/10.2478/v10096-010-0030-3.

Papp, K., 1913. Les ressources houilléres de la Hongrie, in: McInnes, W., Dowling, D.B., Leach, W.W. (eds.), The coal resource of the world, Morang and CO Limited, Toronto.

Pearson, E.J., Farrimond, P., Juggins, S., 2007. Lipid geochemistry of lake sediments from semi-arid Spain: Relationships with source inputs and environmental factors. Org. Geochem. 38, 1169–1195. https://doi.10.1016/j.orggeochem.2007.02.007.

Pedentchouk, N., Turich, C., 2017. Carbon and hydrogen isotopic compositions of *n*-alkanes as a tool in petroleum exploration. in: Lawson, M., Formolo, M.J., EILER, J.M. (Eds.), From Source to seep: geochemical applications in hydrocarbon systems. Geological Society, London, Special Publications 468, 105–125. https://doi.org/10.1144/SP468.1.

Pelikán, P., 2005. Mesozoic, in: Pelikán, P. (ed.), Geology of the Bükk mountains, Explanatory book of the geological map of the Bükk Mountains (1:50 000), Hungarian Geological Society, Budapest, pp. 187–204.

Pepper, A.S., Corvi, P.J., 1995. Simple kinetic models of petroleum formation. Part I: oil and gas generation from kerogen. Mar. Petrol. Geol. 12, 291–319. https://doi:10.1016/0264-8172(95)98381-e.

Peters, K.E., 1986. Guidelines for evaluating petroleum source rocks using programmed pyrolysis. AAPG Bull. 70, 318–329. https://doi.org/10.1306/94885688-1704-11d7-8645000102c1865d.

Peters, K.E., Cassa, M.R., 1994. Applied source rock geochemistry. in: Magoon, L.B., Dow, G.W. (eds.), The petroleum system – from source to trap. AAPG Mem. 60, Tulsa, Oklahoma, pp 93–120.

Peters, K.E., Hackley, P.C., Thomas, J.J., Pomerantz, A.E., 2018. Suppression of vitrinite reflectance by bitumen generated from liptinite during hydrous pyrolysis of artificial source rock. Org. Geochem. 125, 220–228. https://doi.org/10.1016/j.orggeochem.2018.09.010.

Peters, K.E., Moldowan, J.M., 1991. Effects of source, thermal maturity, and biodegradation on the distribution and isomerization of homohopanes in petroleum. Org. Geochem. 17, 47–61. https://doi:10.1016/0146-6380(91)90039-m.

Peters, K.E., Moldowan, J.M., 1993. Interpreting molecular fossils in petroleum and ancient sediments. The biomarker guide. Prentice Hall, Englewood Cliffs, N.J.

Peters, K.E., Moldowan, J.M., Driscole, A.R., Demaison, G.J., 1989. Origin of Beatrice oil by co-sourcing from Devonian and Middle Jurassic source rocks, inner Moray Firth, United Kingdom. AAPG Bull. 73, 454–471. https://doi.org/10.1306/c9ebcd51-1735-11d7-8645000102c1865d.

Peters, K.E., Snedden, J.W., Sulaeman, A., Sarg, J.F., Enrico, R.J., 2000. A new geochemical-sequence stratigraphic model for the Mahakam Delta and Makassar Slope, Kalimantan, Indonesia. AAPG Bull. 84, 12–44. https://doi.org/10.1306/e4fd386f-1732-11d7-8645000102c1865d.

Peters, K.E., Walters, C.C., Moldowan, J.M., 2005. The biomarker guide, second ed. Cambridge University Press, Cambridge.

Petersen H.I., Ratanasthien, B., 2011. Coal facies in a Cenozoic paralic lignite bed, Krabi Basin, southern Thailand: Changing peat-forming conditions related to relative sea-level controlled watertable variations. Int. J. Coal Geol. 87, 2–12. https://doi.org/10.1016/j.coal.2011.04.004.

Petrash, D.A., Bialik, O.M., Bontognali, T.R.R., Vasconcelos, C., Roberts, J.A., McKenzie, J.A., Konhauser, K.O., 2017. Microbially catalyzed dolomite formation: From near-surface to burial. Earth-Sci. Rev. 171, 558–582. https://doi.org/10.1016/j.earscirev.2017.06.015.

Pettijohn, F.J., Potter, P.E., Siever, R., 1973. Sand and sandstone, first ed. Springer-Verlag, New York, Heidelberg, Berlin.

Pickel, W., Kus, J., Flores, D., Kalaitzidis, S., Christanis, K., Cardott, B., Misz-Kennan, M., Rodrigues, S., Hentschel, A., Hamor-Vido, M., Crosdale, P., Wagner, N., ICCP, 2017. Classification of liptinite – ICCP System 1994. Int. J. Coal Geol. 169, 40–61. https://doi.org/10.1016/j.coal.2016.11.004.

Ping, H., Chen, H., George, S.C., Li, C., Hu, S., 2019. Relationship between the fluorescence color of oil inclusions and thermal maturity in the Dongying Depression, Bohai Bay Basin, China: Part 1. Fluorescence evolution of oil in the context of hydrous pyrolysis experi-

ments with increasing maturity. Mar. Pet. Geol. 100, 1–19. https://doi.10.1016/j.marpetgeo.2018.10.053.

Poppe, L.J., Paskevich, V.F., Hathaway, J.C., Blackwood, D.S., 2001. A Laboratory Manual for X-Ray Powder Diffraction. USGS Open-File Report 01-041. 88 p.

Popov, S.V., Akhmetiev, M.A., Bugrova, E.M., Lopatin, A.V., Amitrov, O.V., Andreeva-Grigorovich, A.S., Zherikhin, V.V., Zaporozhets, N.I., Nikolaeva, I.A., Krasheninnikov, V.A., Kuzmicheva, E.I., Sytchevskaya, E.K., Shcherba, I.G., 2001. Biogeography of the Northern Peri-Tethys from the Late Eocene to the Early Miocene: Part 1. Late Eocene. Paleontol. J. 35, Supp. Ser. 1, S1–S68.

Popov, S.V., Rögl, F., Rozanov, A.Y., Steininger, F.F., Shcherba, I.G., Kovac, M., 2004. Lithological-Palaeogeographic maps of Paratethys: 10 maps Late Eocene to Pliocene. Courier Forschungsinstitut Senckenberg, Frankfurt.

Poros, Zs., Mindszenty, A., Molnár, F., Pironon, J., Győri, O., Ronchi, P., Szekeres, Z., 2011. Imprints of hydrocarbon-bearing basinal fluids on a karst system: mineralogical and fluid inclusion studies from the Buda Hills, Hungary. Int. J. Earth Sci. 101, 429–452. https://doi.10.1007/s00531-011-0677-8.

Powers, M.C., 1953. A new roundness scale for sedimentary particles. J. Sediment. Petrol. 23. 117–119. https://doi.org/10.1306/d4269567-2b26-11d7-8648000102c1865d.

Radke, M., Hilkert, A., Rullkötter, J., 1998. Molecular stable carbon isotope compositions of alkylphenanthrenes in coals and marine shales related to source and maturity. Org. Geochem. 28, 785–795. https://doi:10.1016/s0146-6380(98)00048-5.

Radke, M., Schaefer, R.G., Leythaeuser, D., Teichmüller, M., 1980a. Composition of soluble organic matter in coals: relation to rank and liptinite fluorescence. Geochim. Cosmochim. Acta 44, 1787–1800. https://doi.org/10.1016/0016-7037(80)90228-8.

Radke, M., Welte, D.H., 1983. The Methylphenanthrene Index (MPI): A maturity parameter based on aromatic hydrocarbons. In: Bjoroy, M. (Ed.) Advances in Org. Geochem., Wiley, Chichester, pp. 504–512.

Radke, M., Welte, D.H., Willsch, H., 1982. Geochemical study of a well in the Western Canada Basin: relation of aromatic distribution pattern to maturity of organic matter. Geochim. Cosmochim. Acta 46, 1–10. https://doi.org/10.1016/0016-7037(82)90285-x.

Radke, M., Willsch, H., Welte, D.H., 1980b. Preparative hydrocarbon group type determination by automated medium pressure liquid chromatography. Anal. Chem. 52, 406–411. https://doi.org/10.1021/ac50053a009.

Radovics, B.G., Körmös, S., Schubert, F., 2017. A magyar Paleogén-medence szénhidrogén rendszere és eocén tárolóinak kihívása – hatástanulmány (The hydrocarbon system of the Hungarian Palaeogene Basin and the challenges oft he Eocene reservoirs), in: Dégi, J., Király, E., Kónya, P., Kovács, I.J., Pál-Molnár, E., Thamóné-Bozsó, E., Török, K., Udvardi, B. (Eds.), Ahol az elemek találkoznak: víz, föld és tűz határán. MFGI, Budapest, pp. 147–149. (in Hungarian).

Rahman, M.J.J., Worden, R.H., 2016. Diagenesis and its impact on the reservoir quality of Miocene sandstones (Surma Group) from the Bengal Basin, Bangladesh. Mar. Pet. Geol. 77, 898–915. https://doi.10.1016/j.marpetgeo.2016.07.027.

Rákosi, L., 1978. A magyarországi eocén mangrove palinológiai adatai (Données palynologiques de la mangrove éocène de Hongrie). Annual report of the Hungarian Geological Institute of 1976, 357–374. (in Hungarian with extended French summary)

Richter, D.K., Füchtbauer, H., 1978. Ferroan calcite replacement indicates former magnesian calcite skeletons. Sedimentology 25, 843–860. https://doi.10.1111/j.1365-3091.1978.tb00332.x.

Rieley, G., Collier, R.J., Jones, D.M., Eglinton, G., Eakin, P.A., Fallick, A.E., 1991. Sources of sedimentary lipids deduced from stable carbon-isotope analyses of individual compounds. Nature 352, 425–427. https://doi:10.1038/352425a0.

Rögl, F., 1999. Mediterranean and Paratethys. Facts and hypotheses of an Oligocene to Miocene paleogeography (short overview). Geol. Carpath. 50, 339–349.

Rohmer, M., 1993. The biosynthesis of triterpenoids of the hopane series in the Eubacteria: A mine of new enzymatic reactions. Pure App. Chem. 65, 1293–1298. https://doi:10.1351/pac199365061293.

Rooney, M.A., Vuletich, A.K., Griffith, C.E., 1998. Compound-specific isotope analysis as a tool for characterising mixed oils: an example from the West of Shetlands area. Org. Geochem. 29, 241–254. https://doi:10.1016/s0146-6380(98)00136-3.

Rowland, S.J., 1990. Production of acyclic isoprenoid hydrocarbons by laboratory maturation of methanogenic bacteria. Org. Geochem. 15, 9–16. https://doi.org/10.1016/0146-6380(90)90181-X.

Sachsenhofer, R.F., Gratzer, R., Bechtel, A., 2019. Application of compound-specific carbon isotope analysis to improved oil-source correlations in the Paratethys area, in: Tari, G., Sachsenhofer, R.F. (Eds.), Paratethys petroleum systems between Central Europe and the Caspian region, AAPG, Wien, pp. 14.

Sachsenhofer, R.F., Popov, S.V., Bechtel, A., Coric, S., Francu, J., Gratzer, R., Grunert, P., Kotarba, M., Mayer, J., Pupp, M., Rupprecht, B.J., 2018a. Oligocene and Lower Miocene source rocks in the Paratethys: Palaeogeographic and stratigraphic controls. in: Simmons, M. (Ed.), Petroleum Geology of the Black Sea. Geol. Soc. Spec. Publ. 464, 267–306. https://doi.org/10.1144/SP464.1.

Sachsenhofer, R.F., Popov, S.V., Coric, S., Mayer, J., Misch, D., Morton, M.T., Pupp, M., Rauball, J., Tari, G., 2018b. Paratethyan petroleum source rocks: an overview. J. Petrol. Geol. 41, 219–245. https://doi:10.1111/jpg.12702.

Sachsenhofer, R.F., Shymanovskyy, V.A., Bechtel, A., Gratzer, R., Horsfield, B., Reischenbacher, D., 2010. Palaeozoic source rocks in the Dniepr–Donets Basin, Ukraine. Petrol. Geosci. 16, 377–399. https://doi:10.1144/1354-079309-032.

Saigal, G.C., Bjørlykke, K., 1987. Carbonate cements in clastic reservoir rocks from offshore Norway – relationships between isotopic composition, textural development and burial depth, in: Marshall, J.D. (Ed.), Diagenesis of sedimentary sequences. Geol. Soc. Spec. Publ. 36, 313–324. https://doi.10.1144/gsl.sp.1987.036.01.22.

Schmid, S.M., Bernoulli, D., Fügenschuh, B., Matenco, L., Schefer, S., Schuster, R., Tischler, M., Ustaszewski, K., 2008. The Alpine-Carpathian-Dinaridic orogenic system: correlation and evolution of tectonic units. Swiss J. Geosci. 101, 139–183. https://doi:10.1007/s00015-008-1247-3.

Schoell, M., 1984. Stable Isotopes in Petroleum Research. Advances in Petroleum Geochemistry, 215–245. https://doi:10.1016/b978-0-12-032001-1.50009-2.

Schoell, M., Simoneit, B.R.T., Wang, T.G., 1994. Org. Geochem. and coal petrology of tertiary brown coal in the Zhoujing mine, Baise Basin, South China—4. Biomarker sources

inferred from stable carbon isotope compositions of individual compounds. Org. Geochem. 21, 713–719. https://doi:10.1016/0146-6380(94)90014-0.

Scholle, P.A., Ulmer-Scholle, D.S., 2003. A color guide to the petrography of carbonate rocks: grains, textures, porosity, diagenesis. AAPG, Tulsa, Oklahoma, USA. https://doi.10.1306/m77973.

Schulz, H.-M, Bechtel, A., Sachsenhofer, R.F., 2005. The birth of the Paratethys during the Early Oligocene: From Tethys to an ancient Black Sea analogue? Global Planet. Change 49, 163–176. https://doi:10.1016/j.gloplacha.2005.07.001.

Schulz, H.-M., Sachsenhofer, R.F., Bechtel, A., Polesny, H., Wagner, L., 2002. The origin of hydrocarbon source rocks in the Austrian Molasse Basin (Eocene–Oligocene transition). Mar. Pet. Geol. 19, 683–709. https://doi:10.1016/s0264-8172(02)00054-5.

Schwarzbauer, J., Littke, R., Meier, R., Strauss, H., 2013. Stable carbon isotope ratios of aliphatic biomarkers in Late Palaeozoic coals. Int. J. Coal Geol. 107, 127–140. https://doi:10.1016/j.coal.2012.10.001.

Seifert, W.K., Moldowan, J.M., 1978. Applications of steranes, terpanes and monoaromatics to the maturation, migration and source of crude oils. Geochim. Cosmochim. Acta 42, 77–95. https://doi:10.1016/0016-7037(78)90219-3.

Seifert, W.K., Moldowan, J.M., 1980. The effect of thermal stress on source-rock quality as measured by hopane stereochemistry. Physics and Chemistry of the Earth 12, 229–237. https://doi.org/10.1016/0079-1946(79)90107-1.

Seifert, W. K., Moldowan, J. M., 1986. Use of biological markers in petroleum exploration, in: Johns, R.B. (Ed.), Methods in geochemistry and geophysics 24. Elsevier, Amsterdam, pp. 261–290.

Shah, S.R., Griffith, D.R., Galy, V., McNichol, A.P., Eglinton, T.I., 2013. Prominent bacterial heterotrophy and sources of ^{13}C-depleted fatty acids to the interior Canada Basin. Biogeosci. 10, 7065–7080. https://doi.10.5194/bg-10-7065-2013.

Shepherd, T.J., Rankin, A.H., Alderton, D.H.L., 1985. A practical guide to fluid inclusion studies. Blackie, Glasgow.Sieskind, O., Joly, G., Albrecht, P., 1979. Simulation of the geochemical transformation of sterols: superacid effect of clay minerals. Geochim. Cosmochim. Acta 43, 1675–1680. https://doi.org/10.1016/0016-7037(79)90186-8.

Simoneit, B.R.T., Grimalt, J.O., Wang, T.G., Cox, R.E., Hatcher, P.G., Nissenbaum, A., 1986. Cyclic terpenoids of contemporary resinous plant detritus and of fossil woods, amber and coal. Org. Geochem. 10, 877–889. https://doi.org/10.1016/s0146-6380(86)80025-0.

Simoneit, B.R.T., Schoell, M., Stefanova, M., Stojanova, G., Nosyrev, I.E., Goranova, M., 1995. Composition of the extract from a Carboniferous bituminous coal. 2. Compound-specific isotope analyses. Fuel 74, 1194–1199. https://doi:10.1016/0016-2361(95)00038-7.

Shepherd, T.J., Rankin, A.H., Alderton, D.H.L., 1985. A practical guide to fluid inclusion studies. Blackie, Glasgow.

Smith, T., Guild, J., 1931. The C.I.E. colorimetric standards and their use. Trans. Opt. Soc. 33. 73–134.

Sofer, Z., 1984. Stable carbon isotope compositions of crude oils: application to source depositional environments and petroleum alteration. AAPG Bull. 68, 31–49. https://doi.org/10.1306/ad460963-16f7-11d7-8645000102c1865d.

Spötl, C., Pitman, J.K., 1998. Saddle (baroque) dolomite in carbonates and sandstones: a reappraisal of a burial-diagenetic concept, in: Morad, S. (Ed.), Carbonate cementation in sandstones. Blackwell Science Ltd., Cambridge, pp. 437–460. https://doi.10.1002/9781444304893.ch19.

Spötl, C., Vennemann, T.W., 2003. Continuous-flow isotope ratio mass spectrometric analysis of carbonate minerals. Rapid Commun. Mass Spectrom. 17. 1004–1006. https://doi.10.1002/rcm.1010.

Stasiuk, L.D., Snowdon, L.R., 1997. Fluorescence micro-spectrometry of synthetic and natural hydrocarbon fluid inclusions: crude oil chemistry, density and application to petroleum migration. Appl. Geochem. 12, 229–241. https://doi.10.1016/s0883-2927(96)00047-9.

Stock, A.T., Littke, R., Lücke, A., Zieger, L., Thielemann, T., 2016. Miocene depositional environment and climate in western Europe: The lignite deposits of the Lower Rhine Basin, Germany. Int. J. Coal Geol. 157, 2–18. https://doi:10.1016/j.coal.2015.06.009.

Strachan, M.G., Alexander, R., Kagi, R.I., 1988. Trimethylnaphthalenes in crude oils and sediments: Effects of source and maturity. Geochim. Cosmochim. Acta 52, 1255–1264. https://doi:10.1016/0016-7037(88)90279-7.

Sukh Dev, 1989. Terpenoids. In: Rowe, J.W. (Ed.), Natural Products of Woody Plants, vol. 1. Springer, Berlin, pp. 691–807.

Summons, R.E., Volkman, J.K., Boreham, C.J., 1987. Dinosterane and other steroidal hydrocarbons of dinoflagellate origin in sediments and petroleum. Geochim. Cosmochim. Acta, 51, 3075–3082. https://doi.10.1016/0016-7037(87)90381-4.

Sweeney, R.E., Kaplan, I.R., 1973. Pyrite framboid formation: laboratory synthesis and marine sediments. Econ. Geol. 68, 618–634. https://doi.org/10.2113/gsecongeo.68.5.618.

Sykes, R., Snowdon, L.R., 2002. Guidelines for assessing the petroleum potential of coaly source rocks using Rock-Eval pyrolysis. Org. Geochem. 33, 1441–1455. https://doi:10.1016/s0146-6380(02)00183-3.

Sztanó, O., Tari, G., 1993. Early Miocene basin evolution in Northern Hungary: tectonics and eustasy. Tectonophysics 261, 485–502. https://doi.org/10.1016/0040-1951(93)90134-6.

Talbot, H.M., McClymont, E.L., Inglis, G.N., Evershed, R.P., Pancost, R.D., 2016. Origin and preservation of bacteriohopanepolyol signatures in Sphagnum peat from Bissendorfer Moor (Germany). Org. Geochem. 97, 95–110. https://doi:10.1016/j.orggeochem.2016.04.011.

Tao, S., Wang, C., Du, J., Liu, L., Chen, Z., 2015. Geochemical application of tricyclic and tetracyclic terpanes biomarkers in crude oils of NW China. Mar. Pet. Geol. 67, 460–467. https://doi.org/10.1016/j.marpetgeo.2015.05.030.

Tari, G., Báldi, T., Báldi-Beke, M., 1993. Paleogene retroarc flexural basin beneath the Neogene Pannonian Basin: A geodynamic model. Tectonophysics 226, 433–455. https://doi:10.1016/0040-1951(93)90131-3.

Taylor, G.H., Teichmüller, M., Davis, A., Diessel, C.F.K., Littke, R., Robert, P., 1998. Organic Petrology. Gebrüder Bontraeger, Berlin.

Teece, M.A., Fogel, M.L., Dollhopf, M.E., Nealson, K.H., 1999. Isotopic fractionation associated with biosynthesis of fatty acids by a marine bacterium under oxic and anoxic conditions. Org. Geochem. 30, 1571–1579. https://doi.10.1016/s0146-6380(99)00108-4.

Tindall, J., Flecker, R., Valdes, P., Schmidt, D.N., Markwick, P., Harris, J., 2010. Modelling the oxygen isotope distribution of ancient seawater using a coupled ocean–atmosphere GCM: Implications for reconstructing early Eocene climate. Earth Planet. Sci. Lett. 292. 265–273. https://doi.10.1016/j.epsl.2009.12.049.

Tissot, B.T., Welte, D.H., 1984. Petroleum Formation and Occurrences. Springer, Berlin.

Tuo, J., Wang, X., Chen, J., Simoneit, B.R.T., 2003. Aliphatic and diterpenoid hydrocarbons and their individual carbon isotope compositions in coals from the Liaohe Basin, China. Org. Geochem. 34, 1615–1625. https://doi:10.1016/j.orggeochem.2003.08.004.

Viczián, I., 1987. Clay minerals of the sedimentary rocks in Hungary. Academic Doctoral Dissertation. Hungarian Academy of Sciences, Budapest (in Hungarian).

Viczián, I., 1995. Clay minerals in Mesozoic and Paleogene sedimentary rocks of Hungary. Rom. J. Mineral. 77, 35–44.

Volk, H., George, S.C., 2019. Using petroleum inclusions to trace petroleum systems – A review. Org. Geochem.129, 99–123. https://doi.10.1016/j.orggeochem.2019.01.012.

Volkman, J.K., 1986. A review of sterol markers for marine and terrigenous organic matter. Org. Geochem. 9, 83–99. https://doi.org/10.1016/0146-6380(86)90089-6.

Volkman, J.K., Allen, D.I., Stevenson, P.L., Burton, H.R., 1986. Bacterial and algal hydrocarbons from a saline Antarctic lake, Ace Lake. Org. Geochem. 10, 671–681. https://doi.org/10.1016/s0146-6380(86)80003-1.

Volkman, J.K., Barrett, S.M., Blackburn, S.I., 1999. Eustigmatophyte microalgae are potential sources of C_{29} sterols, C_{22}–C_{28} *n*-alcohols and C_{28}–C_{32} *n*-alkyl diols in freshwater environments. Org. Geochem. 30, 307–318. https://doi.org/10.1016/S0146-6380(99)00009-1.

Volkman, J.K., Maxwell, J.R., 1986. Acyclic isoprenoids as biological markers, in: Johns, R.B. (Ed.), Biological markers in the sedimentary record. Elsevier, New York, pp. 1–42.

Wakeham, S.G., Amann, R., Freeman, K.H., Hopmans, E.C., Jørgensen, B.B., Putnam, I.F., Schouten, S., Sinninghe Damsté, J.S., Talbot, H.M., Woebken, D., 2007. Microbial ecology of the stratified water column of the Black Sea as revealed by a comprehensive biomarker study. Org. Geochem. 38, 2070–2097. https://doi.10.1016/j.orggeochem.2007.08.003.

Wakeham, S.G., Schaffner, C., Giger, W., 1980. Polycyclic aromatic hydrocarbons in recent lake sediments. II. Compounds derived from biological precursors during early diagenesis. Geochim. Cosmochim. Acta 44, 415–429. https://doi.org/10.1016/0016-7037(80)90041-1.

Warren, J., 2000. Dolomite: occurrence, evolution and economically important associations. Earth Sci. Rev. 52, 1–81. https://doi.org/10.1016/s0012-8252(00)00022-2.

Wilhelms, A., Larter, S.R., Hall, K., 1994. A comparative study of the stable carbon isotopic composition of crude oil alkanes and associated crude oil asphaltene pyrolysate alkanes. Org. Geochem. 21, 751–759. https://doi.org/10.1016/0146-6380(94)90017-5.

Wilkins, R.V.T., George, S.C., 2002. Coal as a source rock for oil: a review. Int. J. Coal Geol. 50, 317–361. https://doi.org/10.1016/s0166-5162(02)00134-9.

Wilson, M.J., 1992. Inherited grain-rimming clays in sandstones from eolian and shelf environments: their origin and control on reservoir properties, in: Houseknecht, D.W., Pittman, E.D. (Eds.), Origin, diagenesis, and petrophysics of clay minerals in sandstones. SEPM Spec. Publ. 47, pp. 209–225. https://doi.org/10.2110/pec.92.47.0209.

Wilson, M.D., Pittman, E.D., 1977. Authigenic clays in sandstones: recognition and influence on reservoir properties and paleoenvironmental analysis. J. Sediment. Petrol. 47, 3–31. https://doi.org/10.1306/212f70e5-2b24-11d7-8648000102c1865d.

Wingert, W.S., Pomerantz, M., 1986. Structure and significance of some twenty-one and twenty-two carbon petroleum steranes. Geochim. Cosmochim. Acta, 50, 2763–2769. https://doi:10.1016/0016-7037(86)90225-5.

Wolff, G.A., Lamb, N.A., Maxwell, J.R., 1986. The origin and fate of 4-methyl steroid hydrocarbons. I. Diagenesis of 4-methyl sterenes. Geochim. Cosmochim. Acta 50, 335–342. https://doi:10.1016/0016-7037(86)90187-0.

Woodhouse, A.D., Oung, J.-N., Philp, R.P., Weston, R.J., 1992. Triterpanes and ring-A degraded triterpanes as biomarkers characteristic of Tertiary oils derived from predominantly higher plant sources. Org. Geochem. 18, 23–31. https://doi:10.1016/0146-6380(92)90140-s.

Worden, R.H., Morrall, G.T., Kelly, S., Mc Ardle, P., Barshep, D.V., 2019. A renewed look at calcite cement in marine-deltaic sandstones: the Brent Reservoir, Heather Field, northern North Sea, UK, in: Dowey, P.J., Osborne, M., Volk, H., (Eds.), Application of analytical techniques to petroleum systems, Geol. Soc. London, Spec. Publ. 484, pp. 305–335. https://doi.10.1144/sp484-2018-43

Worden, R.H., Burley, S.D., 2003. Sandstone diagenesis: the evolution of sand to stone, in: Burley, S.D., Worden, R.H. (Eds.), Sandstone diagenesis: recent and ancient. Blackwell Publishing Ltd. pp. 1–44. https://doi.10.1002/9781444304459.ch.

Worden, R.H., Morad, S., 2003. Clay minerals in sandstones: controls on formation, distribution and evolution, in: Worden, R.H., Morad, S. (Eds.), Clay mineral cements in sandstones, Blackwell Publishing Ltd. pp. 1–41. https://doi.10.1002/9781444304336.ch1.

Xiao, H., Li, M., Liu, J., Mao, F., Cheng, D., Yang, Z., 2019. Oil-oil and oil-source rock correlations in the Muglad Basin, Sudan and South Sudan: New insights from molecular markers analyses. Mar. Pet. Geol. 103, 351–365. https://doi:10.1016/j.marpetgeo.2019.03.004.

Xiao, H., Wang, T.-G., Li, M., Fu, J., Tang, Y., Shi, S., Yang, Z., Lu, X., 2018. Occurrence and distribution of unusual tri- and tetracyclic terpanes and their geochemical significance in some Paleogene oils from China. Energy Fuels 32, 7393–7403. https://doi.org/10.1021/acs.energyfuels.8b01025.

Zhu, J., Poulsen, C.J., Otto-Bliesner, B.L., Liu, Z., Brady, E.C., Noone, D.C., 2020. Simulation of early Eocene water isotopes using an Earth system model and its implication for past climate reconstruction. Earth Planet. Sci. Lett. 537, 116164. https://doi.10.1016/j.epsl.2020.116164.

Supplementary figures

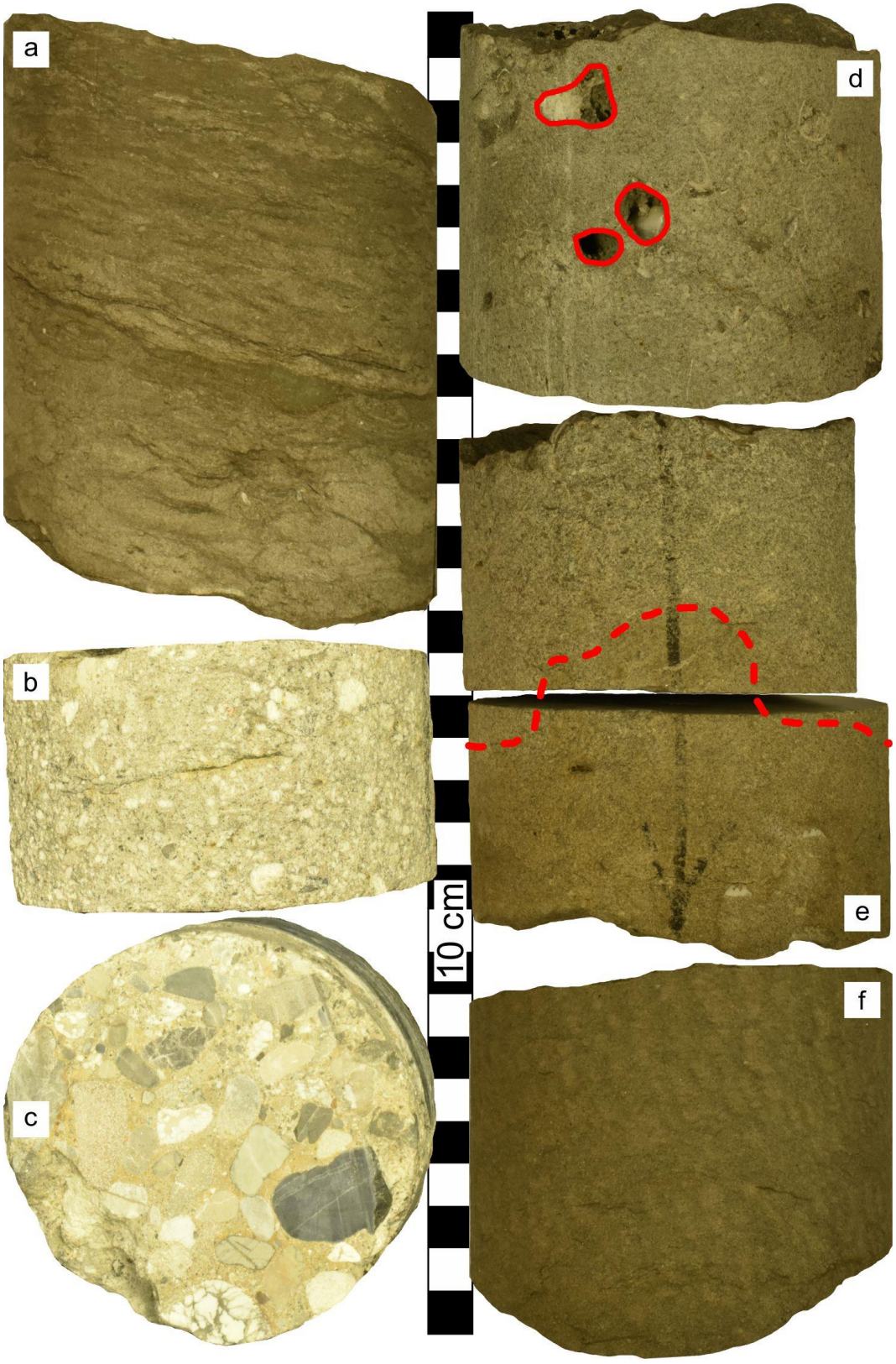

Supplementary Fig. 1. Representative drill cores, collected for the study. Detailed caption is provided on page 132.

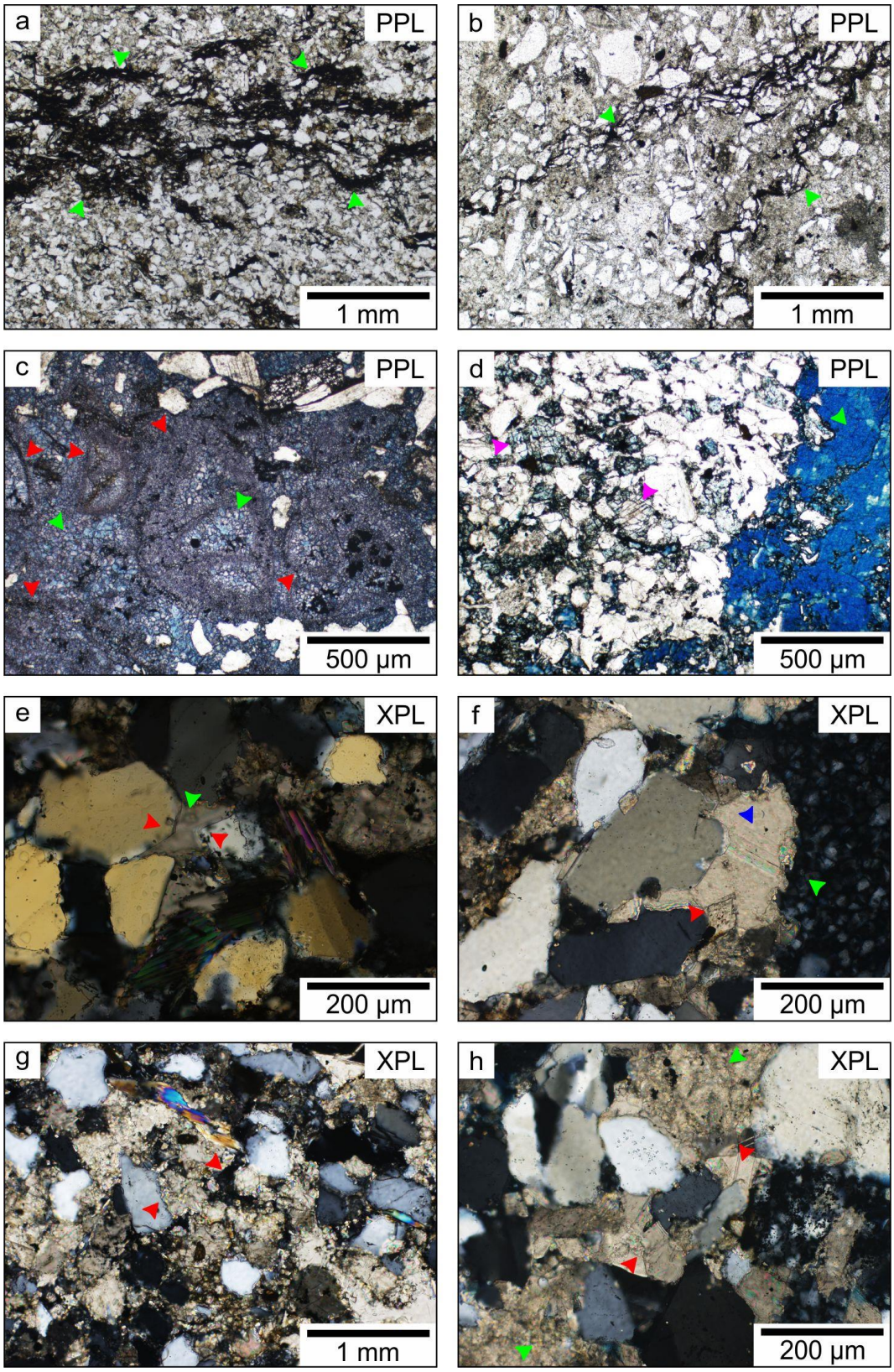

Supplementary Fig. 2. Photomicrographs of the investigated samples. Detailed caption is provided on page 132.

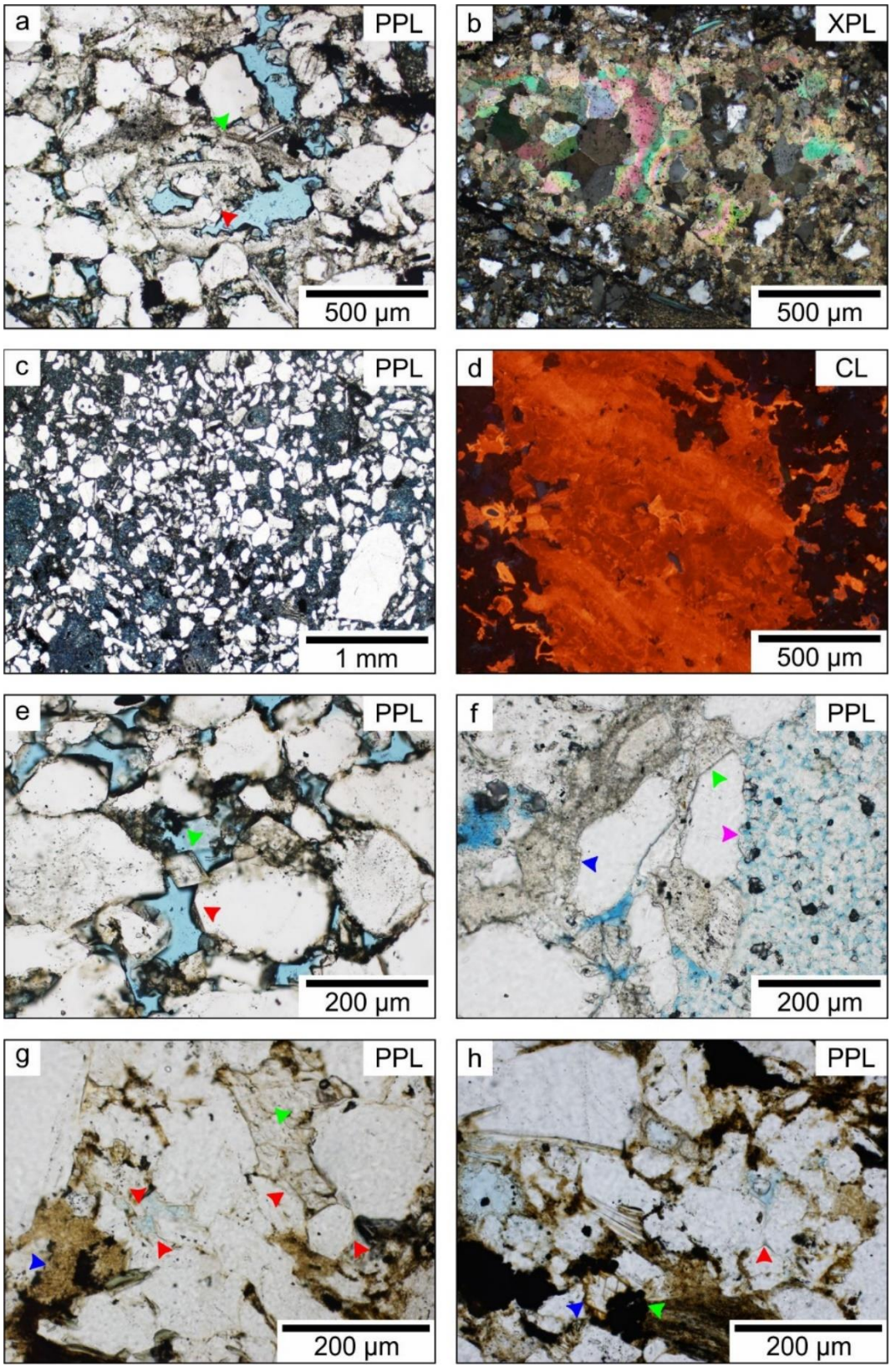

Supplementary Fig. 3. Photomicrographs of the investigated samples. Detailed caption is provided on page 132.

Supplementary Fig. 1. Representative drill cores examined for this study. **a)** Siltstone is interbedded with sandstone; the bedding is destroyed by bioturbation. **b)** Sandstone with granules and pebbles. **c)** Grain-supported conglomerate. **d)** A structureless sandstone (quartz wacke) with cm-sized biomoldic pores partially filled by calcite. Red curves highlight the moldic pores. **e)** The sharp contact of the thick-bedded and structureless sandstone (wacke) and oil-impregnated sandstone (arenite). The contact is highlighted by a red dashed line. **f)** An oil-impregnated massive and structureless sandstone (quartz arenite).

Supplementary Fig. 2. Photomicrographs of the investigated samples. Bitumen-impregnated dissolution seems in **a)** very fine-grained (W–1; 2504.1 m MD) and **b)** fine-to-medium-grained sandstones (W–1; 2468.1 m MD). **c)** Bioclasts marked by micritic envelope and purple-stained calcite (red arrows), the pore space is filled with blue-stained equant calcite (green arrows; W–1; 2461.8 m MD). **d)** Blue-stained ferroan calcite-filled fracture (green arrow) along with medium-crystalline and zoned, non-ferroan and turquoise-stained ferroan dolomite (purple arrows) cemented arenite (W–15; 2354.5 m MD). **e)** Syntaxial quartz overgrowths (red arrows) pointing towards pores, filled with calcite spar (green arrow; W–1; 2455.3 m MD). **f)** Calcite replaces detrital quartz grains (blue arrow), embays dolomite rhomb (red arrow) and shows pitted margins, filled with kaolin crystals (green arrow; W–1; 2455.3 m MD). **g)** Sparry calcite cemented arenite; red arrows point to calcite replacing detrital quartz grains. (W–15; 2354.5 m MD). **h)** The size of the calcite crystals changes from a micro spar (green arrows) to a medium-grained spar (red arrow; W–1; 2455.3 m MD).

Supplementary Fig. 3. Photomicrographs of the investigated samples. **a)** Partially drusy calcite-filled biomold (red arrow). The skeletal grain is highlighted by a micritic envelope (green arrow; W–1; 2455.3 m MD). **b)** Drusy calcite-filled pore (W–1; 2596.8 m MD). **c)** Ferroan-calcite (blue-stained) cemented wacke (W–1; 2461.8 m MD). **d)** Orange luminescent calcite-filled fracture, showing zonation, highlighted by dull and bright bands (W–9; 2811.0 m MD). **e)** Quartz cement forms syntaxial overgrowths (red arrow) pointing towards pores, filled with blue epoxy. Well-developed dolomite rhombs (green arrow) are engulfed by quartz overgrowths (W–1; 2455.3 m MD). **f)** Calcite replaces detrital quartz grain (blue arrow), whereas kaolinite sits in embayed quartz surfaces (pink arrow). Well-developed crystal facets of quartz overgrowths are surrounded by calcite (green arrow). The same view then on Fig. IV.6c. (W–1; 2455.3 m MD). **g)** Syntaxial quartz overgrowths and discrete prismatic crystal (red arrows) pointing towards pores, filled with blue epoxy. The contacts between quartz overgrowths pointed out by brownish coloured clay minerals. Densely packed, brown kaolin crystals (blue arrow) and calcite spar (green arrow) occlude intergranular pore spaces (W–9; 2809.5 m MD). **h)** Syntaxial quartz overgrowths (red arrow) pointing towards pores. Subhedral pyrite crystals (green arrow) consume dolomite rhomb (blue arrow; W–9; 2810.0 m MD and 2810.5 m MD, respectively).

Supplementary tables

Supplementary Table 1. The bulk geochemical parameters of investigated samples from well W–1.

Fms	ID	Depth	TOC	S1	S2	HI	PP	PI	Tmax
	#	[m; MD]	[wt%]	[mg HC/g rock]		[mg HC/g TOC]	[mg HC/g rock]		[°C]
Kiscell Clay	1	2100.0	0.52	0.0	0.4	81	0.43	0.02	434
	2	2120.0	0.48	0.0	0.3	69	0.34	0.03	434
	3	2130.0	0.46	0.0	0.4	83	0.39	0.03	435
	4	2140.0	0.42	0.0	0.3	79	0.34	0.03	438
	5	2150.0	0.38	0.0	0.3	82	0.32	0.03	435
	6	2160.0	0.43	0.0	0.4	93	0.41	0.02	438
	7	2170.0	0.36	0.0	0.3	75	0.28	0.04	437
	8	2180.0	0.42	0.0	0.3	69	0.30	0.03	435
	9	2190.0	0.16	0.0	0.1	56	0.09	0.00	434
	10	2200.0	0.33	0.0	0.2	55	0.19	0.05	434
	11	2210.0	0.31	0.0	0.2	71	0.23	0.04	435
	12	2220.0	0.31	0.0	0.2	61	0.20	0.05	433
	13	2230.0	0.33	0.0	0.2	70	0.23	0.00	435
	14	2240.0	0.41	0.0	0.3	73	0.31	0.03	439
Buda Marl	15	2250.0	0.41	0.0	0.3	80	0.34	0.03	437
	16	2260.0	0.44	0.0	0.3	77	0.35	0.03	442
	17	2270.0	0.44	0.0	0.4	91	0.42	0.05	439
	18	2280.0	0.37	0.0	0.3	84	0.32	0.03	435
	19	2290.0	0.38	0.0	0.3	82	0.32	0.03	441
	20	2300.0	0.39	0.0	0.3	82	0.33	0.03	438
	21	2310.0	0.40	0.0	0.4	98	0.40	0.03	439
	22	2320.0	0.40	0.0	0.3	75	0.30	0.00	439
	23	2330.0	0.31	0.0	0.2	74	0.24	0.04	438
	24	2340.0	0.27	0.0	0.2	70	0.19	0.00	438
	25	2350.0	0.25	0.0	0.1	44	0.11	0.00	439
	26	2360.0	0.30	0.0	0.2	63	0.20	0.05	438
	27	2370.0	0.21	0.0	0.2	71	0.15	0.00	442
	28	2380.0	0.17	0.0	0.1	35	0.06	0.00	444
	29	2390.0	0.26	0.0	0.1	38	0.10	0.00	443
	30	2400.0	0.28	0.0	0.1	46	0.13	0.00	442
	31	2410.0	0.23	0.0	0.1	35	0.08	0.00	439
Kosd	32	2420.0	0.69	0.1	1.3	193	1.40	0.05	440
	33	2430.0	0.63	0.3	0.6	95	0.90	0.33	443
	34	2450.0	0.35	0.0	0.7	200	0.74	0.05	442
	35	2470.0	0.41	0.0	0.5	115	0.51	0.08	445
	36	2490.0	0.62	0.1	0.5	84	0.60	0.13	442
	37	2497.0	0.73	0.2	0.8	114	1.00	0.17	442
	38	2502.0	1.63	0.4	1.8	111	2.17	0.17	442
	39	2510.0	0.37	0.0	0.3	84	0.34	0.09	444
	40	2530.0	0.30	0.0	0.3	107	0.35	0.09	446
	41	2550.0	0.24	0.0	0.2	100	0.26	0.08	447
	42	2570.0	0.40	0.1	0.3	75	0.36	0.17	448
	43	2575.0	0.65	0.2	0.6	98	0.80	0.20	443
	44	2580.0	0.32	0.1	0.4	109	0.46	0.24	442
	45	2585.0	2.00	0.9	3.7	185	4.54	0.19	445
	46*	2590.0	29.55	10.0	71.9	243	81.83	0.12	441
	47*	2590.2	7.23	2.5	20.9	289	23.39	0.11	443
	48*	2594.4	0.39	0.1	0.1	36	0.21	0.33	439
	49*	2594.6	12.72	3.8	31.9	251	35.65	0.11	441
	50*	2594.9	1.45	0.7	1.0	68	1.66	0.40	439
	51	2595.0	13.25	5.1	38.7	292	43.71	0.12	441
	52*	2596.8	0.51	0.5	0.3	66	0.87	0.61	446
	53*	2599.0	1.04	0.4	0.4	39	0.75	0.47	431
	54*	2599.9	78.39	23.4	186.3	238	209.64	0.11	443
	55*	2600.0	2.94	1.1	3.0	103	4.14	0.27	443

Fms	ID	Depth	TOC	S1	S2	HI	PP	PI	Tmax
	#	[m; MD]	[wt%]	[mg HC/g rock]		[mg HC/g TOC]	[mg HC/g rock]		[°C]
Kosd	56	2600.0	20.46	9.2	71.2	348	80.42	0.11	447
	57*	2600.6	2.89	1.5	2.9	101	4.42	0.34	445
	58*	2600.9	45.70	14.6	133.1	291	147.61	0.10	441
	59*	2601.0	3.84	1.8	6.6	171	8.40	0.22	448
	60*	2601.2	25.04	9.3	66.1	264	75.45	0.12	440
	61*	2601.4	2.96	1.1	4.9	165	6.05	0.19	446
	62*	2602.0	21.82	6.6	53.8	247	60.37	0.11	438
	63	2602.0	2.54	1.1	4.8	188	5.82	0.18	450
	64*	2602.4	0.97	0.9	0.8	82	1.67	0.52	444
	65*	2604.1	0.78	0.4	0.7	92	1.16	0.38	443
	66*	2604.9	57.17	17.2	130.8	229	147.97	0.12	444
	67*	2605.0	0.82	0.5	0.9	107	1.41	0.38	444
	68	2610.0	5.10	2.0	13.4	263	15.39	0.13	448
	69	2630.0	1.57	1.1	3.2	204	4.31	0.26	448
	70	2650.0	4.05	1.9	9.1	224	10.94	0.17	442
	71	2670.0	0.42	0.1	0.6	138	0.67	0.13	444
	72	2695.0	0.22	0.1	0.2	86	0.24	0.21	444
	73	2710.0	0.20	0.0	0.1	55	0.13	0.15	447
	74	2730.0	0.32	0.1	0.2	69	0.27	0.19	447
	75	2750.0	0.47	0.0	0.3	66	0.33	0.06	451
	76	2770.0	0.52	0.0	0.4	77	0.44	0.09	442
	77	2790.0	0.10	0.0	0.1	50	0.05	0.00	443

Fms – formations, TOC – total organic carbon content, S1 – free hydrocarbons, S2 – hydrocarbons generated during Rock-Eval pyrolysis, HI – hydrogen Index, PP – petroleum potential, PI – production index, Tmax – temperature of maximum hydrocarbon generation, MD – measured depth, * – drill core sample.

Supplementary Table 2. The bulk geochemical parameters of investigated samples from well W–9.

Fms	ID	Depth	TOC	S1	S2	HI	PP	PI	Tmax
	#	[m, MD]	[wt%]	[mg HC/g rock]		[mg HC/g TOC]	[mg HC/g rock]		[°C]
Kiscell Clay	1	1800	0.54	0.1	0.5	87	0.52	0.10	427
	2	1820	0.59	0.0	0.4	73	0.47	0.09	428
	3	1840	0.59	0.0	0.6	93	0.59	0.07	428
	4	1860	0.64	0.0	0.5	84	0.57	0.05	428
	5	1880	0.64	0.0	0.5	75	0.51	0.06	430
	6	1900	0.65	0.0	0.5	77	0.54	0.07	429
	7	1920	0.71	0.1	0.6	82	0.63	0.08	432
	8	1940	0.71	0.1	0.6	83	0.64	0.08	428
	9	1960	0.71	0.1	0.8	115	0.88	0.07	430
	10	1980	0.67	0.1	0.6	90	0.67	0.10	429
	11	2000	0.66	0.1	0.6	86	0.64	0.11	428
	12	2020	0.66	0.0	0.6	94	0.65	0.05	431
	13	2040	0.69	0.1	0.8	122	0.90	0.07	434
	14	2060	0.65	0.1	0.7	111	0.78	0.08	432
	15	2080	0.65	0.1	0.7	105	0.74	0.08	431
	16	2100	0.71	0.1	0.9	121	0.94	0.09	432
	17	2120	0.65	0.1	0.7	106	0.74	0.07	433
	18	2140	0.62	0.1	0.6	100	0.69	0.10	433
	19	2160	0.69	0.1	0.8	120	0.91	0.09	432
	20	2180	0.66	0.1	0.8	123	0.88	0.08	433
	21	2200	0.50	0.1	0.7	130	0.72	0.10	432
	22	2220	0.52	0.1	0.5	102	0.59	0.10	429
	23	2240	0.44	0.1	0.5	109	0.54	0.11	431
	24	2260	0.52	0.1	0.6	117	0.67	0.09	432
	25	2300	0.35	0.1	0.2	69	0.29	0.17	433
	26	2320	0.35	0.0	0.3	83	0.32	0.09	431
	27	2340	0.41	0.1	0.6	144	0.64	0.08	431
	28	2360	0.33	0.1	0.3	88	0.37	0.22	433
	29	2380	0.28	0.0	0.3	111	0.35	0.11	433
	30	2400	0.24	0.0	0.3	104	0.29	0.14	429
	31	2420	0.27	0.0	0.2	81	0.24	0.08	432
	32	2430	0.30	0.0	0.3	90	0.29	0.07	434
	33	2440	0.29	0.0	0.3	97	0.30	0.07	434
	34	2460	0.23	0.0	0.2	91	0.24	0.13	432
	35	2480	0.21	0.0	0.2	76	0.18	0.11	435
	36	2490	0.27	0.0	0.2	89	0.27	0.11	434
Tard Clay	37	2500	0.28	0.0	0.3	89	0.28	0.11	434
	38	2510	0.34	0.0	0.2	65	0.25	0.12	435
	39	2520	0.26	0.0	0.2	77	0.24	0.17	437
	40	2530	0.25	0.0	0.2	76	0.20	0.05	435
	41	2540	0.22	0.0	0.2	73	0.19	0.16	437
	42	2550	0.21	0.1	0.1	57	0.17	0.29	437
	43	2560	0.15	0.1	0.1	87	0.18	0.28	435
	44	2570	0.19	0.0	0.1	68	0.16	0.19	435
	45	2580	0.19	0.1	0.1	63	0.17	0.29	434
Buda Marl	46	2600	0.21	0.0	0.1	52	0.12	0.08	437
	47	2610	1.66	0.4	2.6	159	3.07	0.14	433
	48	2620	1.37	0.3	2.3	168	2.61	0.12	432
	49	2630	1.34	0.6	2.8	205	3.33	0.17	437
	50	2640	1.27	0.7	3.2	255	3.94	0.18	438
	51	2650	0.96	0.8	2.7	282	3.50	0.23	437
	52	2660	0.90	0.5	2.7	300	3.21	0.16	440
	53	2670	0.89	0.8	2.9	325	3.67	0.21	440
	54	2680	0.88	2.5	2.6	293	5.08	0.49	437
	55	2690	0.71	0.4	1.4	200	1.78	0.20	441
	56	2700	0.96	0.5	2.5	264	3.05	0.17	439
	57	2710	1.08	0.7	2.7	254	3.42	0.20	440

Fms	ID	Depth	TOC	S1	S2	HI	PP	PI	Tmax
	#	[m, MD]	[wt%]	[mg HC/g rock]		[mg HC/g TOC]	[mg HC/g rock]		[°C]
Buda Marl	58	2720	1.52	0.9	3.9	256	4.74	0.18	437
	59	2730	1.55	0.9	4.0	256	4.86	0.18	437
	60	2740	0.65	0.3	1.6	242	1.86	0.16	441
	61	2750	1.12	0.6	2.0	175	2.55	0.23	439
	62	2760	1.14	1.4	2.8	247	4.17	0.32	441
	63	2770	1.61	0.8	2.1	133	2.89	0.26	438
	64	2780	2.59	5.3	5.3	203	10.55	0.50	435
	65	2790	0.73	0.7	1.6	223	2.34	0.30	442
Kosd	66	2800	0.32	0.2	0.5	153	0.67	0.27	438
	67	2810	1.84	2.6	3.2	173	5.76	0.45	437
	68	2820	0.41	0.2	0.5	110	0.69	0.35	437
	69	2830	0.63	0.3	0.9	135	1.19	0.29	440
	70	2840	1.07	0.9	2.3	214	3.19	0.28	435
	71	2850	0.59	0.3	0.9	158	1.26	0.26	439
	72	2860	0.53	0.3	0.8	153	1.08	0.25	437
	73	2880	0.58	0.3	0.7	124	0.98	0.27	440
	74	2890	1.18	0.7	1.6	137	2.32	0.30	434
	75	2900	0.82	0.3	1.2	140	1.49	0.23	442
	76	2910	0.37	0.2	0.5	146	0.74	0.27	441
	77	2920	0.47	0.2	0.7	138	0.88	0.26	431
	78	2930	0.30	0.1	0.3	113	0.45	0.24	438
	79	2940	0.31	0.1	0.3	84	0.38	0.32	437
	80	2950	0.13	0.0	0.1	54	0.10	0.30	–
	81	2960	0.13	0.0	0.0	31	0.06	0.33	–
	82	2970	0.30	0.1	0.2	57	0.26	0.35	–

Fms – formations, TOC – total organic carbon content, S1 – free hydrocarbons, S2 – hydrocarbons generated during Rock-Eval pyrolysis, HI – hydrogen Index, PP – petroleum potential, PI – production index, Tmax – temperature of maximum hydrocarbon generation, MD – measured depth.

Supplementary Table 3. The bulk geochemical parameters of investigated samples from well W–12.

Fms	ID	Depth	TOC	S1	S2	HI	PP	PI	Tmax
	#	[m; MD]	[wt%]	[mg HC/g rock]		[mg HC/g TOC]	[mg HC/g rock]		[°C]
Kiscell Clay	1	1960.0	0.44	0.1	1.2	282	1.32	0.06	431
	2	1970.0	0.41	0.0	0.6	139	0.59	0.03	432
	3	1980.0	0.35	0.0	0.4	126	0.46	0.04	433
	4	1990.0	0.38	0.0	0.4	95	0.37	0.03	432
	5	2000.0	0.39	0.0	0.4	97	0.40	0.05	433
	6	2010.0	0.41	0.1	0.9	220	0.96	0.06	–
	7	2020.0	0.41	0.1	0.9	327	1.43	0.06	–
	8	2030.0	0.40	0.1	1.3	188	0.79	0.05	–
	9	2040.0	0.49	0.0	0.8	237	1.29	0.10	–
	10	2050.0	0.26	0.1	1.2	277	0.78	0.08	–
	11	2060.0	0.48	0.1	0.7	265	1.44	0.12	–
	12	2070.0	0.39	0.2	1.2	256	1.13	0.12	–
	13	2080.0	0.46	0.2	1.3	180	0.92	0.10	–
	14	2090.0	0.40	0.1	1.0	135	0.61	0.11	–
	15	2100.0	0.30	0.1	0.8	110	0.35	0.06	431
	16	2110.0	0.37	0.1	0.5	127	0.51	0.08	–
	17	2120.0	0.35	0.1	0.6	123	0.46	0.07	–
	18	2130.0	0.51	0.0	0.3	186	1.02	0.07	419
	19	2140.0	0.32	0.0	0.4	116	0.40	0.08	–
	20	2150.0	0.33	0.0	0.5	152	0.57	0.12	–
	21	2150.0	0.34	0.0	0.4	171	0.65	0.11	–
	22	2160.0	0.46	0.1	1.0	146	0.76	0.12	–
	23	2170.0	0.44	0.0	0.4	145	0.70	0.09	–
	24	2180.0	0.36	0.1	0.5	94	0.36	0.06	432
	25	2190.0	0.34	0.1	0.6	124	0.45	0.07	425
	26	2200.0	0.32	0.1	0.7	100	0.33	0.03	431
	27	2210.0	0.37	0.1	0.6	130	0.51	0.06	431
	28	2220.0	0.38	0.1	0.6	63	0.24	0.00	435
	29	2230.0	0.36	0.0	0.3	92	0.33	0.00	433
Tard Clay	30	2235.0	1.35	0.0	0.4	378	5.71	0.11	437
	31	2240.0	1.43	0.0	0.3	418	6.57	0.09	438
	32	2245.0	1.71	0.0	0.5	411	7.91	0.11	437
	33	2250.0	1.89	0.0	0.2	439	9.31	0.11	436
	34	2255.0	1.42	0.0	0.3	377	6.07	0.12	436
	35	2260.0	1.38	0.6	5.1	372	5.77	0.11	438
	36	2265.0	1.15	0.6	6.0	307	3.96	0.11	438
	37	2270.0	0.94	0.9	7.0	280	2.93	0.10	439
	38	2275.0	0.94	1.0	8.3	249	2.64	0.11	438
	39	2280.0	0.76	0.7	5.4	270	2.25	0.09	439
	40	2285.0	0.76	0.6	5.1	243	2.04	0.09	438
	41	2290.0	0.92	0.4	3.5	189	1.94	0.10	439
	42*	2294.6	1.48	0.4	3.4	232	3.84	0.10	439
	43*	2296.5	0.94	0.3	1.8	186	2.05	0.14	439
	44*	2296.8	0.89	0.6	1.7	193	2.28	0.25	440
	45*	2297.6	0.99	0.4	1.9	187	2.24	0.17	441
	46*	2298.1	0.79	0.4	1.5	189	1.90	0.21	439
	47	2300.0	0.81	0.3	2.6	314	2.81	0.10	438
Buda Marl	48	2305.0	0.31	0.3	2.3	194	0.61	0.02	437
	49	2310.0	0.21	0.2	2.1	119	0.25	0.00	437
	50	2315.0	0.06	0.2	1.9	117	0.07	0.00	436
	51	2320.0	0.21	0.2	1.7	33	0.07	0.00	434
	52	2325.0	0.04	0.3	2.5	225	0.10	0.10	437
	53	2330.0	0.26	0.0	0.6	77	0.24	0.17	436
	54	2335.0	0.18	0.0	0.3	50	0.09	0.00	435
	55	2340.0	0.27	0.0	0.1	119	0.37	0.14	438
	56	2345.0	0.24	0.0	0.1	63	0.19	0.21	437
	57	2350.0	0.71	0.0	0.1	165	1.47	0.20	438

Fms	ID	Depth	TOC	S1	S2	HI	PP	PI	Tmax
	#	[m; MD]	[wt%]	[mg HC/g rock]		[mg HC/g TOC]	[mg HC/g rock]		[°C]
Buda Marl	58	2355.0	2.61	0.0	0.2	271	8.16	0.13	430
	59	2360.0	2.65	0.0	0.1	258	7.90	0.14	433
	60	2365.0	0.34	0.1	0.3	88	0.33	0.09	437
	61	2370.0	0.30	0.0	0.2	117	0.37	0.05	434

Fms – formations, TOC – total organic carbon content, S1 – free hydrocarbons, S2 – hydrocarbons generated during Rock-Eval pyrolysis, HI – hydrogen Index, PP – petroleum potential, PI – production index, Tmax – temperature of maximum hydrocarbon generation, MD – measured depth, * – drill core sample.

Supplementary Table 4. Modal composition based on counting 400 points in each thin section, following the Gazzi-Dickinson point-counting method (Ingersoll et al., 1984) and porosity of the investigated samples (Boncz, 2013).

Well	ID	a	b	c	d	e	f	g	h	i	j	k	l	m	n	o	p	q	r	s	t	u	v	w	x
	[#]	[%]																							
Well–9	1	31.9	12.6	6.6	1.8	2.0	11.2	1.0	1.4	3.4	2.4	1.2	6.4	0.4	0.6	0.4	0.0	0.4	0.0	0.2	9.4	arg.	1.0	8.1	8.8
	2	30.3	27.3	3.4	1.0	0.4	13.7	0.8	2.6	2.0	1.2	0.4	5.0	0.0	0.2	1.2	0.0	0.2	0.0	0.4	7.5	arg.	0.0	n.d.	9.2
	3	31.1	19.2	3.4	0.6	0.2	11.8	0.2	0.4	2.0	2.2	1.4	5.4	0.0	0.2	0.8	0.0	0.0	0.4	2.0	11.4	arg.	1.8	n.d.	9.6
	4	32.8	18.3	2.6	0.4	0.0	2.4	0.4	1.6	0.4	2.2	0.8	2.6	0.8	1.0	12.9	0.0	0.0	0.4	10.9	4.2	arg.	2.2	7.4	9.1
	5	43.8	27.6	4.1	0.0	0.0	3.4	0.0	0.0	4.1	8.9	0.9	0.5	0.0	0.2	0.2	0.0	1.1	0.0	0.0	3.4	arg.	0.7	2.0	12.1
	6	37.3	32.4	3.0	0.0	0.0	5.3	0.0	0.0	3.0	6.2	1.5	1.9	0.0	0.4	0.9	0.0	1.9	0.0	0.0	4.3	arg.	1.1	4.2	9.3
	7	22.6	11.4	2.2	0.0	0.0	10.8	0.0	24.6	3.0	8.5	1.0	1.4	0.0	0.4	11.2	0.0	0.0	0.0	0.8	2.0	arg.	0.2	0.4	16.5
	8	19.1	8.4	1.2	0.2	0.0	12.2	0.0	21.1	4.2	11.4	0.8	0.6	0.0	0.2	12.7	0.0	0.0	0.0	0.6	7.4	calc.	0.0	0.5	19.9
Well–14	9	40.2	20.2	2.4	0.0	0.0	0.6	0.0	3.1	0.0	0.6	0.0	3.1	0.2	0.0	6.1	1.6	0.0	2.7	5.5	12.7	arg.±calc.	0.2	5.1	9.0
	10	38.4	15.5	2.7	0.0	0.0	0.4	0.0	3.9	0.0	0.4	0.0	4.3	0.2	0.4	7.5	1.6	0.0	4.5	5.7	14.4	arg.±calc.	0.4	8.5	9.3
	11	36.9	20.5	4.2	0.0	0.0	1.0	0.0	6.2	0.0	1.2	0.0	2.0	0.0	0.0	5.0	1.4	0.0	2.0	4.0	14.0	arg.±calc.	0.2	7.0	8.8
	12	38.0	18.1	3.9	0.0	0.0	0.6	0.0	3.7	0.0	0.4	0.0	3.7	0.2	0.2	5.5	1.0	0.0	3.5	4.9	12.8	arg.±calc.	0.4	5.6	5.9
	13	28.4	13.9	1.0	0.0	0.0	4.4	2.2	17.5	2.6	2.0	1.8	0.2	0.0	0.6	8.5	0.0	1.2	13.5	0.0	1.0	arg.	0.8	12.1	16.5
	14	29.0	12.5	2.2	0.0	0.0	4.7	1.5	18.2	0.9	0.6	0.7	2.2	0.0	0.9	9.7	0.2	1.7	10.5	0.0	2.8	arg.	1.1	n.d.	17.3
	15	26.4	14.3	1.5	0.0	0.0	3.6	1.5	17.5	1.5	1.7	0.8	1.7	0.0	1.1	6.5	0.2	2.9	14.3	0.0	2.3	arg.	1.5	11.8	15.6
	16	34.2	12.1	1.4	0.0	0.0	5.9	0.6	17.8	1.8	2.2	1.6	1.0	0.2	0.6	9.2	0.0	1.6	6.5	0.0	1.6	arg.	0.8	11.4	11.8
Well–1	17	65.5	1.0	7.5	0.1	0.0	12.7	0.0	0.0	0.2	0.3	0.0	0.9	0.1	0.8	6.5	0.2	0.0	0.0	0.5	2.9	arg.	0.8	4.3	13.2
	18	26.7	0.0	1.9	0.3	0.0	4.3	0.0	0.4	0.0	0.3	0.0	0.4	0.4	1.8	34.6	0.0	0.0	1.1	2.2	25.4	calc.	0.4	1.9	4.4
	19	19.0	2.6	4.6	0.0	0.0	6.7	0.0	0.7	0.0	0.0	0.0	0.5	0.3	1.3	33.3	0.0	0.0	0.4	3.6	26.1	calc.	0.6	1.9	4.4
	20	70.6	0.0	4.8	0.0	0.0	8.7	0.3	0.3	0.0	0.6	0.0	0.9	0.2	0.8	3.4	0.1	0.0	0.0	2.2	2.5	arg.	4.6	12.2	4.6
	21	31.4	0.0	1.6	0.0	0.0	7.1	0.3	0.4	0.0	0.4	0.0	0.6	0.1	1.1	30.7	0.0	0.0	0.3	0.5	25.2	calc.	0.5	2.4	6.0
	22	25.9	0.9	1.8	0.0	0.0	0.6	0.0	0.0	0.0	0.1	0.0	0.4	0.1	0.8	42.1	0.0	0.0	0.5	2.5	24.1	calc.	0.2	6.2	8.1
	23	17.8	1.3	3.9	0.0	0.0	3.4	0.0	0.4	0.0	0.2	0.0	1.0	0.3	0.8	40.6	0.0	0.0	0.0	2.0	28.3	calc.	0.0	6.2	8.1
	24	10.8	0.0	2.8	0.1	0.0	8.0	0.0	0.6	0.2	0.1	0.0	0.3	0.2	0.5	42.9	0.1	0.0	0.3	7.3	25.0	calc.	0.6	12.4	11.3
	25	13.3	0.0	5.7	0.0	0.0	8.7	0.0	0.9	0.0	0.0	0.0	0.3	0.1	0.5	38.3	0.1	0.0	0.4	4.9	26.4	calc.	0.4	n.d.	11.4
	26	32.0	1.9	5.5	0.0	0.0	1.4	0.0	0.0	0.1	0.4	0.0	0.6	0.0	1.6	29.3	0.1	0.0	0.0	1.4	23.7	calc.	2.0	n.d.	10.9
	27	37.1	2.1	6.7	0.0	0.0	8.7	0.8	0.3	0.2	0.0	0.0	0.9	0.2	1.1	23.3	0.0	0.0	0.0	2.1	16.4	calc.	0.0	n.d.	10.1
	28	27.5	0.6	3.6	0.0	0.0	0.6	0.0	0.9	0.0	0.0	0.0	1.2	0.1	1.7	37.6	0.0	0.0	0.0	0.7	25.3	calc.	0.1	12.4	11.3
	29	23.0	0.3	2.1	0.1	0.0	1.6	0.0	0.6	0.0	0.0	0.0	1.3	0.2	2.1	37.5	0.0	0.0	0.0	0.8	30.1	calc.	0.2	n.d.	10.3

Well	ID	a	b	c	d	e	f	g	h	i	j	k	l	m	n	o	p	q	r	s	t	u	v	w	x
	[#]	[%]																							
Well–1	30	75.6	0.6	4.6	0.0	0.0	1.8	0.0	0.3	0.0	0.0	0.0	1.8	0.2	1.8	7.2	0.0	0.0	0.2	1.1	4.0	arg.+calc.	0.7	n.d.	11.1
	31	62.6	2.4	7.8	0.0	0.0	8.6	0.0	1.2	0.0	0.0	0.0	1.1	0.4	2.5	10.4	0.0	0.0	0.1	0.0	2.2	arg.+calc.	0.5	12.4	11.3
	32	47.8	3.4	7.7	0.0	0.0	5.8	0.0	0.3	0.0	0.1	0.0	1.0	0.0	2.2	14.6	0.1	0.0	0.0	3.9	3.3	arg.+calc.	9.8	12.4	11.3
	33	56.4	0.3	3.2	0.0	0.0	8.2	0.0	0.0	0.0	0.8	0.0	0.4	0.1	0.9	1.1	0.2	0.0	0.2	0.5	26.4	calc.	1.1	12.5	11.3
	34	20.1	0.8	3.6	0.3	0.0	4.8	0.0	0.5	0.0	0.0	0.0	0.3	0.1	0.6	39.7	0.0	0.0	1.3	4.9	21.4	calc.	1.1	2.6	7.1
	35	13.0	0.1	3.2	0.2	0.0	6.5	0.2	0.7	0.0	0.2	0.0	0.6	0.2	0.7	44.9	0.0	0.0	0.4	4.0	24.6	calc.	1.0	2.6	7.1
	36	39.9	2.3	5.3	0.0	0.0	6.7	0.0	0.3	0.0	0.2	0.0	1.4	0.2	1.9	18.5	0.2	0.0	0.2	2.3	19.6	calc.	0.8	2.5	10.2
	37	38.0	1.9	4.1	0.2	0.0	8.0	0.0	0.2	0.0	0.2	0.0	1.3	0.2	2.3	19.4	0.2	0.0	0.0	1.4	21.4	calc.	0.9	8.3	5.3
	38	24.5	1.4	6.3	0.3	0.0	4.0	0.2	0.5	0.0	0.0	0.0	0.6	0.2	1.4	42.9	0.0	0.0	0.3	3.2	13.4	calc.	0.6	7.2	8.4
	39	45.1	0.8	4.6	0.0	0.0	6.0	0.0	0.3	0.2	0.0	0.0	1.4	0.2	2.5	11.8	0.3	0.3	0.0	2.0	23.2	calc.	1.1	9.6	11.9
	40	40.9	1.5	9.7	0.0	0.0	2.1	0.0	0.0	0.0	0.0	0.0	3.3	0.1	5.4	7.0	0.0	0.0	0.0	0.0	30.0	calc.	0.0	3.8	10.6
	41	44.0	0.0	1.7	0.1	0.0	2.1	0.1	0.0	0.0	1.5	0.0	0.7	0.0	0.6	45.7	0.0	0.0	0.0	0.4	3.3	calc.+arg.	0.0	1.4	10.3
	42	62.2	0.0	3.9	0.0	0.0	3.1	0.0	0.0	0.0	1.3	0.0	2.2	0.2	1.8	6.5	0.0	0.0	0.0	0.0	18.4	calc.	0.0	1.9	12.4
	43	52.6	1.0	6.3	0.3	0.0	4.7	0.0	0.0	0.0	1.0	0.0	2.9	0.2	4.2	10.5	0.0	0.0	0.0	0.0	15.7	calc.	0.0	3.3	12.5
	44	50.9	0.3	5.3	0.2	0.0	2.6	0.0	0.0	0.0	1.2	0.0	3.6	0.2	3.1	16.9	0.0	0.0	0.0	0.0	15.0	calc.	0.0	3.6	12.2
	45	47.1	0.2	5.9	0.3	0.0	4.4	0.2	0.0	0.0	1.2	0.0	2.9	0.2	3.0	19.2	0.0	0.0	0.0	0.2	14.8	calc.	0.0	3.1	8.6
	46	48.8	0.9	5.1	0.2	0.0	2.0	0.0	0.0	0.0	1.6	0.0	3.3	0.2	4.4	12.3	0.0	0.0	0.0	0.2	20.9	calc.	0.0	3.3	8.2
	47	51.3	0.3	4.9	0.8	0.0	5.9	0.5	0.0	0.0	1.1	0.0	2.5	0.0	2.9	26.0	0.0	0.0	0.0	0.0	3.5	calc.+arg.	0.0	2.5	11.2
	48	37.0	0.6	4.5	0.1	0.0	1.6	0.5	0.0	0.0	1.2	0.0	2.2	0.0	6.2	24.5	0.0	0.0	0.0	0.0	19.8	calc.	0.0	3.3	3.2
	49	44.3	0.2	3.9	0.3	0.0	7.8	0.0	0.0	0.0	1.2	0.0	2.9	0.1	3.9	10.2	0.0	0.0	0.0	0.0	25.0	calc.	0.0	n.d.	7.4
	50	37.0	20.1	0.6	0.2	0.0	6.2	0.2	4.4	0.0	0.0	0.0	3.0	0.4	1.4	12.7	0.0	0.0	0.0	0.4	7.6	arg.	0.0	5.0	12.2
	51	42.8	10.8	2.0	0.2	0.0	5.2	0.0	3.0	0.0	0.0	0.0	4.2	0.4	1.0	15.1	0.0	0.0	0.0	0.6	8.4	arg.	0.0	5.0	9.8
	52	47.0	6.7	1.8	0.4	0.0	8.5	0.2	1.8	0.0	0.4	0.0	4.7	0.2	1.4	16.0	0.0	0.0	0.0	0.6	5.1	arg.	0.0	2.3	10.6
	53	53.8	2.1	4.1	0.2	0.0	5.0	0.3	0.0	0.0	0.5	0.0	3.3	0.3	2.6	11.7	0.0	0.0	0.0	0.0	15.0	calc.	0.0	1.4	11.1
	54	45.6	1.2	4.4	0.2	0.0	5.8	0.3	0.2	0.0	0.0	0.0	4.8	0.3	4.9	11.8	0.0	0.0	0.0	0.0	20.1	calc.	0.0	2.7	9.2
	55	44.2	0.0	6.1	0.0	0.0	4.4	0.0	0.0	0.0	0.0	0.0	7.2	0.5	7.0	12.3	0.0	0.0	0.0	0.8	11.6	calc.±arg.	0.0	3.1	12.6
	56	42.8	0.0	6.6	0.0	0.0	2.3	0.0	0.4	0.0	0.2	0.0	9.1	0.4	6.3	5.2	0.0	0.0	0.0	0.3	21.8	calc.	0.0	n.d.	12.1
	57	44.8	0.0	3.8	0.0	0.0	7.0	0.0	0.0	0.0	0.0	0.0	8.4	0.4	8.7	9.7	0.0	0.0	0.0	0.4	15.4	calc.±arg.	0.0	2.2	12.6
	58	23.6	0.0	2.9	0.0	0.0	1.7	0.0	0.0	0.0	0.2	0.0	3.6	0.0	5.8	21.4	0.0	0.0	0.0	11.2	24.6	calc.±arg.	0.0	0.9	23.7
	59	47.8	0.0	3.6	0.0	0.0	2.5	0.0	0.0	0.0	0.2	0.0	6.3	0.3	5.3	14.2	0.0	0.0	0.0	2.0	16.4	calc.±arg.	0.0	0.3	14.2
	60	47.6	0.0	2.6	0.0	0.0	2.6	0.0	0.5	0.0	0.0	0.0	7.5	0.2	6.2	11.9	0.0	0.0	0.0	4.2	14.0	calc.±arg.	0.0	1.4	13.0
	61	41.7	0.0	3.9	0.0	0.0	2.8	0.0	0.3	0.0	0.1	0.0	6.8	0.3	4.1	12.2	0.0	0.0	0.0	9.5	15.2	calc.±arg.	0.0	0.9	9.1
	62	47.5	0.0	2.2	0.0	0.0	4.5	0.0	0.0	0.0	0.0	0.0	6.7	0.2	2.6	11.9	0.0	0.0	0.0	2.8	18.5	calc.±arg.	0.0	1.2	12.1

Well	ID	a	b	c	d	e	f	g	h	i	j	k	l	m	n	o	p	q	r	s	t	u	v	w	x
	[#]	[%]																							
Well–7	63	39.0	27.7	7.8	0.4	0.0	8.1	0.4	0.6	0.6	1.0	0.0	1.7	0.0	3.3	0.0	0.0	0.0	0.0	0.0	4.5	arg.	5.0	3.6	4.2
	64	35.2	13.2	1.2	0.6	0.0	18.0	2.2	1.0	1.4	0.6	4.2	1.2	0.0	0.8	6.9	0.0	0.0	0.4	0.0	12.8	arg.±calc.	0.2	3.3	3.7
	65	37.0	12.3	0.4	0.2	0.0	5.0	0.6	0.0	0.6	0.4	0.0	4.8	0.0	3.4	13.1	0.4	0.0	0.0	0.0	20.2	arg.+calc.	0.2	2.6	8.6
	66	37.2	11.0	1.5	0.0	1.5	4.8	0.0	0.2	0.0	0.2	0.0	3.3	0.0	1.7	0.0	0.6	0.7	0.0	0.0	29.9	arg.	1.1	2.0	6.3
	67	39.5	27.2	2.4	0.0	0.0	4.8	0.0	0.0	0.0	0.6	0.2	4.4	0.0	1.8	4.4	0.0	0.0	0.0	0.0	11.7	arg.	0.6	2.6	7.1
	68	30.5	11.0	0.8	0.2	0.0	2.6	0.0	1.2	0.0	0.2	0.2	2.0	0.0	0.8	18.2	0.0	0.0	0.0	9.5	11.0	calc.±arg	0.5	0.7	9.0
	69	31.3	14.3	2.2	0.1	0.0	3.8	0.0	0.7	0.1	0.1	0.1	3.8	0.0	1.6	13.0	0.1	0.4	0.1	7.4	8.9	calc.±arg.	0.7	1.8	4.6
	70	31.4	10.3	2.8	0.2	0.0	4.8	0.0	0.9	0.2	0.2	0.2	3.7	0.0	1.5	11.2	0.3	0.3	0.0	4.9	13.8	calc.±arg.	0.9	1.3	6.4
Well–15	71	41.2	7.2	0.5	0.0	0.0	0.3	0.0	0.2	0.0	0.0	0.0	3.5	0.3	0.8	32.1	0.0	0.0	0.0	0.0	8.9	arg.+calc.	4.6	2.5	5.7
	72	53.2	24.2	1.0	0.0	0.0	2.4	0.0	0.6	0.0	1.0	0.0	2.0	0.0	2.2	1.2	0.0	0.0	4.8	0.0	4.2	calc.±arg	0.6	7.3	5.3
	73	54.2	20.9	3.2	0.0	0.0	1.7	0.0	1.3	0.0	0.4	0.0	1.1	0.0	1.7	1.9	0.0	0.0	3.8	0.0	5.2	calc.±arg	0.0	9.1	9.9
	74	63.9	12.0	1.7	0.0	0.0	1.3	0.0	0.4	0.0	0.2	0.0	4.3	0.0	3.4	2.6	0.2	0.2	2.6	0.2	5.5	calc.±arg	0.0	9.3	8.6
	75	48.5	21.3	1.2	0.0	0.0	2.5	0.0	0.2	0.0	0.0	0.0	3.9	0.0	2.9	0.7	0.5	0.0	7.1	0.0	9.0	calc.±arg	0.0	4.3	8.6
	76	54.2	20.4	2.2	0.0	0.0	2.0	0.0	1.8	0.0	0.4	0.0	0.4	0.0	2.0	4.2	0.2	0.2	3.5	0.2	5.0	calc.±arg	0.4	3.8	12.0
	77	54.0	24.0	0.9	0.0	0.0	1.6	0.0	1.1	0.0	0.0	0.0	3.0	0.0	2.1	2.3	0.5	0.5	3.4	0.5	4.3	calc.±arg	0.2	3.7	6.3
	78	61.8	19.1	1.3	0.0	0.0	0.7	0.0	0.7	0.0	0.2	0.0	3.3	0.0	2.4	1.3	0.0	0.0	2.6	0.0	4.6	calc.±arg	0.2	6.4	6.0

a – monocrystalline quartz, b – polycrystalline quartz, c – undulose (>5°) quartz, d – plagioclase, e – potassium feldspar, f – metamorphic rock fragment, g – volcanic rock fragment, h – carbonate rock fragment, i – claystone rock fragment, j – chert fragment, k – sandstone rock fragment, l – mica (muscovite±biotite), m – heavy minerals, n –pyrite, o – diagenetic calcite, p – diagenetic dolomite, q – diagenetic quartz, r – diagenetic kaolin minerals, s – fossil fragments, t – matrix, u – type of matrix, v – porosity (2D), w – Hg-porosity, x – neutron porosity, arg. – argillaceous matrix, calc. – calcareous matrix, arg.+calc. – slight dominance of the argillaceous matrix, calc.+arg. – slight dominance of the calcareous matrix, arg.±calc. – mainly argillaceous matrix, calc.±arg – mainly calcareous matrix, n.d. – not determined.

Declaration of the Supervisor

Hereby, I certify that the contents of the Ph.D. dissertation are based on the independent work of the doctoral candidate and that he made a decisive contribution to the results with his independent creative activity. I consider the whole dissertation to be eligible for support from a professional and academic point of view, and I recommend its acceptance.,

Szeged, 29th August 2022

…….
Félix Schubert Ph.D
supervisor

This page was left blank intentionally.